

**Experimental Investigation and CFD Simulation of
Multiphase Flow in a Three Phase Pipe Separator**



By

Eyitayo Amos Afolabi

A thesis submitted for the degree of

Doctor of Philosophy

School of Chemical Engineering and Advanced Materials

Newcastle University

November, 2012

NEWCASTLE UNIVERSITY LIBRARY

210 26678 0

THESIS L10308

ABSTRACT

This thesis describes an experimental study and CFD simulation of the hydrodynamic behaviour of multiphase flow in a 30mm pipe separator. Stereoscopic particle image velocimetry (SPIV) technique was used for the three-dimensional velocity measurements of water and air water flows in a pipe separator. The instantaneous and time averaged whole field velocities at three different axial positions were recorded and velocity profiles across the diameter of the pipe separator extracted. Three-phase flow experiments were then conducted to determine the separation efficiency of the air-water-oil flow in a pipe separator. Numerical simulation of the single and multiphase flow behaviour within the separator was then performed through the commercially available CFD software ANSYS FLUENT.

The results showed that the tangential velocity profile is a combination of a forced vortex at the centre of the tube and a free vortex near the wall of the pipe separator. The axial velocity measurements showed a downward flow near the wall of the pipe separator and an upward flow near the centre of the tube. The major effect of air flow in the air-water flow appears to be an increase in the magnitude of the velocity profiles, since the flow pattern of the air-water flow is found to be the same as that of a water-only flow. It was observed that a clean water stream at the water-rich outlet of the pipe separator is achievable at high water volume fractions and low oil content. This showed the possibility that this pipe separator can function as a free water knock-out device.

A comparison of the experimental and computational results showed that good qualitative agreement was obtained at most axial positions within the pipe separator and considerable insight was gained into the flow mechanism. However, there were some discrepancies in the numerical results at some axial positions away from the inlet section. Therefore, Reynolds stress model (RSM) coupled with Eulerian multiphase model are deemed to be a good methodology for modelling the hydrodynamic behaviour and phase separation of the multiphase flow in a pipe separator system.

I would first like to express my gratitude to my supervisor, Dr J.G.M Lee, for his invaluable guidance, enthusiasm, constructive criticism and enlightening discussions during the PhD programme.

This work would not have been possible without the financial support of the PTDF overseas scholarship scheme. Thank you for giving an opportunity to pursue this work.

I gratefully acknowledge the EPSRC and TSI Inc. for their financial support and loan of the stereoscopic PIV instrument used in the research.

For advice and allowing the use of the super-computer in the School of Mechanical Engineering Fluid Lab, I must thank Dr Ian Potts.

My appreciation also goes to Mr Brian Grover, who built the experimental rig, with further thanks to Mr Stewart Latimer and Simon Daley and other technical staff in the school workshop at CEAM for their help and advice throughout the project.

I would like to thank my colleagues in Room C500 Merz court who have contributed directly or indirectly in the completion of this research.

I also thank all members of LTM and MFM church for their invaluable help and prayers throughout my study.

My sincere and profound appreciation to my parents for their patience while I have been far away from them.

Finally I want to thank my family who have supported me throughout this programme, especially my wife Kemi and two children Dorcas and David for their constant support and encouragement throughout this research.

God bless you all

TABLE OF CONTENTS

	Page
List of Figures	ix
List of Tables	xiv
Nomenclature	xv
CHAPTER ONE INTRODUCTION	
1.1 Phase Separation	1
1.2 Three Phase Flow Cylindrical Cyclone Development	4
1.3 Aim and Objectives of this Research	8
1.4 Outline of the Thesis	9
CHAPTER TWO LITERATURE REVIEW	
2.0 Introduction	10
2.1 Principles of internal Swirling Flow	10
2.2 Experimental Measurements of Swirling Flow in the Cylindrical Cyclone	12
2.3 Flow Pattern in the Cyclone Separator	17
2.3.1 Tangential Velocity	17
2.3.2 Axial Velocity	19
2.3.3 Radial Velocity	20
2.4 Numerical Simulation of Swirling Flow Fields	22
2.5 Past Work on the Gas-Liquid-Liquid Cylindrical Cyclone	28
2.6 Flow regimes in gas-liquid flows	30
2.7 Summary	32

3.1 Principles of Stereoscopic Particle Image Velocimetry (SPIV)	34
3.1.1 SPIV System	36
3.1.1.1 Tracer Particles	36
3.1.1.2 Illumination System	37
3.1.1.3 Image Recording	38
3.1.1.4 Synchronizer	38
3.1.1.5 Image Analysis and 2D Vector Validation	39
3.1.1.6 Stereoscopic Camera Configurations	39
3.1.1.7 Calibration Procedure	41
3.1.2 PIV Measurement of Multiphase Flows	42
3.1.2.1 Laser Induced Fluorescence	44
3.1.2.2 Shadow Image Technique	45
3.1.3 Sources of Error in Stereoscopic PIV Systems	46
3.2 Experimental Set-up	47
3.2.1 Experimental Facility and Flow Loop	47
3.2.2 S-PIV Set-up	54
3.2.3 Camera Calibration	58
3.2.4 S-PIV Enclosure Design	59
3.3 Measurement Strategy	61
3.3.1 Water Flow Experiment	61
3.3.2 Air-Water Flow Experiment	61
3.3.3 Air-Water-Oil Experiment	65

CHAPTER FOUR NUMERICAL SIMULATION OF TURBULENCE AND MULTIPHASE FLOW

4.1	The Navier Stokes Governing Equations	67
4.2	Numerical Analysis of Turbulence	69
4.2.1	Direct Numerical Simulation (DNS)	69
4.2.2	Reynolds Averaged Navier Stokes Models	70
4.2.2.1	Standard $k - \varepsilon$ model	71
4.2.2.2	RNG $\kappa - \varepsilon$ Model	73
4.2.2.3	Reynolds Stress Model	74
4.2.3	Large Eddy Simulation (LES)	75
4.2.4	Comparison of Different Models of Turbulence	75
4.3	Numerical Simulation of Multiphase Flow	78
4.3.1	Euler-Lagrange Approach	78
4.3.2	Euler-Euler Approach	80
4.3.2.1	The Volume of Fluid (VOF) Model	80
4.3.2.2	The Mixture Model	80
4.3.2.3	The Eulerian Model	81
4.4	Numerical Methodology	84
4.4.1	Model Geometry and Mesh	84
4.4.2	Numerical Simulation with ANSYS-FLUENT	86
4.4.2.1	Grid Independence Study	86
4.4.2.2	Single Phase Simulation	86
4.4.2.3	Multiphase Flow Simulations	89
4.4.2.3.1	Air-Water Simulations	91

4.4.2.3.2 Air-Water-Oil Simulations	92
CHAPTER FIVE: ANALYSIS OF SINGLE PHASE MEASUREMENTS	
5.1: Experimental Results and Discussion of the Single Water Phase Flow	95
5.1.1 Tangential Velocity	95
5.1.2 Axial Velocity	98
5.1.3 Radial Velocity	99
5.2 Comparison of the Numerical Simulation of the Velocity Field with the Experimental Measurements	101
5.2.1 Tangential Velocity	101
5.2.2 Axial Velocity	103
5.2.3 Radial Velocity	108
CHAPTER SIX: ANALYSIS OF AIR-WATER FLOW MEASUREMENTS	
6.1 Results and Discussion of Two Phase Flow	110
6.1.1 Tangential Velocity	110
6.1.2 Axial Velocity	117
6.1.3 Radial Velocity	122
6.2 Effect of Air Volume Fraction on the Velocity Field	127
6.3 Comparison of the Numerical Simulation of the Velocity Field with the Experimental Measurements	131
6.3.1 Tangential Velocity	131
6.3.2 Axial Velocity	138
6.3.3 Radial Velocity	143
6.4 Verification of Computation Results with Experimental Data	152

CHAPTER SEVEN: SEPARATION EFFICIENCY OF A PIPE SEPARATOR

7.1 Experimentally Determined Separation Efficiency 157

7.2 Comparison between Measured and Predicted Separation Efficiency 159

CHAPTER EIGHT: CONCLUSIONS AND RECOMMENDATIONS

8.1 Conclusions 162

8.2 Recommendations 164

APPENDIX A

Uncertainty Analysis for Stereoscopic PIV Measurements 165

APPENDIX B

Grid Independence Studies 170

APPENDIX C

Calculation of the Pressure Drop in a pipe Separator 175

APPENDIX D

Detailed Drawing of the Test Section 176

REFERENCES 177

Figure	Page
Figure 1.1: Three-phase horizontal separator schematic	4
Figure 1.2: Two stage cylindrical cyclone system	6
Figure 1.3: Single stage cylindrical cyclone system	7
Figure 2.1: Three types of swirl generators	11
Figure 2.2: Cylindrical velocity components in the 3D domain	17
Figure 2.3: The tangential velocity profile in cyclones and swirl tube	19
Figure 2.4: Axial velocity profile in cyclone and swirl tubes	20
Figure 2.5: Tangential and axial velocity distributions in a hydrocyclone based on the observations of Kelsall (1952) and Slack (1997)	21
Figure 2.6: Flow regimes in gas – liquid Flows	31
Figure 3.1: Outline of PIV steps	40
Figure 3.2: Stereoscopic translation camera arrangement	41
Figure 3.3: Stereoscopic angular camera arrangement	41
Figure 3.4: Image perspective effect due to camera tilt in Scheimpflug arrangement	42
Figure 3.5: Schematic diagram of a PIV/SIT experimental set up	45
Figure 3.6: Schematic of cylindrical cyclone	48
Figure 3.7: Inlet Configuration of the pipe separator	49
Figure 3.8: Diagram of the air-water-oil separation experimental flow loop	50
Figure 3.9: A 30-mm ID cylindrical cyclone separator	51
Figure 3.10: Metering section	52
Figure 3.11: Photograph of the cyclone pumping section	53

Figure 3.12: S-PIV experimental set-up	56
Figure 3.13: Lasers used for S-PIV system	57
Figure 3.14: Water prism	58
Figure 3.15: Calibration target	59
Figure 3.16: S-PIV enclosures design	60
Figure 3.17: Measurement locations	62
Figure 3.18: Stratified flow pattern for pipe separator Inlet	63
Figure 3.19: Co-current flow map of gas/vapour and a liquid in a horizontal/inclined plane	64
Figure 3.20: Co-current Flow of Gas/Vapour and a Liquid in a Horizontal/Inclined Plane.	64
Figure: 4.1: Turbulence scales and prediction methods	78
Figure 5.1: Experimental data: Position of $y=0$ sections at $Z=-75$ mm	96
Figure 5.2: Comparison between the tangential velocity profiles at three axial positions in the cyclone	96
Figure 5.3: Comparison between the axial velocity profiles at three axial positions in the Cyclone	99
Figure 5.4: Comparison between the radial velocity profiles at three axial positions in the cyclone	100
Figure 5.5: Comparison of the CFD result and experimental data for mean tangential velocity at axial positions of (A) $Z= -395$ mm (B) -75 mm (C) 295 mm.	102
Figure 5.6: Comparison of the CFD result and experimental data for mean axial velocity at axial positions of (A) $Z= -395$ mm (B) -75 mm (C) 295 mm axial positions	105
Figure 5.7: Schematic representation of axial velocity profile by: (A) experimental measurements (B) CFD simulation	106

velocity at axial positions of (A) $Z = -395$ mm (B) -75 mm (C) 295 mm.	107
Figure 5.9: Schematic representation of radial velocity vector map as obtained by: (A) experimental measurements (B) CFD simulation	109
Figure 6.1: Experimental data: Position of Y sections at $Z = 295$ mm	111
Figure 6.2: Profiles of the mean tangential velocity for water flow and air-water flow at $Z = -395$ mm axial position;	114
Figure 6.3: Profiles of the mean tangential velocity for water flow and air-water flow at $Z = -75$ mm axial position	115
Figure 6.4: Profiles of the mean tangential velocity for water flow and air-water flow at $Z = 295$ mm axial position	116
Figure 6.5: Profiles of the mean axial velocity for water flow and air-water flow at $Z = -395$ mm axial position	119
Figure 6.6: Profiles of the mean axial velocity for water flow and air-water flow at $Z = -75$ mm axial position	120
Figure 6.7: Profiles of the mean axial velocity for water flow and air-water flow at $Z = 295$ mm axial position	121
Figure 6.8: Profiles of the mean radial velocity for water flow and air-water flow at $Z = -395$ mm axial position	124
Figure 6.9: Profiles of the mean axial velocity for water flow and air-water flow at $Z = -75$ mm axial position	125
Figure 6.10: Profiles of the mean radial velocity for water flow and air-water Flow at $Z = 295$ mm axial position	126

Figure 6.11: Effect of air volume fraction on the averaged tangential velocity of water-air Flow at axial positions of (A) Z=-395mm (B) Z=-75mm (C) Z=295mm	128
Figure 6.12: Effect of air volume fraction on the averaged axial velocity of water-air flow at axial position of (A) Z=-395 mm (B) Z=-75 mm (C) Z=295 mm.	129
Figure 6.13: Effect of air volume fraction on the averaged radial velocity of water-air flow at axial positions of (A) Z=-395 mm (B) Z=-75 mm (C) Z=295 mm.	130
Figure 6.14: Comparison of the CFD results with experimental data for mean tangential velocity of air-water flow at the Z= -395 mm axial position	135
Figure 6.15: Comparison of the CFD results with experimental data for mean tangential velocity of air-water flow at the Z= -75 mm axial position	136
Figure 6.16: Comparison of the CFD results with experimental data for mean tangential velocity of air-water flow at the Z= 295 mm axial position	137
Figure 6.17: Comparison of the CFD results and experimental data for mean axial velocity of air-water flow at the Z= -395 mm axial position	140
Figure 6.18: Comparison of the CFD results and experimental data for mean axial velocity of air-water flow at the Z= -75 mm axial position	141
Figure 6.19: Comparison of the CFD results and experimental data for mean axial velocity of air-water flow at the Z= 295 mm axial position	142
Figure 6.20: Comparison of the CFD results and experimental data for mean radial velocity of air-water flow at the Z= -395 mm axial position	144

Figure 6.22: Comparison of the CFD results and experimental data for mean radial velocity of air-water flow at the $Z= 295$ mm axial position	146
Figure 6.23: Contours of the air volume fraction at the $Z= -395$ mm axial position	148
Figure 6.24: Contours of the air volume fraction at the $Z= -75$ mm axial position	149
Figure 6.25: Contours of the air volume fraction at the $Z= 295$ mm axial position	150
Figure 6.26: Contours of the air volume fraction at the axial position of: (A) $Z= -395$ mm (B) $Z= -75$ mm (C) $Z= 295$ mm	151
Figure 7.1: Percentage of water at the water-rich outlet against water volume fraction	158
Figure 7.2: Percentage of water at the water-rich outlet against oil volume fraction	158
Figure 7.3: Plot of percentage of water at the water outlet against split ratio	159
Figure 7.4: Comparison of the percentage of water at the water rich outlet against water volume fraction at the inlet as measured experimentally and CFD prediction	160
Figure 7.5: Comparison of the percentage of water at the water rich outlet against oil volume fraction at the inlet as measured experimentally and CFD prediction	161
Figure B: 1 Tangential velocity profiles for different grids	171
Figure B: 2 Axial velocity profiles for different grids	171
Figure B: 3 Radial velocity profiles for different grids	172
Figure B: 4 Contour of tangential velocity at axial position of $Z= -0.05$ mm	173
Figure B: 5 Contour of tangential velocity at axial position of $Z= -0.05$ mm	174

LIST OF TABLES

Table	Page
Table 3.1: Summary of SPIV parameters	56
Table 3.2: Properties of the fluids	61
Table 3.3: Flow rates for air-water experiments	63
Table 3.4: Planned experiments for air-water-oil flow	66
Table 4.1: Comparison of different turbulence models	77
Table 4.2: Models used in single phase simulation	89
Table 4.3: Discretization scheme and solution method for single phase simulation	89
Table 4.4: Properties of water, air, and oil phases	91
Table 4.5: Boundary condition at inlet for air-water experiment	92
Table 4.6: Boundary condition at inlet for air-water-oil experiment	93
Table 4.7: Boundary condition at inlet for air-water-oil experiment	93
Table 4.8: Boundary type for multiphase flow simulation	93
Table 4.9: Model and discretization scheme for multiphase flow simulation	94
Table 6.1: Experimental plan for air-water flow	111
Table A.1: Uncertainty analysis for water flow measurements	166
Table A.2: Uncertainty analysis for air-water flow measurements	168
Table B.1: Details of grids used in mesh independence studies	170

General

C_D	Drag coefficient (dimensionless)
C_μ	Constant, k- ϵ turbulence model (dimensionless)
	Constant, RNG k- ϵ turbulence model (dimensionless)
$C_{1\epsilon}$	Constant, k- ϵ turbulence model (dimensionless)
$C_{2\epsilon}$	Constant, k- ϵ turbulence model (dimensionless)
C_1	Constant (RSM pressure strain correlation term) (dimensionless)
C_2	Constant (RSM pressure strain correlation term) (dimensionless)
D	Diameter (m)
D_{ij}	Diffusion term (RSM) (m^2/s)
F_{ij}	Rotation production (RSM) (m^2/s)
\vec{F}	Force vector (N)
F_D	Drag force (N)
\vec{g}	Gravitational acceleration (m^2/s)
k	Turbulent kinetic energy (m^2/s^2)
L	Length (m)
m	Mass (kg)
\dot{m}	Mass flow rate (kg/s)
\dot{m}_{pq}	Mass transfer (kg)
p	Pressure (N/m^2)

P_{ij}	Production term of RSM (m^2/s)
S_k	Stokes number (dimensionless)
r	Distance (m)
n	Vortex exponent (dimensionless)
Q	Volume flow rate (m^3/s)
Re	Reynolds number (dimensionless)
\overrightarrow{R}_{pq}	Interaction force between phases (N)
t	Time (s)
U_p	Particle velocity (m/s)
V	Volume (m^3)
\overrightarrow{V}_{pq}	Interphase velocity (m/s)
U	X component of mean flow velocity (m/s)
V	Y component of mean flow velocity (m/s)
W	Z component of mean flow velocity (m/s)
u, v, w	fluctuating components in the r, θ, z directions (m/s)

Coordinates

i, j, k	Computational coordinates system
r, θ, z	Cylindrical coordinates
x, y, z	Rectilinear coordinates

ε	Dissipation of turbulent kinetic energy (m^2/s^3)
ε_{ij}	Rate of dissipation of Reynolds stress ($\text{kg}/\text{m}^3\text{s}$)
μ	Dynamic viscosity (kg/ms)
μ_t	Turbulent dynamic viscosity (kg/ms)
μ_{eff}	Effective viscosity (m^2/s)
μ_{mol}	Molecular viscosity (m^2/s)
ρ	Density (kg/m^3)
ρ_f	Fluid density (kg/m^3)
ρ_p	Density of the tracer particle (kg/m^3)
σ	Surface tension (N/m)
σ_ε	Constant, k- ε turbulence model (dimensionless)
σ_k	Constant, k- ε turbulence model (dimensionless)
α	Volume fraction (dimensionless)
τ	Shear stress (Pa)
τ_{ij}	Surface stress tensor (Pa)
$\overline{\tau}_q$	Phase stress-strain tensor (Pa)
$\tau_{ij,t}$	Reynolds stress tensor (Pa)
ν	Kinematic viscosity (m^2/s)
ν_t	Kinematic turbulent viscosity (m^2/s)
δ	Delta function (dimensionless)
Φ_{ij}	Pressure strain

Acronyms and abbreviations

CCD	Charged-coupled device (image sensor)
CFD	Computational fluid dynamics
CMOS	Complementary metal oxide semiconductor (image sensor)
DNS	Direct numerical simulation
FFT	Fast Fourier transforms
PIV	Particle image velocimetry
PTV	Particle tracking velocimetry
LES	Large eddy simulation
LDV	Laser doppler velocimeter
k- ϵ	Turbulence model
Nd: YAG	Neodymium-doped yttrium aluminium garnet
RANS	Reynolds-averaged Navier Stokes
RSM	Reynolds stress model
RMS	Root mean square
RNG	Renormalization group (k- ϵ model variant)
SPIV	Stereoscopic particle image velocimetry

CHAPTER ONE

INTRODUCTION

1.1 Phase Separation

In the petroleum industry, water trapped in underground formations is brought to the surface along with oil or gas. Because the water has been in contact with the hydrocarbon-bearing formation for centuries, it contains some of the chemical characteristics of the formation and the hydrocarbon itself. It may include water from the reservoir, water injected into the formation, and any chemicals added during the production and treatment processes. It is the largest volume by-product or waste stream associated with oil and gas exploration and production. Both formation and injection water are produced alongside oil and, as oil fields age, the amount of produced water is increasing. Large quantities of contaminated water can have a significant environmental impact if not handled properly. No single piece of equipment can tackle the complex process of treating produced water to meet increasingly stringent regulations for discharge or re-use (Veil et al., 2004).

Liquid - Gas Separation

Removing liquids and solids from a gas stream is very important in refining and gas processing applications. Effective removal of these contaminants can prevent costly problems and downtime with downstream equipment like compressors, turbines, and burners. Mechanisms used to remove liquids and solids from gases can be divided into four categories. The first and easiest to understand is gravity settling, which occurs when the weight of the droplets or particles (i.e. the gravitation force) exceeds drag created by the flowing gas. A second mechanism is centrifugal separation, which occurs when the centrifugal force exceeds the drag created by the flowing gas. The centrifugal force can be several times greater than gravitational force. The third separation mechanism is called inertial impaction which occurs when a gas passes through a network, such as fibers and impingement barriers. In this case, the gas stream follows a tortuous path around these obstacles while the solid or liquid droplets tend to go in straighter paths, impacting these obstacles. Once this occurs, the droplet or particle loses velocity and/or coalesces, and eventually falls to the bottom of the vessel or remains

trapped in the fiber medium. And finally, diffusional interception or Brownian motion is the fourth mechanism of separation that occurs when small aerosols collide with gas molecules. These collisions cause the aerosols to deviate from the fluid flow path around barriers increasing the likelihood of the aerosols striking a fiber surface and being removed (Schweitzer, 2004; Coker, 1993; Perry et al, 1984; Halter, 1966).

The mechanisms discussed above provide selection criteria for the following gas/liquid separation technologies (Perry et al, 1984):

- gravity separators
- centrifugal separators
- filter vane separators
- mist eliminator

Liquid-Liquid Separation

Separation of two liquid phases, immiscible or partially miscible liquids, is a common requirement in the process industries. For example, it is frequently necessary to separate small quantities of entrained water from process streams. The simplest form of equipment used to separate liquid phases is the gravity settling tank, the decanter. Various equipments such as centrifugal separators are used to promote coalescence and improve separation in difficult systems, or where emulsions are likely to form (Perry et al, 1984). Hydrocyclones are used for some liquid-liquid separations, but are not as effective in this application as in separating solids from liquids. The high efficiency liquid/liquid hydrocyclone provides maximum oil/water separation efficiency, and is used in industrial process water, industrial reuse, oil/water separation, and clarification/separation applications. At low and moderate liquid velocities, a Gas-Liquid Cylindrical Cyclone (GLCC) was reported to provide a water-rich stream and oil-rich stream at the overflow and underflow outlets (Coulson et al, 2002).

Gas/Liquid -Solid Separation

Separation processes that are central to gas–solid flow systems include dust removal, particulate collection, sampling particle recirculation, and other operations. Gas–solid separation can be achieved by application of the principles involving centrifugation, electrostatic effects, filtration, gravitational settling, and wet scrubbing.

Gas–solid separators applying these principles employ rotary flow dust separators, electrostatic precipitators, filters, settling chambers, and scrubbers. In order to yield highly efficient solids collection or removal processes, multistage gas–solid separators based on a combination of several of these components are also commonly employed. An example of separation by rotating gas-solid flow is exemplified by a cyclone separator (Fan and Zhu, 1998).

The separation of particulate solids from liquid by filtration is achieved by placing a permeable filter in the path of the flowing suspension. The cyclone clarifier is an example of compact solid/liquid hydrocyclones that provides maximum efficiency for the separation of liquid-solid flow. The solid-liquid flow is fed tangentially to initiate a high radial velocity and the resulting spinning motion accelerated by the tapered shape of the clarifier. The spinning motion of the fluid creates high centrifugal force, which causes the solids to rapidly separate from the liquid. Solids are forced towards the internal wall and exit through the underflow apex. Liquid exits the larger overflow end of the liner. The solid/liquid hydrocyclone can handle high levels of solids, with removal capabilities down to five micron. It is used in industrial process water, desanding of injected water and other clarification applications (Coulson et al, 2002).

Three Phase Separation

Three-phase separations involve the separation of three-phase inlet stream into separate phases. In other words, it is the removal of a combination of more than one phase from a continuous phase stream. A good example of the three phase separation is the separation of gas, oil and water using a three phase separator (Figure 1.1) commonly referred to as free-water knockout vessel. Three phase separator can be horizontal, vertical or spherical in shape. Some of the internal components of this separator includes inlet deflector, vane pack, coalescer, wave breaker, adjustable weir plates, and mist extractor. All these are primarily used to facilitate and improve the phase separation process within the separator. Generally, a gas-liquid-liquid separator is divided into four sections. The first is the inlet section which ensures an initial gas/liquid(s) separation and a good flow distribution across the vessel. Secondly is the gas/liquid gravity separation section that allows the creation and fall out of large liquid droplets. Also included in the gravity section is a coalescer stage.

The next stage is the demisting section where the finer mist particles are removed. The last is the liquid separation section where liquids are degassed and the light and heavy liquid phases are separated, and further treated in vessels called treaters (Sayda and Taylor, 2007; Arnold and Stewart, 1999).

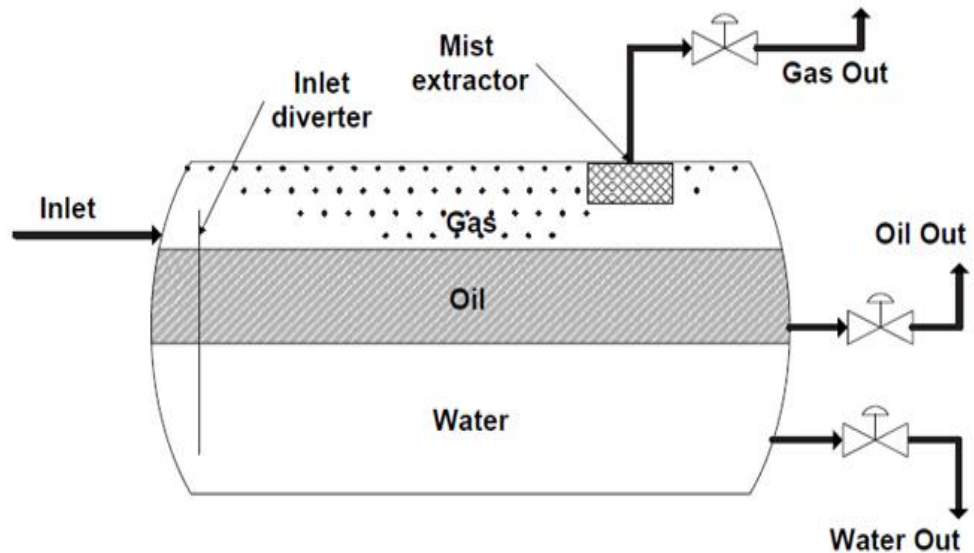


Figure 1.1 Three- phase Horizontal Separator Schematic (Sayda and Taylor, 2007).

1.2 Three Phase flow Cylindrical Cyclone Development

In the past, the multiphase separation technology used in the oil and gas industry has been based on conventional vessel-type separators which are expensive, heavy and bulky in size. Nowadays, compact separators are widely used as an effective and economical alternative to conventional separators especially in offshore platforms in oil and gas production operations. The compact separator is simpler to operate, more lightweight, has neither moving nor internal parts, requires less floor space, and involves lower capital and operational costs. A cyclone is a device that spins a continuous phase stream to remove entrained dispersed phases by centrifugal force.

Presently, the cylindrical cyclone or pipe separator has potential application as a free water knockout system in equipment for the upstream oil and gas production. This includes down-hole, surface (onshore and offshore) and subsea separation.

Other applications include, use in flare gas scrubbers, slug catchers and portable well testing equipment. The main application of the three phase cylindrical cyclone is to clean oily water for disposal by reducing oil concentrations to the order of parts per million in effluents.

The Gas-Liquid-Liquid Cylindrical Cyclone (GLLCC) is a compact separator which was patented by the University of Tulsa, USA (Vasquez, 2001). It is an extension of the Gas-Liquid and Liquid-Liquid cylindrical cyclone technologies developed to separate gas-liquid-liquid mixtures. An extensive study has been conducted by Vasquez (2001) on the performance of this three phase cylindrical cyclone which concluded that it worked effectively as a free water knock-out device for mixtures with high water content and low oil volume. As shown in Figures 1.2 and 1.3, Vasquez (2001) proposed two geometric configurations for three phase separation.

The first configuration is referred to as the two stage system. The first stage is designed to effect gas-liquid separation with the liquid outlet connected to the second stage where liquid-liquid separation occurs. In the two stage system, the gas-oil-water mixture enters a vertically installed pipe through an inclined tangential inlet. The multiphase flow forms a swirling fluid motion, producing a centrifugal force as a result of the tangential inlet being inclined at an angle of 27° . Separation of the incoming mixture is effected due to centrifugal and gravity forces.

The gas flows to the top and exits the system. The remaining liquid, which is the oil-water mixture, flows through the liquid outlet of the first stage into the second stage. The inlet fitted with a nozzle ensures that the water-oil mixture enters the second stage at high velocity. Then, a swirling motion is generated which promotes an inertia-dominated separation of the oil-water mixture. Therefore, an oil rich stream exits through the top and the water-rich stream leaves the system through an outlet at the bottom of the second stage.

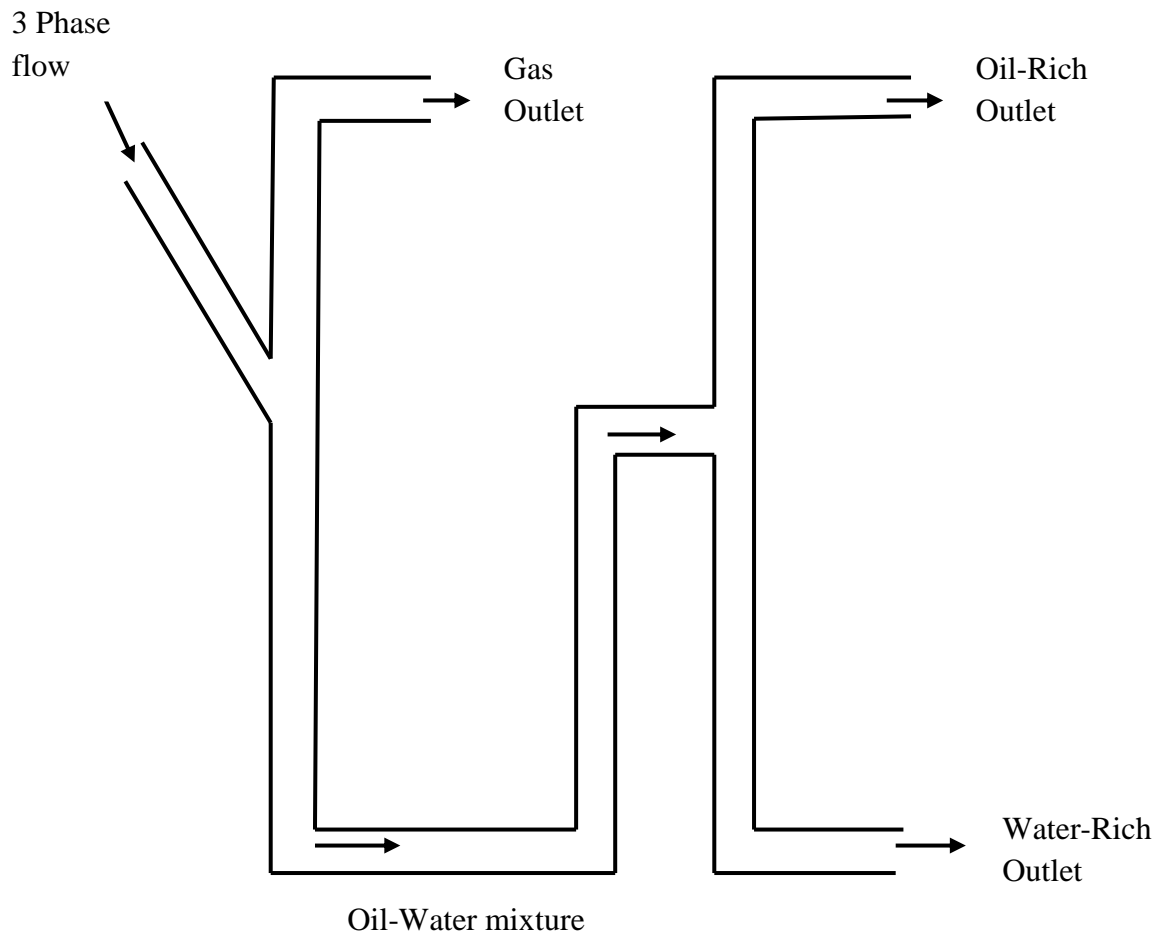


Figure 1.2: Two Stage Cylindrical Cyclone System

Figure 1.3 shows the second configuration, which is a single system called the Gas-Liquid-Liquid Cylindrical Cyclone (GLLCC). It consists of a tangential inlet inclined at an angle of 27° to the vertical cylindrical body and an oil finder which is an inner concentric pipe extended through the bottom. In the single stage system, the air-oil-water mixture enters through the inclined inlet designed to promote the pre-separation of the gas-liquid mixture. The tangential inlet with reduced area produces a swirling motion in the vertical cylindrical pipe. The gas flows upwards to the gas outlet and leaves the single system compact separator. The liquid-liquid mixture moves to the lower section of the vertical pipe. As a result of differences in density, the centrifugal effect segregates the oil-water mixture, thereby concentrating the oil at the centre of the pipe whereas the water moves toward the wall region.

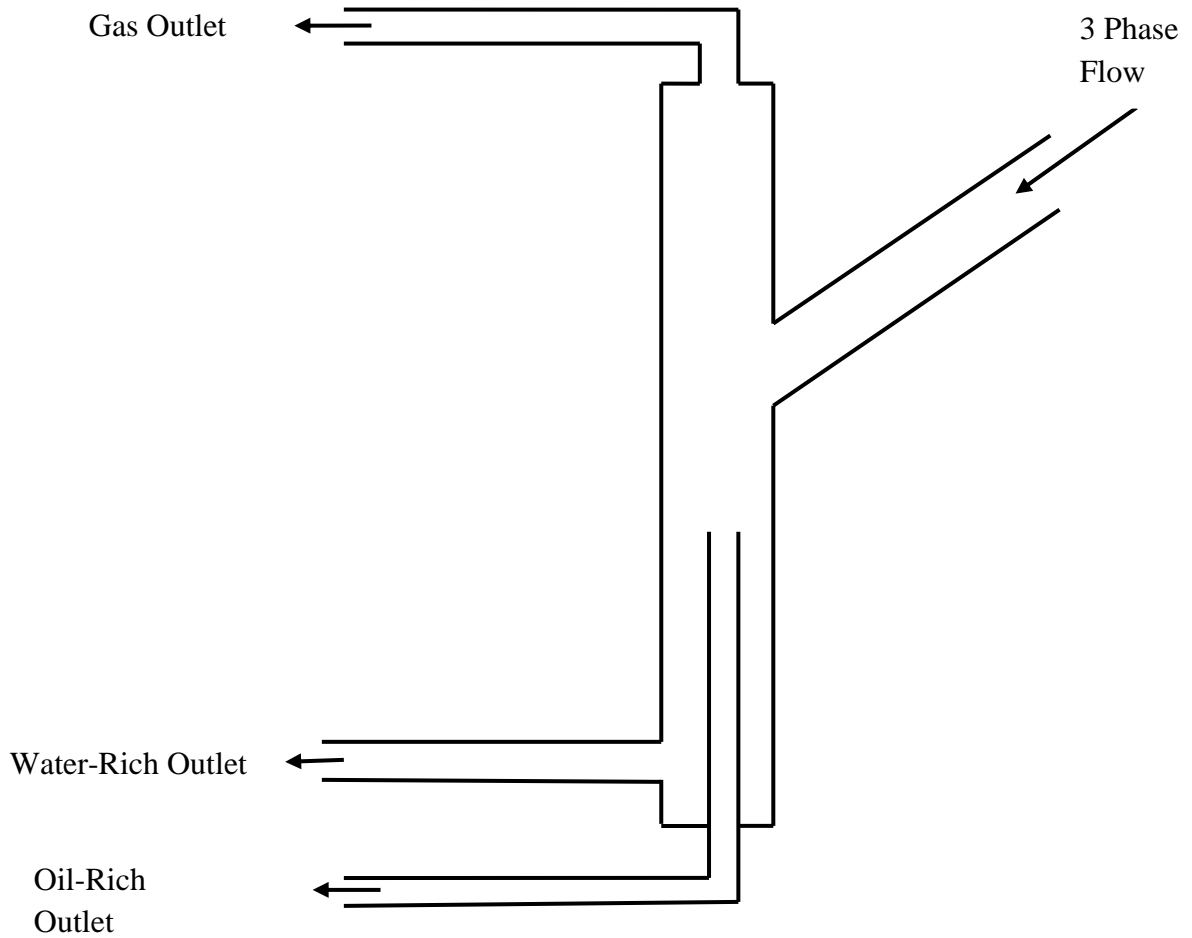


Figure 1.2: Single Stage Cylindrical Cyclone System

The oil rich core formed at the centre flows through the oil finder and the water rich fraction flows to the annulus between the pipe wall and the oil finder, leaving the single stage three phase separator through the water-rich outlet. Preliminary studies have shown that the three phase separator is an effective device to perform the partial separation of air-oil-water mixtures at moderate velocities (Vazquez, 2001). However, the cylindrical cyclone performs as a mixer rather than separator at high velocities. Vasquez (2001) has already carried out experimental and mechanistic modelling to ascertain the separation performance of the three phase cylindrical cyclone as a device that effects the partial separation of air-oil-water mixtures at moderate velocities. However, a lack of understanding of the complex multiphase flow behaviour inside the three-phase cylindrical cyclone prevents complete confidence in its design. This shows the need for additional research, which the present work seeks to provide.

A detailed investigation of hydrodynamic flow behaviour will allow the correct prediction of separation performance, which is necessary for appropriate design in all applications.

1.3 Aim and Objectives of this Research

The main aim of this research is to investigate the hydrodynamic behaviour of the multiphase flow within the three phase pipe separator. This aim is achieved by the completion of the following steps;

- (1) Measurement of the single and two phase velocity field within the three phase separator using the Stereoscopic Particle Image Velocimetry (PIV) technique.
- (2) Analysis of experimental data so as to determine the flow pattern within the pipe separator.
- (3) Prediction of single and two phase flow within the pipe separator using the commercial Computational Fluid Dynamics (CFD) package ANSYS FLUENT.
- (4) Comparison and evaluation of the ability of the CFD model to predict single and 2 phase flow within the pipe separator.
- (5) Determination of the air-oil-water separation performance of a three phase pipe separator.

1.4 Outline of the Thesis

Following this introduction, Chapter 2 reviews the relevant literature, including the experimental and computational modelling of the swirling flow within the cylindrical cyclone. Chapter 3 discusses the principles and application of the stereoscopic PIV technique. It also gives detailed information about the experimental facility and set up used, as well as the measurement strategy. Chapter 4 reviews the numerical simulation of turbulence and multiphase flow. It also discusses the model geometry and numerical simulation set-up used in this thesis. Chapter 5 presents the experimental analysis of the single phase flow within the pipe separator and a comparison of the results with the CFD computed velocity profiles for single phase flow.

Chapter 6 discusses the experimental analysis of air-water velocity profiles within the pipe separator, and then compares the results with the CFD computed velocity distributions. The separation performance for air-oil-water flow within the pipe separator is presented in chapter 7, which also compares the experimental and CFD predicted separation performance. Finally, chapter 8 summarizes the conclusions of this investigation and makes recommendations for future work.

CHAPTER TWO

Literature Review

2.0 Introduction

The literature review is divided into four sections and examines significant research related to the hydrodynamic behaviour of multiphase flow within the cylindrical cyclone. The first section considers research using experimental techniques to investigate flow dynamics within the cyclone. The second section examines relevant numerical simulations of turbulence and multiphase flow within the cyclone. The third section summarizes the different flow patterns observed within the cyclone.

2.1 Principles of internal Swirling Flow

In order to study turbulent swirling flow, three different methods may be used to generate axi-symmetry swirling flow in a pipe (Beer and Chigier, 1972). These methods can be briefly explained as

- (a) Fluid flow passing through a rotational section acquires tangential momentum and enters the pipe in the form of a swirling flow (Fig. 2.1a).
- (b) A swirling flow can be generated by using mechanical devices that impart swirling motion to the fluid passing through them. This includes rotating vanes (blades) or grids and rotating tubes (Fig. 2.1a and b), (Ashrul Ishak and Jaafar, 2004).
- (c) By mean of tangential inlet, fluid flow enters to the pipe and acquires rotational momentum and enters the pipe in the form of a swirling flow (Fig. 2.1c).

Swirl Intensity

A measure for the swirl intensity is given by the swirl number, S , the non-dimensional angular momentum flux;

$$S = \frac{\rho \int_0^{2\pi} \int_0^R U_z U_\theta r dr d\theta}{\rho \pi R^3 U_b} \quad (2.1)$$

Here U_z, U_θ, U_b are the axial, azimuthal and bulk axial velocities respectively.

Benim et al. (2007) observed that the decay of swirl number along the pipe length occurs at different rates for different shapes of the inlet swirl velocity profile. They

concluded that parameters such as the circulation or swirl number do not uniquely prescribe the shape of the swirl velocity profile. A simplified swirl velocity profile shape at the inlet was suggested in order to investigate the role of the inlet swirl velocity profile on decay of swirl in pipe flow. This consists of a perfect solid body rotation in the core, which can be defined by:

$$W_o = \frac{W_{max.}}{a} r \quad \text{for } r \leq a \quad (2.1a)$$

and a perfect free vortex outside

$$W_o = \frac{W_{max.}}{r} a \quad \text{for } a \leq r \leq R \quad (2.1b)$$

where the parameter a denotes the vortex core radial extension and R is the pipe radius. For the axial velocity at the inlet, a constant value U is assumed (Benim et al., 2007; Chen et al., 1999). Based on these inlet velocity profiles, the inlet swirl number can be expressed as $S_o =$

$$\frac{W_{max}}{U} \left[\frac{a}{R} - \frac{1}{2} \left(\frac{a}{R} \right)^3 \right] \quad (2.1c)$$

The free parameters of the swirl velocity profile are the core radius a and the maximum swirl velocity W_{max} .

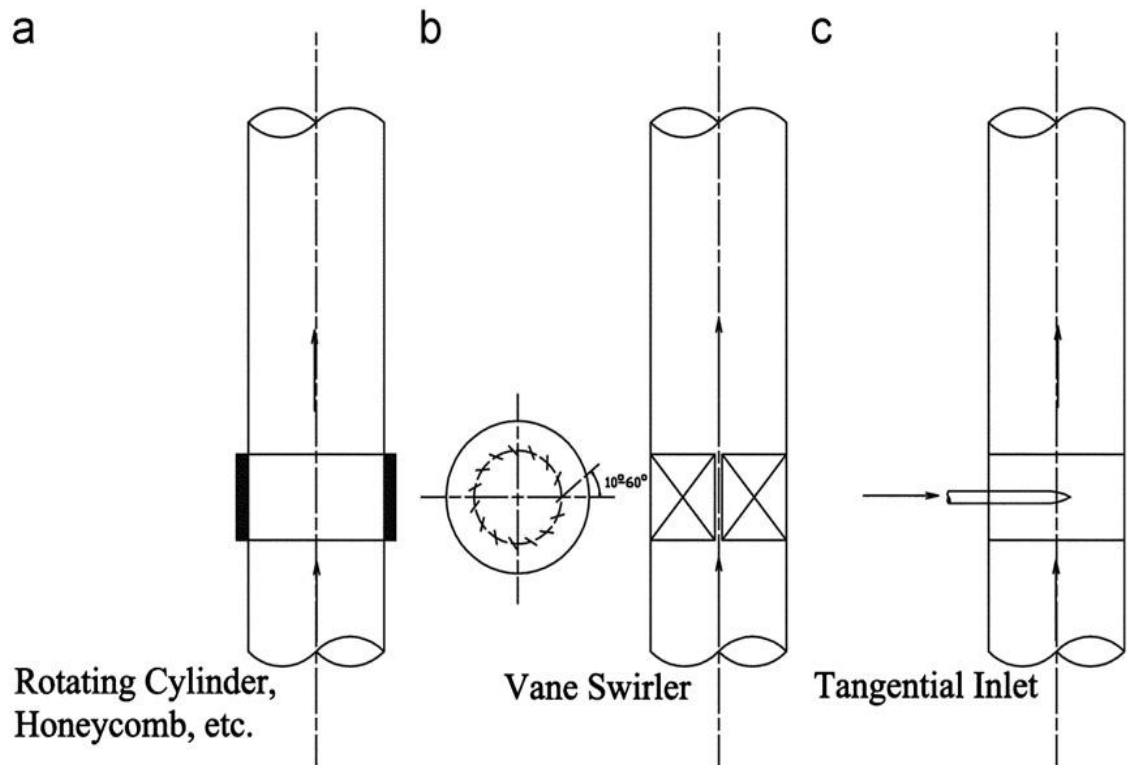


Figure 2.1. Three Types of Swirl Generators (Nafaji et al. 2011).

Effect of geometrical configuration on cyclone efficiency

The geometrical configuration is probably the most crucial aspect affecting the performance of a cyclone separator. The cyclone flow field is axially-asymmetric by virtue of the geometry inlet asymmetric. In addition, a feature of streamline curvature associated with cylindrical geometry often leads to the development of secondary flows that promotes particle separation mechanism. Performance of the cyclone can, therefore, be improved by modifying the geometrical parameters or flow characteristics. The cyclones' separation efficiency is observed to be increasing with an increase in the inlet flow rate which is a direct function of swirl velocity that causes an increase in centrifugal force field. However, for fine particles, separation efficiency decreases as the flow rate increases. This arises from the fact that fine particles move alongside the flow path lines, thereby causes its separation ratio to be directly proportional to flow split ratio.

Many geometrical designs have been proposed using CFD studies that can be used to improve the performance of cyclone separators. The list of these modifications include, (i) the use of different inlet types (scroll, helicoidal, axial spiral double inlet and square cyclone inlets) can be found in Cortes and Gil (2007), Wang et al. (1999) and Zhao et al. (2006), (ii) including a long cone (Lee et al., 2006), and (iii) the variation in body and cone height (Xiang et al., 2005).

2.2 Experimental Measurements of Swirling Flow in the Cylindrical Cyclone

Cyclones operate at velocities where the flow is found to be typically turbulent and often quite complex. This is due to the fact that the cyclone operates with strong swirl intensity together with a flow reversal, flow separation and three-dimensional boundary layers with strong streamline curvature. Experimental studies are performed to obtain data about the flow in order to understand its physics. At present, there is no experimental data available on the hydrodynamic behaviour of multiphase flow in a three phase pipe separator.

Despite the invention of the conventional cyclone in late eighteenth century, thorough work to understanding its principles began only in the mid-1950s (Kelsall, 1952). Kelsall (1952) used a stroboscope with a rotating microscope objective lens to

determine the velocities of aluminium flakes that seeded the flow in a transparent test section. He resolved the fluid velocity into three components, tangential, axial and radial, aiming to determine the exact mechanisms of separation in the hydrocyclone. The experimental work of Kelsall showed that the tangential velocity increases sharply with radius in the central core zone and thereafter decreases with radius. The radial velocity of the flow is so small when compared with the axial and tangential velocities in the body of the cyclone that it is generally ignored.

Nissan and Bressan (1961) injected water through two tangential inlets and used impact probes to measure the velocity profiles of the swirling flow in pipes. They reported that the axial velocity profile included a double flow reversal, with water flowing forward near the wall and in the centre of the tube and moving backward in the region in between.

Ito et al (1979) used multi-electrode probes to investigate swirl decay in a tangentially injected water swirling flow. They concluded that swirl intensity decreases with axial distance. The tangential velocity profile measured indicated a free vortex structure close to the wall and a forced vortex structure near the centre of the tube. It was shown that the axial velocity was lower in the middle portion of the tube than near the wall, with a flow reversal region at the centre. The radial velocity was found to be much smaller than either the axial velocity or the tangential velocity, and thus it was subsequently ignored.

In a study by Millington and Thew (1987), the velocity profile inside a cylindrical cyclone was measured by Laser Doppler Anemometry (LDA). They reported that the tangential velocity distribution consisted of a forced vortex structure. Algifri et al (1988) used radial cascade blades to generate a swirling air motion in a pipe. A hot wire anemometer was used to measured velocity profiles and the tangential velocity profiles were described as a Rankine type vortex which is a combination of free and forced vortices.

Kitoh (1991) generated swirling flows using guide vanes and measured the flow field using a hot wire anemometer. He found that the swirl intensity decays exponentially with axial distance. In a study by Chang and Dhir (1994), four to six different horizontal tangential injectors were used to generate air swirling flow in a tube. Velocity fields in

the axial and tangential directions as well as Reynolds stresses were obtained using hot wire anemometers. They represented swirl intensity decay as a function of the product of the dimensionless axial distance and the reciprocal of the Reynolds number. This investigation showed an increased axial velocity near the wall and the tangential velocity profiles with a local maximum, the location of which moves radially inwards with distance. As a result of the destabilizing distribution of angular momentum in the free vortex region and the large shear near the boundary of the reversed flow, turbulence intensities are found to increase significantly.

Kurokawa (1995) characterized swirling flow using Laser Doppler Velocimetry (LDV) and a pitot tube. He identified three regions of the tangential velocity component of a swirling flow in a pipe. These were a jet region with extremely high swirl in the centre, a reverse flow region with high swirl and the outer flow region with low swirl. However, the reverse flow region disappears and the swirl in the centre region becomes very weak when the pipe is long enough. He discovered that the boundary condition at the downstream section of the cyclone greatly influence the characteristic of the liquid swirling flow.

Chen et al (1999) conducted research to investigate the penetration of the precessing vortex core into the cyclone, the extent of reverse flow and the impact of cyclone geometry on the flow field. The time-averaged axial velocity profiles measured using Laser Doppler Anemometry at different elevations indicated that the backflow region shrank down the gas outlet tube.

A majority of experimental laboratory and pilot plant studies conducted so far of flow in cyclones have covered the influence of operating parameters or changes in geometry on the separation efficiency. For examples, higher inlet velocity give higher separation efficiency for most cyclones, but this also increases the pressure drop across the cyclone. Therefore, a trade off must be made between higher separation efficiency and low pressure drop across the cyclone. The size of the vortex finder affects the cyclone performance as it plays a critical role in defining the flow field inside the cyclone especially the pattern of the outer and inner spiral flows (Dai et al., 1999; Bradley and Pulling, 1994; Hsieh, 1988; Dabir and Petty, 1984).

Bradley and Pulling (1994) studied the flow pattern in a hydraulic cyclone in terms of performance by injecting dye into the fluid flowing in the hydrocyclone. The results obtained were discussed with reference to their implications for the theoretical correlation of separation efficiency. However, this correlation was found to be imprecise due to uncertainties in the path followed by an individual particle.

Dabir and Petty (1984) investigated the behaviour of a water-fed Rietema hydrocyclone using Laser Doppler Anemometry. In a follow up study, Hsieh (1988) used Laser Doppler Velocimetry to determine the tangential and axial velocity components in a hydrocyclone operating with an air core. A comparison study of the axial velocity for different vortex finder configurations showed that the vortex design influences the core region, but not the outer region.

Erdal (2001) used tangential, horizontal and inclined inlets to generate strongly non-axisymmetric flow within a Gas-Liquid Cylindrical Cyclone (GLCC). He ran a single phase glycerine and water flow through a vertical cylindrical pipe. Tangential and axial velocity profiles with associated velocity fluctuations were measured using a Laser Doppler Velocimetry (LDV) system. The axial velocity contour map showed that the reversed axial velocity region has a helical (spiral) shape. The axial velocity measurements showed downward flow near the wall and small upward flow near the centre of the tube. He found that the tangential velocity measurements showed that free vortex occurs near the wall region and forced vortex at the centre of the cyclone. Turbulent kinetic energy is relatively high near the vortex centre and in the region near the inlet. The experimental results were then used to develop a new correlation to predict wavelength of the vortex (upward flow) and to improve existing correlations for swirl intensity, axial and tangential velocities (Erdal, 2001).

Fisher and Flack (2002) studied the internal three-dimensional water flow field in a hydrocyclone using Laser Doppler Velocimetry. The results showed that the peak non-dimensional tangential velocity decreases as the distance from the inlet region increases. Also, backflow is observed in the axial velocity profile near the inlet region, and these reversed flows disappear in the exit region. An experimental investigation was performed by Solero and Coghe (2002) to study the flow fields of both the gas and solid phases in a gas cyclone separator. They used Laser Doppler Velocimetry to measure the

velocity components of the gas phase. The measurements performed provided evidence of the presence of fluid dynamic instabilities such as vortex breakdown and precessing vortex core in the outflows induced by the high swirling motion inside the cyclone.

Bai et al (2009) used Laser Doppler Velocimetry (LDV) to capture flow patterns in a 35mm deoiling hydrocyclone. The results obtained showed that the magnitudes of velocity are dependent on the flow rate and the characteristics of the flow are affected by changes in inlet flow rate.

Pitot-static tubes and miniature hot wire anemometry techniques suffer from inaccuracies when dealing with unsteady flow, since the probe can intrude into the flow itself which possibly leads to deterioration. In addition, the Laser Doppler Velocimetry technique is a point based method and cannot simultaneously provide a three-dimensional velocity field associated with the swirl flow in the cyclone. Although three-dimensional velocity has been reported (Peng et al., 2002; Solero and Coghe, 2002), the radial velocity was obtained indirectly and its measurement is associated with undesirable levels of error. Kelsall (1952) and Dabir and Petty (1986) used continuity calculations over different vertical levels to estimate radial velocity. Their results disagree markedly with the results that were later acquired using the Stereoscopic Particle Image Velocimetry (SPIV) technique.

Stereoscopic Particle Image Velocimetry (SPIV) is a new non-intrusive visualization experimental technique which is ideally suited to determining the whole field three-dimensional fluid velocity in a cyclone. Stereoscopic PIV allows the determination of mean velocity and detailed turbulence quantities such as Reynolds stresses.

One of the first attempts to measure the velocities in a cylindrical cyclone using Stereoscopic PIV was presented by Liu et al (2006c). They investigated the swirling flow structure in a gas cyclone by measuring the instantaneous whole field tangential, axial and radial velocities of air flow. The time-averaged tangential velocity profile showed that the tangential velocity of the gas generated an inner quasi-forced vortex and outer quasi-free vortex. The axial velocity profile revealed an inner upward flow and outer downward flow. Furthermore, they observed a reverse flow at the inner core of the forced vortex around the cyclone axis. This flow reversal is generated by the

motion of precessing vortex core (PVC), which is usually associated with vortex breakdown and insurgence of reverse flow(Liu et al., 2006c).

2.3 Flow Pattern in Cyclone separator

The separation performance and pressure drop of the cyclone separator are a direct result of the flow patterns of the multiphase flow field inside the cyclone. The flow field inside a cylindrical cyclone is complex due to a combination of pipe flow with a vortex motion (swirling flow). There are three velocity components, namely axial, radial and tangential. A schematic of a pipe and the velocity components is shown in Figure 2.2, where u , v and w are the velocity components in the axial, radial and tangential direction respectively.

2.3.1 Tangential Velocity

Tangential velocity component is the main velocity component that affects the swirling flow field and its interaction with strong shear in the radial direction produces centrifugal forces that determine particle separation. Therefore, much discussion of velocity distribution within cyclone separators has focused on tangential velocity (Chine and Concha, 2000; Chang and Dhir, 1994).

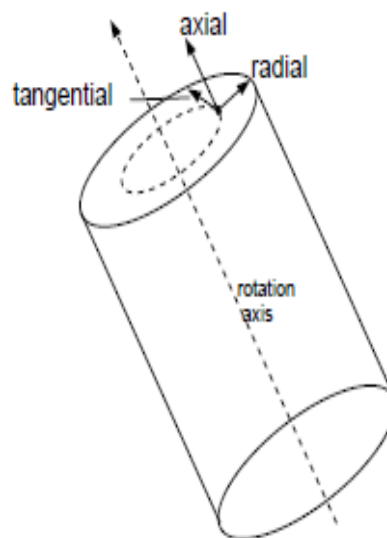


Figure 2.2: Cylindrical Velocity Components in the 3D Domain

It has been observed experimentally that the tangential velocity profile is a combination of a forced vortex at the centre of the tube, and a free vortex close to the wall (Kitoh, 1991; Kelsall, 1952).

Generally, tangential velocity increases sharply with the radial position from the centre of the tube, reaching a maximum value and then decreasing according to radial position near the wall region as depicted in Figure 2.3. The velocity gradient near the wall is steep, and thus the tangential velocity rapidly decreases to zero at the wall. As shown in Figure 2.3, the tangential velocity profile can be divided into two regions; the forced and free vortex regions. However, there is a transition zone in between the two. The forced vortex corresponds to the inner region and free vortex occurs at the outer region of the tube. After entering the cyclone, the fluid forms a confined vortex such that the tangential velocity, V_θ , is related to the distance, r , from the cyclone axis in equation (2.2),

$$V_\theta r^n = \text{Constant} \quad (2.2)$$

The vortex exponent, n , depends on the cyclone's geometry, wall roughness and particle concentration. For free vortex rotation, n is equal to 1 and this represents the complete conservation of angular momentum.

However, the empirical expression represents the fluid rotating as a solid body with constant angular velocity at $n = -1$. Slack (1997) found that there is a high shearing action in the free vortex flow of the cyclone. Here, the movement of concentric layers of fluids produces shear forces as tangential velocity increases with a decrease in radius. However, in the forced vortex fluid rotates as a solid body and consequently there are no shear forces. An increasing tangential velocity profile towards the centre supports the assumption of the free vortex flow typical of the anisotropic turbulent flow field in the cyclone. This means, flow shear is present in the free vortex region and thereby promotes particle dispersion. However, molecular viscosity becomes more dominant in the forced vortex region at the centre of the tube (Slack, 1997).

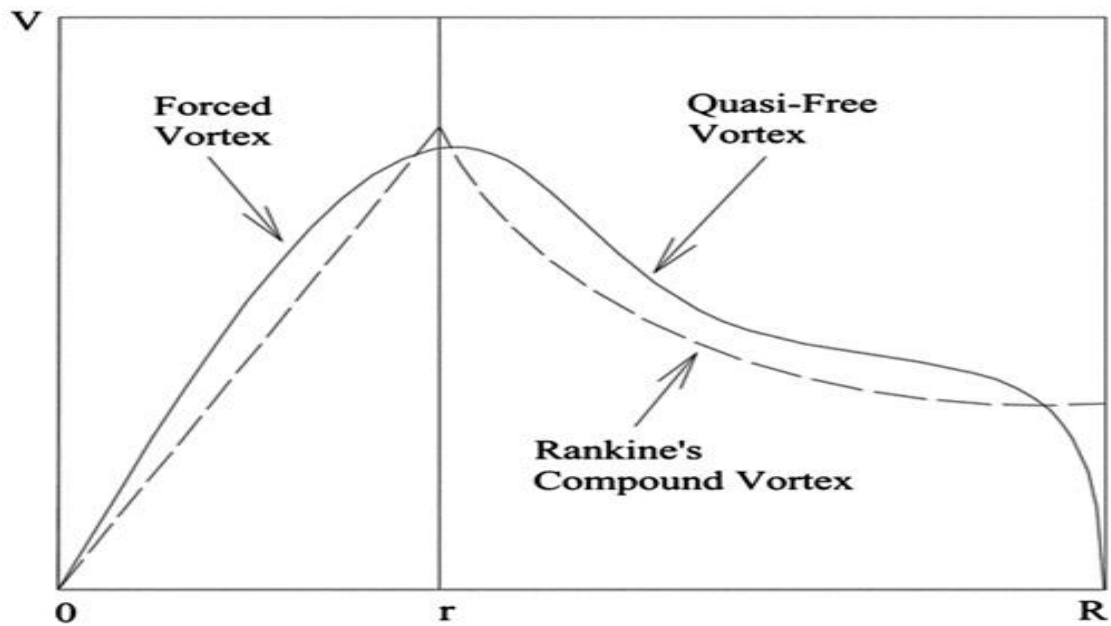


Figure 2.3: The Tangential Velocity Profile in Cyclones and Swirl Tubes (Peng et al., 2002).

2.3.2 Axial Velocity

The axial velocity component is an indication of the magnitude of the two spirals and determines the volumetric distribution of the fluid between the overflow and underflow streams. A significant feature of axial velocity profiles is the Locus Zero Axial Velocity (LZAV), which divides the axial velocity profile into outer downward flow and inner upward flow regions (Dlamini et al., 2005; Monredon et al., 1992). As shown in Figure 2.4, the axial velocity profile indicates a downward flow close to the cyclone wall and upward flow towards the centre of the tube. At high swirl intensity, a positive pressure gradient in the axial direction could result in the development of flow reversal at the central region in the main flow. Some observations by Wang et al (2006) and Liu et al (2006) indicate that the centre of the upward flow does not always coincide with the geometrical centre of the cyclone. This is attributed to the chaotic flow within the cyclone. Figure 2.5 shows the shape of the experimentally measured tangential and axial velocity profiles plotted at different axial positions with changing radius, and the flow patterns that can exist in a hydrocyclone.

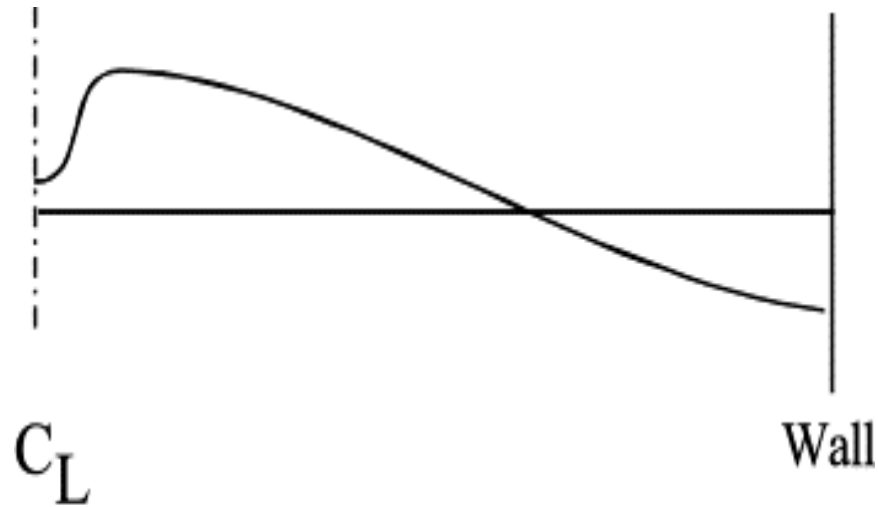


Figure 2.4: Axial velocity profile in cyclone and swirl tubes (Peng et al., 2002).

2.3.3 Radial Velocity

The radial component of fluids in cyclones has not been measured as extensively as have the tangential and axial velocities. An explanation for this could be due to its absolute value which has been assumed to be much smaller so that it is expected to have only a very small impact on the dispersed phase trajectories (Bergström and Vomhoff, 2007). Most available data on radial velocity have been calculated using the continuity equation, assuming an axisymmetric flow (Chang and Dhir, 1994; Kitoh, 1991; Algifri et al., 1988).

Generally, radially velocity profiles are found to exhibit irregular positive and negative velocity fields which are difficult to interpret (Dlamini et al., 2005; Cullivan et al., 2003b). A separation of a particle always requires a difference in radial displacement, which is usually related to a difference in morphology or material properties of the particle.

In conventional and cylindrical cyclone models, radial velocity is often assumed to be constant over the area of zero axial velocity. Peng et al (2002) found that radial velocity is fairly uniform over the length of the separation zone in the cylinder-on-cone cyclone except for a strong, but localized, inward radial flow just under the vortex finder wall.

Hreiz et al (2011) found that the magnitude of radial velocity from CFD simulation is not negligible at all radial coordinates. They suggested that magnitude of the radial velocity magnitude is minimal when the vortex centre is located in the measuring plane, and then increases when the distance from the vortex centre to the measurement plane increases.

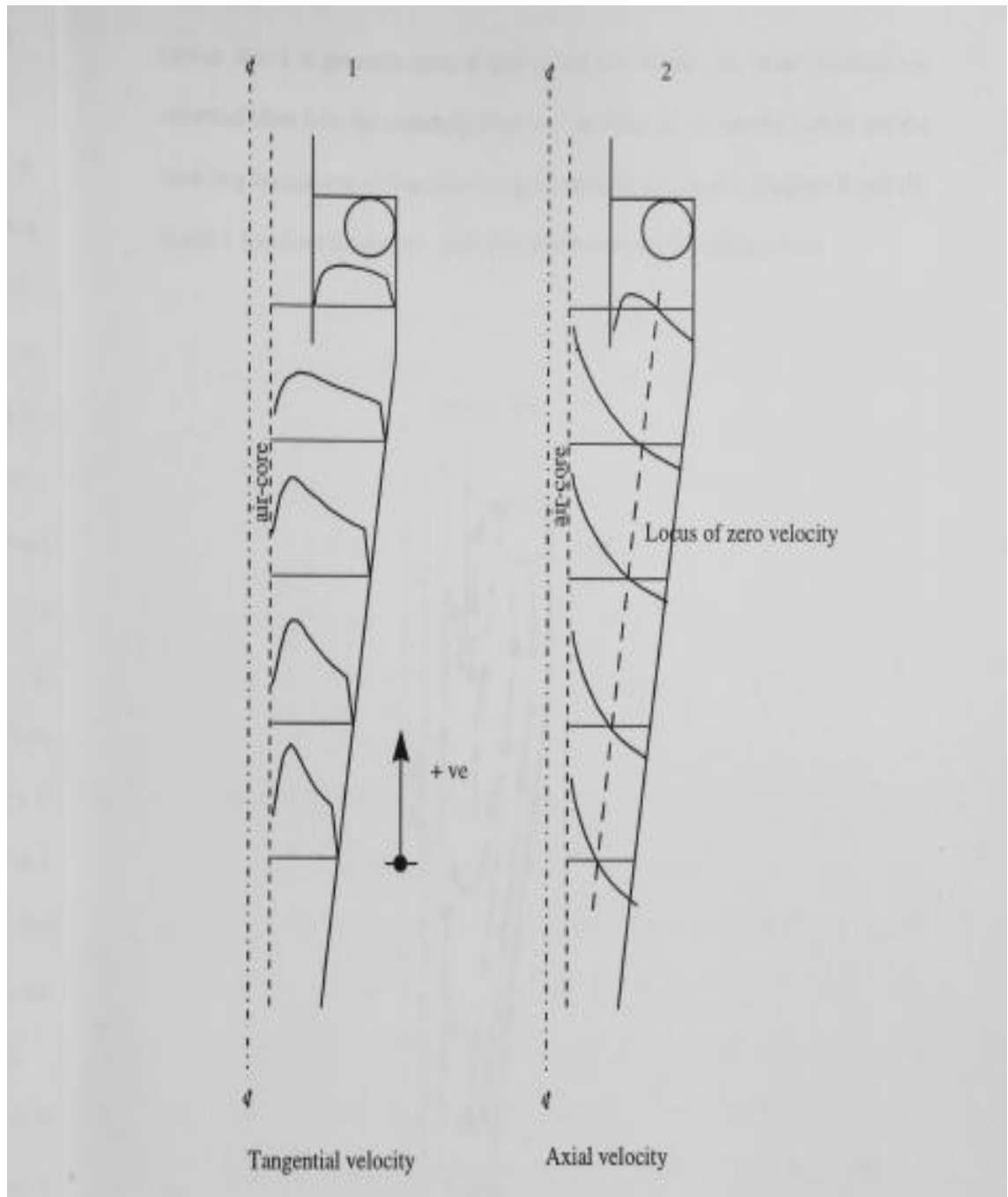


Figure 2.5: Tangential and Axial Velocity Distributions in a Hydrocyclone Based on the Observations of Kelsall (1952) and Slack (1997).

2.4 Numerical Simulation of Swirling Flow Fields

The complex phenomenon involved in cyclones coupled with the non-availability of high speed computational systems has until recently restricted most research work to focusing on empirical modelling. Empirical models were usually developed based on one or more simplifying assumptions such as a pre-defined correlation between azimuthal velocities and radial positions, absence of an air core or one with a fixed cylindrical shape and absence of viscous effects of the fluid within the hydrocyclone separator (Lim et al., 2010). In recent years, however the emergence of more powerful computers with large storage and high capacity processing facilities has provided the basis whereby computational fluid dynamics (CFD) can be used to predict flow pattern velocity profiles under a wide range of design and operating conditions. This has led to a better understanding of the turbulent flow behaviour in cyclones (Wilcox, 1993).

There are several features of cyclone modelling that are essential in providing the opportunity for design modifications to achieve improved separation. These include detailed knowledge of the flow structure, the nature of air-core development and fluid-fluid and fluid-wall interactions. The following features make turbulence inside the cyclone separator highly anisotropic:

- (a) High curvature of the average streamlines: This leads to the developments of secondary flows which continue to evolve due to the cylindrical geometry (He *et al.*, 1999).
- (b) High swirl intensity and radial shear: as a result of the tangential inlet, high swirl flow develops with shear stress as the fluid moves along the solid boundary.
- (c) Adverse pressure gradients and recirculation zones. When any of the outlets are open to the atmosphere, there is a negative pressure difference at the centre of the tube, and this result in the formation of an air core along the cyclone axis (Cullivan *et al.*, 2004).

Boysan et al (1983) employed an algebraic turbulence model to predict velocity fields and particle distribution in a hydrocyclone. They realized that the standard $k-\epsilon$ turbulence model is not able to accurately simulate the flow inside the cyclone separator. In a follow up study, Pericleous and Rhodes (1986) and Pericleous (1987) used an algebraic slip model (ASM) to represent the relative migration of particles and air in the

liquid mixture. It was discovered that the presence of an air core significantly influenced recirculation zones and velocity and particle distributions. They concluded that differential pressure conditions will need to be properly maintained at the outlet open to the atmosphere in order to achieve a good qualitative agreement between the measured data and the simulation results.

Hargreaves and Silvester (1990) proposed a four equation model of Reynolds stress and in addition used algebraic stress model to simulate the anisotropic turbulent flow in a conical hydrocyclone. The predicted results were compared with laser Doppler velocimetry measurements and confirmed that the maximum reversed axial velocity is not necessarily positioned along the cyclone axis. Therefore, an axisymmetric model could not represent the phenomenon observed in cyclone as there was a tendency to over-predict the tangential velocity distribution.

Hsieh and Rajamani (1991) developed a mathematical model based on the physics of fluid flow in a hydrocyclone. The predicted velocity profiles and the separation efficiency curve showed fairly good agreement with experimental measurements obtained through the laser Doppler anemometry technique. Sevilla and Branion (1993) and Malhotra et al (1994) used TEACH Code, a computational procedure to predict the flow field and particle trajectories in conical hydrocyclones of different geometries operating under a wide range of flow conditions. They included a new equation to represent the turbulence dissipation and concluded that the geometry of the hydrocyclone has a significant influence on the magnitude of the axial velocity.

Motta et al (1997) presented a simplified CFD simulation of single phase and two phase flow in the Gas Liquid Cylindrical Cyclone (GLCC) separator. Two phase flow simulations predicted the gas void fraction distribution in the GLCC using a dedicated model developed specifically for GLCC separators. The results obtained indicated that a vortex is formed causing the gas and liquid to separate due to centrifugal force.

An analysis presented by Mantilla et al (1999) included how CFX code is used to develop correlations for swirl intensity in the GLCC. The correlation accounted for the effects of fluid properties as well as inlet geometry. In addition, the influence of Reynolds number was investigated by simulating different flow conditions and fluids.

The correlations for axial and tangential velocities based on the swirl intensity gave good results for moderate to high value of swirl intensity.

The air-core diameter in a hydrocyclone was analysed by Davidson (1988, 1995) using the physics of uniform density, inviscid flow at each outlet, modified by an empirical factor to account for viscous effects. An expression for the air-core diameter in terms of flow variables at the outlets were applied iteratively during a hydrocyclone flow calculation with the computational grid adjusted accordingly at each step. He compared the prediction of air-core diameter with corresponding measured values and showed that an accurate predictions for the size of the air-core in hydrocyclone can be achieved using the new air-core sub-model. Predictions of both axial and tangential velocity distributions have been provided through the application of k- ϵ models (Concha, 2007; He et al., 1999; Malhotra et al., 1994; Dyakowski and Williams, 1993; Hargreaves and Silvesters, 1990) and modified k- ϵ models (Dueck et al., 2003; Dai et al., 1999).

However, the evidence shows that the fluctuating motion in the presence of swirl intensity is anisotropic and this invalidates some of the assumptions upon which simple turbulence models are based. Therefore, mixing-length and the standard k- ϵ models are insufficient for computing strong swirling flows in cyclones (Cullivan et al., 2004; Cullivan et al., 2003a; Suasnabar, 2000; Slack and Wraith, 1997). In order to solve this problem, the Renormalization Group (RNG) k- ϵ model was developed with a correction for swirl and showed significant improvement for modelling fairly rotational flow (Pericleous, 1987; Pericleous and Rhodes, 1986).

Turbulence in cyclones is anisotropic and two-equation turbulence models such as standard and RNG k- ϵ failed to represent correctly the effects on turbulence of extra strain and body forces. Slack (1991) found that the anisotropic turbulence typical of hydrocyclone flows requires a form of Reynolds stress model for effective computation as results obtained through the conventional k- ϵ model are observed to be misleading.

A new method to quantify turbulence anisotropy in conical hydrocyclone using FLOW-3D simulator was proposed by Small and Thew (1995). They used a differential Reynolds stress (DRS) as a reference to investigate the validity of the eddy viscosity model. The predicted results show that for turbulent flow of swirl number of 0.1 or

greater, the $k-\varepsilon$ model is not suitable to reproduce the anisotropic turbulent effects observed in the hydrocyclone.

A basic understanding of the operation of the cyclone has been obtained from the application of a second order differential stress turbulence model (DSM) along with the fully three-dimensional computational fluid dynamics (CFD) modelling of the hydrocyclone. Firstly, a symmetrical shape was assumed for the purpose of modelling. This is due to the reported measurements that indicate particle trajectories to be virtually symmetric within the main conical body except in the region adjacent to the underflow. Secondly, the formation of the air-core along the axis of the hydrocyclone is observed when the outlets, and especially the underflow, are open to the atmosphere. Thirdly, particle separation is understood to be governed by the simple balancing of the centrifugal force and the drag (Cullivan *et al.*, 2004). Three dimensional simulations allow detailed investigation of the complicated swirling flows in cyclone. However, they are very expensive in terms of computational time and the amount of computational space required for accurate numerical solutions.

In the last ten years, Slack *et al* (2000) and Cullivan *et al* (2003) were among those who made early attempts toward to apply full three-dimensional modelling to the hydrocyclone. They used more recent simulation methods such as Large Eddy Simulation and Reynolds Stress Method to capture time-dependent vortex oscillations and non-equilibrium turbulence within the hydrocyclone. Cullivan *et-al* (2003) used a full Differential Stress Model (DSM) with higher order treatment of the pressure strain term to account for significant anisotropy and turbulence generation mechanisms. However, the use of DSM represents a compromise between accuracy and computational cost; it does not give a completely accurate description of turbulence. In DSM, sub-grid scale modelling and equilibrium turbulence are all assumed, based on the rate of transfer of turbulence energy down through the constant energy containing length-scales. This is not commonly found in reality because cyclone flow fields develop rapidly with short residence time.

Devulapalli and Rajamani (1996) proposed a new approach called stochastic transport of particles to predict the particle concentration gradients inside a hydrocyclone. This technique involves tracking particle clouds rather than individual particles in a

Lagrangian frame of reference. The numerical results showed good agreement when compared with the experimental data for both LDV velocity measurements and particle classification.

In a study by Erdal (2001), the $k - \varepsilon$ turbulence model was used to simulate single and two phase flow in a Gas-Liquid Cylindrical Cyclone. In the single phase simulations, only a statistically insignificant difference was found when flow fields were computed from the axisymmetrical simulation compared with the three dimensional simulation. Therefore, the two phase simulation was performed with axisymmetrical geometry and a similar pattern was found. However, the decay of the swirling flow was over-predicted.

Mousavian and Najafi (2008) used a Reynolds stress model (RSM) together with the volume of fluid (VOF) multiphase model to simulate the gas-liquid-solid flow field inside the hydrocyclone in order to investigate its separation efficiency. They discussed their results in terms of the prediction of velocity distributions and proportions of separation. The Reynolds stress model gives better predictions of a complex 3-D turbulent flow with large streamline curvature and swirl. However, it is found to be more difficult to converge when compared to the use of eddy viscosity models (Mousavian and Najafi, 2008b; Wang and Yu, 2008; Zhao et al., 2007).

Recently, large eddy simulation (LES) is increasingly used as a practical tool for solving engineering flow problems. This is due to its ability to resolve large turbulent scales without modelling, while eddies smaller than mesh size are modelled. Slack et al (2000) modelled gas cyclones using LES and found good predictions of axial and tangential velocity profiles when compared with measured data. In addition, LES has been used to study the separation process within a 76mm hydrocyclone with a flow of high Reynolds number, but no consideration was given to the air core (De Souza and Neto, 2002). Here, the sub-grid scale modelling of LES was used to predict the behaviour of a water-fed hydrocyclone. The numerical results captured the main features of the flow pattern and agreed reasonably well with experiments.

Delgadillo and Rajamani (2007) used the large eddy simulation and volume of fluid models to compute the dynamics of flow in 75mm and 250mm internal diameter hydrocyclone.

They investigated the effect of spigot diameter, conical length, and vortex finder diameter, diameter of the hydrocyclone and viscosity of the fluid on the prediction of air-core structure. An increase in hydrocyclone diameter is found to be associated with an increase in air-core diameter, while the vortex finder or an increase in fluid viscosity inversely influences air-core structure. The computational time required to reach solution convergence increases as the grid size increases. The reason for this high computational time is because of the large eddies that is responsible for transporting momentum, mass and energy of flow, required much finer meshes and smaller time step sizes than those typically used for RANS calculations. They concluded that the LES model cannot be used in everyday cases to optimise a hydrocyclone. However, the LES model is proven to be an outstanding tool to study new designs.

In addition, many researchers agree that LES can be used as a good alternative to classical turbulence models when applied to the numerical solution of fluid flows within hydrocyclones (Delgadillo and Rajamani, 2009; Mousavian and Najafi, 2008a; Brennan et al., 2007; Narasimha et al., 2006; Slack et al., 2004). The LES approach seems to offer a very realistic simulation. However, because of the high number of grids required and the complexity of today's industrial cyclone separator simulations, the unsteady Reynolds Averaged Navier Stoke (RANS) approach with higher order turbulence closure is a better option that gives affordable and realistic predictions of flow fields inside cyclones (Utikar *et al.*, 2010).

Siangsnum et-al (2011) worked on the numerical calculations of 3D water flow fields using the k- ϵ and Reynolds Stress Model (RSM) of the FLUENT CFD. Measurements and CFD simulations were performed on two hydrocyclone geometries, and close agreement was found between the CFD results and Laser Doppler Velocimetry measurements.

Huang (2005) used FLUENT software to simulate a three-dimensional oil-water turbulent flow and oil separation process in a double-cone liquid-liquid hydrocyclone. The Euler-Euler and Reynolds stress models were combined to simulate the anisotropic turbulent two-phase flow with volumetric ratio greater than 10% in the dispersed phase. The predicted flow field and phase concentration distribution were used to observe how separation, aggregation and shift of oil and water proceed in the liquid-liquid

hydrocyclone. He determined the oil separation efficiency based on flow field and phase concentration distribution. The predicted result was compared with the measured separation efficiency, and concluded that the CFD simulation can be an effective tool for optimization design of the cyclone.

Reyes-Gutierrez et al (2006) presented a 3D CFD investigation of a two phase flow field in a Gas-Liquid Cylindrical Cyclone separator using CFX. At atmospheric conditions, the numerical simulation of the air-water mixture was conducted using the Eulerian-Eulerian approach, where the two phases were considered as an inter-penetrating continuum. The free surface shape and liquid angular velocity profile showed a reasonable agreement with experimental data. The CFD results proved to be useful in predicting bubble and droplet trajectories. However, a moderate difference was found between the predicted gas carry-under and experimental measurements, which suggested that adjustments to the numerical model were needed to improve its accuracy. Most of the previous CFD studies on cyclones are limited to single phase flow, and those that considered two phase flow focused on bubble trajectory analysis. Therefore, CFD methods for two phase flow are not so well developed as those for single phase flow.

2.5 Past work on the Gas-Liquid-Liquid Cylindrical Cyclone

Vasquez (2001) studied the separation efficiency of multiphase flow in a single stage Gas-Liquid-Liquid Cylindrical Cyclone (GLLCC) separator both experimentally and theoretically in order to evaluate its performance as a free water knockout device. Air, water and oil were used as the test fluid and the superficial air velocity was kept constant in order to ensure a stratified flow pattern at the inclined inlet. Consequently, the flow pattern in the inlet did not vary. Experimental data for oil-water separation efficiency in the GLLCC were acquired for different combinations of the superficial oil and water velocities, and the location of the oil finder and split ratio were all varied for each combination.

Preliminary results from Vasquez (2000) shown that as the swirl decays rapidly in the liquid section of the separator, there is no good separation effect for an oil-dominated mixture.

He observed that at low liquid velocities, the flow in the inlet is found to be unstable due to churning in the vertical pipe that feeds the separator. As a result of these disturbances and a weak swirling effect, no oil core is formed and poor separation is obtained. Secondly, at high liquid velocities a gas core is observed all the way through the liquid phase. This enables gas to be carried to the underflow, thereby limiting the gas-liquid separation. It was observed that the position of the oil finder did not have any significant effect on the oil-water separation efficiency with different oil-water conditions and at varying split ratios. The experimental data showed the capability of the GLLCC to provide a clean water stream in the water outlet pipe for low oil contents and high water superficial velocities.

A mechanistic model was developed for the prediction of air-oil-water separation performance of the GLLCC. The model consists of several sub-models such as inlet flow pattern analysis, nozzle analysis, droplet size distribution model and separation model based on droplet trajectories in swirling flow. The inclined inlet analysis was based on a two-fluid model for gas-liquid flow and aimed at predicting the spatial configuration and velocities of both gas and liquid phases at the inlet. The oil-water separation in the GLLCC liquid region was predicted based on droplet trajectory analysis from the inlet slot to the top of the oil finder.

By analysing oil droplet trajectories, the purity of the liquid at the water and oil outlets was determined. The developed model was found capable of predicting both the trend of the experimental data as well as the absolute measured values. The work of Vasquez (2001) did not provide the hydrodynamic flow behaviour of the complex, turbulent, swirling, multiphase flow in the three-phase pipe separator. This is the main focus that this research work is going to address. Previous study by Erdal (2001) was limited to LDV measurement of a single phase flow that passed through a cyclone with a single outlet. However, this research work is aimed at providing SPIV measurement of both single and multiphase flow passing through three different outlets of a pipe separator.

Garcia et al (2003) and Sierra (2003) analysed the separation performance of a compact cyclonic separator (CCS) with main cylindrical body height/diameter aspect ratios ranging from 2.5 to 3.8. A 3D solution of the three-phase flow of gas/oil-propane-coal in the CCS was obtained using a combination of the mixture model and the discrete -

phase model (DPM) of Fluent CFD for the gas-liquid mixture and the particulate phase respectively. They used the RNG model to account for the turbulence in the three-phase flow in CCS.

The validation of the CFD results against experimental data was presented in the form of parametric studies. Among the parameters varied was the viscosity, inlet velocity, particle size and exit pressures. The tangential velocity was found to be in perfect agreement with experimental values near the wall, but over-predicted by 14% near the inner core. They used contour plots on axial slice in conjunction with particle track to show good separation performance for the three-phase mixture.

2. 6 Flow regimes in gas-liquid flows

When a gas and a liquid flow together inside a pipe, there are different geometrical configurations, or flow regimes as shown in Figure 2.6, that are expected to occur. The regime depends on the fluid properties, the size of the conduit and the flow rates of each of the phases. The flow regime can also depend on the configuration of the inlet; the flow regime may take some distance to develop and it can change with distance as (perhaps) the pressure, which affects the gas density, changes. For fixed fluid properties and conduit, the flow rates are the independent variables that when adjusted will often lead to changes in the flow regime (McQuillen et al., 1981).

A stratified flow pattern is observed when gas and liquid flow in a pipe such that the flow is dominated by the gravity force. This two phase flow separates from each other by a continuous interface and the liquid stratify at the bottom of the pipe (Figure 2.6). The structure of the interface may be smooth or wavy depending on the gas flow rate. At low gas velocity, the interface is smooth or may be rippled by small capillary waves of a few millimetre lengths. However, small amplitude regular waves appear with an increase in the gas velocity.

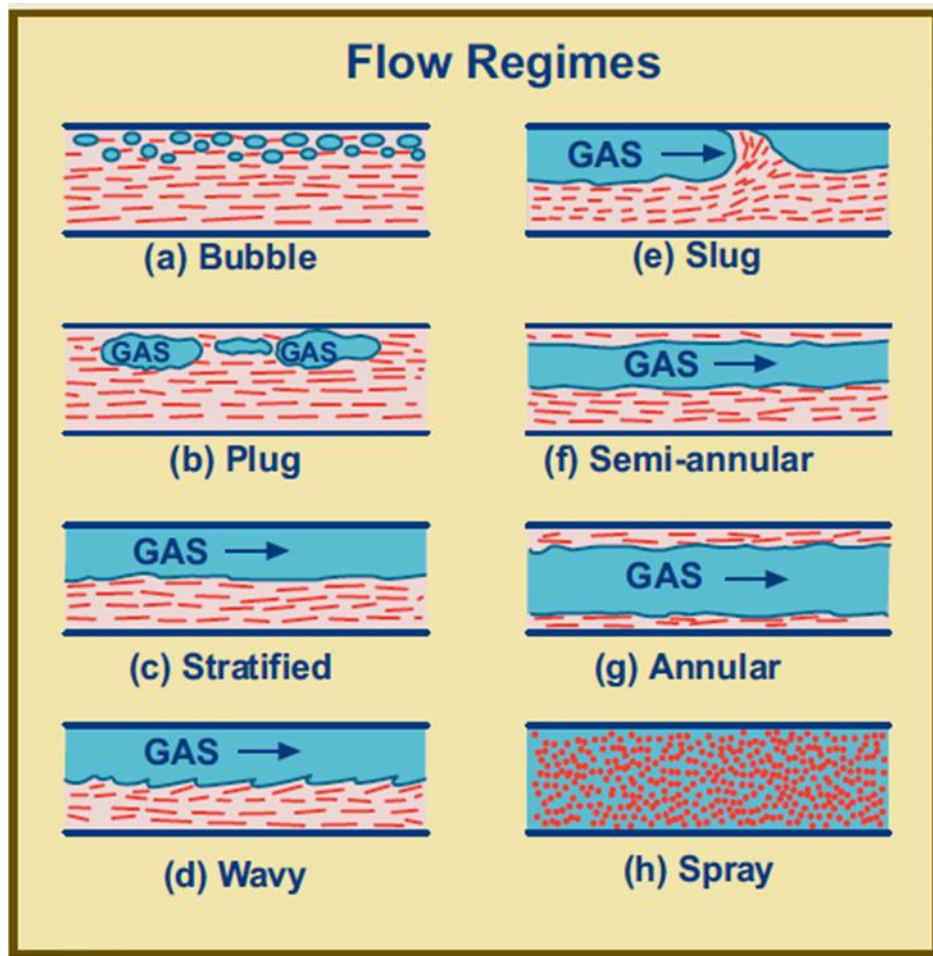


Figure 2.6: Flow Regimes in Gas – liquid Flows

2.7 Summary

To summarise the literature review a number of conclusion can be reached. These are as follows:

- (1) For many years, flow patterns in cyclone separator have been successfully explained. Many researchers have compared the predicted flow patterns in cyclone with experimental data for different phases and a range of flow rate. They concluded that computational models give good qualitative agreement with experimental measurements especially the tangential and axial velocity distributions. However, there are discrepancies in the quantitative analysis.
- (2) Advances in numerical modelling techniques and computers, have provided engineers with a wide selection of commercially available fluid flow models based on the Navier-Stokes equations. As shown in the literature review, commercial Navier-Stokes equation solvers can reproduce measured data for a different range of cyclone geometries and flow rates. It is believed that commercial solvers can be used to predict velocity flow fields in cyclone. Most commercial CFD package offers three RANS turbulence models, the $k-\epsilon$ model, the renormalisation group model and the anisotropic Reynolds stress model. Earlier discussion of the numerical simulation advocated that RSM gives the best approximation of the measured velocity profiles and is a good indication of its suitability to model the anisotropic turbulence feature in a cyclone. However, RSM simulation can be inherently unstable and slow. It is therefore better to obtain a solution using the $k-\epsilon$ model before activating the RSM calculation.
- (3) Experimental researchers have used different inlet configurations to generate axi-symmetry swirling flow in a cyclone. Many geometrical designs such as variation in cyclones' height and diameter have been proposed so as to improve the performance of cyclone separators.
- (4) The literature review demonstrates that different flow measurement methods have been used successfully in many cyclone experimental studies to measure both the tangential and axial velocity components. In contrast to the methods for one point measurement such as the Pitot tube, the hot wire anemometer and the laser Doppler velocimeter, PIV system can carry out two-dimensional and three-

dimensional instantaneous velocity measurement without any contact with the fluid under investigation.

- (5) Vasquez (2001) has already carried out experimental work that concentrated on the separation efficiency of the three-phase cylindrical cyclone. In addition, mechanistic models have been developed for the prediction of the complex flow behaviour and separation efficiency in the GLLCC. However, the velocity flow field data of the complex, swirling multiphase flow missing in the work of Vasquez (2001) will be investigated by the SPIV system. A previous study by Erdal (2001) was limited to LDV measurement of a single phase flow that passed through a cyclone with a single outlet. However, this research work is aimed at providing SPIV measurement of both single and multiphase flow passing through three different outlets of a pipe separator.
- (6) The commercial CFD package, ANSYS FLUENT will be used to predict single and multiphase flow in the pipe separator. By comparing the predicted velocity profile against those measured data, the numerical model's ability to describe the flow patterns that occur in the real flow system could be determined, and subsequently validated for use in the optimisation study.

CHAPTER THREE

STEREOSCOPIC PIV MEASUREMENTS

This chapter starts with a brief discussion of the principles and techniques of stereoscopic PIV. The second part gives an overview of the experimental facility constructed to study the hydrodynamics behaviour of multiphase flow in the cylindrical cyclone separator. The third part describes the experimental set up and the measurement strategy used.

3.1 Principles of Stereoscopic Particle Image Velocimetry (SPIV)

The technique of particle image velocimetry is an optical method of fluid visualization used to obtain instantaneous velocity measurements and related quantities such as vorticity, Reynolds stress and turbulence. Stereoscopic particle image velocimetry (SPIV) is an extension of conventional 2D PIV for measuring the third velocity component in the laser light sheet plane. The determination of the velocity of a fluid using SPIV consists of a number of separate processes (see Figure 3.1 and details below);

- Tracer particles that are assumed to faithfully follow the fluid dynamics (the degree to which the particles faithfully follow the flow is represented by the Stokes number) are added to the flow (Adrian, 2004; Raffel et al., 1998; Westerweel, 1997; Willert, 1997; Adrian, 1991).
- At least two cameras are to be used to view a flow field from different perspective positions.
- A laser beam illuminates a plane of the flow under investigation twice within a short time interval.
- The test section is enclosed within a clear water prism in order to minimize the effect of refraction.
- The laser light is scattered by tracer particles and recorded in a sequence of frames using equipment such as a CCD camera, photographic film or holographic plates.

- Computer hardware with suitable software is used to process the recorded images and extract velocity information indirectly through the tracer particles.
- The calibration of the camera is achieved using a target mounted on an accurate traversing mechanism. The calibration images are then used to map locations between the fluid and the cameras and also to calculate the local magnification factor.
- The combination of a set of 2-dimensional vector fields from a pair of cameras is used to obtain a three dimensional vector field.

The advantages of PIV include that it is a non-intrusive, whole field velocity measurement technique. Excellent references for the history and up-to-date development of the PIV technique and its applications are the review work of Adrian (2004), Raffel et al (1998), Westerweel (1997) and Willert (1997).

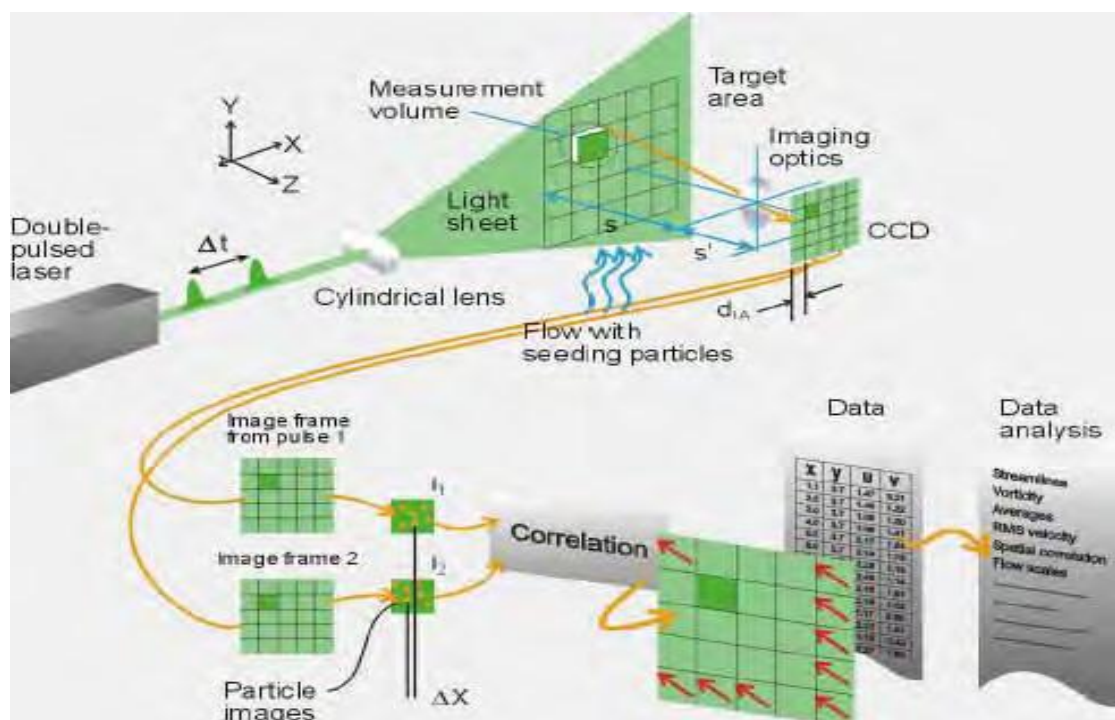


Figure 3.1: Outline of PIV steps (Dantec Dynamics, 2008).

The theory of PIV is quite simple. A fluid seeded with thousands of tiny tracer particles assumed to faithfully follow the flow is illuminated by 2 pulses of laser light. The images of the particles in the light sheet create an exposure in the camera, each time the laser is pulsed. Double pulsing the laser gives two images for each particle, and dividing the distance moved by a particle by the time between pulses gives the velocity for that particle. By determining the particle image displacements at many points in the image, a flow velocity field is produced. In order to capture the out-of-plane velocity component, SPIV uses two cameras to view a flow field from two perspectives. The pair of two-dimensional velocity vectors for all points in the flow is then combined to yield a three-dimensional velocity field. The major differences between classical PIV and SPIV are the number of cameras used, their positioning and the velocity components which can be measured.

3.1.1 SPIV System

3.1.1.1 Tracer Particles

The technique of particle image velocimetry is an indirect flow visualization method in which the seeding particle velocity is determined as the fluid velocity. Therefore, the choice of seeding particle is important in the successful implementation of PIV experiments. An ideal seed particle is characterized as inert, neutrally buoyant and small enough to accurately follow the flow of interest, but large enough to generate a strong scattering signal. Therefore, there is a need for compromise between the tracer particle's size and its ability to scatter enough light within the laser sheet plane to give the ability to accurately follow the flow under investigation (Melling, 1997).

The degree to which the particles faithfully follow the flow is represented by the Stokes number (S_k), which is given by:

$$S_k = \frac{\tau U_o}{d_c} \quad (3.1)$$

where τ is the relaxation time of the particle, U_o is the fluid velocity of the flow, and d_c is the characteristic diameter of the particle. The time τ_p , can be determined from equation 3.2 for the particle used in the experiment:

$$\tau_p = \frac{(\rho_p - \rho_f) g d_p^2}{18\mu_f} \quad (3.2)$$

In determining acceptable tracing accuracy, the Stokes number is expected to be very small (that is much less than 1). This means that the tracer particle motion is tightly coupled to the fluid motion and will closely follow fluid streamlines. If the Stokes number is large, the tracer particles are not influenced by the fluid and their response time is longer than the time the fluid has to act on it. Therefore, the particle will pass through the flow without much deflection in its initial trajectory. (Prasad, 2000a; Hassan et al., 1998).

On the other hand, in order for the tracer particle not to float or sink, or to be influenced by centrifugal forces, it should have a density close to that of the fluid under study. Good density matching with the flow medium and maximum reflected light are characteristics associated with hollow, coated seeding particles. Seeding particles used to follow fluid motion can be in the form of solid particles, gas bubbles or liquid droplets such as plastic sphere or poly-crystalline particles, and olive oil droplets or fog. Also important is the particle concentration, which must be high enough to give reliable velocity measurements. Adrian et al (1991) suggested that 8-10 particle pairs per interrogation spot are desirable to give reliable data. For multiphase flow, fluorescent particles are sometimes used due to their ability to radiate light at a different wavelength than they absorb, and this enables the background light to be filtered thereby making the particles more visible.

3.1.1.2 Illumination System

The laser and light sheet optics are parts of the illumination system for PIV measurements. Sufficient laser light sheet intensity is a basic requirement in order to record good images of the small tracer particles used to follow the fluid flow. Typically, a laser is used predominantly because of its ability to produce a bright light sheet with almost constant thickness without aberration or diffusion within short pulse durations (Prasad, 2000a). The optics consists of a combination of cylindrical and spherical lenses in order to diverge the light beam in one direction and to control the thickness of the light sheet respectively.

Generally, two types of lasers are used for illuminating a PIV experimental setup: these may be either continuously emitting lasers (continuous wave lasers) or pulsating lasers which are obtained by either chopping or sweeping the light beam. Nowadays, pulsed lasers are preferred due to their ability to produce high intensity light with short pulse duration.

Also, pulse lasers can store and deliver all of the laser power at exactly the desired instant. Continuous wave lasers, such as helium-neon lasers or argon lasers, can be used for PIV applications involving low velocity fluid flows. As a general practice, for fluid flow with velocity greater than a few meters per second, a pulsed Nd: YAG (neodymium-doped yttrium aluminium garnet) laser system is used (Raffel et al., 1998).

3.1.1.3 Image Recording

The basic requirement for PIV recording is that the camera should be able to record two images within a short period of time so that the same individual particles appear in both. PIV images can be recorded on CCD/CMOS (Charge Coupled Device/Complimentary Metal-Oxide Semi Conductor) sensors and holographic plates for holographic PIV. Currently PIV measurements favour the usage of electronic cameras with either a CCD or CMOS pick-up device. These provide immediate feedback concerning image quality and enable instant analysis. A double exposure electronic camera is capable of recording two images within a very short inter-frame interval (Prasad and Jensen, 1995). These frames can then be transferred to the host computer system for processing using relevant software through the frame grabbers, and the camera is then prepared to record the next image (Stanislas, 1997).

3.1.1.4 Synchronizer

Through the host computer the synchronizer performs the task of controlling the sequence and timing of all of the components of the PIV system so that they can function as an integrated system. Thus, the synchronizer ensures that the laser pulse and the camera are triggered in the correct order and appropriate timing for the flow conditions being investigated.

3.1.1.5 Image Analysis and 2D Vector Validation

The PIV analysis of a pair of images recorded successively from one illuminated plane of the tracer particle seeded flow starts with the division of the recorded image into a grid of sub-areas which are called interrogation areas. Each interrogation area is then statistically analysed using Fourier transformation. This is a mathematical cross-correlation procedure designed for a multiple frame, single camera exposure in which the relative displacement of the particle in the interrogation area is determined in order to achieve the best match between images.

By multiplying the shift in pixels within the interrogation area by the image magnification and dividing by the time delay between images, the average velocity within each interrogation area is given (Keane and Adrian, 1992). The process of the selection of an interrogation area, cross-correlation, finding of peak and determination of the velocity vector is repeated over the whole image, thereby resulting in a complete vector representation of the flow field. Since SPIV uses two cameras to view a flow field, a pair of two dimensional velocity vectors is then combined through the 3-D calibration proposed by Soloff et al (1997) which gives a single three dimensional velocity vector field.

In post-processing, each vector is compared against neighbouring vectors. Vectors that vary by more than the validation tolerance from the neighbourhood average are removed. This helps to avoid incorrect data or data drop-outs that will produce spurious result. Places that are left empty can be filled in by interpolating the neighbouring vectors to get the best estimate of the velocity at that point. After the vector field has been validated and the missing points filled in, the properties of the flow can be computed (TSI Inc, 2006; Westerweel, 1997).

3.1.1.6 Stereoscopic Camera Configurations

There are generally two optical arrangements for stereoscopic particle image velocimetry: translation and angular displacement arrangements. Today, the angular displacement arrangement is the most commonly used stereoscopic camera configuration, as it allows for large stereoscopic viewing angles (see Figure 3.3).

This enables the accurate measurement of the out-of-plane component, as long as the calibration target can be placed in the flow domain. Despite the advantage of greater accuracy associated with the angular displacement system, its image field is still affected by variable magnification. As shown in Figure 3.2, the translation arrangement is simple to set up and enjoys uniform magnification in the image field. However, the range of stereoscopic viewing angles is limited due to the occurrence of optical aberrations at large angles (Adrian and Westerweel, 2011; Prasad, 2000b; Prasad and Jensen, 1995).

The Scheimpflug configuration is an angular lens displacement system that uses two cameras whose axes are rotated inward such that they intersect at the midpoint of the domain to be recorded. The Scheimpflug configuration requires the object plane, image plane, and lens plane to intersect at a common point, as schematically depicted in Figure 3.2. The plane of best focus is adjusted to overlap the lightsheet by tilting the image sensor plane and the lens plane into the Scheimpflug configuration. When the Scheimpflug configuration is satisfied, all of the tracer particles within the camera's field of view are in good focus (Raffel *et al.*, 1998).

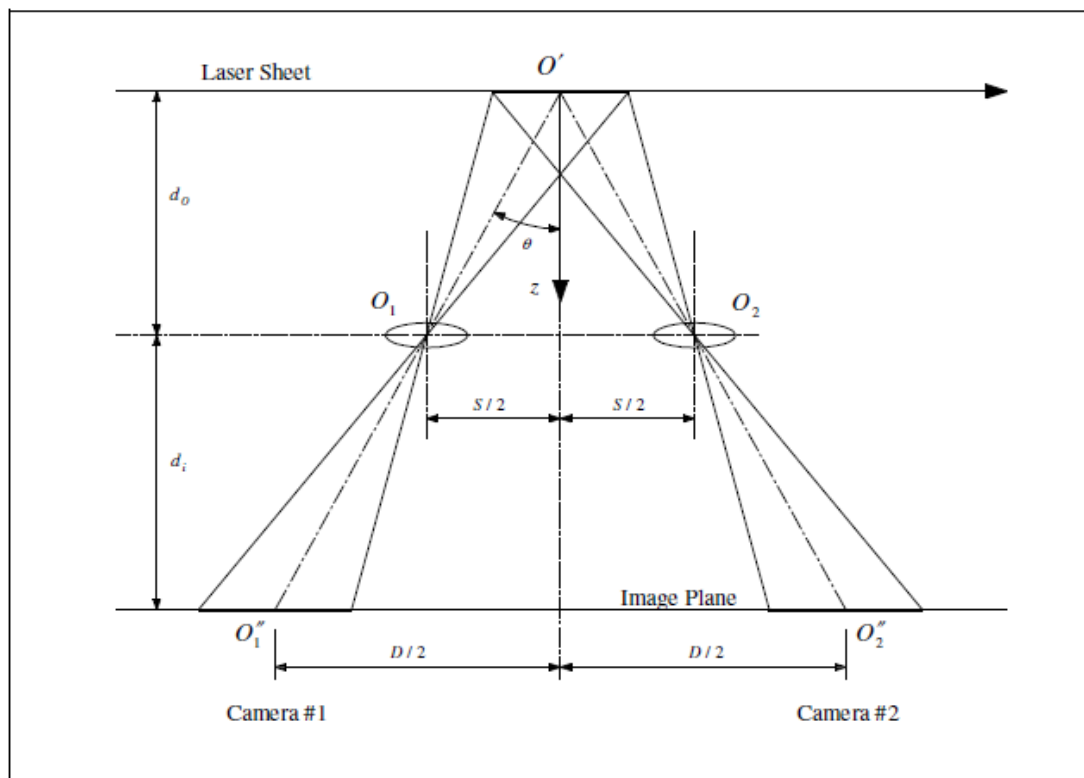


Figure 3.2: Stereoscopic Translation Camera Arrangement

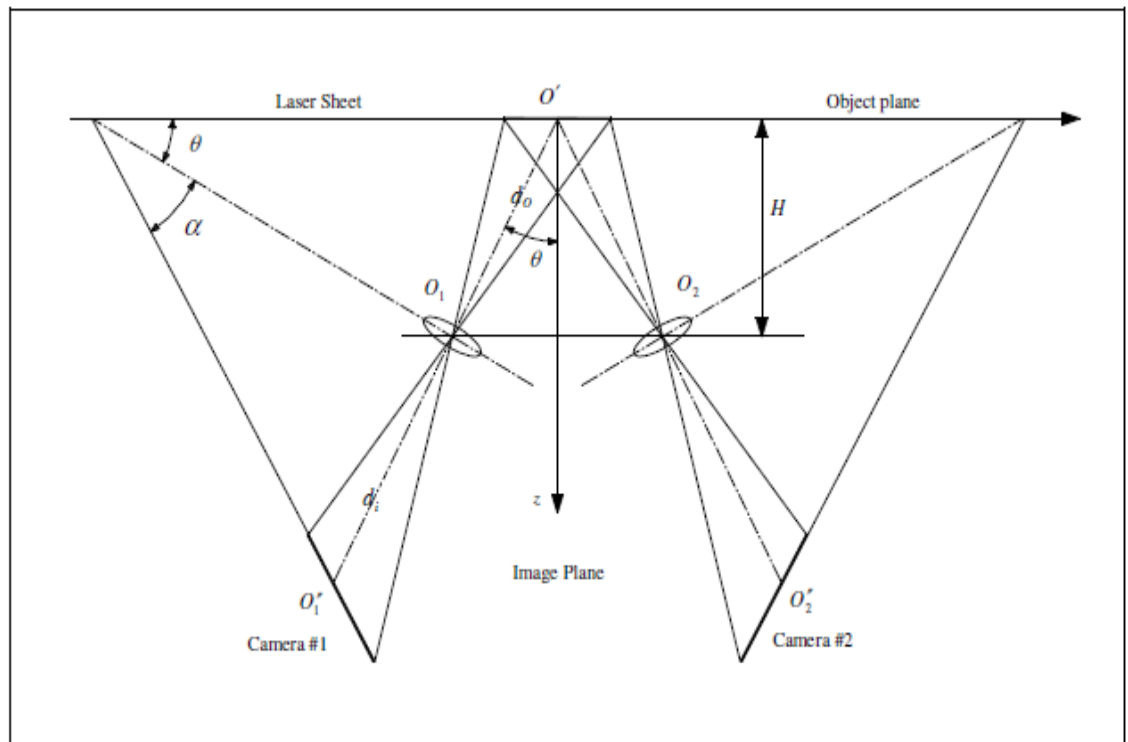


Figure 3.3: Stereoscopic Angular Camera Arrangement.

3.1.1.7 Calibration Procedure

A calibration procedure is needed to remove perspective distortions introduced by the Scheimpflug camera arrangement. Perspective distortion of the images causes a rectangle in the lightsheet plane to be imaged as a trapezoid on the image sensor, as shown in Figure 3.4. The calibration method uses a target with a grid of markers placed in or near the lightsheet.

The stereo camera is aligned in its final configuration, and calibration commences by acquiring an image of the calibration target on each camera. The location of the grid points in the image plane is usually obtained by template matching; the template must match the characteristic marks that represent the grid points on the original target.

The stereo-PIV from TSI Inc uses the 3-dimensional calibration-based method to reconstruct the 2-D displacement fields of the cameras and then obtain the 3-dimensional vector fields (TSI Inc, 2006). This approach, as described by Soloff et al (1997), does not require knowledge of the system's geometry at any stage of the

reconstruction. This is because the 3D calibration method involves the acquisition of calibration data at different z-locations.

Therefore, the 3D calibration-based method is found to be best suited for recording geometries which cannot easily be mathematically modelled. In addition, the spatial calibration of the images is used for mapping locations between the fluid and the cameras in order to correct the perspective distortion caused by variable magnification across the field of view.

It is necessary to recalibrate the cameras every time a new plane of measurement is chosen (Soloff, 1997). The images of the target captured are then analysed using the perspective calibration program of INSIGHT 3G. This results in a mapping function that gives the relationship between the particle image displacements in the captured images and the motion of the tracer particles in the fluid in all three directions. More information about the calibration procedure and stereoscopic PIV can be found in Kompenhans et al (2002), Prasad (2000b) and Willert (1997).

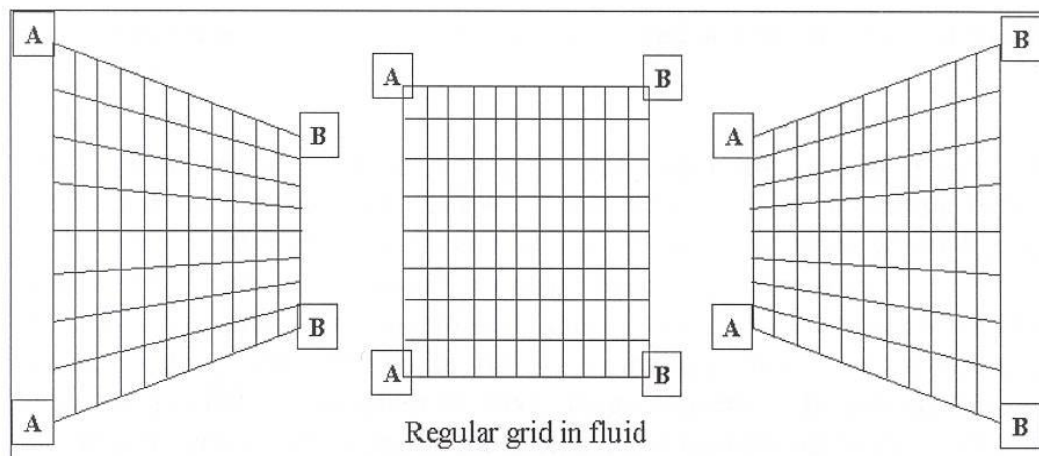


Figure 3.4: Image Perspective Effect Due to Camera Tilt in Scheimpflug Arrangement.

3.1.2 PIV Measurement of Multiphase Flows

The PIV technique has been successfully used to obtain measurements of single phase flow velocity fields, and it can be extended to multiphase flows in order to obtain full field velocity measurements for each phase. Simultaneous measurements of the continuous and dispersed phases are extremely important to understand interphase

interaction and the concentrations, sizes and shapes of the dispersed phases. The PIV measurement of a multiphase flow is more complicated than that of a single phase, and this is due to the presence of dispersed phases that introduce the following additional problems;

- (a) Strong reflection at interfaces between the phases (particularly gas-liquid interfaces).
- (b) In the region on the PIV image where the concentration of the dispersed phase is rather high, there is little space left for the tracer particles, resulting in low valid detection probability.
- (c) The dispersed phase can introduce shadows, which together with the dispersed phase in front of the light plane hamper visibility in the measurement plane. This reduces the amount of information present in the PIV images.
- (d) The deformation of the dispersed phase, such as gas bubbles, during the time delay between the recordings of flow may reduce the precision of PIV measurement.
- (e) Problems associated with the different refractive indices of the phases.

When the conventional PIV system is used for the measurement of a multiphase flow such as a bubbly flow, the intensity of light reflected from the surfaces of bubbles not only saturates the CCD camera but also overwhelms the intensity of light refracted from the seeding particles for PIV in its vicinity (Bellani, 2011). The continuous phase can be differentiated from the dispersed phase by using fluorescent dyes and optical band pass filters (Raffel et al., 1998). For example, the combination of the PIV technique with laser induced fluorescence (LIF) and/or the shadow image technique (SIT) are options available to measure the velocity distributions of the phases and their interaction (Adrian and Westerweel, 2011). Nevertheless, PIV measurement techniques are limited to relatively low volume fractions of the dispersed phase where usually $\alpha \leq 5\%$ (Hassan, 1999; Hassan et al., 1998).

The application of conventional PIV image processing technique to a multiphase flow PIV image can only give velocity maps which do not differentiate between each of the phases present in the velocity field. Therefore, multiphase flow PIV measurement usually needs additional analytical algorithms or even supplementary techniques.

3.1.2.1 Laser Induced Fluorescence

Laser Induced Fluorescence (LIF) has been used for combustion diagnostics and to characterize gas and liquid fluid flow situations. LIF techniques can be used for imaging properties such as species concentration, partial pressure, temperature, and flow velocity flow distribution or visualization.

The multiphase flow is seeded with fluorescent tracer which absorbs energy at the laser wavelength and emits light at a longer wavelength and thus with a different colour. A laser light sheet illuminates a field of view containing both fluorescent tracer particles and dispersed phase particles. One of the cameras is equipped with an appropriate long pass optical filter with wavelength greater than 532 nm which allows the fluorescent light to pass and therefore records only the light scattered by the fluorescent tracer particle. The other camera is fitted with an optical narrow band filter with a wavelength of 532 ± 3 nm, so that only the bright light from the dispersed phase is effectively recorded. Because of the difference in size between the fluorescent tracer and dispersed particles, the small fluorescent particles are hardly visible in the image. With the help of a pulse generator, both cameras and the laser are synchronised in order to provide simultaneous images of the test section.

The velocities of the two phases are determined by means of the digital image processing of the two consecutive images for the tracer and fluorescent particles. However, the possibility of the strong absorption of the penetrating laser light sheet by scattering on the surface of the dispersed phase (gas bubbles) located within the sheet at higher void fractions restrict this method to small gas volume fractions (Bröder and Sommerfeld, 2002). Lindken et al (1999) reported the PIV measurement of the velocity field in multiphase flows, where a digital mask in combination with the Minimum Quadratic Difference (MQD) method (Gui and Merzkirch, 1996) was adopted to enhance the evaluation of the velocity field in the area of contact between the gas and liquid phases. The application of the digital mask technique is effective due to the significant difference between the sizes of the gas bubbles and the tracer particles seeded in the liquid phase which appear on the PIV images.

3.1.3.2 Shadow Image Technique

A combination of planar shadow imaging and particle image velocimetry (PIV) is another approach often used to simultaneously measure the continuous and dispersed phase velocity fields. The continuous phase is seeded with fluorescent tracer particles and illuminated by a laser light sheet. One of the cameras is equipped with an appropriate optical filter to record only the light scattered by the fluorescent particle.

However, a shadow image of the dispersed phase is produced with back lighting using a red light emitting diode (LED) array and recorded by the second camera. The velocities of the continuous and dispersed phase are determined by the application of the PIV and particle tracking velocimetry (PTV) processing. The shadow image technique differentiates the bubbles as shadows, because the pixels of the bubble image are of much smaller brightness than those representing the background. The shadow image method is found to give more precise estimates of the sizes and shapes of bubbles when compared with the LIF method. However, in cases of large volume fractions of the dispersed phase, it is difficult to detect the bubble shadows from the dispersed phase within the multiphase flow. An example of this experimental set-up is shown in Figure 3.5.

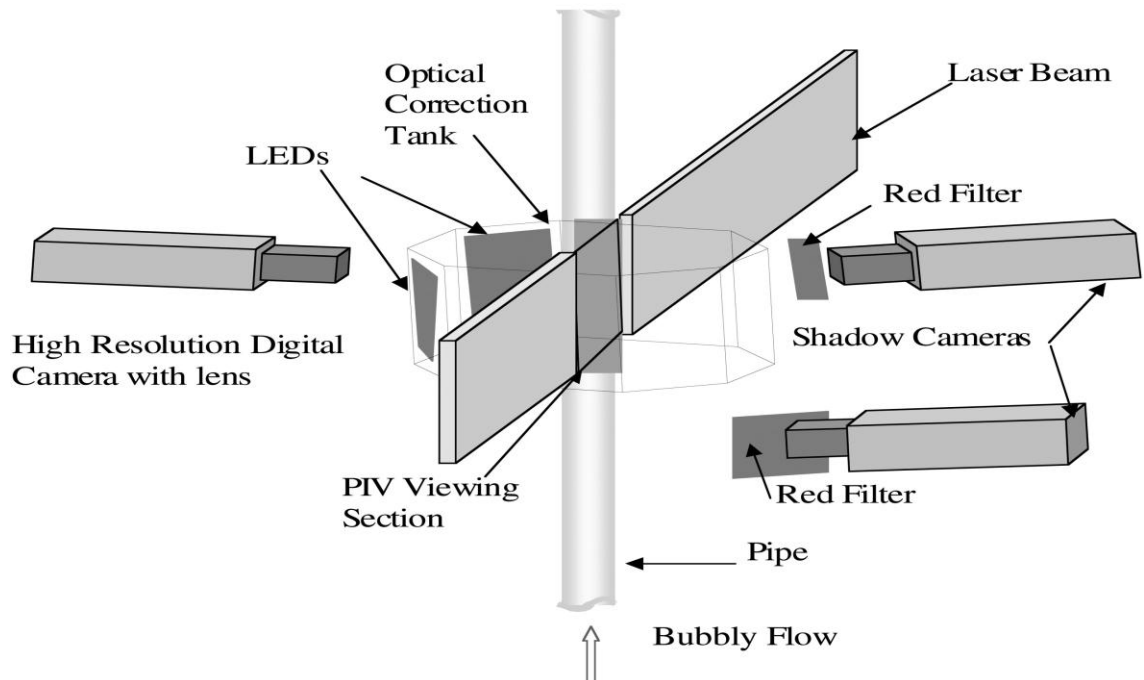


Figure 3.5 : Schematic Diagram of a PIV/ SIT Experimental set up (Hassan, 2002).

3.1.3 Sources of Uncertainty in Stereoscopic PIV Systems

All measurements are prone to uncertainty, as there is likely be difference between the real value of an observed quantity and the value estimated from measurements. Errors in PIV are usually categorised as either random or systematic. Green and McAlister (2004) referred to random uncertainty as due to aspects of the experiment that are difficult to control and which contribute to general uncertainty in the results.

Typical examples of random uncertainty occur as a result of noise in the light field, such as background speckles, aberrations of the lenses or electronic noise in the image recording medium. Systematic uncertainty in PIV measurements is associated with illumination, particle size, the image recording equipment and image analysis procedures. For example, systematic uncertainty may result from:

- The inability of a particle to follow the flow without slipping.
- The rotation and deformation of the flow within an interrogation spot leading to a loss of correlation.
- Perceptive distortion caused by stereoscopic camera configuration.
- When the calibration procedure is performed in only one z position.
- The non-uniformity of the illumination and the non-uniform reflection of particles at different locations and angles (Huang *et al.*, 1997).

Systematic uncertainty can be minimized by the careful selection of experimental conditions (Green and McAlister, 2004; Prasad, 2000c). Camera calibration helps in removing the perspective distortion from the velocity vector fields. The Scheimpflug mount supplied by TSI Inc helps to reduce the out-of-focus area created by the oblique viewing directions of the cameras (Prasad and Jensen, 1995). Also, the use of a water prism ensures paraxial recording and is extremely efficient at reducing the radial distortion arising from a liquid-air interface.

3.2 Experimental Set-up

This section describes the experimental facility used for the SPIV measurements.

3.2.1 *Experimental Facility and Flow Loop*

The three phase flow facility used in this study is based on one of the geometries developed for multiphase flow separation by the Separation Technology Project of the University of Tulsa, USA. Two different configurations, namely single stage and two stage systems were developed to separate a gas-oil-water mixture. A single stage configuration was selected due to its associated robust separation efficiency and compactness when compared to the two stage configuration. A scaling factor based on the inlet flow rate and pipe diameter was used to design a 30 mm ID laboratory prototype gas-liquid-liquid cylindrical cyclone (GLLCC) separator henceforth referred to as the pipe separator. The experimental facility was fabricated and installed in order to obtain experimental measurements of hydrodynamic flow behaviour for single and multiphase flow in the cylindrical cyclone under different flow conditions at atmospheric pressure and room temperature.

The separator test section was constructed using a transparent perspex tube. As shown in Fig. 3.6, the main body of the separator is a 30-mm ID vertical cylinder with a height of 1675 mm. The inlet is a 30-mm ID pipe, inclined at an angle of 27 degrees from the horizontal and connected tangentially at 585 mm from the top of the vertical main body. The inlet configuration was constructed by inserting a gradually reduced inlet nozzle at 400mm by length of the inlet section.

The gradually reduced nozzle was designed narrowing down from a full bore cross sectional area to 25% of the inlet cross sectional area, and connected tangentially to the vertical pipe. Detailed drawing of the inlet configuration of the pipe separator is given in Figure 3.7. The gas outlet is a 20-mm ID pipe attached to the top of the vertical main pipe. The water outlet is a 20-mm ID pipe connected at 185-mm from the bottom of the vertical main pipe. The oil outlet is a 10mm ID pipe, 700-mm long inserted into the main vertical pipe through its base. A seal was used to keep the oil outlet located in a concentric position. Detailed drawing of the pipe separator test section is given in Appendix D.

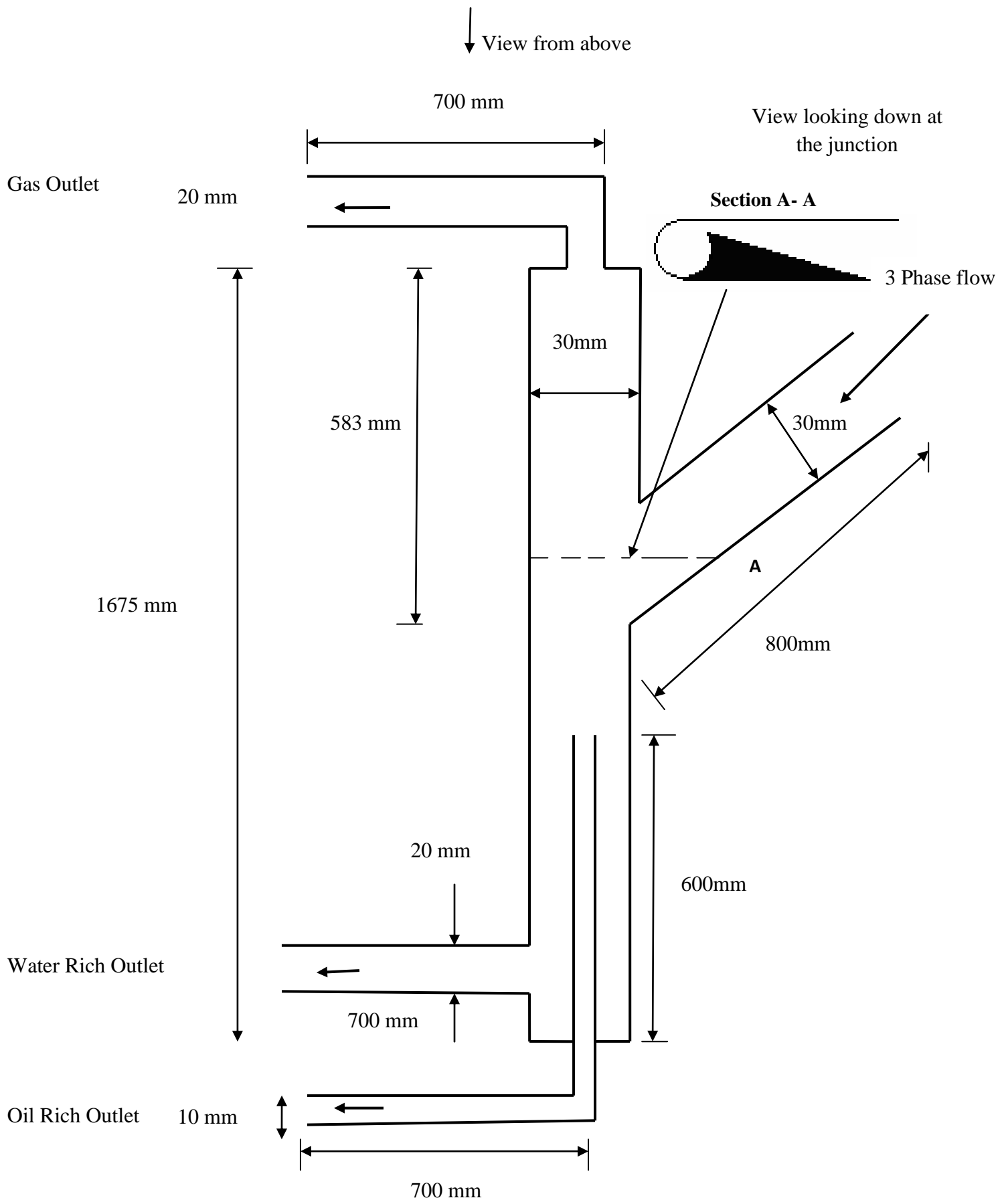


Figure 3.6: Schematic of Cylindrical Cyclone.

Water was stored in a 640 litre storage tank situated just below the experimental rig and pumped by an ES 6000 peripheral pump (manufactured by Stuart Turner) at atmospheric pressure into the water flow line. As shown in Figures 3.8, 3.9 and 3.10, the water flow rate is controlled by both globe and ball valves and metered to the desired flow rate using a rotameter.

A recycle loop was installed to allow part of the water flow to be returned to the water storage tank. This arrangement ensured flow stability and allowed better control of the inlet water flow rate. Air was supplied at 3.5 bar from a central compressed air line and passed through a PCL (Pneumatic Component Ltd) filter regulator to filter the air supply and maintain a constant pressure, which was controlled by both globe and ball valves and metered by a rotameter.

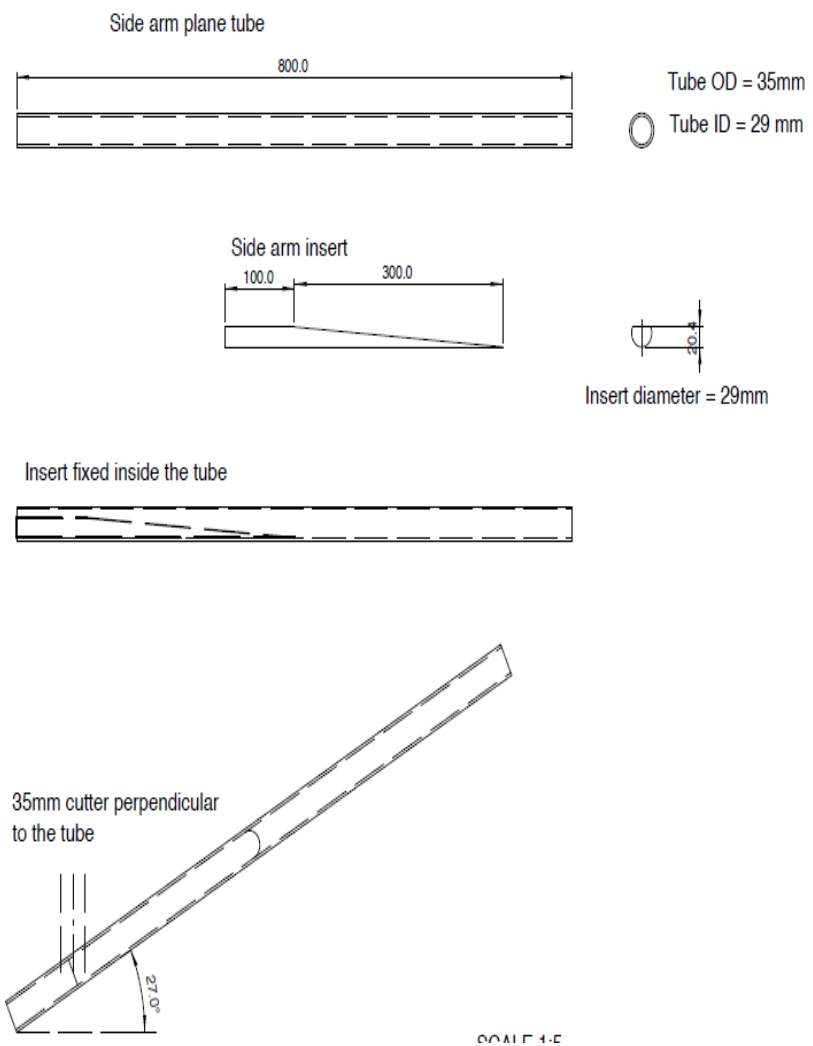


Figure 3.7: Inlet Configuration of the Pipe Separator.

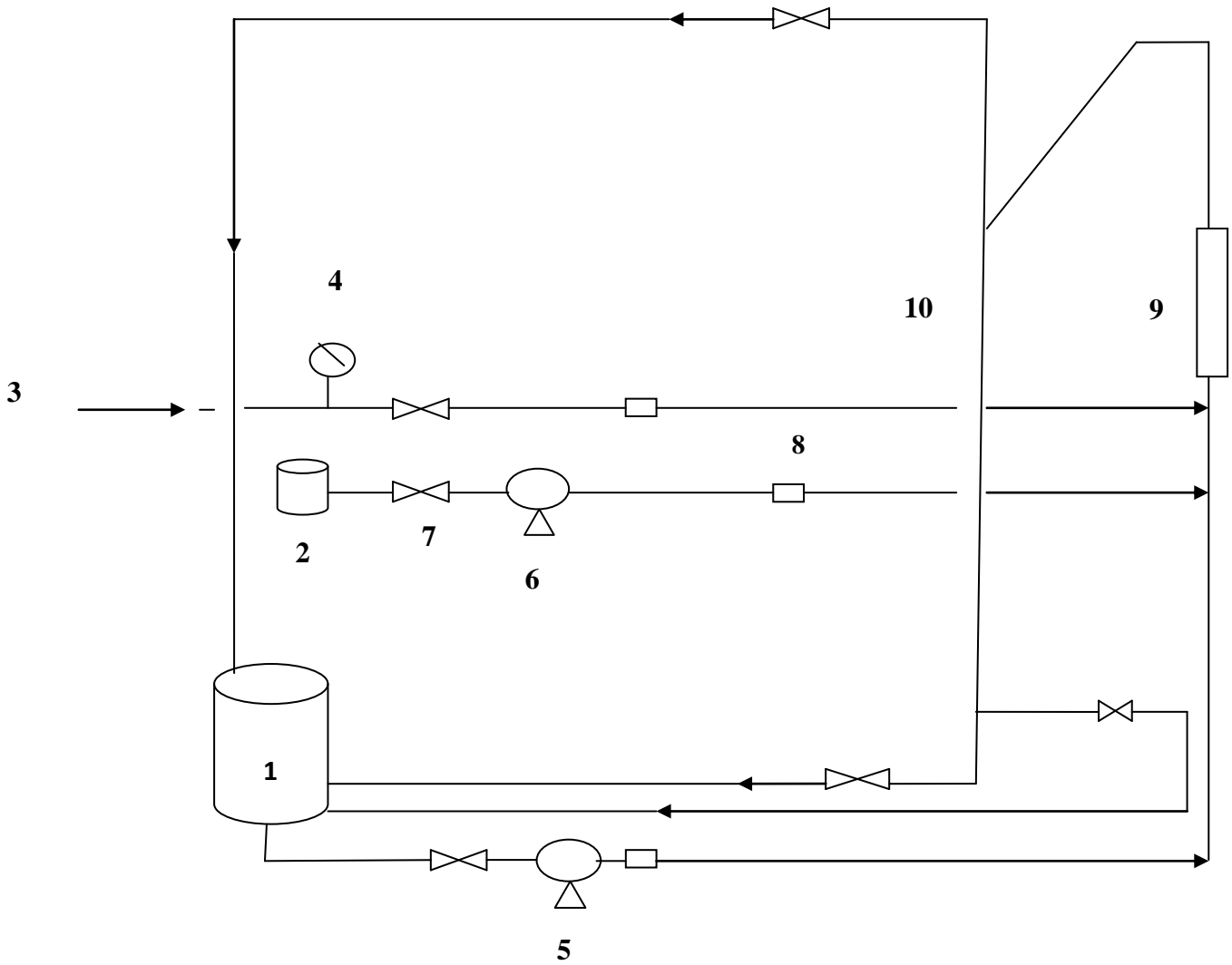


Figure 3.8: Diagram of the Air-Water-Oil Separation Experimental Flow Loop

1- Water tank,

6- Oil pump,

2- Oil tank,

7-Valve,

3- Air flow,

8- Flow rate,

4-Pressure gauge,

9- In line mixer,

5- Water pump,

10- Cylindrical cyclone.

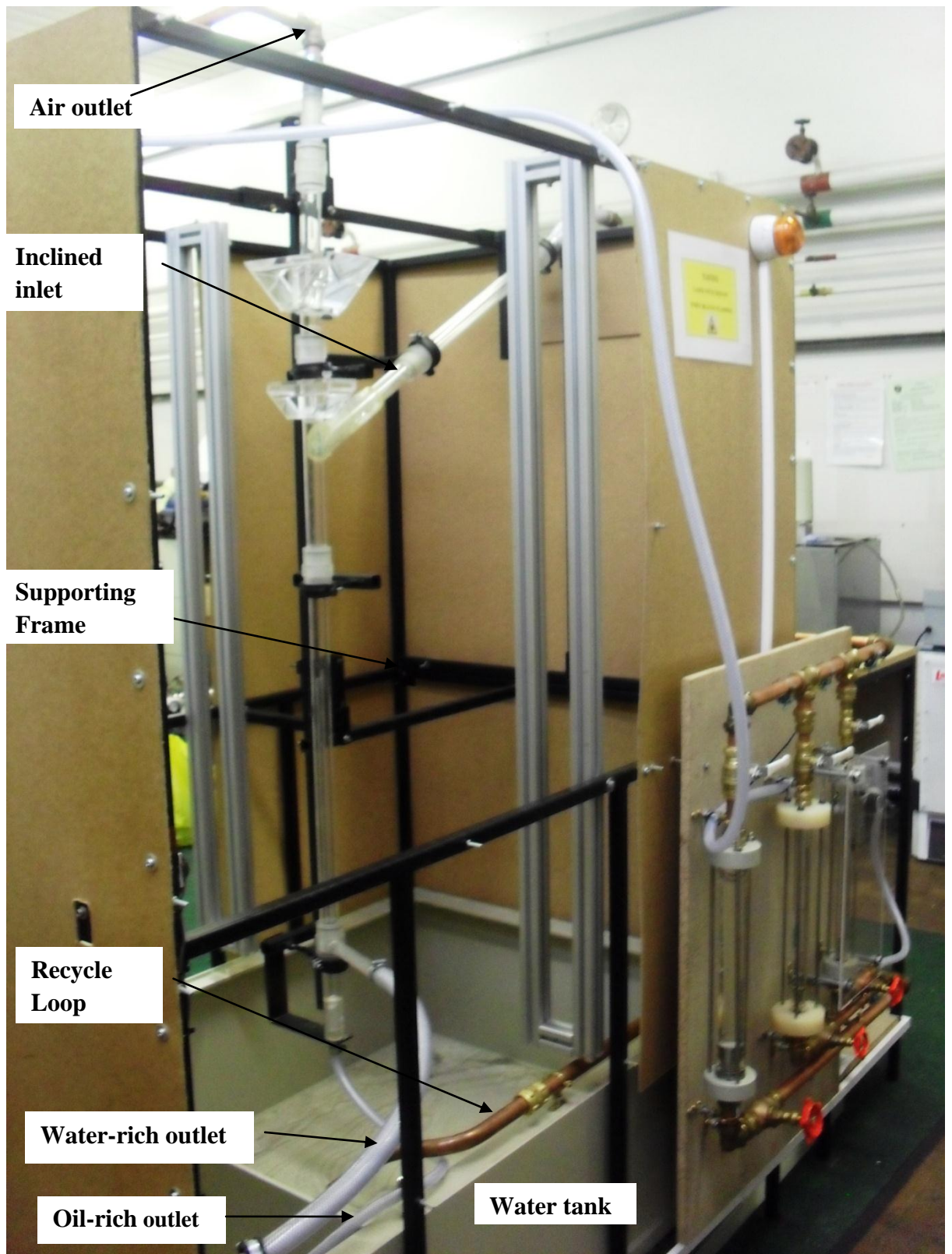


Figure 3.9: A 30-mm ID Cylindrical Cyclone Separator.

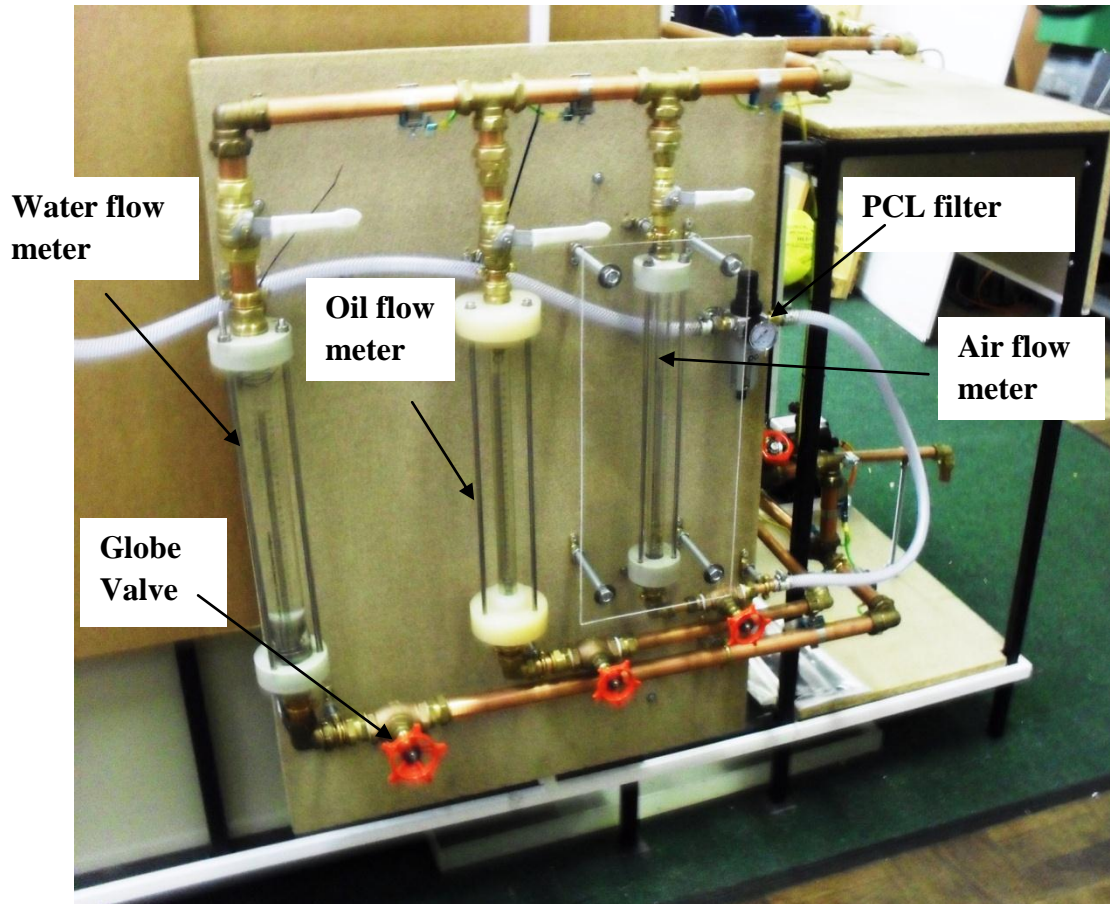


Figure 3.10: Metering Section.

As shown in Figure 3.11, a JABSCO flexible impeller pump was used to pump oil from the oil storage tank to the oil flow line, which was later controlled by valves and metered by rotameter to the desired flow rate. The flow loop was run with only the water for the single phase experiments and combinations of water, air and oil at desired flow rates for the multiphase flow investigations.

The water, air and oil lines are combined using a clear PVC schedule 40 pipe in-line mixer (Cole-Parmer, 2010) and the mixture then flows through the inclined inlet to the cyclone separator. The flow from the three outlets was controlled using natural rubber bungs to specify the split ratio as a function of mass flow rate passing through each outlet. Partially separated flow mixtures at the water, air and oil outlets were directed back into the partitioned water tank. Air was vented to the atmosphere. A baffle was installed in the storage tank to separate oil from the partially separated mixture via a siphon at the end of each experimental trial. Then, the separated water was passed through the 10mm baffle clearance to recirculate back to the water loop.

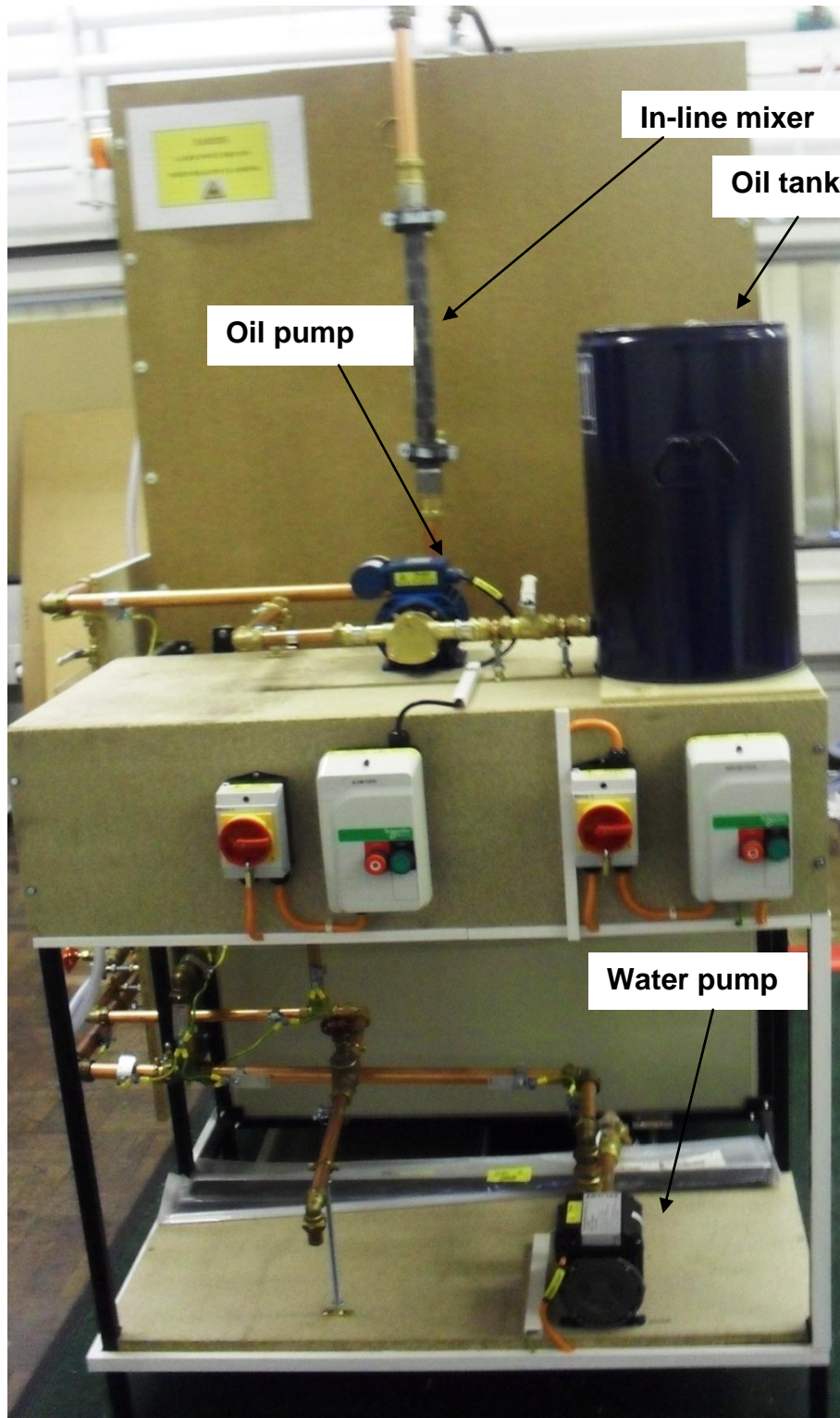


Figure 3.11: Photograph of the Cyclone Pumping Section

3.2.2 S-PIV Set-up

The stereo-PIV system used for this investigation was manufactured by TSI Inc and loaned from the EPSRC engineering instruments pool. A CFR-200 double pulsed Nd:YAG laser system designed by Big Sky Laser was used as the light source to illuminate the tracer particles in the flow under investigation with a 200mJ per pulse laser, and each light pulse had duration of 9ns at a wavelength of 532nm.

As shown in Figure 3.13, the laser beam passed through a TSI Model 610015 light arm, which helped in aligning the beam to the arm's optical axes so that the beam was not clipped but transmitted properly. Cylindrical and spherical lenses were adjusted to achieve a lightsheet of 1 mm thickness, which was used to illuminate the flow in the test section under investigation. Two TSI Model 630059 POWERVIEW TM Plus 4MP PIV cameras with CCD sensors were installed on the Scheimpflug mounts so as to satisfy the stereoscopic camera condition (see Figure 3.12). The two cameras looked at angle of $+45^\circ$ and -45° to the light sheet. By tilting the image sensor plane and the lens plane to the Scheimpflug condition, the plane best of focus could be found so that it was aligned with the lightsheet (Prasad, 2000c). These cameras were positioned at both sides of the light sheet 300mm away from the measuring plane and then connected to a 64 bit frame grabber to capture and digitize images and communicate with a computer. A TSI 610035 laser pulse synchronizer was used to synchronize the image capturing and laser pulses.

A water prism of 45 degrees was constructed as shown in Figure 3.14 and moved to the test section of the experimental rig in order to minimize optical distortion arising from refraction through the perspex wall. The prism was filled with water and optical rails were fitted to the frame supporting the experimental rig in order to align the cameras with the laser beam. This set-up was designed so that the cameras could be repositioned vertically up and down on the rails with reference to the illuminated plane and according to the needs of the experiment.

The single phase water flow was seeded with silver coated hollow glass spheres marketed by TSI Inc (10089-SLV). The density of these particles is 1.65 g/cc with a nominal mean diameter of $14\mu\text{m}$. They were mixed with water in the storage tank and allowed to be uniformly dispersed in a few complete circulations of the flow loop.

This seeding material has very good fluid and imaging properties for the current experiment (Melling, 1997).

The stereo-PIV imaging of the multiphase flow field was carried out using the same experimental set-up as the single phase, with the addition of long wavelength pass filters fitted to the cameras in order to prevent the reflection of scattered light from the gas bubbles. In addition, the continuous phase was seeded with 10070-3 fluorescent microsphere tracer particles (from TSI inc.) capable of absorbing light of wavelength 532 nm and emitting it at 542 nm, so that the light reflected from the tracer particles could be used to measure the velocity field of the flow under investigation. For air-water experiment, we are interested in investigating the effect of air flow on the water flow field as the phases separate within the pipe separator.

Two hundred pairs of images were recorded by the acquisition system at each measuring location. The software used for controlling the hardware while collecting the images was INSIGHT 3G from TSI Inc. The same software has been used for retrieving and processing raw images in order to gain data on velocity vector fields. In order to evaluate the recorded images via cross-correlation, the complete image is divided into many interrogation windows. The correlation function operates on the intensities inside each interrogation window. The window overlap is the overlap among neighbouring interrogation windows, and together with interrogation window size determine the grid size of a vector field. This is the spacing between two neighbouring vectors in the vector field.

In this work, a multi-pass processing scheme was used; consisting of two passes with interrogation windows of 64 x 64 pixels and 50% overlap. Then another pass was applied with an interrogation area of 32 x 32 pixels and 50% overlap. Erroneous vectors were removed and replaced by a global velocity filter and local 3 x 3 median filters. The outliers were finally interpolated to fill gaps in the vector fields. An overview of the relevant parameters used in the SPIV image processing is presented in Table 3.1.

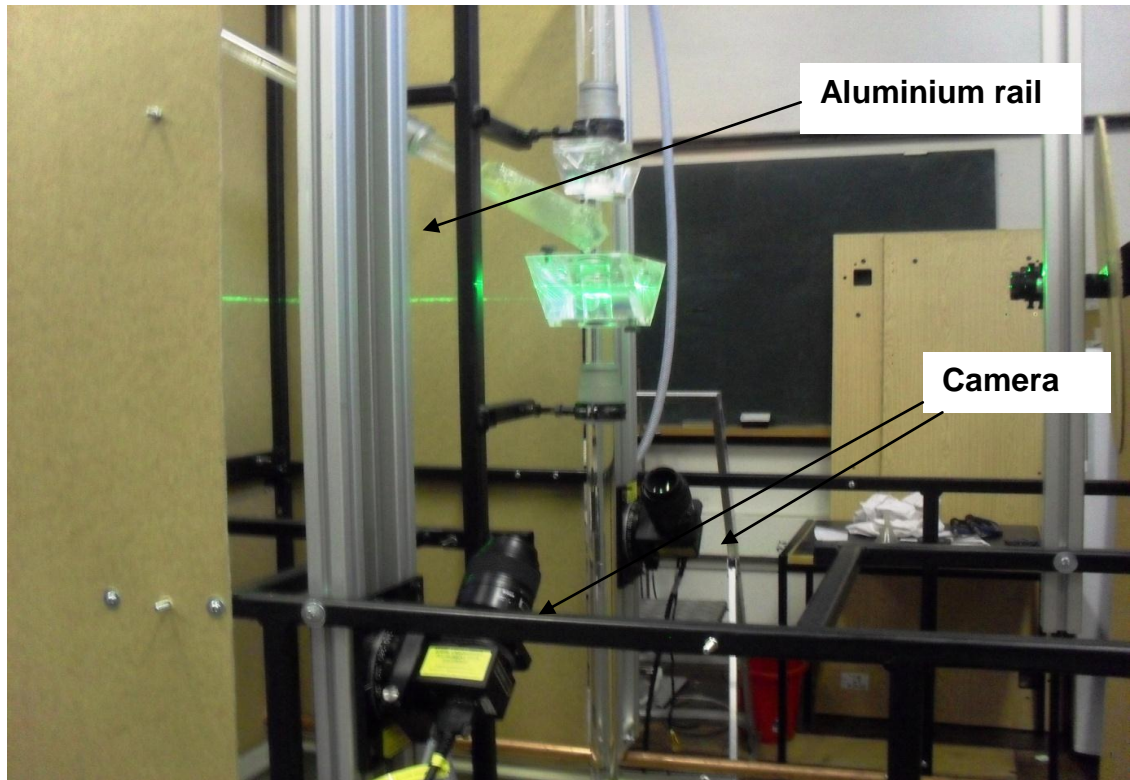


Figure 3.12: S-PIV Experimental Set-up

Tracer particle (single phase)	Silver coated glass sphere
Tracer particle (multiphase flow)	Fluorescent microspheres
Laser type	Nd:YAG
Pulse duration	6 ns
Laser light thickness	1 mm
Laser light wavelength	532 nm
Filter (multiphase flow)	Long wavelength pass filters
Field of view	30 x 30 mm ²
Number of images acquired/plane	200
Processing software	INSIGHT 3 G (TSI Inc.)
PIV analysis reconstruction method	Three dimensional calibration

Table 3.1: Summary of SPIV Parameters



Figure 3.13: Lasers Used for S-PIV System

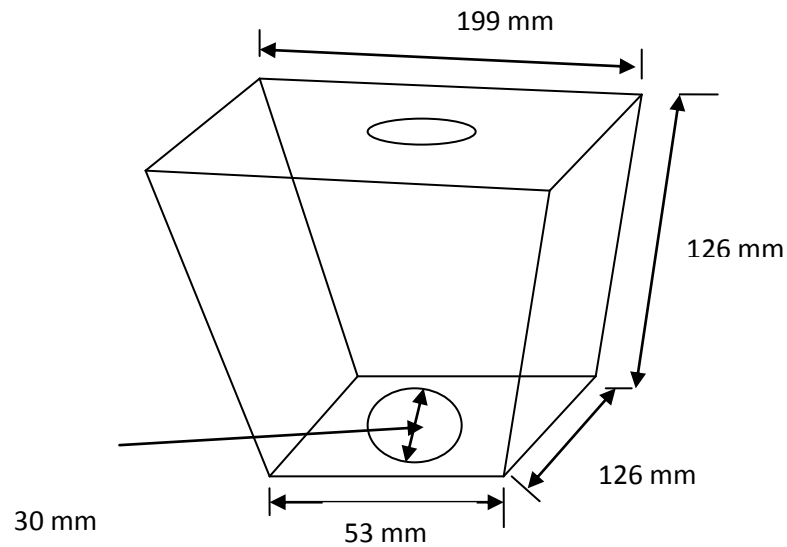


Figure 3.14: Water Prism

3.2.3 Camera Calibration

A single plane calibration target populated by a Cartesian grid of 2mm white marker dots with a 3-mm cross at the centre on a black background was cut to size to fit into the test section, as shown in Figure 3.15. The calibration target was mounted on a flat plate and inserted into the test section to coincide exactly with the light sheet, and it was moved using a micrometer in seven steps of 0.5mm ($Z=-1.5, -1, -0.5, 0, 0.5, 1, 1.5$ mm). The error in the movement of the micrometer was found to be less than 0.01mm.

At each location, the stereo-cameras were set to satisfy the Scheimpflug condition and images of the target were recorded and analysed by the perspective calibration method of the INSIGHT 3G software. The calibration image analysis produced a set of calibration points used to create a calibration mapping function, which was then used to combine 2-D PIV vector fields in order to obtain the three-dimensional vector field.

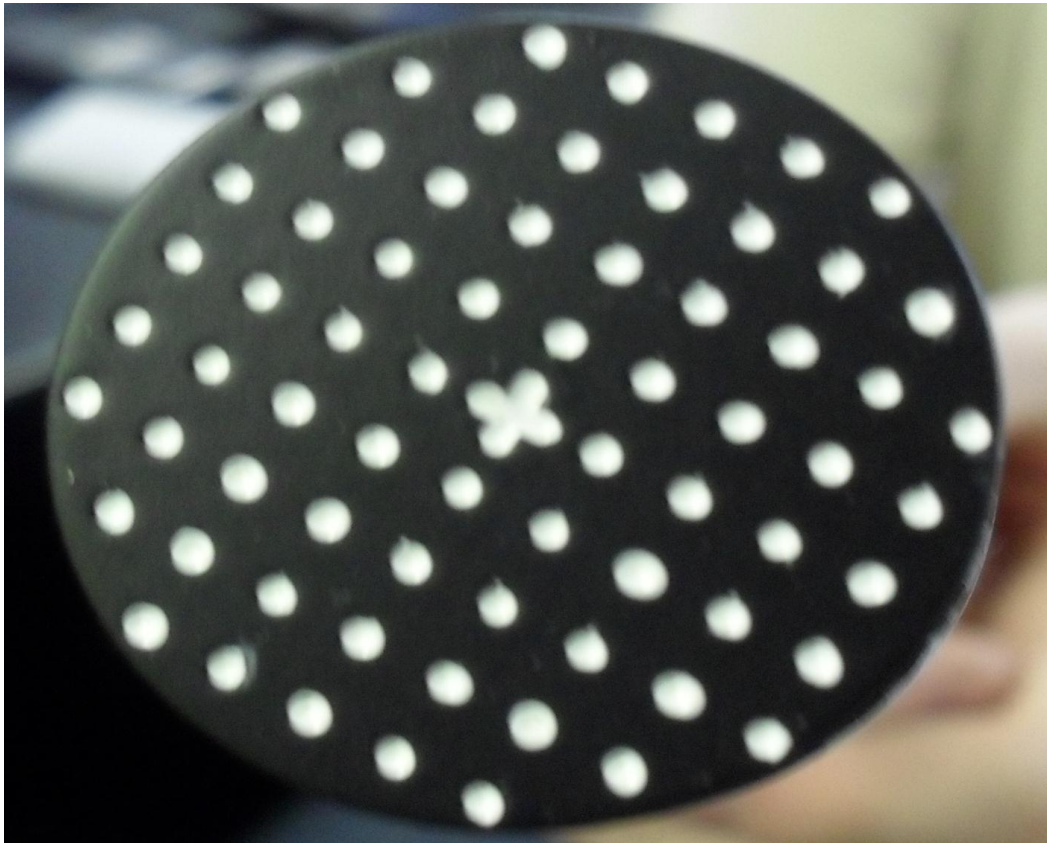


Figure 3.15: Calibration Target

3.2.4 S-PIV Enclosure Design

This PIV system used an Nd:YAG laser which is classified as a class IV laser. The laser beam is very powerful and for safety reasons, a PIV enclosure was built and used in all the PIV experimental work carried out in this study. Although a laser controlled area was established for this work and laser goggles were worn for personal eye protection, there was still a need to design the experiment so that extraneous laser light did not escape from the enclosure.

Hardboard sheets were used to cover the experimental facility, as shown in Figure 3.16. The light arm passed through the hardboard and the stereo-cameras were positioned within the enclosure. In order to reduce the possibility of beam reflection, the frame holding the experimental rig was painted with non-reflective matt black paint sold by RS components.

An interlock was installed between the laser and the enclosure so that the laser beam was immediately shut off as soon as the hardboard was either partially or completely open.

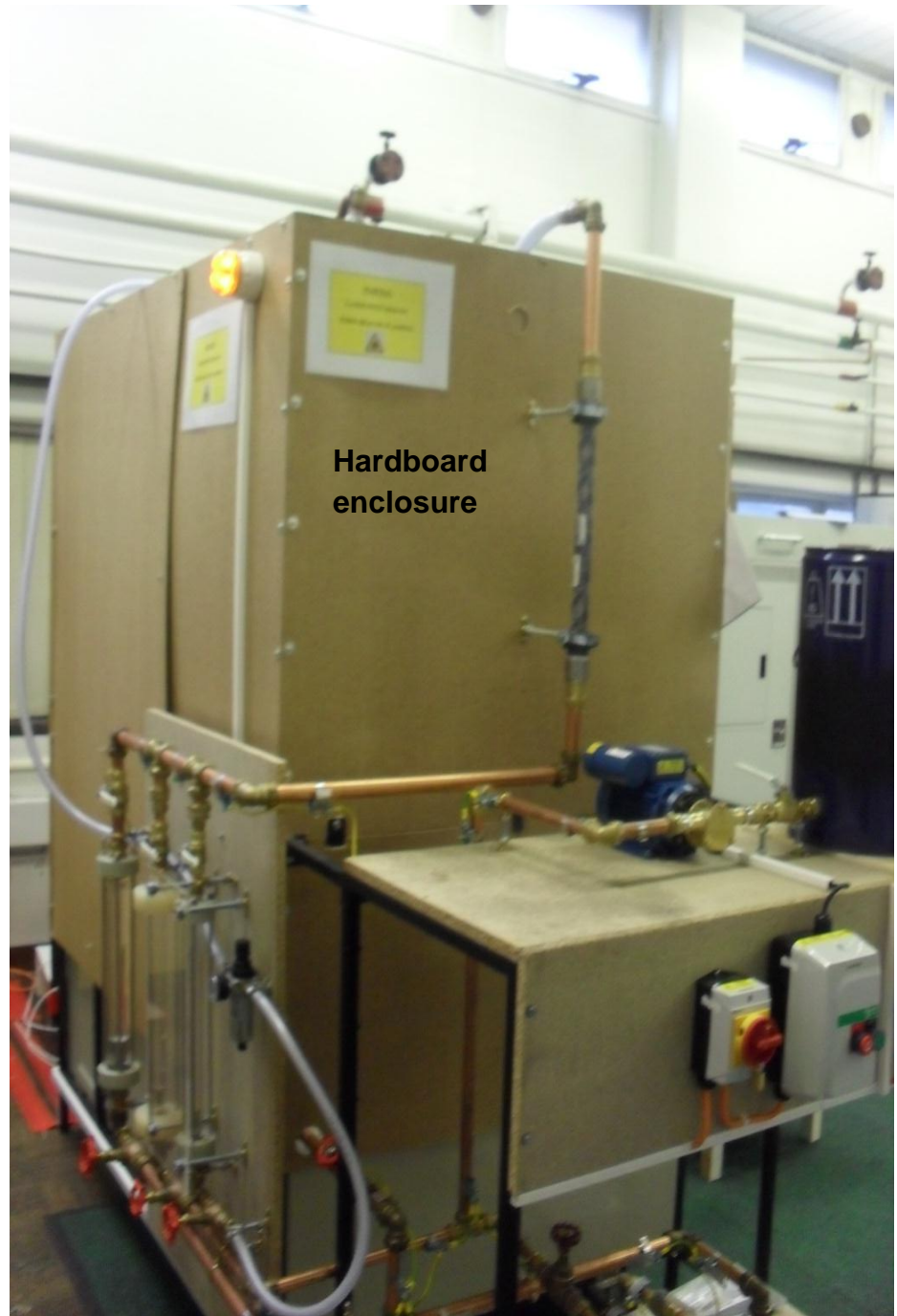


Figure 3.16: S-PIV Enclosure Design

3.3 Measurement Strategy

A clear, viscous mineral oil (BPE 2629-1) marketed by Fisher Scientific, UK was used as the experimental fluid along with tap water and air. The properties of the three fluids used in this experiment are as shown in Table 3.2.

	ρ kg/m ³	μ kg/ms
Water	998.2	0.001003
Air	1.225	0.000018
Oil	845-905	0.03120

Table 3.2: Properties of the Fluids.

SPIV measurements were conducted along the separator's main axis at three axial positions $Z = -395$ mm, -75 mm and 295 mm. Figure 3.17 shows the measurement locations. The main objective of this work is to study the hydrodynamic flow behaviour as a function of multiphase flow separation within the pipe separator. Therefore, measurement location $Z = -75$ mm was selected because it represents the area where the dynamic flow behaviour of the multiphase flow is expected to be more pronounced. Whereas $Z = -395$ mm and 295 mm were selected based on the fact that most of the multiphase flow has already been separated at these locations.

3.3.1 Water Flow Experiment

The flow loop was run with water for a single phase experiment with a flow rate of $0.000338 \text{ m}^3/\text{s}$ defined at the inlet and split ratios of 0.6, 0.33 and 0.007 for water-rich, air and oil-rich outlets respectively. These values were chosen so as to allow water flow through all the three outlets.

3.3.2 Air-Water flow Experiment

Preliminary investigations by Vazquez (2001) concluded that cylindrical cyclone achieves more efficient separation with stratified flow pattern at the inclined inlet, especially for low oil content and water-dominated mixtures. Therefore, we decided to work on stratified wavy flow pattern at the inclined inlet of the pipe separator.

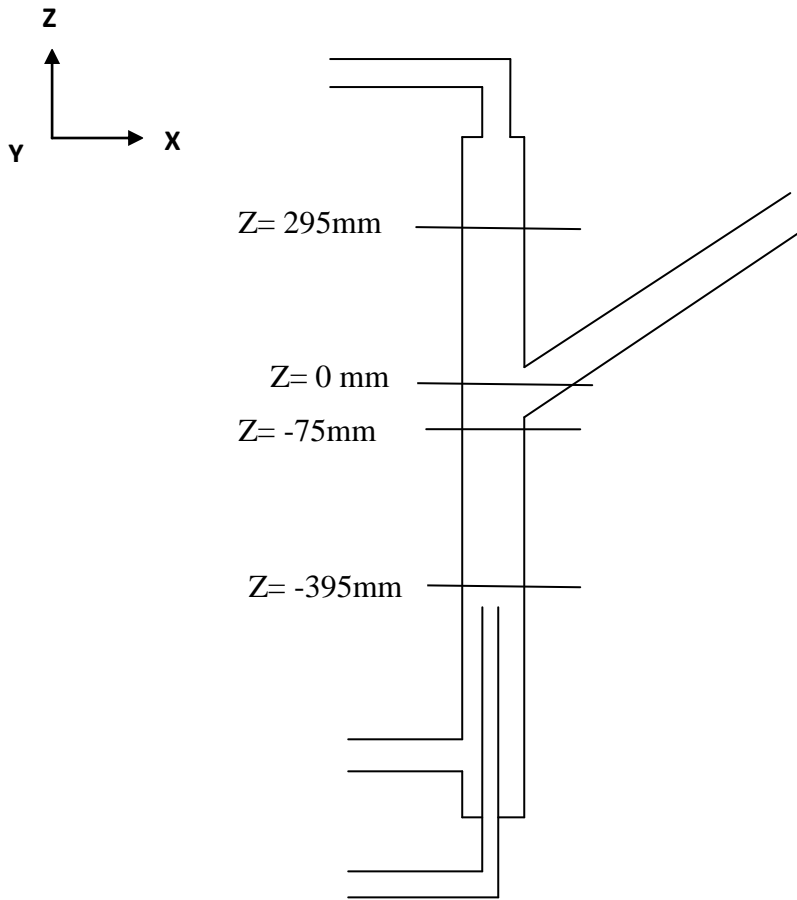


Figure 3.17: Measurement Locations

At atmospheric pressure and room temperature with air flow rate of $0.000045\text{m}^3/\text{s}$, a stratified wavy flow pattern at the inlet section of the separator was observed. This air flow rate and corresponding water flow rates with their associated properties as shown in Tables 3.2 and 3.3 were then used to calculate and plot the Martinelli (X), and Taitel and Dukler (K) parameters onto the air-water flow map for inclined pipe (Figures 3.19 and 3.20). These parameters were observed to lie in the stratified wavy region and confirmed a segregated flow pattern occurring at the inlet section of the pipe separator (Figure 3.18). As a result of the nozzle inserted at the inlet junction, the swirling motion of the segregated flow changes to different flow patterns away from the inlet section. During regular operation, a bubble, slug, churn or annular flow pattern is established inside the main body of the pipe separator (Reyes-Gutiérrez, et al, 2006; Barnea, 1986).

The experimental investigation of the two phases was carried out with the flow loop run with a combination of water and air. A stratified flow pattern was set with the air volumetric flow rate kept constant at $0.000045\text{ m}^3/\text{s}$ and SPIV measurements were taken

at five different water volume fractions between 0.8200 and 0.7458 as shown in Table 3.3. In addition, the split ratio for the water rich outlet is defined as the ratio of liquid flow rate passing through the water rich outlet to the total liquid flow rate at the inlet.

	Gas flow rate (litre/min)	Water flow rate (litre/min)	Gas volume fraction (%)	Split ratio (water outlet)	Split ratio (air outlet)	Split ratio (oil outlet)
A	2.7	12.3	18.0	0.317	0.066	0.617
B	2.7	11.76	18.67	0.332	0.069	0.599
C	2.7	11.1	19.57	0.352	0.072	0.576
D	2.7	9.48	22.17	0.40	0.1	0.5
E	2.7	8.88	23.32	0.439	0.1	0.47
F	2.7	7.92	25.42	0.48	0.11	0.41

Table 3.3: Flow Rates for Air-Water Experiments.

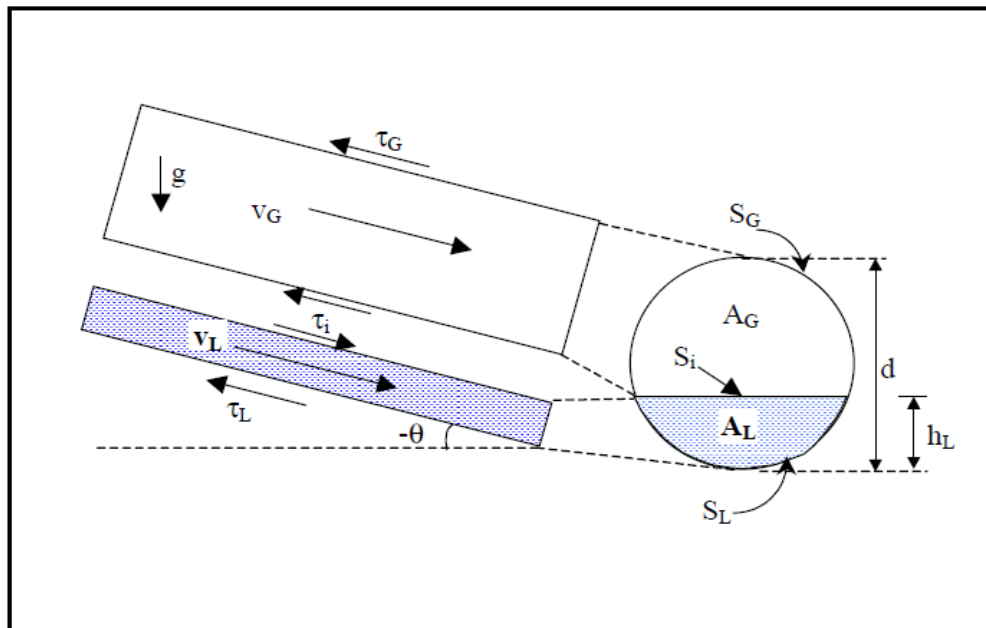


Figure 3.18: Stratified flow Pattern for Pipe Separator Inlet (Vazquez, 2001).

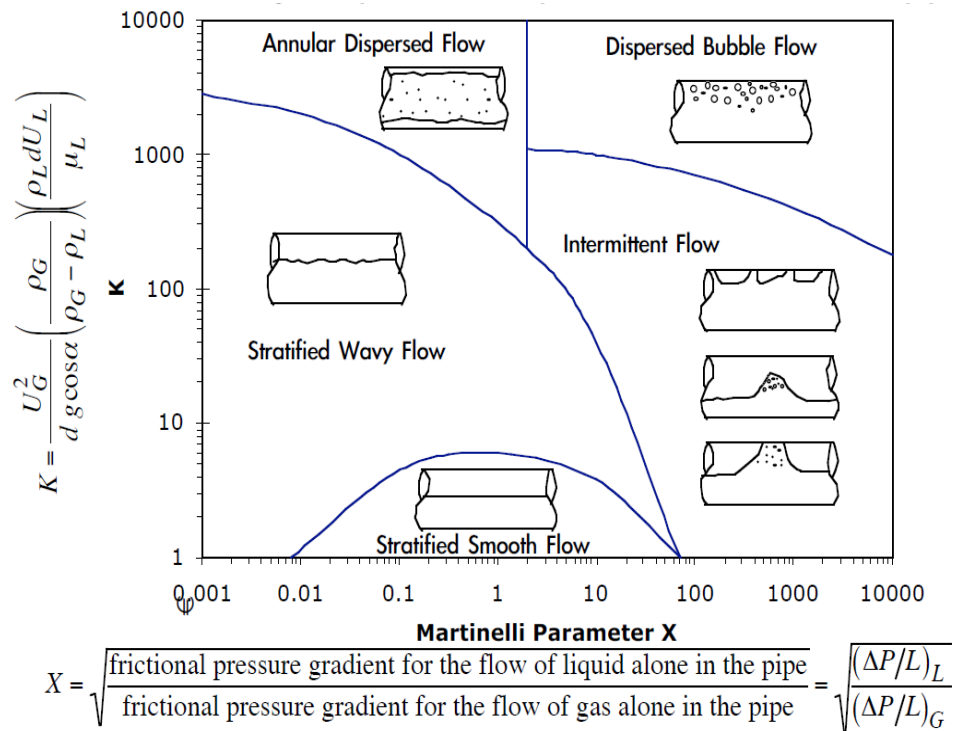


Figure 3.19: Co-current Flow Map of Gas/Vapour and a Liquid in a Horizontal/Inclined Plane (Barnea, 1986).

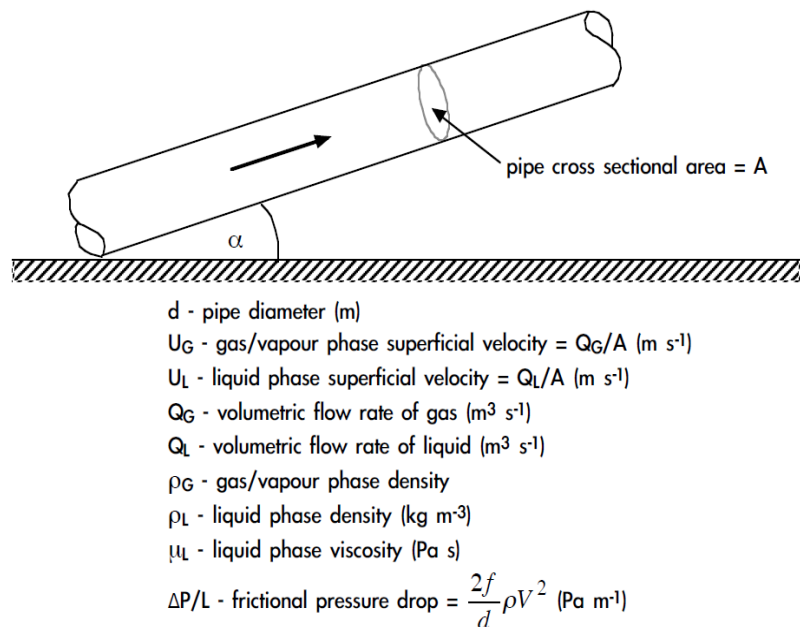


Figure 3.20: Co-current Flow of Gas/Vapour and a Liquid in a Horizontal/Inclined Plane (Barnea, 1986).

SPIV measurements were obtained for both water and water-air multiphase flow at three different planes along the vertical axis of the cyclone (see Figure 3.14). In this work, two hundred double-frame images were captured per measuring plane which were processed to obtain instantaneous velocity fields. These 2-D instantaneous vector fields were then combined using the 3-D calibration-based method to obtain the 3-D vector fields. In addition to the 3-D instantaneous flow field information, the mean velocity field and turbulence quantities of the flow can be extracted by the statistical treatment of the instantaneous data set. It was not possible to measure the velocity distribution of each of the phases due to the high volume fraction of air. Therefore, the conventional SPIV image processing technique was applied to the air-water flow velocity maps that cannot differentiate between each of the phases present in the air-water multiphase flow.

3.3.3 Air-Water-Oil Experiment

For a stratified flow pattern at the inclined inlet, the assumption is made that the oil and water are properly mixed and the three phases behave almost as if they were a two-phase flow of gas and a water-oil mixture with water as the continuous phase. Here, the liquid phase has the physical properties of the mixed water and oil phases (Barnea and Taitel, 1994; Barnea, 1987). The air flow rate and corresponding water-oil mixture flow rates with their associated properties as shown in Tables 3.2 and 3.4 were then used to calculate and plot the Martinelli (X), and Taitel and Dukler (K) parameters onto the air-water flow map for inclined pipe (Figures 3.19 and 3.20). These parameters were observed to lie in the stratified waxy region and confirmed a segregated flow pattern occurring at the inlet section of the pipe separator (Barnea, 1986).

The flow loop was run with combinations of water, air and oil at desired flow rates for the three phase flow investigations. The separation efficiency experiments were carried out with varying volume fractions of air, water and oil as shown in Table 3.4.

It was not possible to obtain SPIV measurements for the three phase flow, because an emulsion formed between the tracer particles and the mineral oil. The captured images were not good enough to process. Therefore, an investigation was carried out on the separation efficiency of the cyclone at different phase flow rates, as specified in Table 3.4.

	α	Split ratio
	Volume fraction, %	
Water	56.8 - 78.3	0.4
Air	18.0 - 25.8	0.5
Oil	0.2 - 22.3	0.1

Table 3.4: Planned Experiments for Air-Water-Oil Flow.

CHAPTER FOUR

NUMERICAL SIMULATION OF TURBULENCE AND MULTIPHASE FLOW

In order to better understand the dynamics of turbulence and multiphase flow, section 4.1 highlights the basic equations used for numerical simulation of turbulence. Sections 4.2 and 4.3 then describe the principles and techniques used in the numerical analysis of turbulence and multiphase flow. In section 4.4, the model geometry and numerical simulation set-up used in the present study are described.

4.1 The Navier Stokes Governing Equations

The Navier Stokes equations are the basic equations describing fluid flow and are derived from momentum balances on a fluid element. Either directly or indirectly, the Navier Stokes equations are used in the numerical simulation of turbulent flow. The significantly different mixing-length scales involved in turbulent flow makes their solution extremely difficult. In this study, an incompressible air flow is assumed based on the pressure drop calculated from the CFD simulation of a single phase in a pipe separator (Appendix C). The pressure drop (ΔP) of 29.9 Pa was considered negligible when compared with the atmospheric pressure used at the inlet. For a long pipe, pressure drop reduces the density of the air. Therefore, air density varies insignificantly in response to a negligible change in pressure (Anderson, 2007). The separation process in cyclone occurs in an extremely short residence time, so that there is no opportunity for significant heat exchange with the surroundings (Almgren et al., 2006). Therefore, a flow in pipe separator is with low dissipation (as indicated by low pressured drop) and hence little internal heating.

For an incompressible, isothermal Newtonian flow (density $\rho = \text{constant}$, viscosity $\mu = \text{constant}$), with a velocity field $\vec{V} = (u_r, u_\theta, u_z)$, only the mass and momentum balance equations need to be considered. In cylindrical coordinates, (r, θ, z) , the continuity equation for an incompressible fluid is (Tu et al., 2008; Versteeg and Malalasekera, 2007)

$$\frac{1}{r} \frac{\partial}{\partial r} (ru_r) + \frac{1}{r} \frac{\partial}{\partial \theta} (u_\theta) + \frac{\partial}{\partial z} (u_z) = 0 \quad (4.1)$$

The Navier-Stokes equations of motion for an incompressible fluid of constant dynamic viscosity, μ , and density, ρ , are

$$\left. \begin{aligned} \rho \left[\frac{Du_r}{Dt} - \frac{u_\theta^2}{r} \right] &= -\frac{\partial p}{\partial r} + f_r + \mu \left[\nabla^2 u_r - \frac{u_r}{r^2} - \frac{2}{r^2} \frac{\partial u_\theta}{\partial \theta} \right] \\ \rho \left[\frac{Du_\theta}{Dt} + \frac{u_\theta u_r}{r} \right] &= -\frac{1}{r} \frac{\partial p}{\partial \theta} + f_\theta + \mu \left[\nabla^2 u_\theta - \frac{u_\theta}{r^2} - \frac{2}{r^2} \frac{\partial u_r}{\partial \theta} \right] \\ \rho \frac{Du_z}{Dt} &= -\frac{\partial p}{\partial z} + f_z + \mu \nabla^2 u_z \end{aligned} \right\} \quad (4.2)$$

Where the velocities are in the r, θ, z cylindrical coordinate directions, p is the pressure, f_r, f_θ, f_z are the body force components in the r, θ, z directions and the operators are $\frac{D}{Dt}$ and ∇^2 are

$$\left. \begin{aligned} \frac{D}{Dt} &= \frac{\partial}{\partial t} + u_r \frac{\partial}{\partial r} + \frac{u_\theta}{r} \frac{\partial}{\partial \theta} + u_z \frac{\partial}{\partial z} \\ \nabla^2 &= \frac{\partial^2}{\partial r^2} + \frac{1}{r} \frac{\partial}{\partial r} + \frac{1}{r^2} \frac{\partial^2}{\partial \theta^2} + \frac{\partial^2}{\partial z^2} \end{aligned} \right\} \quad (4.3)$$

and for an incompressible, Newtonian fluid

$$\left. \begin{aligned} \sigma_{rr} &= -p + 2\mu \frac{\partial u_r}{\partial r} & \sigma_{r\theta} &= \mu \left(\frac{1}{r} \frac{\partial u_r}{\partial \theta} + \frac{\partial u_\theta}{\partial r} - \frac{u_\theta}{r} \right) \\ \sigma_{\theta\theta} &= -p + 2\mu \left(\frac{1}{r} \frac{\partial u_\theta}{\partial \theta} + \frac{u_r}{r} \right) & \sigma_{rz} &= \mu \left(\frac{\partial u_r}{\partial z} + \frac{\partial u_z}{\partial r} \right) \\ \sigma_{zz} &= -p + 2\mu \frac{\partial u_z}{\partial z} & \sigma_{\theta z} &= \mu \left(\frac{1}{r} \frac{\partial u_z}{\partial \theta} + \frac{\partial u_\theta}{\partial z} \right) \end{aligned} \right\} \quad (4.4)$$

In 1883, a dimensionless Reynolds number was suggested by Osborne Reynolds and is used to characterize different flow regimes such as turbulent or laminar flow:

$$\text{Re} = \frac{\rho V D}{\mu} = \frac{V D}{\nu} = \frac{Q D}{\nu A} \quad (4.5)$$

When the Reynolds number is low, laminar flow occurs, while turbulent flow occurs at high Reynolds numbers. At transitional Reynolds number, there is instability across different scales and with different fluids. This defines the transition between the two regimes of flow, from laminar to turbulent conditions or vice versa.

Analytical solutions of equation 4.3 are possible for laminar flows. However, the numerical solution of the Navier-Stokes equations for turbulent flow is extremely

difficult. This is due to the significantly different mixing-length scales that are involved, which requires a fine mesh resolution such that the computational time becomes significantly infeasible for highly turbulent flow calculations. Two alternative methods can be employed to solve the Navier Stokes equations so that small scale turbulent fluctuations do not have to be directly simulated. These methods are Reynolds averaging and filtering.

4.2 Numerical Analysis of Turbulence

The most commonly used computational fluid dynamics (CFD) techniques for turbulent flows are:

- (a) Reynolds averaged Navier Stokes (RANS);
- (b) Large eddy simulation (LES);
- (c) Direct numerical simulation (DNS).

Turbulent flows are characterized by fluctuating velocity fields which mix and fluctuate together with quantities transported such as momentum, energy and mass. These fluctuations are found to be too computationally expensive to simulate, especially for complex, high Reynolds flows. Therefore, different approaches which are computationally less expensive are used to remove the need for small scale turbulent fluctuations to be directly simulated (Versteeg and Malalalsekera, 2007; Gatski et al., 1996; Davidson, 1995; Theodore, 1971).

4.2.1 Direct Numerical Simulation (DNS).

The direct numerical method involves direct computation of the whole spectrum of scales without any turbulence model. This includes everything from the smallest dissipative scales up to the largest scales associated with the types of motion involving most of the kinetic energy. DNS solves the Navier Stokes equations without averaging or approximation and is therefore referred to as the most exact approach to turbulence simulation. However its cost is extremely high as the computing requirements increase rapidly with Reynolds number and its applicability is limited to flows of low to moderate Reynolds numbers. For example, DNS is restricted to pipe flow where Reynolds number is between 2300 and 4000.

Grid spacing in DNS solution must be on the order of the Kolmogorov scale of the flow (smallest scale within the flow). A three-dimensional DNS requires a number of mesh points N^3 , where $N^3 \geq Re^{9/4}$. But its ability to yield all of the flow variables at a large number of spatial locations over many instants of time has made it a valuable tool in investigating and understand fundamentals of fluid flow dynamics and turbulence phenomena (Ferziger and Peric, 2002).

4.2.2 Reynolds Averaged Navier Stokes Models

The Reynolds averaged Navier- Stokes (RANS) method uses the time-averaged equations of motion for fluid flow to approximate the averaged solutions to the Navier-Stokes equations (Ferziger and Peric, 2002). The total velocity, u , is decomposed into the averaged (mean) component, \bar{u} , and its fluctuating component, \hat{u} , where:

$$\hat{u} = u - \bar{u} \quad (4.6)$$

The decomposition of flow variables provides length scale and time scale information which RANS models use as a basis in modelling various turbulent and multiphase flows (Pope, 2000). In RANS models, the Reynolds-averaging is based on the decomposition of the flow variables into means (ensemble averaged or time averaged) and fluctuating parts. For the velocity component:

$$u(r_i) = \bar{u}(r_i) + \hat{u}(r_i, t) \quad (4.7)$$

where \bar{u} and \hat{u} are the mean and fluctuating velocity components, r is the direction and $i = (1, 2, 3)$.

Likewise for pressure:

$$p = \bar{p}(r_i) + \hat{p}(r_i, t) \quad (4.8)$$

\bar{p} and \hat{p} are the mean and fluctuating components respectively. The average of any flow variable ϕ is given by equation 4.9:

$$\bar{\phi} = \lim_{T \rightarrow \infty} \frac{1}{T} \int_0^T \phi(r_i, t) dt \quad (4.9)$$

where $\bar{\phi}$ denotes any flow quantity, t is time and T is the averaging interval which must be greater than the typical time scale of the fluctuations.

Substituting expressions of these forms from equations 4.7, 4.8 and 4.9 for the flow variables into the continuity and momentum equations gives the general equations for an incompressible fluid which can be written as:

$$\frac{\partial \rho}{\partial t} + \frac{\partial}{\partial r_i} (\rho u_i) = 0 \quad (4.10)$$

$$\frac{\partial}{\partial r_i} (\rho u_i) + \frac{\partial}{\partial r_j} (\rho u_i u_j) = -\frac{\partial p}{\partial r_i} + \left\{ \frac{\partial}{\partial r_j} \mu \left[\frac{\partial u_i}{\partial r_j} + \frac{\partial u_j}{\partial r_i} - \frac{2}{3} \delta_{ij} \right] \right\} \frac{\partial u_i}{\partial r_i} + \left\{ \frac{\partial}{\partial r_j} (-\rho \overline{u'_i u'_j}) \right\} \quad (4.11)$$

Equations 4.10 and 4.11 are called Reynolds-averaged Navier-Stokes (RANS) equations. The presence of the Reynolds stress term $-\rho \overline{u'_i u'_j}$ in equation 4.11 means that there is a need to introduce additional terms in the governing equations.

The two main approaches used to solve the Reynolds stress terms that appear as unknowns in the RANS equations are, firstly, to find an expression to represent the Reynolds stress (Eddy viscosity modelling). Secondly, to use additional equations such as differential transport equations for Reynolds stress in second moment closure modelling (Pope, 2000).

4.2.2.1 Standard $k - \varepsilon$ model

The standard $k - \varepsilon$ model proposed by Launder and Spalding (1972) bases its derivation on the assumption that the flow is fully turbulent (for flow in a pipe, $Re > 4000$), and the effects of molecular viscosity are negligible. The standard $k - \varepsilon$ model is based on an eddy viscosity model which assumes that the Reynolds stresses in equation (4.11) are proportional to the mean velocity gradients with turbulent viscosity as the constant of proportionality (Hinze, 1975). This was first proposed by Boussinesq, who postulated that the momentum transfer caused by turbulent eddies can be modelled with an effective eddy viscosity in a similar way as the momentum transfer caused by molecular diffusion (i.e. friction) is modelled with a molecular viscosity (Schmitt, 2007). The Boussinesq assumption states that the Reynolds stress tensor, τ_{ij} , is proportional to the mean strain rate tensor S_{ij}^* and can be written as;

$$-\rho \overline{u'_i u'_j} = \mu_t \left(\frac{\partial u_i}{\partial r_j} + \frac{\partial u_j}{\partial r_i} - \frac{2}{3} \frac{\partial u_k}{\partial r_k} \delta_{ij} \right) - \frac{2}{3} \rho_k \delta_{ij} \quad (4.12)$$

where μ_t is a scalar property called the eddy viscosity. The turbulent viscosity μ_t is assumed to be proportional to the product of a turbulent velocity and length scale. The $k - \varepsilon$ turbulence model defines the velocity and length scales according to the turbulent kinetic energy, k , and the rate of dissipation of turbulent kinetic energy, ε .

$$\text{Turbulent Viscosity, } \mu_t = \rho C_\mu \frac{k^2}{\varepsilon} \quad (4.13)$$

$$\text{Turbulent Kinetic Energy, } k = \frac{1}{2} (\overline{u'^2} + \overline{v'^2} + \overline{w'^2}) \quad (4.14)$$

Where u' , v' and w' are the components of the velocity fluctuations.

The transport equation for k is (Wilcox, 1993)

$$\frac{\partial k}{\partial t} + u \frac{\partial k}{\partial r} + v \frac{\partial k}{\partial \theta} + w \frac{\partial k}{\partial z} = P + G + D_k - \varepsilon \quad (4.15)$$

Where P is the turbulence production term and in cylindrical coordinates is

$$P = C_{sp} \mu \left[2 \left(\frac{\partial u^2}{\partial r} \right) + 2 \left(\frac{\partial v^2}{\partial \theta} \right) + 2 \left(\frac{\partial w^2}{\partial r} \right) + \left(\frac{\partial v}{\partial r} + \frac{\partial u}{\partial \theta} \right)^2 + \left(\frac{\partial u}{\partial z} + \frac{\partial w}{\partial r} \right)^2 + \left(\frac{\partial v}{\partial z} + \frac{\partial w}{\partial \theta} \right)^2 \right]$$

Here, C_{sp} is the shear production shear production coefficient. In equation, G is the buoyancy production term

$$G = - \frac{C_\rho \mu}{\rho^3} \left(\frac{\partial \rho}{\partial r} \frac{\partial p}{\partial r} + \frac{\partial \rho}{\partial \theta} \frac{\partial p}{\partial \theta} + \frac{\partial \rho}{\partial z} \frac{\partial p}{\partial z} \right)$$

The diffusion term, D_k is

$$D_k = \frac{\partial}{\partial r} \left(\frac{v_T}{\sigma_k} \frac{\partial k}{\partial r} \right) + \frac{\partial}{\partial \theta} \left(\frac{v_T}{\sigma_k} \frac{\partial k}{\partial \theta} \right) + \frac{\partial}{\partial z} \left(\frac{v_T}{\sigma_k} \frac{\partial k}{\partial z} \right)$$

The transport equation for ε is

$$\frac{\partial \varepsilon}{\partial t} + u \frac{\partial \varepsilon}{\partial r} + v \frac{\partial \varepsilon}{\partial \theta} + z \frac{\partial \varepsilon}{\partial z} = C_{\varepsilon 1} \frac{\varepsilon}{k} (P + C_{\varepsilon 3} G) + D_\varepsilon - C_{\varepsilon 2} \frac{\varepsilon^2}{k} \quad (4.16)$$

The diffusion term for the dissipation, D_ε is

$$D_\varepsilon = \frac{\partial}{\partial x} \left(\frac{v_T}{\sigma_k} \frac{\partial \varepsilon}{\partial r} \right) + \frac{\partial}{\partial y} \left(\frac{v_T}{\sigma_k} \frac{\partial \varepsilon}{\partial \theta} \right) + \frac{\partial}{\partial z} \left(\frac{v_T}{\sigma_k} \frac{\partial \varepsilon}{\partial z} \right)$$

Where $C_{\varepsilon 1}$, $C_{\varepsilon 2}$ and $C_{\varepsilon 3}$ are user-adjustable, non-dimensional parameters.

The advantage of this approach is the relatively low cost associated with the computation of the turbulent viscosity, μ_t . The main disadvantage of this model is the assumptions that the Reynolds stresses are isotropic especially for free shear flows.

4.2.2.2 RNG κ - ε Model

The RNG model was developed using Re-Normalisation Group (RNG) methods by Yakhot and Orszag (1986) to renormalize the Navier-Stokes equations in order to account for the effects of smaller scales of motion. The RNG approach models the transport of turbulence as opposed to the empirical method used in the standard k - ε model. This analytical derivation results in a model with constants different from those in the standard k - ε model, and adds terms and functions in the transport equation for ε . The analytical derivation of the RNG model enables it to be responsive to changes in the rate of strain, which cannot be modelled in the dissipation energy used in the standard κ - ε model (Yakhot et al., 1992; Yakhot and Orszag, 1986).

The RNG κ - ε model calculates the effective viscosity as;

$$\mu_{eff} = \mu_{mol} \left[1 + \sqrt{\frac{C_{\mu}}{\mu_{mol}}} \frac{k}{\sqrt{\varepsilon}} \right]^2 \quad (4.17)$$

Where μ_{mol} is the molecular viscosity and C_{μ} is a constant equal to 0.0845. Since turbulence is affected by rotation or swirl in the mean flow, the RNG model in ANSYS-FLUENT provides an option to account for the effects of swirl or rotation by modifying the turbulence viscosity appropriately. The modification takes the following functional form:

$$\mu_t = \mu_{t0} f \left(\alpha_s, \Omega, \frac{k}{\varepsilon} \right) \quad (4.18)$$

where μ_{t0} is the value of turbulent viscosity calculated without the swirl modification using equation (4.13). Ω is a characteristic swirl number and α_s is a swirl constant.

The RNG κ - ε model has shown improved results for high streamline curvature and strain rate, transitional flows and wall heat and mass transfer, but shows no improvement over the standard model for predicting vortex evolution. The RNG κ - ε model relaxes the assumption of isotropy inherent in the standard κ - ε model.

However, it has a similar inability, for example to predict the spreading of a round jet correctly (Choudhury, 1993; Wilcox, 1993). The RNG κ - ε model has a similar form to the standard κ - ε model, but with some modifications such as shown in equations 4.17 and 4.18. The turbulent kinetic energy (k) and its rate of dissipation (ε) are:

$$\frac{\partial}{\partial t}(\rho k) + \frac{\partial}{\partial r_j}(\rho k u_i) = \frac{\partial}{\partial r_j} \left\{ \left(\mu + \frac{\mu t}{\sigma_k} \right) \frac{\partial k}{\partial r_j} \right\} + P_k - \rho \varepsilon \quad (4.19)$$

$$\frac{\partial}{\partial t}(\rho \varepsilon) + \frac{\partial}{\partial x_j}(\rho u_i \varepsilon) = \frac{\partial}{\partial r_j} \left[\left(\mu + \frac{\mu t}{\sigma_\varepsilon} \right) \frac{\partial \varepsilon}{\partial r_j} \right] + c_{\varepsilon 1} \frac{\varepsilon}{k} P_k - c_{\varepsilon 2} P_k \frac{\varepsilon^2}{k} \quad (4.20)$$

The constants of the RNG model (Yakhot et al., 1992; Yakhot and Orszag, 1986) are:

$$C_\mu = 0.0845, c_{\varepsilon 1} = 1.42, c_{\varepsilon 2} = 1.68, \sigma_k = 0.7194, \sigma_\varepsilon = 0.7194$$

4.2.2.3 Reynolds Stress Model

The previous analysis of both standard $\kappa - \varepsilon$ and RNG models reveals that the turbulent viscosity hypothesis cannot effectively model the anisotropic features of swirling or rotating flows. The Reynolds stress model (RSM) adopts an approach whereby the model transport equations are solved for the individual Reynolds stresses and for the dissipation rate so as to close the Reynolds-averaged Navier Stokes equations. The exact Reynolds stress transport equation accounts for the directional effects of the Reynolds stress fields.

The transport equations for the Reynolds stresses may be written as follows:

$$\tau_{ij} = \overline{\rho u'_i u'_j} \quad (4.21)$$

$$\frac{\partial \overline{\rho u'_i u'_j}}{\partial t} + \frac{\partial}{\partial r_k}(\rho u'_k \overline{u'_i u'_j}) = P_{ij} + F_{ij} + D_{Tij} + \Phi_{ij} - \varepsilon_{ij} \quad (4.22)$$

$$P_{ij} \text{ (stress production)} = - \left(\overline{u'_i u'_k} \frac{\partial u_j}{\partial r_k} + \overline{u'_j u'_k} \frac{\partial u_i}{\partial r_k} \right) \quad (4.23)$$

$$F_{ij} \text{ (rotation production)} = -2\rho\Omega_k \left(\overline{u'_j u'_m} \varepsilon_{ikm} + \overline{u'_i u'_m} \varepsilon_{jkm} \right) \quad (4.24)$$

$$D_{Tij} \text{ (turbulent diffusion)} = - \frac{\partial}{\partial x_k} \left(\overline{\rho u'_i u_j u'_k} + \rho \overline{(\delta_{kj} u'_i - \delta_{ik} u'_j)} \right) \quad (4.25)$$

$$\Phi_{ij} \text{ (pressure strain)} = \left(\overline{\frac{\partial u'_i}{\partial r_j} + \frac{\partial u_j}{\partial r_i}} \right) \quad (4.26)$$

$$\varepsilon_{ij} \text{ (dissipation)} = -2\mu \overline{\frac{\partial u'_i}{\partial r_k} \frac{\partial u'_j}{\partial r_k}} \quad (4.27)$$

In order to mathematically close equation (4.22), approximations are made for the diffusion, dissipation rate and pressure strain terms. Further information on the underlying equations for the Reynolds stress method can be found in Launder (1989), Gibson and Launder (1978) and Launder et al (1975).

4.2.3 Large Eddy Simulation (LES)

Large eddy simulation (LES) involves the spatial filtering of the turbulence field whereby the large scales are resolved and the types of motion smaller than the computational grid are modelled using a sub grid-scale (SGS) model. This means, that the large scale of turbulences are solved directly using direct numerical simulation and those of smaller scale are represented by a turbulence model (Ferziger and Peric, 2002) .

In LES, a filtering operation is defined to decompose the velocity $U(r, t)$ into the sum of a filtered component $\bar{U}(r, t)$ and a subgrid-scale component $u'(r, t)$. The resulting filtered velocity field $\bar{U}(r, t)$ can now be adequately resolved on a relatively coarse grid. The underlying theory in LES is that the large eddies contain most of the energy and are responsible for most of the conserved property transport which varies from flow to flow. Whereas the smaller eddies are believed to be more universal and less important in terms of momentum transfer but important near the wall and are expected to be more easily modelled (Pope, 2000; Gatski et al., 1996).

4.2.4 Comparison of Different Models of Turbulence

There is not yet a single general turbulence model that can reliably predict with sufficient accuracy all turbulent flows found in industrial applications. However, certain models have been specifically developed to provide accurate simulation for certain types of flows without requiring unnecessarily long computational time.

RANS turbulence models are designed to predict the effect of turbulence on the mean flow, whereas DNS and LES models are both capable of predicting the instantaneous fluctuations in any flow. Table 4.1 compares the major turbulence models. Figure 4.1 shows the relationship between the scale of turbulence and the prediction methods.

For DNS, all turbulence scales are resolved, whereas in LES, large scale turbulence is resolved and smaller scales are modelled. All turbulence scales are modelled in RAN.

	<i>k-ε</i>	<i>RSM</i>	<i>LES</i>	<i>DNS</i>
Level of Description	The dependent variables provide a description of the scales of velocity, length and time. The Reynolds stress tensor is modelled by an isotropic, non-linear viscosity model or by an algebraic stress model.	The direct representation of the Reynolds stress removes the intrinsic assumption of the turbulent-viscosity model used in <i>k-ε</i> .	Describes the unsteady, large scale turbulent structures, and eddies smaller than the mesh sizes are modelled. The filtered velocity field provides a direct representation of the energy containing motions.	Resolves the whole spectrum of scales. No modelling is required.
Cost and ease of use	Easy to use, computationally inexpensive when used in conjunction with wall functions	The Reynolds stress equation requires substantially more CPU time and memory than the <i>k-ε</i> . Typically, RSM requires on average 50-60% more CPU time/iterations and 15-20 % more memory than that of <i>k-ε</i> (Dinesh Suresh et al., 2010; Pope, 2000).	Less expensive than DNS, but requires computational resources that are still too large for most practical applications.	The computational cost required to resolve the entire range of scales is proportional to Re^3 (Pope, 2000).
Accuracy	Robust and reasonably accurate for 2D thin shear flows in which the mean streamline curvature and mean pressure gradient are small. Suitable for initial iterations, the initial screening of alternative designs, and parametric studies. Performs excellently in confined flows such as pollutant dispersion in the atmosphere and lakes where the Reynolds shear stresses are important (Versteeg and Malalalsekera, 2007).	Suitable for complex 3D flow with strong streamline curvature, flows with strong swirl or mean rotation, secondary flows in ducts, and flows with rapid variations in the mean flow.	LES can be reasonably accurate for free shear flows such as the turbulent plume from a smoldering cigarette. Compared with RANS, the higher level of description provided by LES increases its accuracy in aero acoustics and more complex turbulent flow phenomena such as high speed compressible flows and reacting flows.	Useful in the development of turbulence models for practical applications, such as sub-grid scale models for LES and models for methods that solve the RANS equations. This is done through priori and posteriori tests.

Table 4.1: Comparison of Different Turbulence Models

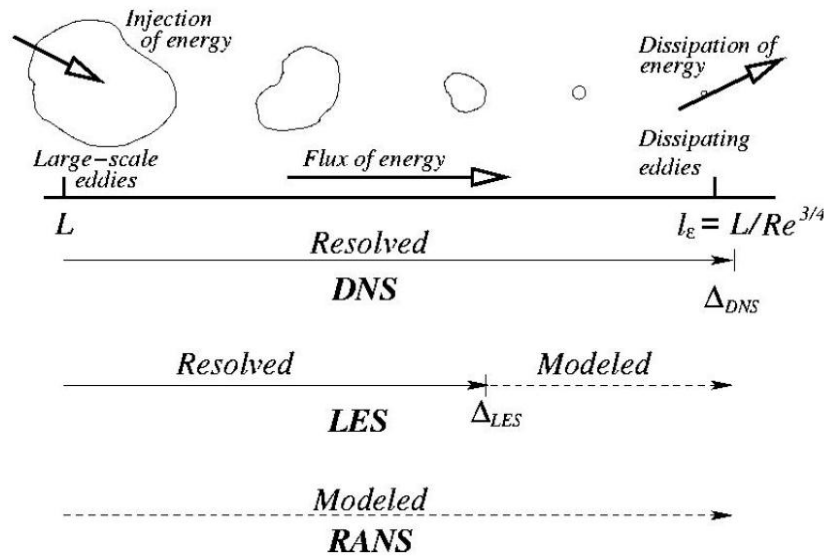


Figure: 4.1: Turbulence Scales and Prediction Methods (Hinze, 1975)

4.3 Numerical Simulation of Multiphase Flow

A large number of flows encountered in nature and technology involve a mixture of phases. Multiphase flow can be classified in the following types:

- Gas- liquid or liquid-liquid flows
- Gas-solid flows
- Liquid-solid flows
- Three phase flows

Generally there are two approaches for the numerical simulation of multiphase flows; the Euler-Lagrange approach and the Euler-Euler approach.

4.3.1 Euler-Lagrange Approach

This approach is based on the application of the Eulerian framework to the continuous fluid and the Lagrangian framework to the dispersed phase of a multiphase flow. The continuous phase is modelled by solving the time averaged Navier-Stokes equations, while the dispersed phase is solved by tracking a large number of particles, bubbles or droplets through the calculated continuous flow field. The dispersed phase can exchange momentum, mass and energy with the continuous fluid phase.

In order to compute the state or location of each dispersed particle or droplet, ordinary differential equations representing mass, momentum and energy balances are solved with the inclusion of appropriate interaction terms to represent interaction of the phases with the continuous phase. A fundamental assumption made in this approach is that the dispersed phase occupies a low volume fraction, which would suggest that the dispersed phase elements are not too close and should be treated as isolated (Crowe et al.,1998). Therefore, mass, momentum and heat transfer for each element in Eulerian-Lagrangian approach are not influenced by the neighbouring element. The particle or droplet trajectories are computed individually at specified intervals during the fluid phase calculations. This model is appropriate for modelling particle separation and classification in cyclone and spray dryers, coal and liquid fuel combustion, and some particle-laden flows (Cokljat et al., 2006; Baxter and Smith, 1993).

Particle Force Balance

By integrating the force balance on the particle, the trajectory of a discrete phase particle (or droplet or bubble) can be equated as the particle inertia with the forces acting on the particle. For the r direction in cylindrical coordinate, the force balance can be written in a Lagrangian reference frame as

$$\frac{du_p}{dt} = F_D (u - u_p) + \frac{g_x(\rho_p - \rho)}{\rho_p} + F_x \quad (4.28)$$

Where F_x is an additional acceleration term, $F_D (u - u_p)$ is the drag force per unit particle mass and

$$F_D = \frac{18\mu}{\rho_p d_p^2} \cdot \frac{C_D R_e}{24} \quad (4.29)$$

Here, u is the fluid phase velocity, u_p is the particle velocity, μ is the molecular viscosity of the fluid, ρ is the fluid density, ρ_p is the density of the particle, and d_p is the particle diameter. R_e is the relative Reynolds number, which is defined as

$$R_e \equiv \frac{\rho d_p |u_p - u|}{\mu} \quad (4.30)$$

4.3.2 Euler-Euler Approach

The Euler-Euler approach is based on treating the different phases mathematically as inter-penetrating continua. Therefore, the phases share the same volume and penetrate each other in space and exchange mass, momentum and energy. However, a fundamental assumption made in this approach is that the phases mix or separate, and that the dispersed phase occupies a high volume fraction (Cokljat et al., 2006; Crowe et al., 1998). The high volume fraction suggests that the dispersed phase elements are too close to be treated as isolated. Therefore, the interaction between the multiphase flow and the effect of the secondary phase will be large enough to need accounting for. The three different Euler-Euler multiphase flow models available in the ANSYS-FLUENT code are; the Volume of Fluid, mixture and Eulerian-Eulerian models.

4.3.2.1 The Volume of Fluid (VOF) Model

The VOF is a numerical technique for tracking and locating the fluid-fluid interface of two or more immiscible fluids where the position of the interface between the fluids is of interest. In the VOF model, a single set of momentum equations is shared by the fluids, and the volume fraction of each of the fluids in each computational cell is tracked throughout the domain (Hirt and Nichols, 1981). Typical applications of the VOF model include flows with stratified patterns, the prediction of jet breakup (surface tension), and the steady and transient tracking of any liquid-gas interface.

4.3.2.2 The Mixture Model

The mixture model is a simplified multiphase model that can be used to model multiphase flows where the phases move at different velocities, but assume local equilibrium over short spatial length scales. The mixture model simplification is based on the main assumption that the Stokes number is small so that the magnitude and direction of the particle velocity vector is close to that of the primary fluid (Cokljat et al; 2006; Crowe et al; 1998). The mixture model is valid only when the velocity of the secondary phase or phases is in the same direction as that of the primary phase, but this criterion can be violated in the recirculation pattern. This model allows the solution of the momentum, continuity, and energy equations for the mixture, the volume fraction equations for the secondary phases, and algebraic expressions for the relative velocities. Unlike the VOF approach, the mixture and Eulerian models allow the multiphase flow to be interpenetrating.

The secondary phase is represented by a volume fraction equation and the transport equation for each dispersed phase allows for relative movement between the dispersed and continuous phases. In addition, the mixture model can be used to model homogeneous multiphase flows with strong coupling and where the phases move at the same velocity. Therefore, the mixture approach treats the combination of continuous and dispersed phases as a single entity. As a result of this, the mixture density and viscosity are calculated on the basis of individual phase fractions. Applications of the mixture model include particle-laden flows with low loading, bubbly flows, and sedimentation and cyclone separators (Syamlal et al., 1993). The mixture model is computationally the least expensive compared to the other Euler-Euler models since it solves the least number of equations. However the accuracy of the flow detail captured by the mixture model is low when compared to the comprehensive Eulerian-Eulerian model.

4.3.2.3 The Eulerian Model

The Eulerian model is the most complex of the multiphase models in ANSYS-FLUENT and is often used to model multiple separate but interacting phases. The Eulerian model's solution is based on a single pressure shared by all phases with continuity, momentum and energy equations solved for each phase. Several interphase drag coefficient functions are available in the Eulerian model, which are appropriate for various types of multiphase regimes. Typically drag coefficient models described in term of local Reynolds numbers are often used to describe phase coupling through the inter-phase exchange terms. The Eulerian multiphase model is the most sophisticated of multiphase flow models, and this is because of the strong coupling effect which exists between the continuous and dispersed phases.

Volume fraction equation

The description of multiphase flow in the Eulerian model as interpenetrating continua incorporates the concept of phase volume fractions, denoted by α_q . In multiphase simulation, the space occupied by each phase is often referred to according to the volume fraction since the laws of the conservation of mass and momentum are satisfied for each phase individually. V_p denotes the volume of the phase p and is defined by:

$$V_p = \int \alpha_p dV \tag{4.31}$$

where the sum of the volume fractions of each phase in the computational cell is equal to 1.

$$\sum_{p=1}^n \alpha_p = 1 \quad (4.32)$$

Conservation Equations

The general conservation equations for the Eulerian-Eulerian approach are presented in this section.

Conservation of Mass (Equation of Continuity)

The conservation of mass for phase q is given by:

$$\underbrace{\frac{\partial}{\partial t}(\alpha_q \rho_q)}_{\text{Accumulation term}} + \underbrace{\nabla \cdot (\alpha_q \rho_q \vec{v}_q)}_{\text{Convection term}} = \underbrace{\left\{ \sum_{p=1}^n \dot{m}_{pq} - \alpha_q \frac{d\rho_q}{dt} \right\}}_{\text{Interphase mass transfer term}} \quad (4.33)$$

Accumulation term

Convection term

Interphase mass transfer term

Here \vec{v}_q , α_p , ρ_q are the velocity, volume fraction and density of phase q, and \dot{m}_{pq} characterizes the mass transfer from the p^{th} to the q^{th} phase.

For steady-state incompressible flow in the absence of mass transfer, equation 4.30 becomes;

$$\nabla \cdot (\alpha_q \vec{v}_q) = 0 \quad (4.34)$$

Conservation of Momentum

The momentum balance for phase q yields

$$\frac{\partial}{\partial t}(\alpha_q \rho_q \vec{v}_q) + \nabla \cdot (\alpha_q \rho_q \vec{v}_q \vec{v}_q) = -\alpha_q \nabla p + \nabla \cdot \bar{\bar{\tau}}_q + \alpha_q p_q \vec{g} + F + \sum_{p=1}^n (\overrightarrow{R}_{pq} + \dot{m}_{pq} \vec{v}_{pq} - \dot{m}_{qp} \vec{v}_{qp}) \quad (4.35)$$

where $\bar{\bar{\tau}}_q$ is the phase stress-strain tensor, and F is the external body force including gravity, lift force and virtual mass force. \overrightarrow{R}_{pq} is an interaction force between phases, \vec{v}_{pq} is the interphase velocity and p is the pressure shared by all phases.

Turbulence Models for Air-Water Multiphase flow

It is important to include the effect of turbulent fluctuations of velocities and the scalar quantities of flow in the numerical simulation of multiphase flows. Additional turbulence modelling for multiphase flows becomes necessary due to the inability of single phase turbulence models to capture the complex physics associated with a multiphase flow. In comparison to single phase flow, the number of terms to be modelled in the momentum equations in multiphase flows is large, and this makes the modelling of turbulence in multiphase simulations extremely complex. The correct approach to accurately capture the underlying multiphase flow physics is to combine suitable multiphase algorithm with either the mixture, dispersed or per-phase turbulence models available in ANSYS-FLUENT. Details of the multiphase turbulence models can be found in a comprehensive description by Cokljat (2006) and hence are omitted here

The choice of multiphase turbulence model depends on the importance of the secondary phase turbulence. In the present work, the volume fraction of the dispersed phase is high enough to ensure that the inter-particle collision is significant. The dominant process in the random motion of the mixture turbulence model is the influence of the primary and secondary phases. Hence, a mixture turbulence model is sufficient to capture important features of the multiphase turbulent flow within the pipe separator .

4.4 Numerical Methodology

The CFD code ANSYS-FLUENT 12.1 commercially developed and marketed by ANSYS Inc was used to investigate the 3-D swirling, single and multiphase flow in the pipe separator. In addition, GAMBIT 2.4, a commercial pre-processor, was used for the creation of geometry, mesh generation and quality examination and boundary zone assignment. ANSYS-FLUENT software uses the finite volume method to discretize the system of partial and ordinary differential equations with an algebraic segregated solver and collated grid arrangement where pressure and velocity are both stored at cell centres. Details of the finite volume method discretization can be found in a comprehensive description by Versteeg and Malalasekera (2007) and hence are omitted here.

4.4.1 Model Geometry and Mesh

Figure 3.6 shows a side view of the cylindrical cyclone used in the fluid simulation. The geometry was constructed by creating volumes in the form of cylinders which were then manipulated through Boolean operations such as summation and subtraction. The vertical cylinder section measured 1675 mm by height and 30 mm ID with an equal diameter tangential inlet inclined at an angle of 27 degrees. The inclined inlet was designed in such a way that its dimensions gradually reduce to 25% of the cross-sectional area and it was attached to the vertical cylinder 585 mm from the top. The diameter of the overflow, water-rich and oil-rich underflow tubes are 20 mm, 20 mm and 10 mm respectively. The water rich outlet was located at right angles to the cyclone 185 mm above the base, while the overflow and oil rich outlets were located at the top and bottom of the cyclone respectively. This geometry corresponds to a numerical solution domain with dimension of 0.885m, 1.82m and 0.646m in radial, axial and tangential direction respectively.

Hexahedral and tetrahedral meshing schemes of a commercial pre-processor, GAMBIT from ANSYS Fluent Inc. were used to mesh the model geometry. It is not possible to automatically mesh the full geometry with hexahedral mesh due to the presence of some curved faces created through the blending operation. The hexahedral mesh failed to satisfy the criteria available for hexahedral meshing scheme. In order to generate a hexahedral dominant mesh, the whole geometry was decomposed into different meshable portions using Boolean operations and splits.

The section where the tangential inlet joins the main cyclone body and the point where the water rich outlet joins the main body were both meshed using a tetrahedral mesh type. This mesh type was used because it can be easily adjusted to suit the complex geometry. An unstructured hexahedral mesh type was selected to mesh the rest of the separator, as this was to align easily with flow direction, thereby reducing numerical diffusion when compared with other mesh types such as the tetrahedral (Slack et al., 2000). A more detail information about the mesh interval size used for this work can be found in Appendix B.

Fine mesh was needed at the core region and the section where the tangential inlet joined the main separator due to the high flow gradients expected there. Therefore, a sufficient number of cells were allocated to these regions (as discussed in section 4.4.2.1) in order to capture the rapidly changing mean flow. Full resolution of the boundary layer was not necessary due to the fact that most of the turbulence in the cyclone is generated in the core flow (Dyakowski and Williams, 1993).

The three outlets as shown in Figure 4.3 were all defined as outflows and this was based on the assumption that the diffusion fluxes in the direction normal to the outlet are zero. The tangential inlet was prescribed as a velocity inlet and the rest of the body surfaces (with the exception of the three outlet faces) were treated as solid walls with no slip boundary condition applied. That is, all of the three components of velocity were zero at the wall.

4.4.2 Numerical Simulation with ANSYS-FLUENT

4.4.2.1 Grid Independence Study

Grid independence testing was carried out to determine the mesh size that is sufficiently small to capture the turbulence flow structure within the pipe separator. This was necessary because the numerical simulation results of turbulent flow tend to be affected by successively smaller cell sizes associated with strong interaction of the mean flow and turbulence. Grid independence refers to a mesh size when the numerical solution no longer changes with changes in grid size. The grid independence study was conducted with five different grid sizes with cell counts varying from 50,000 to 300,000. The results are presented in Appendix B. This was conducted by increasing the mesh cells around the inlet section, since this region is regarded as an area where high turbulence gradients are expected and sufficient numbers of cells are allocated to these areas so as to capture the rapidly changing mean flow.

The grid file was read by ANSYS-FLUENT 12.0 software and a grid check carried out in order to detect any grid problems such as having negative values for the minimum volume of the geometry. Such a negative value indicates that one or more cells have improper connectivity.

A segregated, 3-D double precision implicit solver was used for the numerical simulation of the single flow of water inside the 30 mm ID pipe separator. The Cartesian coordinate system was applied with the SIMPLE (Semi-Implicit Method for Pressure Linked Equations) algorithm used to couple the continuity and momentum equations. In order to correctly predict the characteristic of the prevailing highly swirling flow within the pipe separator, the Pressure Staggered Option (PRESTO) was adopted for the pressure interpolation scheme in order to discretize the pressure gradient term (Versteeg and Malalalsekera, 2007).

The standard wall function (Launder and Spalding, 1974) was used for the near-wall treatments of the wall boundaries. Operating conditions were specified as being standard atmospheric pressure (101325 Pa) with gravitational acceleration taken as 9.81 m/s^2 and defined to act downwards in the main body of the pipe separator. The water velocity at the inlet was assumed to be constant with a magnitude of 0.5m/s and the

turbulent intensity at the inlet calculated using Equation 5.1 with a hydraulic diameter of 0.03 m.

$$\text{Turbulent Intensity (Tu et al., 2008)} = 0.16Re^{-\frac{1}{8}} \quad (4.1)$$

The R_e is defined according to equation 4.4 and for fluid properties of water-liquid, the turbulent intensity in percentage is calculated to be 4.8.

It has been reported that higher order discretization schemes provide better accuracy than first and second order schemes for grids aligned with the flow direction, especially for rotating and swirling flows (Slack et al., 2000). However, for the initial simulation, the default first order scheme was used to discretize the momentum, turbulent kinetic energy, dissipation rate and Reynolds stress terms. Then, after it was converged, the second-order scheme and then QUICK (Quadratic Upwind Interpolation for Convective Kinetic) was used after converging with the second order scheme. In ANSYS FLUENT 12.0, the QUICK scheme is based on a weighted average of the second order-upwind and central interpolations of the variable.

The Reynolds Stress Model (RSM) has been proven to be an appropriate turbulence model for the numerical simulation of flow within cyclone separators. Although RSM is computationally more expensive when compared with the k- ϵ models, it can account for the anisotropy of turbulence and gives good results for swirling flows. The same boundary and discretization conditions as with RSM were used for all simulations of the flow, with the convergence criteria for all the normalised residuals set at 1×10^{-4} . A total flow time in excess of one mean residence time was simulated, and convergence was achieved at each time step. The residence time is defined as the average time that fluid spends in a pipe separator.

$$t_r = \frac{V}{q} \quad (4.2)$$

Where t_r is used as the variable for residence time, V is the capacity of the system, and q is the flow for the system. The residence time for this separator is calculated to be 10seconds. The magnitudes of axial, radial and tangential velocities were the quantities used to evaluate the grid independence of the water flow simulation in this separator (Appendix B).

The grid independence studies indicated that better predictions are obtained at higher cell counts. It was observed that the numerical results obtained became independent of the total number of computational cells beyond 225,000. In the rest of this work, the total number of computational cells used to discretize the entire geometry was 225,000. This was found optimal for good predictions using RSM and in consideration of the computational time required.

4.4.2.2. Single Phase Simulation

A single phase turbulent simulation was carried out with a water flow rate of 0.000196 m³/s set at the inlet and the turbulent intensity of 4.8% calculated using equation 5.1. The outflow boundary condition was chosen for this study since the flow pressure was not known prior to the solution of the flow problem so that the split ratios could be specified. In this study, the water flowed out of the outlet such that the percentage of water as a fraction of the inlet mass flow was 60% through the air outlet, 33% through the water-rich outlet and the balance through the oil-rich outlet.

The water flow field was pre-established through the steady state simulation using the standard k - ϵ model with a convergence criterion of at least 10^{-4} . The residuals exhibited a cyclic pattern, indicating the inadequacy of the steady state solver. To overcome this problem, the transient solver with time step of 0.001seconds was subsequently activated. Therefore, the single phase water flow in this pipe separator was treated as the unsteady, isothermal flow of a viscous, incompressible fluid. Since the flow field in the pipe separator was found to be highly swirling and anisotropic in nature, the converged k - ϵ model solution is then switched to Reynolds Stress Model (RSM). In order to ensure that the flow features were fully developed, the transient simulation was run for at least 12 seconds (more than mean residence time of 10 seconds).

Model	Settings
Space	3D
Time	Steady, unsteady (1 st order Implicit)
viscous	RSM
Wall treatment	Standard wall function

Table 4.2: Models used in Single Phase Simulation

Variable	Scheme
Pressure	PRESTO
Pressure-Velocity Coupling	SIMPLE
Momentum	QUICK
Turbulent Kinetic Energy	QUICK
Turbulent Dissipation rate	QUICK

Table 4.3: Discretization scheme and Solution Method for Single Phase Simulation

4.4.2.3 Multiphase Flow Simulations

In the multiphase simulation the flow rates were set such that a stratified flow pattern exists in the inclined inlet. Despite the fact that a stratified flow pattern was observed at the inclined inlet, VOF is not an appropriate model for the current case of numerical simulation of multiphase flow. This is because high level of mixing or interaction of the phases occurs in the tangential inlet section of the pipe separator. Although the Eulerian model is computationally expensive, it is expected to give a more realistic prediction than the mixture model in this case. This is due to the possibility that the dispersed phases concentrating mostly in the upper and lower sections of the separator domain. In addition, the presence of recirculation flow patterns within the separator flow field would violate the basic assumptions of the mixture model that the dispersed phase velocity must be in the same direction as that of the continuous phase.

Although each of the outlets was expected to be mostly occupied by one of the phases, there was also a strong possibility that two phases could be present at the outlets. Therefore, the following assumptions become necessary;

- (a) All of the air phase at the inlet is assumed to move to the top of the cyclone and to pass out through the air outlet.
- (b) At least 20% by mass of the liquid fed to the pipe separator is specified to flow through the water rich outlet (Vazquez, 2001).
- (c) The numerical computation ignored droplet/bubble size distributions and used an average sizes obtained from a grade efficiency curve provided by Patterson and Munz (1989). Hence, diameters of air bubbles and oil droplets of $100\mu m$ and $10\mu m$ respectively were used for this study.
- (d) The boundary conditions for the inflow velocities and volume fractions at the pipe separator inlet were assumed to be uniform.
- (e) No slip boundary condition for which all three components of velocity are identically zero at the wall was used for all numerical simulations in this study.
- (f) The primary and secondary phases move at different velocities. Therefore, the slip velocity equation is solved according to equation 4.3.

$$\vec{V}_{pq} = \vec{V}_p - \vec{V}_q \quad (4.3)$$

Where \vec{V}_{pq} is the slip velocity, p and q is primary and secondary phase respectively.

The Eulerian numerical solution is based on the following assumptions:

- (a) A single pressure field is shared by all phases;
- (b) Momentum and continuity equations are solved for each phase;
- (c) The drag and gravity forces are of significance due to the large water-air density ratio. The Schiller-Naumann model is used to calculate drag coefficient and the gravitational acceleration of $9.81m/s^2$ specified in the operating conditions panel.
- (d) As the default options, wall reflection effects and linear pressure-strain of the RSM multiphase model are applied to the mixture.
- (e) In addition, other factors such as lift, collision, transfer of heat and mass, and surface tension, are neglected (Utikar et al., 2010; Huang, 2005).

The outflow boundary condition was chosen for the three outlets since the split ratio can be specified and is expected to modify the flow field inside the pipe separator to a large extent. This outflow boundary condition influences the flow distribution and the gas concentration within the cyclone.

	ρ kg/m ³	μ kg/ms	α Volume fraction, %
Water	998.2	0.001003	59.6 - 82.0
Air	1.225	0.000018	18.0 – 30.8
Oil	845-905	0.0312	0.2 – 9.9

Table 4.4: Properties of Water, Air, and Oil Phases.

4.4.2.3.1 Air-Water Simulations

In the first stage, the Eulerian multiphase model in ANSYS-FLUENT was used to model the air-water multiphase flow in the pipe separator. Here, the primary water phase is treated as a continuum, and air flow is defined as the dispersed phase in the water flow field in the form of bubbles. However, the basic assumption made in this approach is that the dispersed air flow occupies a high volume fraction. Therefore, the dispersed phase elements are too close to be treated as isolated and the effect of air dispersed phase on the water flow field was pronounced enough to require full consideration of the air-water phase interaction. Data used in this work as boundary conditions is shown in Table 4.5. These boundary conditions are largely taken from the SPIV measurements of air-water flow with the exact geometry and Reynolds numbers.

An initial numerical solution was established using the standard $k - \varepsilon$ model with the mixture model and this was run for at least 5 seconds before switching to the Eulerian model. The multiphase version of the SIMPLE algorithm (Phase-Coupled SIMPLE) was used for pressure-velocity coupling. A transient solver with a 0.01 seconds time step and convergence criteria of at least 10^{-4} were used for the air-water simulations. In addition, the Reynolds Stress Model was used to capture the anisotropic features associated with the turbulent flow within the pipe separator.

4.4.2.3.2 Air-Water-Oil Simulations

In addition to the air-water simulation discussed in the previous section, the volume fraction of the oil dispersed phase was assumed to be very low such that each element of the oil droplets is not influenced by the neighbouring water phase. Hence, the Dispersed Phase Model (DPM) in ANSYS-FLUENT12.1 was used to track the dispersed oil droplets in the cyclone. Particle tracking, using the Lagrangian dispersed phase model is assumed to interact only with the primary phase and thereby neglected interactions between the disperse phases. This interaction causes coalescence and breakage that are proved to generate a considerate influence on the separation efficiency in the pipe separator (Utikar et al., 2010; Crowe et al., 1998).

The fluid velocities at the inlet were specified according to the data shown in Tables 4.6 and 4.7. In addition, the split ratio of 0.5, 0.4 and 0.1 were specified for the air, water-rich and oil-rich outlets respectively.

	Gas superficial velocity (m/s)	Water superficial velocity (m/s)	Gas volume fraction (%)	Split ratio (water outlet)	Split ratio (air outlet)	Split ratio (oil outlet)
A	0.0636	0.290	18.0	0.317	0.066	0.617
B	0.0636	0.277	18.67	0.332	0.069	0.599
C	0.0636	0.262	19.57	0.352	0.072	0.576
D	0.0636	0.224	22.17	0.40	0.1	0.5
E	0.0636	0.209	23.32	0.439	0.1	0.47
F	0.0636	0.187	25.42	0.48	0.11	0.41

Table 4.5: Boundary Condition at the Inlet for Air-Water Experiments.

	Gas superficial velocity (m/s)	Oil superficial velocity (m/s)	Water superficial velocity (m/s)
A	0.0636	0.0256	0.177
B	0.0636	0.0256	0.188
C	0.0636	0.0256	0.200
D	0.0636	0.0256	0.212

Table 4.6: Boundary Condition at the Inlet for Air-Water-Oil Experiments

	Gas superficial velocity (m/s)	Water superficial velocity (m/s)	Oil superficial velocity (m/s)
A	0.0636	0.201	0.00350
B	0.0636	0.201	0.011
C	0.0636	0.201	0.0169
D	0.0636	0.201	0.0467
E	0.0636	0.201	0.0704

Table 4.7: Boundary Condition at the Inlet for Air-Water-Oil Experiments.

Boundary Type	
Inlet	Velocity inlet
Outlets	Outflow
Wall	No slip Wall

Table 4.8: Boundary Types for Multiphase Flow Simulation

<i>Settings</i>	<i>Choice</i>
Simulation type	3D, Unsteady
Solver	Double precision, Pressure based Implicit
Temporal discretization	1st order
Multiphase model	Mixture, Eulerian, DPM (implicit)
Turbulence model	RSM mixture model
Pressure-velocity	SIMPLE, Phase Coupled SIMPLE
Momentum	1 st , 2nd order upwind, QUICK
Volume fraction	1 st , 2nd order upwind, QUICK
Turbulent kinetic energy	1 st , 2nd order upwind, QUICK
Turbulent dissipation rate	1 st , 2nd order upwind, QUICK
Reynolds stress	1 st , 2nd order upwind, QUICK
Convergence criteria	1.0×10^{-4}

Table 4.9: Model and Discretization Scheme for Multiphase Flow Simulation

CHAPTER FIVE

ANALYSIS OF SINGLE PHASE MEASUREMENTS

In this chapter, the results of the stereoscopic PIV measurements and the CFD simulation of single phase water flow in the pipe separator are presented and discussed. The experimental equipment used to capture the experimental data is presented in section 3. Section 5.1 presents the mean velocity profiles extracted from the time-averaged velocity fields of single phase flow. In section 5.2, the results of a single phase flow simulation are then compared with the experimental data.

5.1: Experimental Results and Discussion of the Single Water Phase Flow

All experimental measurements of the tangential, axial and radial velocity fields are presented in this section at the three axial positions $Z = -395\text{mm}$, -75 mm and 295 mm in the vertical axis of the pipe separator (see Figure 3.12). The single phase flow experiment was run with a water flow rate of $0.000196\text{m}^3/\text{s}$. The outlets were restricted with rubber bungs such that the percentage of water as a fraction of the inlet mass flow was 60% through the air outlet, 33% through the water-rich outlet and the balance through the oil-rich outlet. This allows water flow to pass through all the three outlets of the pipe separator in order to obtain SPIV measurements at all the axial positions selected.

The mean velocity fields from the SPIV system were computed using Tecplot software by averaging a sequence of two hundred valid vector fields at each measurement location within the plane. The experimental data presented in the form of graphical plots for all three axial positions were extracted along the $y=0$ line for the separator, as shown in Figure 5.1.

5.1.1 Tangential Velocity

Figure 5.2 shows the comparison of the mean tangential velocities of the water flow at the $Z = -0.395\text{ mm}$, -0.075 mm and 0.295 mm axial positions. At all axial positions, it can be observed that the tangential velocity increases moving away from the centre of the tube before reaching a maximum and then dropping close to the wall due to wall friction. At $Z = 295\text{mm}$, the maximum tangential velocity occurs at a radius of 7mm .

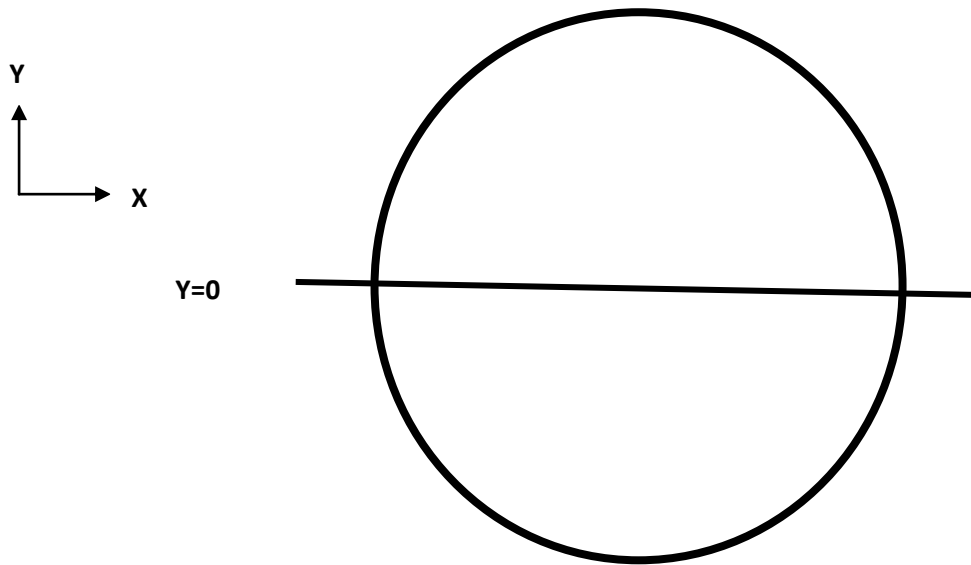


Figure 5.1: Experimental Data: Position of $Y=0$ sections at $Z=-75\text{mm}$

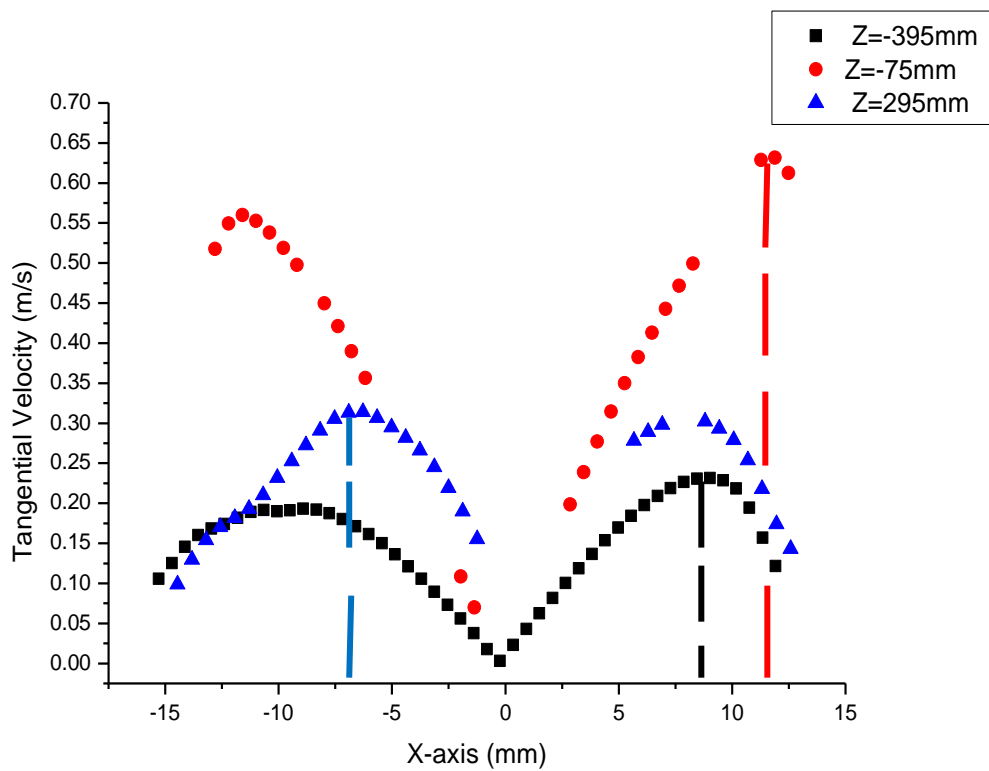


Figure 5.2: Comparison between the Tangential Velocity Profiles at Three Axial Positions in the Cyclone

At $Z=-395\text{mm}$ the maximum velocity occurs at a radius of 9.5mm and at $Z= -75\text{mm}$, maximum velocity is observed at a radius of 12mm . By identifying this location, the tangential velocity distribution can be described as a continuous flow stream with an outer and inner region. The inner region is characterized as a forced vortex where tangential velocity increases directly with radius. However, the outer region is characterized as a free vortex and the rate of rotation is greatest at the centre and then decreases progressively (Kelsall, 1952). The observations made are similar to the reports of earlier researchers in the literature (Leeuwner and Eksteen, 2008; Slack and Wraith, 1997). At $Z=-75\text{mm}$, the forced vortex extends over 80% of the surface area of the separator's plane and decreases to 60% and 40% at $Z= -395\text{mm}$ and 295mm respectively. However, the free vortex occupies 50% of the surface area of the separator's plane at $Z=295\text{mm}$, decreases to 30% and 5% at the $Z= -395\text{mm}$ and -75mm axial positions respectively. This means that the surface area occupied by the forced vortex decreases moving away from the inlet section. However, the free vortex increases when moving away from $Z=-395\text{mm}$.

The comparison of the tangential velocity profiles at the three axial positions shown in Figure 5.2 reveals that the magnitude of mean tangential velocity decreases as we move away from the inlet section towards the outlets. For example, at an axial position of $Z= -75\text{ mm}$, the maximum tangential velocity observed is 0.64 m/s and at axial positions $Z= 295\text{ mm}$ and -395mm , the maximum values are 0.32 m/s and 0.225 m/s respectively. The reason for this is mainly the decay in swirl intensity as the flow moves away from the inlet. Therefore, as we move away from the inlet section, the tangential velocity gradually decreases and relatively less strong centrifugal fields are generated. Tangential velocity magnitude is a measure of the centrifugal force in the vortex region and this helps to improve the separation efficiency of the pipe separator. It is generally accepted that tangential velocities are directly proportional to separation efficiencies. Therefore, most of the fluid separation occurs immediately at the region where the inlet section joins the vertical axis of the cyclone. The measured tangential profiles show retardation of the velocity near the walls, which satisfy no slip boundary conditions.

As can be seen in Figure 5.2, the tangential velocity patterns are similar irrespective of the measuring plane as we move from the axial position of $Z= -395\text{ mm}$ to $Z= 295\text{ mm}$.

Therefore, the shape of the tangential velocity profile is found to be independent and the area occupied by free/forced vortex is a function of the axial positions.

5.1.2 Axial Velocity

Figure 5.3 shows the comparison between the axial velocity profiles at the three different axial positions in the separator. In accord with other researchers such as Peng, et al (2002) and Monredon et al (1992), the positive axial velocity profile is hereby referred to as region of flow in an upward direction with respect to the rotation axis. A negative axial velocity profile will be taken as a region of flow in a downward direction from the rotation axis. This division is shown in Figure 5.3 by dark lines and it represents the so called locus of zero axial velocity (LZAV).

Furthermore, at $Z=-395\text{mm}$ and -75mm , the positive values of axial velocity decrease with an increase in radial distance. It reaches zero at some distance away from the centre of the tube. However, close to the separator wall, the axial velocity reaches a maximum and then decreases. This is due to high friction associated with fluid layer interacting with the wall, indicating a no slip boundary condition at the wall. Axial velocity profiles at $Z=-395$ and -75mm reveal a combination of downward and upward flow patterns at the wall and centre of the tube respectively. However, at $Z=295\text{mm}$ there is no negative axial velocity at any x-axis coordinate.

As can be seen in Figure 5. 3, a large amount of water flows in an upward direction at the centre of the tube and in a downward direction near to the wall at $Z=-75\text{mm}$. For example, the maximum positive and negative axial velocities are 0.175m/s at $Z=-75$ mm. The maximum positive axial velocity among the three axial positions is 0.175m/s at $Z=-75\text{mm}$. At $Z=-395\text{mm}$, a large downward flow is observed close to the wall together with small amounts of upward flow at the centre of the tube. For example, the maximum of positive axial velocity here is 0.05m/s and of negative velocity is 0.225m/s . The maximum negative axial velocity among the three axial positions is 0.225m/s at $Z=-395$ mm. The axial velocity profile is observed to be symmetry at $Z=-75\text{mm}$ and unlike the case at $Z=-395\text{mm}$, where the location of the maximum axial velocity shifted off centre of the tube. Similar observations of axial velocity flow patterns were made by Dlamini et al (2005) and Leeuwner and Eksteen (2008).

As shown in Figure 5.3, there is no data at the centre and close to the wall of the tube for $Z = -75\text{mm}$ and 295mm . This is due to the wall reflection and large acceleration at the centre of the vortex that shifted tracer particles away, indicating no tracer particle to scattered light that can be recorded by the SPIV technique. That is, the tracer particle slip and its streamline shifted away from the centre of the tube associated with lower acceleration.

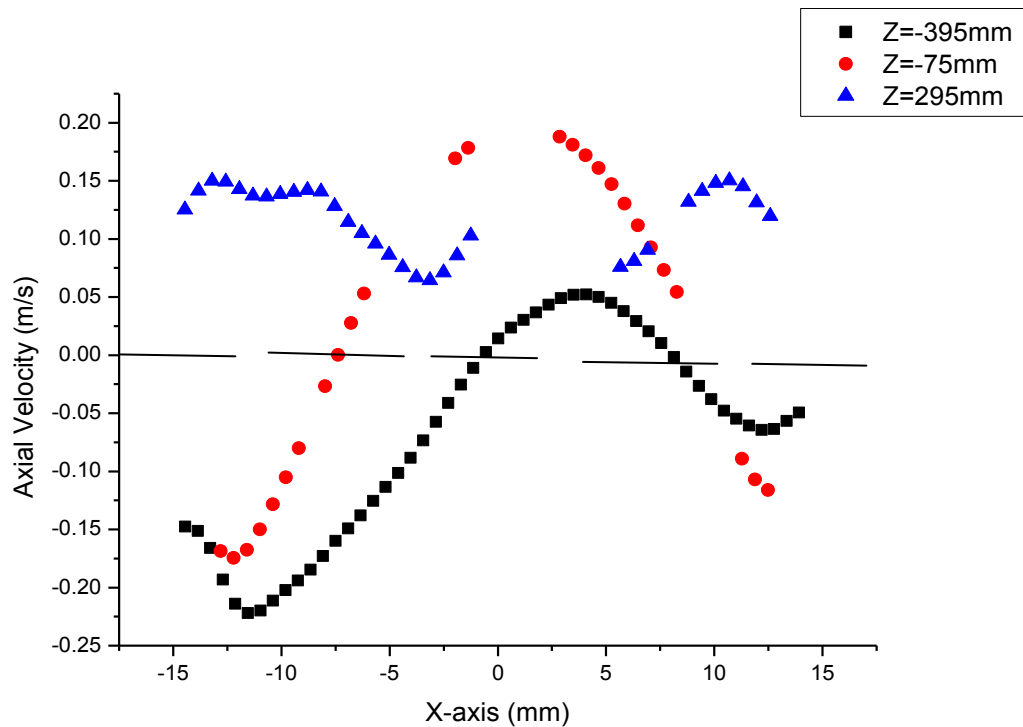


Figure 5.3: Comparison between the Axial Velocity Profiles at three axial positions in the Cyclone

5.1.3 Radial Velocity

Figure 5.4 shows a graph of the comparison between the mean radial velocity profiles at the three axial positions in the cyclone. In accordance with other researchers such as Kelsall (1952) and Peng et-al (2007), radial velocity flow is said to be directed inward when the radial velocity is negative and outward when its value is positive. As can be seen in Figure 5.4, radial flow is found to be inwards as we move away from the centre of the tube at $Z = -395\text{mm}$. However, close to the wall at the positive value of the x-axis, outward radial velocity begins to develop.

At $Z = -75\text{mm}$, radial velocity is observed to be directed outwards at all values of the x -axis. The radial velocity profile at $Z = 295\text{mm}$ shows inward flow as we move away from the centre of the tube. However, close to the wall at a negative value of the x -axis, outward flow is observed.

In Figure 5.4, it can be observed that the magnitude of radial velocity decreases as the flow moves towards the outlets. The maximum radial velocity at $Z = -75\text{mm}$ is 0.23m/s . However, at $Z = -395\text{mm}$ and 295mm , the maximum radial velocities are 0.15m/s and 0.14m/s respectively. The high radial velocity at the axial position below the inlet section is attributed to the decay in swirl intensity as the flow moves away from the inlet. The wall effect on the radial velocity profiles is observed by no velocity data beyond the wall region. This shown that the wall of the pipe separator is found to be impenetrable as the flow reflected back or bounces at the wall.

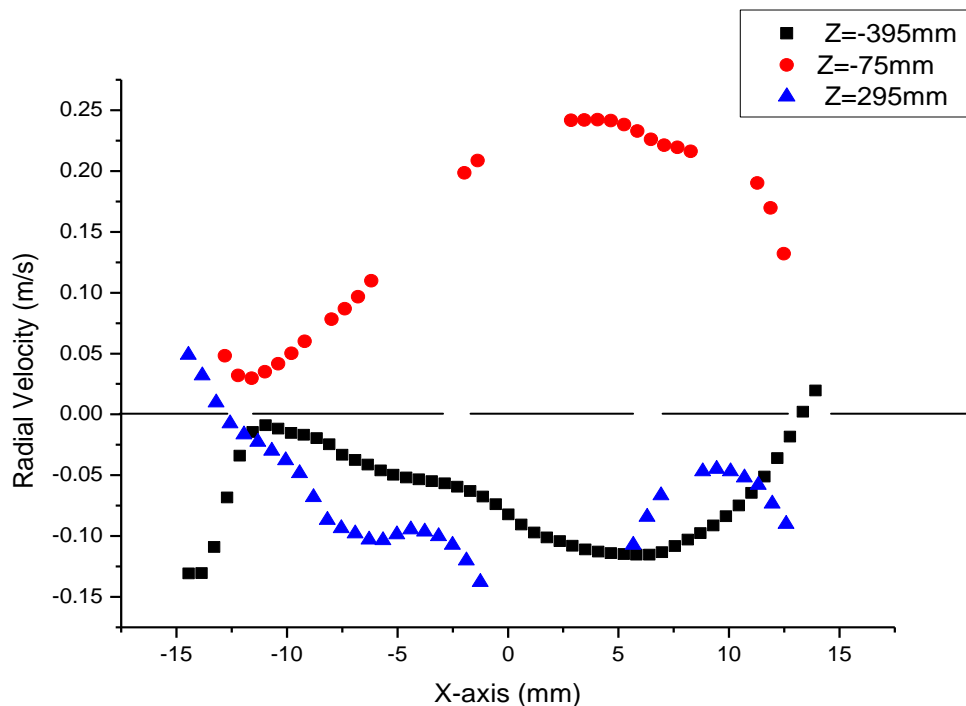


Fig. 5.4: Comparison between the Radial Velocity Profiles at Three Axial Positions in the Cyclone

5.2 Comparison of the Numerical Simulation of the Velocity Field with the Experimental Measurements

Here, the CFD simulation of the single water flow field is compared with the stereoscopic PIV measurements at the three different axial positions of $Z = -395\text{mm}$, -75mm and 295mm . The CFD simulation using Reynolds Stress Model has been described in section 4.4.3.

5.2.1 Tangential Velocity

Figure 5.5 compare the CFD simulation results with the experimentally measured mean tangential velocity profiles at the axial positions of $Z = -395\text{mm}$, -75mm and 295mm respectively. All of the results clearly show that the tangential velocity distribution inside the pipe separator are of similar shapes and consists of two regions. Firstly, there is an outer free vortex region where the tangential velocity decreases with increasing distance from the centre of the tube. Secondly, is that a forced vortex at the centre where tangential velocity increases with radius. Generally, it is observed that the experimental profiles have similar flow patterns to the ones obtained in the CFD simulations.

In Figure 5.5 (A), the maximum tangential velocity values from the CFD simulation at $Z = -395\text{mm}$ are larger than the experimentally measured data. For example, the maximum tangential velocities from the experimental data are 0.175m/s at $x = -7.5\text{mm}$ and 0.225m/s at $x = 11\text{mm}$. However, the maximum tangential velocities in the simulation results are 0.25m/s at $x = -4\text{mm}$ and 0.275m/s at $x = 9.5\text{mm}$. In addition, the free vortex region starts at smaller values of the radius for the CFD simulation in comparison with the experimental data.

Figure 5.5 (B) shows that, the predicted tangential velocity profile agrees well with the experimental data at the centre of the tube. The best agreement occurs at $x = \pm 7.5\text{mm}$, where the prediction is within 2% of the experimental profile for the majority of the x -axis coordinates. As we approach the wall region, the values of the simulated tangential velocity are found to be smaller when compared with the experimental data. For example, the maximum tangential velocities from the experimental data are 0.55m/s at $x = -11.50\text{mm}$ and 0.60m/s at $x = 11\text{mm}$.

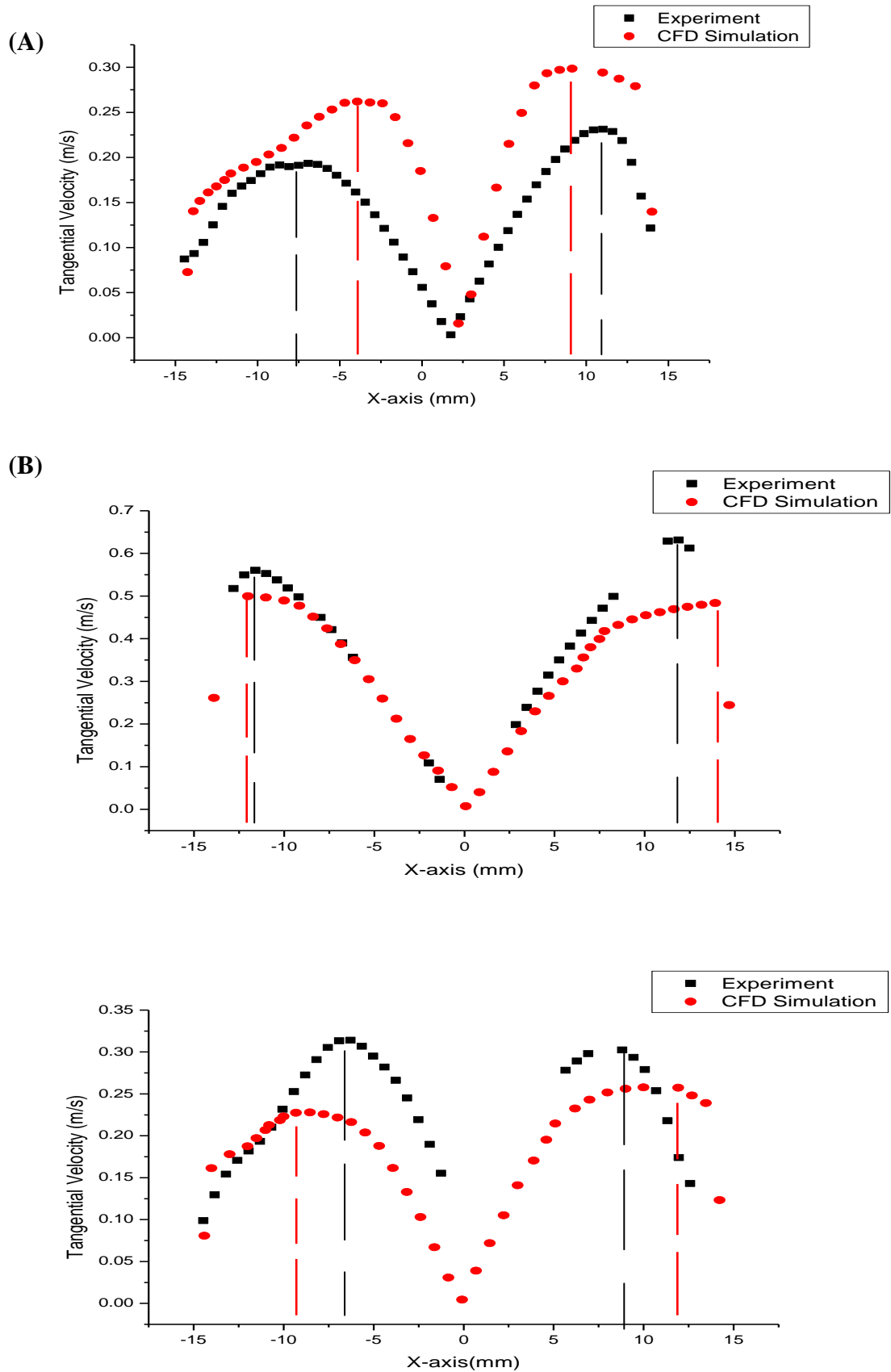


Figure 5.5: Comparison of the CFD Result and Experimental Data for Mean Tangential Velocity at Axial Positions of (A) $Z = -395\text{mm}$ (B) -75 mm (C) 295 mm .

However, the maximum tangential velocities in the simulated results are 0.50m/s at $x = -12.25$ mm and 0.40m/s at $x = 14$ mm. In addition, the free vortex region begins at larger values of the radius in the CFD simulation in comparison with the experimental data. Here, the predicted tangential velocity profile is found to be under-predicted by 5% and 12% near to the wall at the negative and positive values of the x-axis respectively.

It can be seen in Figure 5.5(C) that the values of maximum tangential velocity from the experimental data are larger than those in the simulated results. However, as we move closer to the wall, the values of tangential velocity from the experimental data are found to be smaller than the simulated results. In addition, the free vortex region starts at larger values of radius for the CFD simulation in comparison with the experimental data. The predicted maximum tangential velocities occur at $x = -9.5$ mm and 12mm, whereas, the maximum tangential velocity in the experimental data occur at $x = 7$ mm and 9mm. This means, that the cores of the tangential velocity distributions within the pipe separator are transient.

In Figure 5.5(C), the simulated profile clearly shows that the CFD package is able to capture the lowest velocity profiles at the centre of the tube which are absent in the experimentally determined profile. This is due to high swirl that displace tracer particles away from the centre of the tube, thereby reducing the amount of tracer particles to be illuminated and recorded during SPIV measurement. Furthermore, the tangential velocity profile is found to be over-predicted in the CFD simulation at $Z = -395$ mm and under-predicted at the $Z = -75$ mm axial position. At $Z = 295$ mm, the tangential velocity profile is observed to be under predicted as we move away from the centre of the tube and over-predicted at the wall.

5.2.2 Axial Velocity

Figure 5.6 presents a comparison of the mean axial velocity profiles obtained by the CFD simulation and the SPIV measurements. As can be seen in Figure 5.6 (A), the experimental axial velocity profile clearly shows the existence of a region of upward flow at the centre of the tube and a region of downward flow as we move close to the wall. The predicted axial velocity profile shows a flow pattern downward directed at all x-axis coordinates. Therefore, it is concluded that the CFD model failed to predict the

upward flow observed from the experimentally measured axial velocity profile at $Z = -395\text{mm}$.

In Figure 5.6(A), the simulated results are found to over-predict axial velocity as the x-axis increases from $x = -2.5\text{mm}$ when compared with the experimental data. However, the simulated results under-predict axial velocity as we away from $x = -2.5\text{mm}$ to the positive values of x-axis. For example, the maximum downward axial velocity from the CFD simulation is 0.20m/s at $x = -13.75\text{mm}$. However, the experimental data shows that maximum downward axial velocity is 0.225m/s at $x = -11.75\text{mm}$.

In Figure 5.6 (B), the measured and predicted axial velocity profiles show an upward flow region at the centre of the tube, and a downward flow region at the wall of the separator. The axial velocity is found to be over-predicted by the CFD model at negative values of the x-axis. However, the axial velocity profile is found to be under-predicted by the CFD model at positive values of the x-axis. For example, the maximum downward axial velocity from the CFD simulation is 0.40m/s at $x = 13.75\text{mm}$. However, the experimental data shows that the maximum downward axial velocity is 0.20m/s at $x = 12.25\text{mm}$. The location of the maximum upward flow is observed to be off centre when comparing the simulated results with experimental data.

Figure 5.6(C) shows that the experimentally measured axial velocity is positive at all x-axis coordinates. This means that an upward flow region is observed as we move away from the centre of the tube. The profile predicted by CFD indicates that the axial velocity distribution is negative at the centre of the tube, and positive as we move away from the centre of the tube. However, there is no experimental data at the centre of the tube. This is due to slippage of the tracer particle caused by large acceleration at the centre of the tube. As a result, there is no particle to scatter light to be recorded with SPIV system.

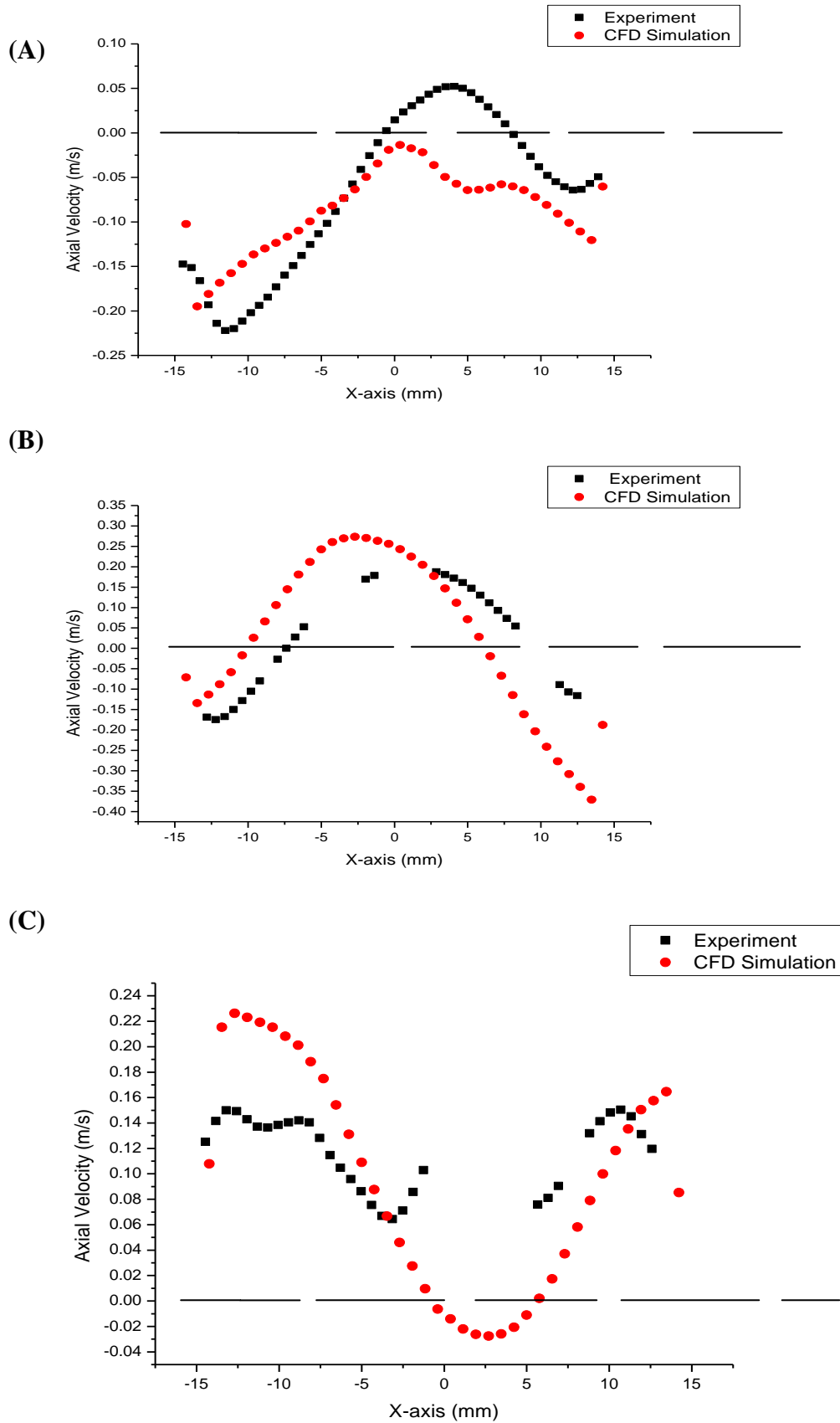


Figure 5.6: Comparison of the CFD Result and Experimental Data for Mean Axial Velocity at Axial Positions of (A) $Z = -395\text{mm}$ (B) -75 mm (C) 295 mm axial positions.

Figure 5.7 presents a general overview of the axial velocity flow pattern in the pipe separator as obtained by experimental measurement and CFD simulation. At $Z = -75$ mm position, the computational model gives qualitative agreement with the experimental measurements. There is disagreement between measured and CFD results at $Z = -395$ mm and 295mm especially at the centre of the tube. At $Z = -395$ mm, the measured profile indicated the presence of an upward flow at the centre of the tube but absence in the predicted profile. However at $Z = 295$ mm position, the predicted profile indicated the presence of a downward flow at the centre of the tube, but absence in the measured profile. This discrepancy is probably due to the effect of natural rubber bungs used in experimental measurements to specify the split ratio as a function of mass flow rate passing through each outlet.

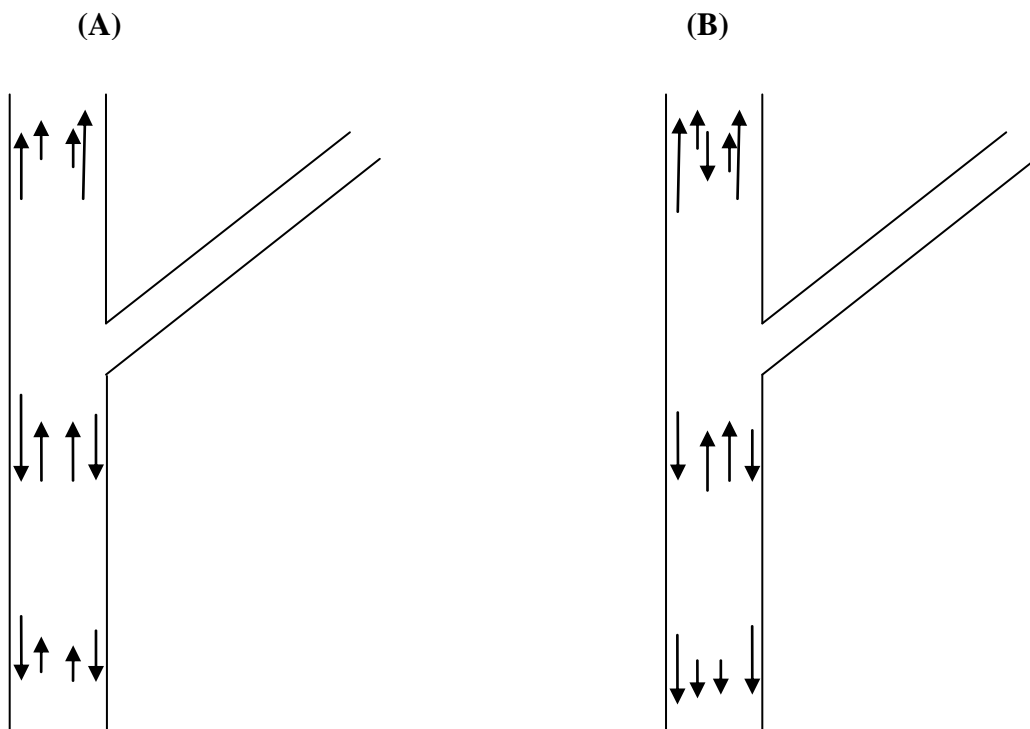


Figure 5.7: Schematic Representation of Axial Velocity Profile by:

(A) *Experimental Measurements*

(B) *CFD Simulation*

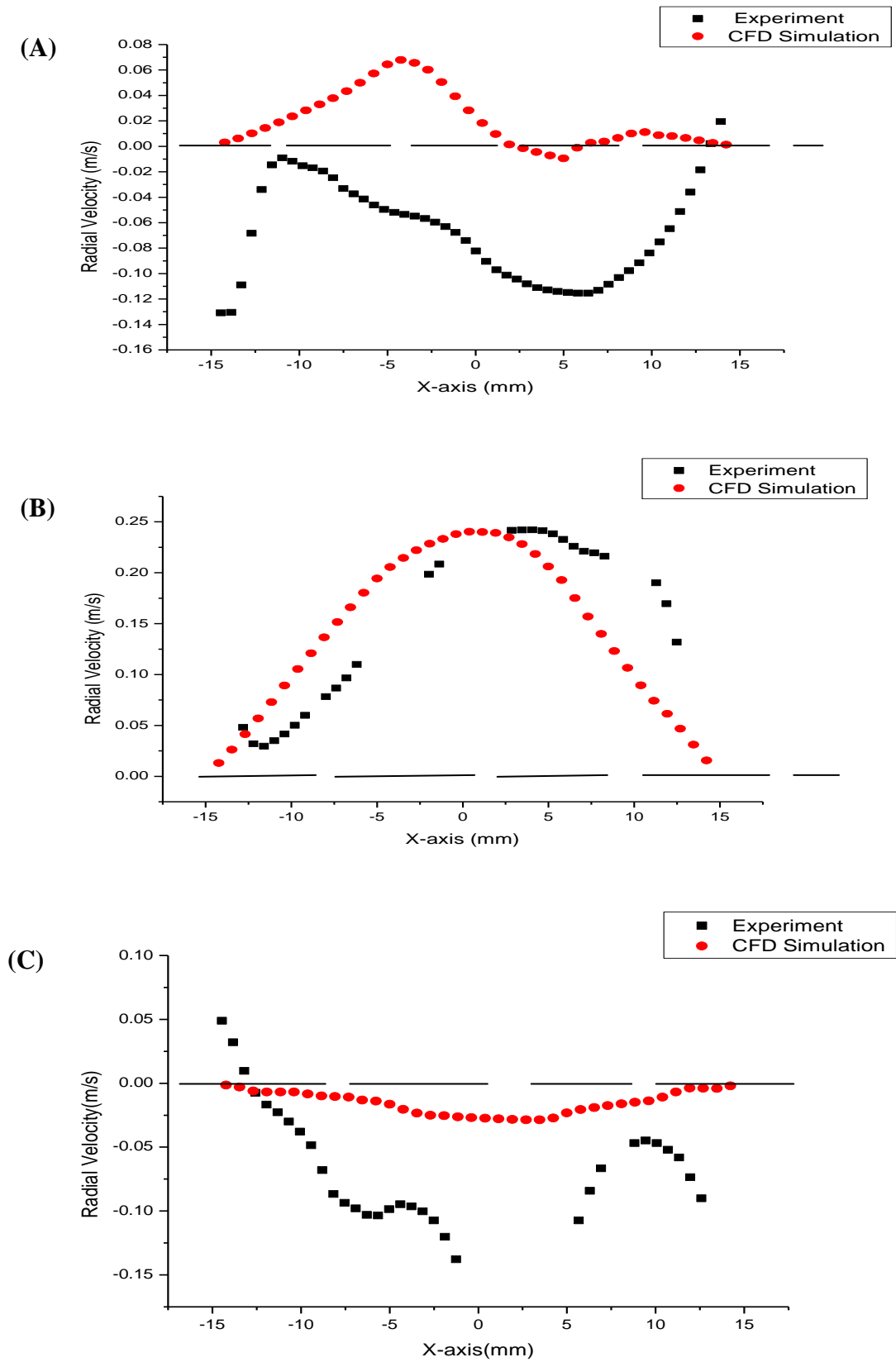


Figure 5.8: Comparison of the CFD Result and Experimental Data for Mean Radial Velocity at Axial Positions of (A) $Z = -395\text{mm}$ (B) -75 mm (C) 295 mm axial positions.

5.2.3 Radial Velocity

Figure 5.8 shows the comparison of the mean radial velocity distributions at the three axial positions as measured experimentally and simulated using CFD. At $Z = -395\text{mm}$, the experimental results reveal an inward radial flow pattern as we move away from the centre of the tube. However, close to the wall of positive values of the x-axis, an outward flow begins to develop. The simulated radial velocity profile indicates that water flows outwards at negative values of x-coordinates and both inwards and outwards, at the positive values of x-coordinates.

As can be seen in Figure 5.8(B), the experimentally measured and simulated radial velocity profiles show that water flows outwards as we move away from the centre of the tube. In addition, the measured radial velocity profile indicates that, close to the wall with a negative value of the x axis, the value of radial velocity reaches a minimum and then gradually begins to increase. The value of the predicted radial velocity is larger at negative values of the x-axis in comparison with the measured radial velocity. However, the value of the predicted radial velocity is smaller for positive values of the x-axis. For example, the measured radial velocity at $x = 7.5\text{mm}$ is 0.21m/s , whereas the predicted radial velocity is 0.15m/s .

In Figure 5.8(C), the simulated and measured radial velocity profiles indicate that water flows inwards at most of the x-axis coordinates. However, the experimental data shows an outward flow pattern at the wall on the negative values of x-axis coordinates.

Figure 5.9 presents a general overview of the radial velocity flow pattern in the pipe separator as obtained by experimental measurement and CFD simulation. The CFD flow pattern at $Z = -75\text{mm}$ and 295mm compare favourably with experimental data except at few x axis coordinates where measured profile shows an outward flow pattern. However, there is disagreement between the flow patterns as measured and predicted at axial position of $Z = -395\text{mm}$.

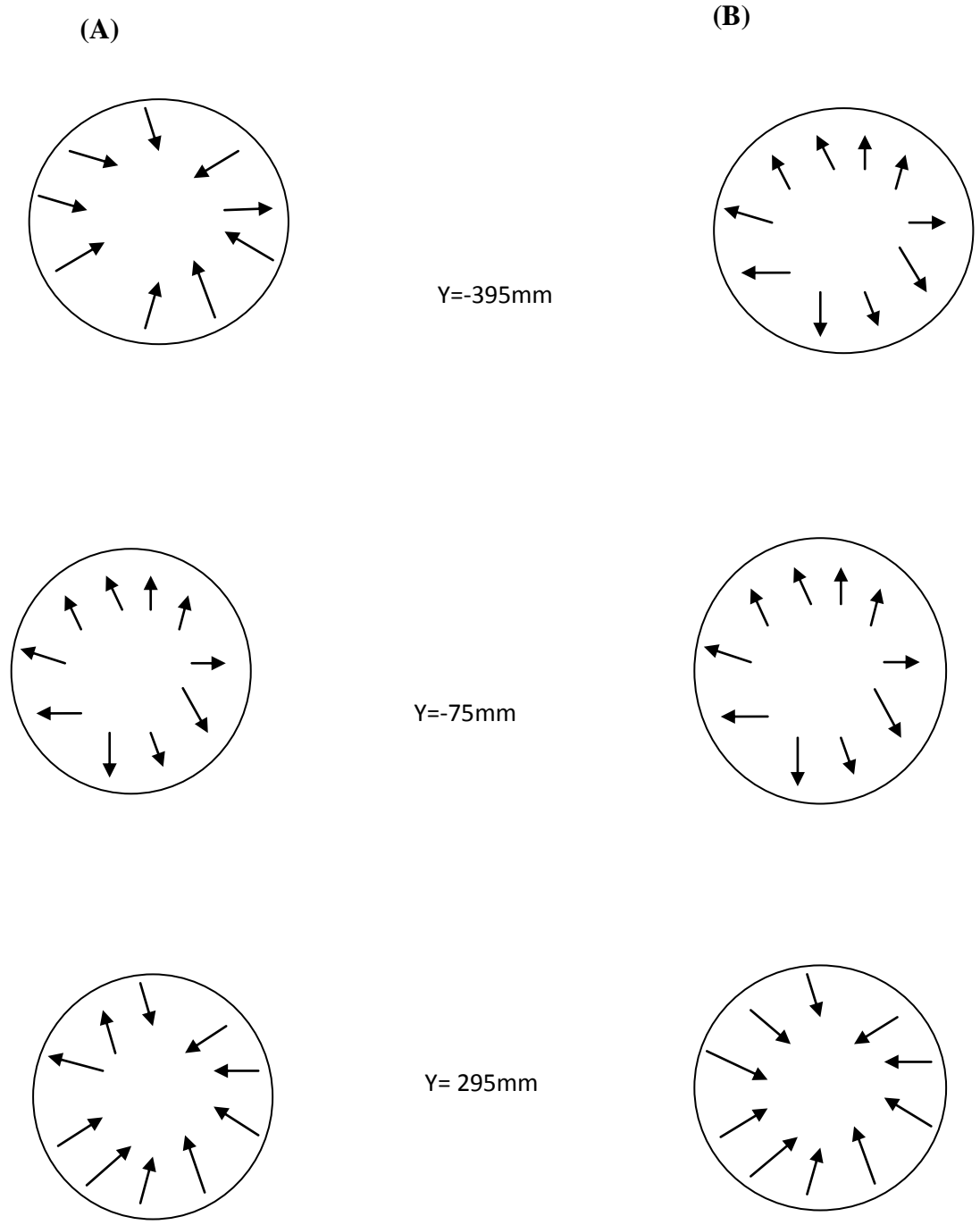


Figure 5.9: Schematic Representation of Radial Velocity Vector Map as Obtained by:

(A) Experimental Measurements

(B) CFD Simulation

CHAPTER SIX

ANALYSIS OF AIR-WATER FLOW MEASUREMENTS

In this chapter, the results of the Stereoscopic PIV measurements and CFD simulations of air-water flow in the pipe separator are presented and discussed. Sections 6.1 and 6.2 show the comparison between mean velocity profiles of the air-water flow and those of the water flow fields by through the SPIV measurements. In section 6.3, the results of the air-water flow simulation are then compared with the experimental data.

6.1: Results and Discussion of Two Phase Flow

A comparison is made between the measured velocity distributions of the air-water flow and water-only flow fields, as shown in Figures 6.2-6.13. This comparison is intended to determine the effect of air flow in air-water flow field. Each of the presented profiles has the same water flow rate for the water only flow and constant air flow rate added for air-water flow fields. Table 6.1 gives a detailed overview of the experimental conditions of the air-water flow in the pipe separator. All experimental measurements at $Z=-395\text{mm}$ and -75mm presented in this chapter were extracted along the $y=0$ line for the separator, as shown in Figure 5.1. It was not possible to extract any data at $Z=295\text{mm}$ along the $y=0$ section, due to the fact that the SPIV set-up for this investigation (as discussed in Section 3.2) could only capture velocity distributions in the liquid phase. The air-water mixture flows through the inlet, and the air separates and flows upward and passes through the air outlet of the pipe separator. Therefore, most of the area of the plane at $Z=295\text{mm}$ is occupied by the separated air flow. As shown in Figure 6.1, velocity data were extracted at the $Z=295\text{mm}$ plane along the lines at $Y=11.6\text{mm}$ (for A and B), $Y=12.3\text{mm}$ (for C) and $Y=-10.4\text{mm}$ (for D, E and F).

6.1.1 Tangential Velocity

Figures 6:2-6.4 compare the mean tangential velocities of the water and air-water flows at $Z= -395\text{mm}$, -75mm and 295mm respectively. Figures 6.2 and 6.3 indicate that the tangential velocity distributions of both the water and air-water flow fields increase as we move away from the centre of the tube, reaching a maximum and then rapidly decreasing close to the wall.

	Gas flow rate (litre/min)	Water flow rate (litre/min)	Gas volume fraction (%)	Split ratio (water outlet)	Split ratio (air outlet)	Split ratio (oil outlet)
A	2.7	12.3	18.0	0.32	0.066	0.62
B	2.7	11.76	18.7	0.33	0.069	0.6
C	2.7	11.1	19.6	0.35	0.072	0.58
D	2.7	9.48	22.2	0.40	0.1	0.5
E	2.7	8.88	23.3	0.44	0.1	0.47
F	2.7	7.92	25.4	0.48	0.11	0.41

Table 6.1: Experimental Plan for Air-Water Flow.

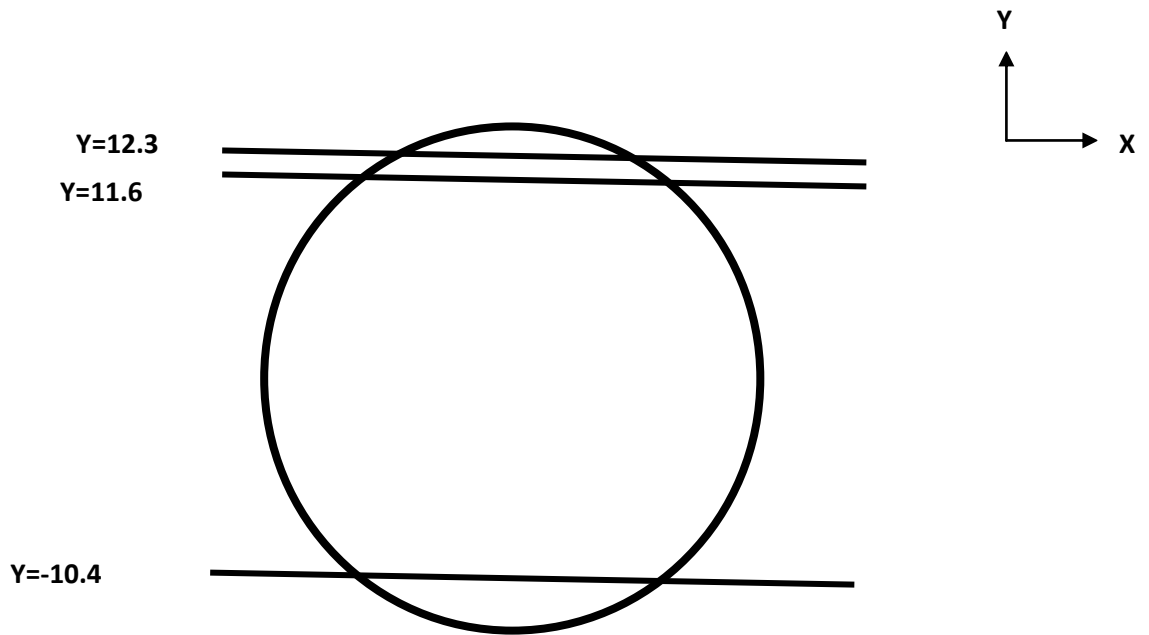


Figure 6.1: Experimental Data: Position of Y Sections at Z=295 mm

This clearly implies that the tangential velocity profiles of both the water and air-water flows show a forced vortex near the centre surrounded by a free vortex at the wall of the pipe separator.

At planes below the inlet ($Z=-395$ mm and -75 mm), as air flow is added to the water flow field, the magnitudes of both the free vortex and forced vortex in the air-water flow field gradually increase when compared with those of the water flow field. Therefore, the effect of air flow on the air-water velocity field when compared with that of water alone is an increase in values of tangential velocity. This is expected, since there is an increase in the air-water flow rate at the inlet section of the pipe separator. Therefore, it is concluded that the magnitude of the tangential velocity profile is proportional to the flow rate of the fluid at the inlet. In addition, it was observed that air flow does not have any effect on the flow pattern of the water flow field, as the profiles for tangential velocity remain similar at the $Z=-395$ mm and -75 mm axial positions.

As can be seen in Figure 6.2(A-C), the free vortex region begins at smaller values of radius for air-water profiles in comparison with water-only profiles. For example, Figure 6.2(B) shows that the free vortex starts at $x=-8$ mm and at 11 mm for the water flow profile. However, for the measured air-water profile, the free vortex begins at $x=-5.75$ mm and 5.75 mm. In Figure 6.2(D-F), the free vortex region starts at larger values of the radius for the air-water flow profiles. For example, Figure 6.2(E) shows that the free vortex region starts at $x=-4.75$ mm and 7.5 mm for the water flow profile. However, for the measured air-water profile, the free vortex region begins at $x=-6$ mm and 10 mm. Therefore, it can be concluded that the location at which the free vortex region begins depends on the volume fraction of water. At high water volume fractions, the free vortex of the air-water flow begins at smaller values of radius. However, at lower water volume fractions, it begins at larger values of the radius. This is probably due to an increase in the air volume fractions associated with lower water volume fractions that cause interfacial waves and mixing at the interface.

Figure 6.3 (B-F) shows that the free vortex region begins at larger values of radius for air-water profiles in comparison with the water-only profiles. For example, Figure 6.3(E) shows that the free vortex starts at $x=-12.25$ mm for the water flow profile, but at $x=-12.5$ mm for the measured air-water profile.

Figures 6.4(A-C) indicate an increase in the magnitude of the tangential velocity profile of the air-water flow in comparison with that of the water-only flow. For example, Figure 6.4(A) show that the maximum tangential velocity of the air-water flows is 0.065 m/s at $x=-4$ mm. However, for the water flow it is 0.035 m/s at $x=-5.25$ mm.

It can be seen from Figures 6.4 (D-F) that, a meaningful comparison of the tangential velocity profiles for the water and air-water flow fields could not be established, due to insufficient data for the air-water flow.

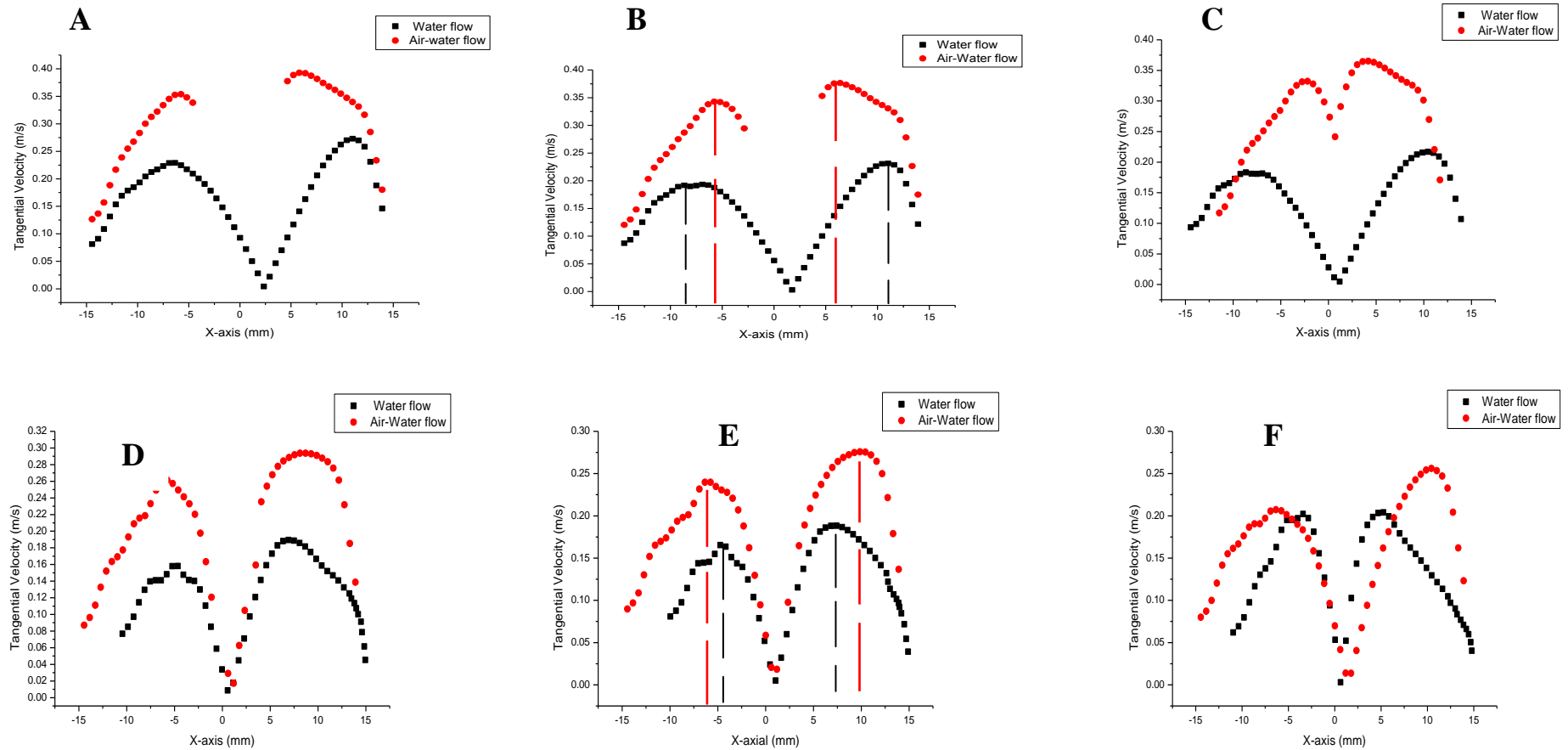


Figure 6.2: Profiles of the Mean Tangential Velocity for Water Flow and Air-Water Flow at $Z = -395$ mm Axial Position;

A: 12.3 litre/min (water), 2.7 litre/min (air); **B:** 11.76 litre/min (water), 2.7 litre/min (air); **C:** 11.1 litre/min (water), 2.7 litre/min (air);

D: 9.48 litre/min (water), 2.7 litre/min (air); **E:** 8.88 litre/min (water), 2.7 litre/min (air); **F:** 7.92 litre/min (water), 2.7 litre/min (air)

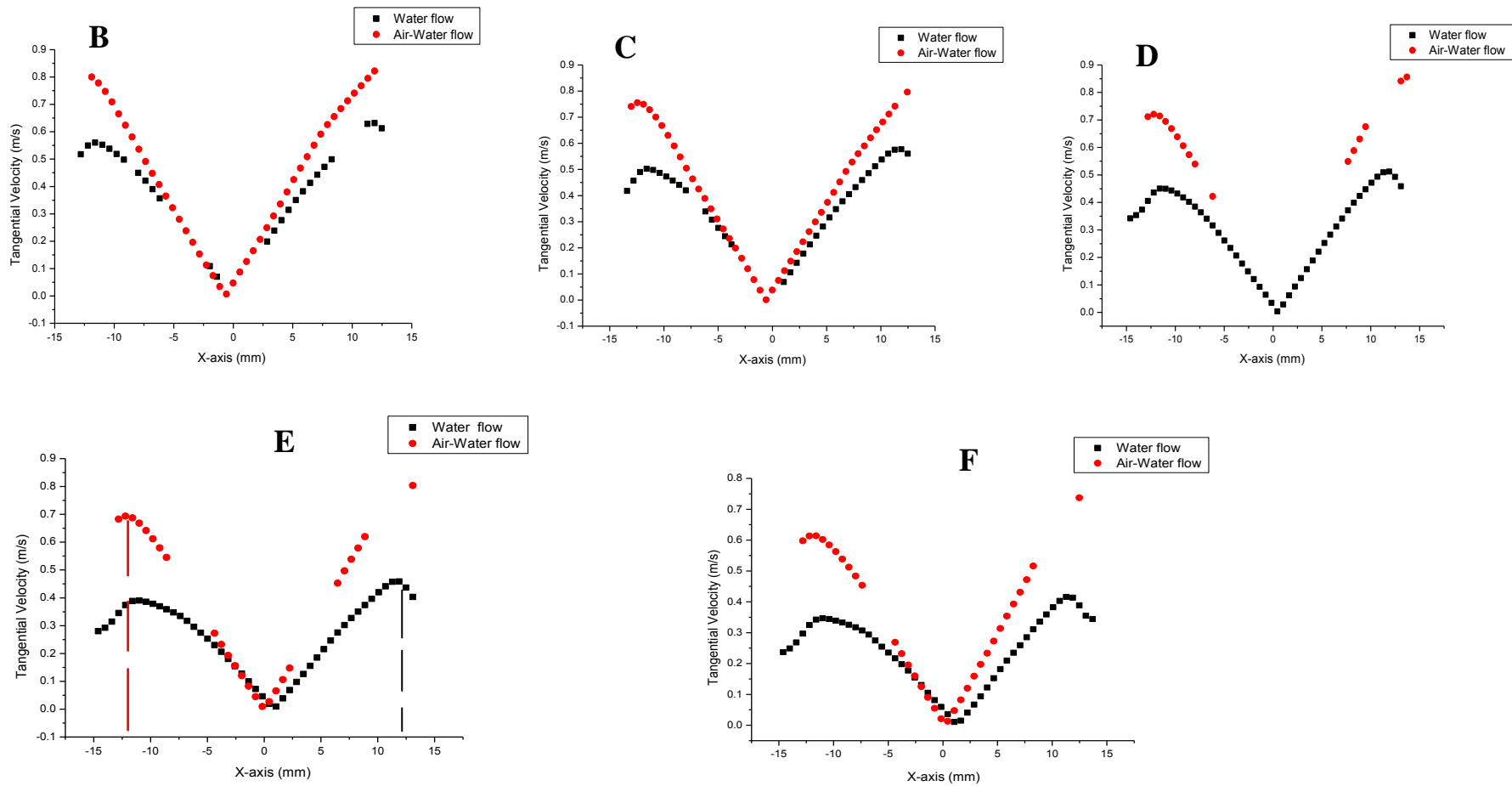


Figure 6.3: Profiles of the Mean Tangential Velocity for Water Flow and Air-Water Flow at Z = -75 mm Axial Position;
B: 11.76 litre/min (water), 2.7 litre/min (air); **C:** 11.1 litre/min (water), 2.7 litre/min (air); **D:** 9.48 litre/min (water), 2.7 litre/min (air)
E: 8.88 litre/min (water), 2.7 litre/min (air); **F:** 7.92 litre/min (water), 2.7 litre/min (air)

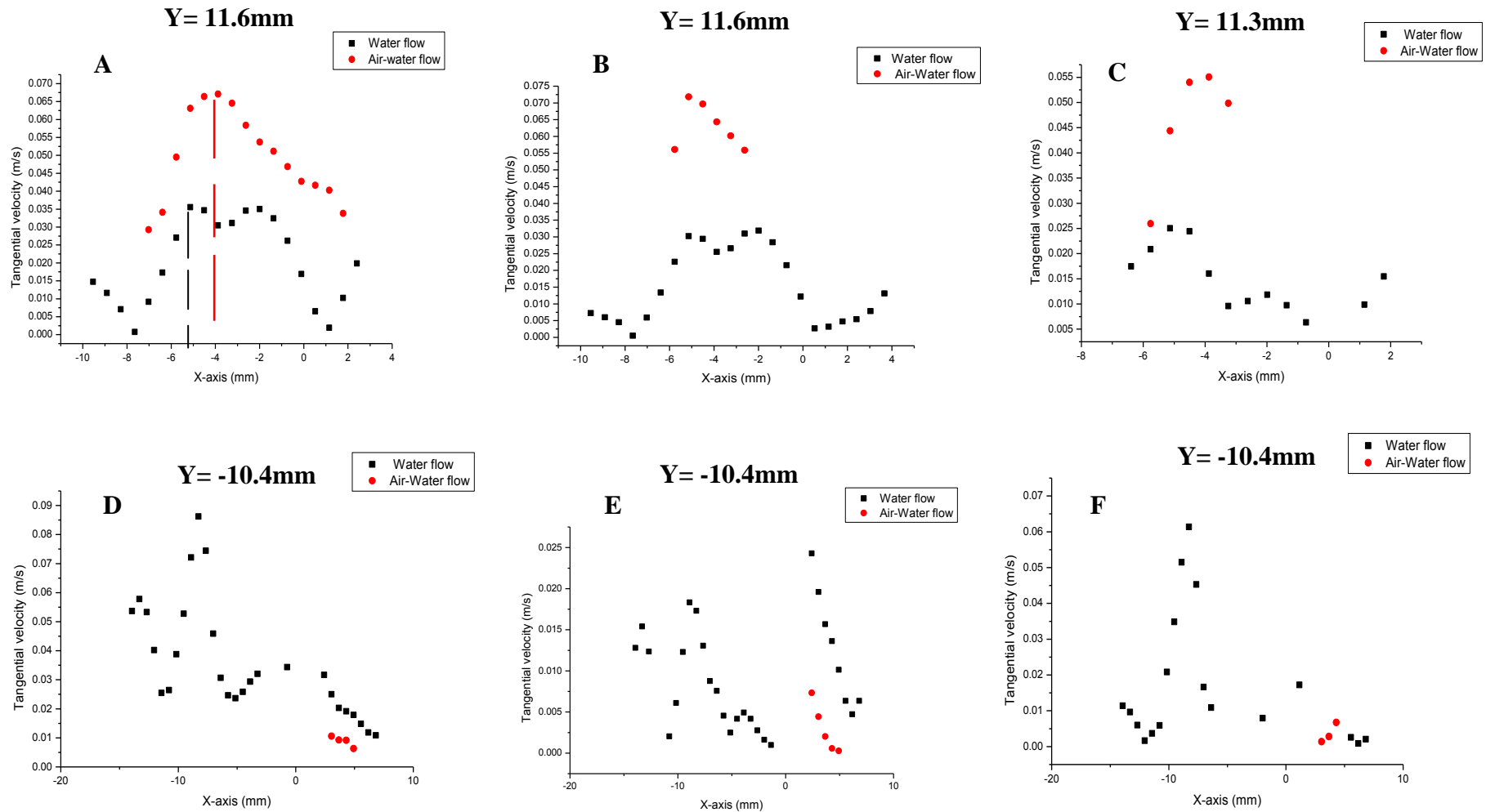


Figure 6.4: Profiles of the Mean Tangential Velocity for Water Flow and Air-Water Flow at $Z = 295$ mm Axial Position;
A: 12.3 litre/min (water), 2.7 litre/min (air); **B:** 11.76 litre/min (water), 2.7 litre/min (air); **C:** 11.1 litre/min (water), 2.7 litre/min (air);
D: 9.48 litre/min (water), 2.7 litre/min (air); **E:** 8.88 litre/min (water), 2.7 litre/min (air); **F:** 7.92 litre/min (water), 2.7 litre/min (air)

6.1.2 Axial Velocity

Figures 6.5-6.7 show the relationship between the mean axial velocity profiles of the water and air-water flow fields at $Z = -395\text{mm}$, -75 mm and 295mm respectively. In Figure 6.5 (A, B and C), the axial velocity profiles of the water and air-water flow fields consist of an upward flow pattern at the centre of the tube and a downward flow pattern closer to the wall. As can be seen in Figure 6.5 (D, E and F), the axial velocity profile of the water-only flow clearly indicate the presence of an upward flow at all x-axis coordinates. However, the axial velocity profiles of the air-water flow indicate the presence of upward and downward flow regions at the centre of the tube and near the wall respectively.

Figure 6.5 (A-C) also shows an increase in the values of the downward air-water flow at positive values of the x-axis in comparison with those of the water-only flow. Figure 6.5(A) shows that the maximum downward water velocity at a positive x value of is 0.06m/s , and for the air-water flow it is 0.13m/s . However, at negative values of the x-axis, there is a decrease in the values of downward air-water flow in comparison with that of the water-only flow. For example, the maximum downward water velocity at a negative value of x-axis is 0.25m/s , and for the air-water flow it is 0.15m/s .

From Figure 6.5(D-E), the values of the downward air-water flow are smaller at positive values of the x-axis compared with those of the water-only flow. For example, Figure 6.5(E) shows that the maximum downward air-water flow at a positive value of the x-axis is 0.06m/s , and for the water flow it is 0.14m/s . However, at negative values of the x-axis, the values of downward air-water flow are larger than those of the water-only flow. For example, the maximum downward air-water flow in Figure 6.5(E) at a negative value of x-axis is 0.16m/s , and for the water flow it is 0.1m/s .

Figure 6.6 (B-F) reveals that the axial velocity flow profiles consist of an upward flow at the centre of the tube and a downward flow at the wall. The value of the axial velocity of the air-water flow is greater than that of the water-only flow at all x-axis coordinates. This shows that the magnitude of axial velocity profiles increases with the flow rate of fluid at the inlet. For example, the flow rate of air-water is greater than that of the water-only flow for all experimental conditions.

Figure 6.7(A) shows that the axial velocity profiles of both the water and air-water fields show an upward flow region at the centre and a downward region at the wall for negative values of the x-axis. The value of the air-water axial velocity is greater than that of the water-only flow at the centre of the tube, but gradually decreases close to the wall. In Figure 6.7 (B-C), the axial velocity profiles of the air-water and water-only flows are observed to be directed upward as we move away from the centre of the tube to the negative x-axis. The addition of air to the water flow field results in an increase in the magnitude of the axial velocity profile of the air-water flow on comparison with that of the water-only flow.

It can be seen from Figure 6.7 (D-F) that a meaningful comparison between the axial velocity profiles of the water and air-water flow fields could not be established due to insufficient experimental data for the air-water flow. Figures 6. 5 to 6.7 shows a decrease in values of the velocity near the walls and this satisfy no slip boundary conditions.

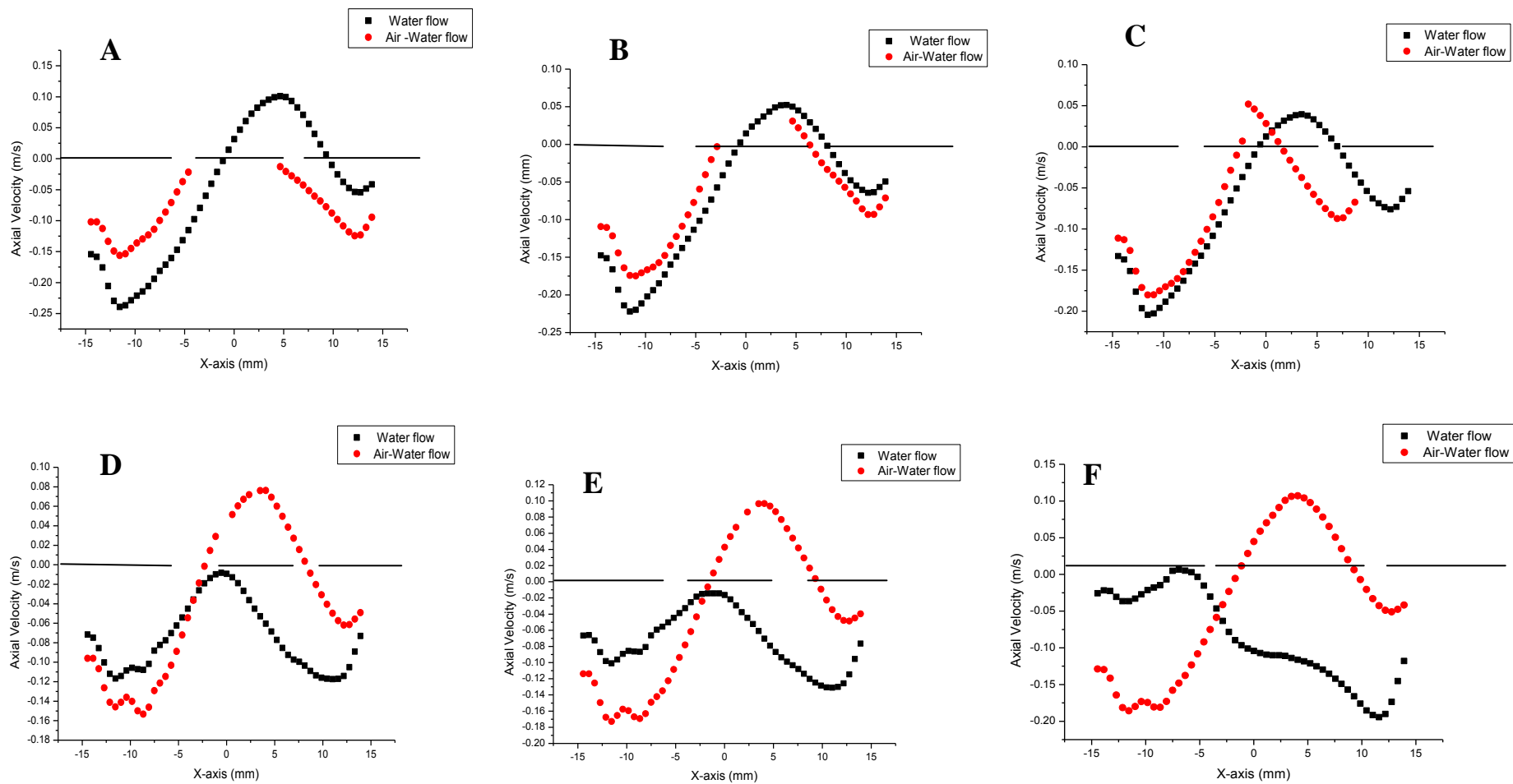


Figure 6.5: Profiles of the Mean Axial Velocity for Water Flow and Air-Water Flow at $Z = -395$ mm Axial Position;

A: 12.3 litre/min (water), 2.7 litre/min (air); **B:** 11.76 litre/min (water), 2.7 litre/min (air); **C:** 11.1 litre/min (water), 2.7 litre/min (air);
D: 9.48 litre/min (water), 2.7 litre/min (air); **E:** 8.88 litre/min (water), 2.7 litre/min (air); **F:** 7.92 litre/min (water), 2.7 litre/min (air)

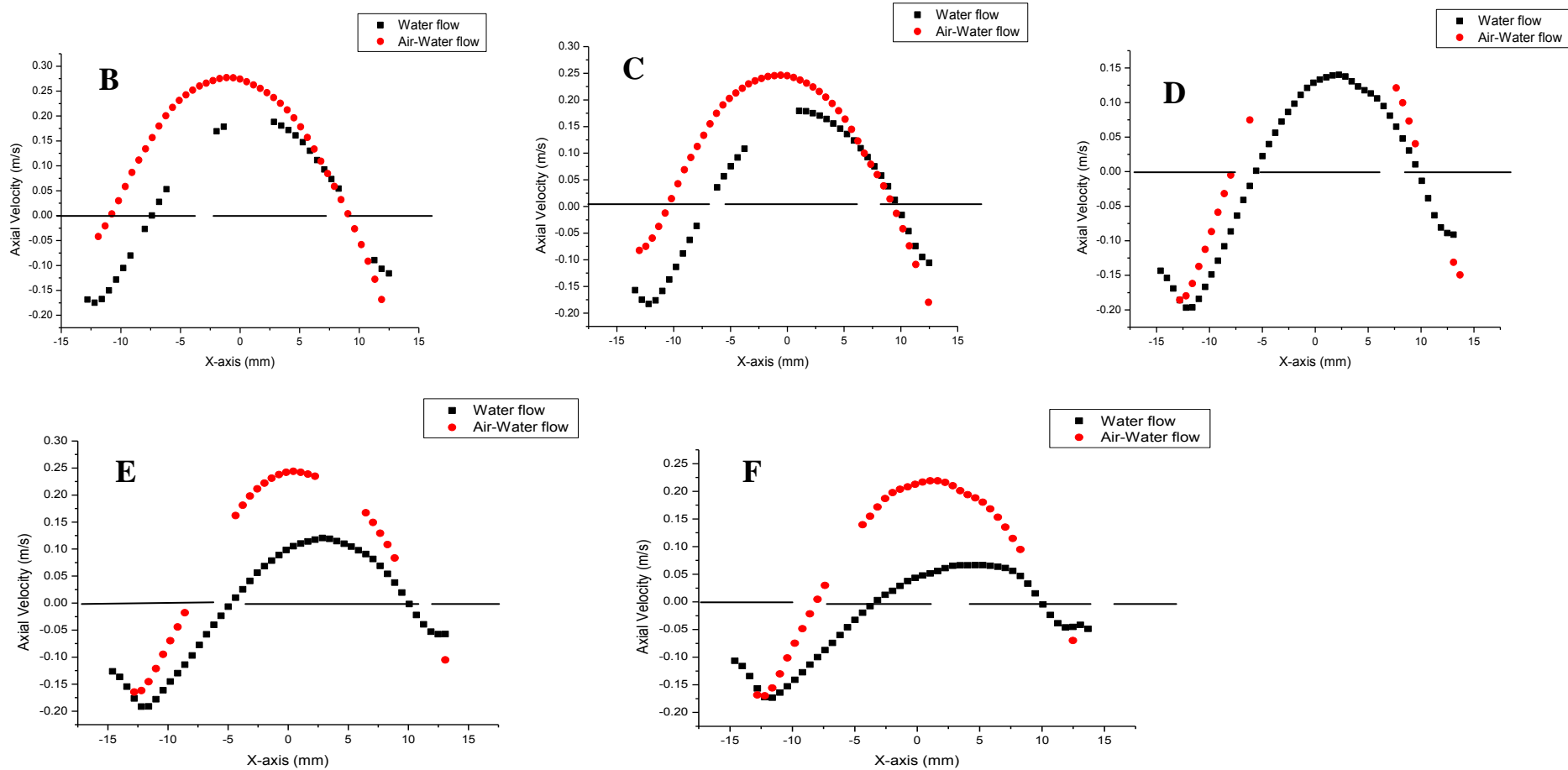


Figure 6.6: Profiles of the Mean Axial Velocity for Water Flow and Air-Water Flow at $Z = -75$ mm Axial Position;

B: 11.76 litre/min (water), 2.7 litre/min (air);

C: 11.1litre/min (water), 2.7 litre/min (air);

D: 9.48 litre/min (water), 2.7 litre/min (air);

E: 8.88 litre/min (water), 2.7 litre/min (air);

F: 7.92 litre/min (water), 2.7 litre/min (air)

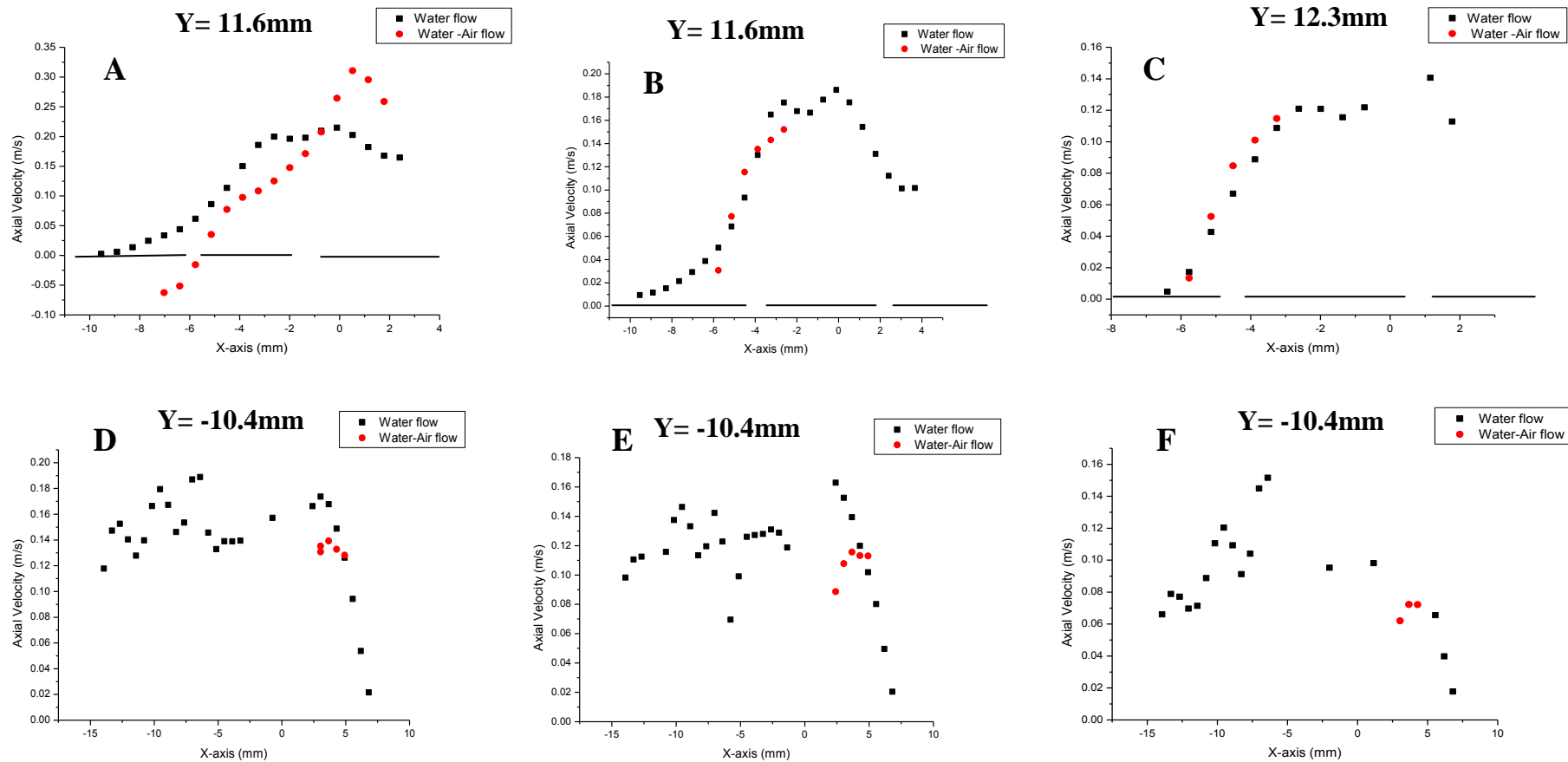


Figure 6.7: Profiles of the Mean Axial Velocity for Water Flow and Air-Water Flow at $Z = 295$ mm Axial Position;
A: 12.3 litre/min (water), 2.7 litre/min (air); **B:** 11.76 litre/min (water), 2.7 litre/min (air); **C:** 11.1 litre/min (water), 2.7 litre/min (air);
D: 9.48 litre/min (water), 2.7 litre/min (air); **E:** 8.88 litre/min (water), 2.7 litre/min (air); **F:** 7.92 litre/min (water), 2.7 litre/min (air)

6.1.3 Radial Velocity

Figures 6.8-6.10 display a graphical comparison between the mean radial velocity profiles of the water and water-air flows at three axial positions in the pipe separator. In Figure 6.8(A-C), the radial velocity profiles of the water-only flow show an inwards directed pattern for all x-axis coordinates. However, the radial velocity profile of the air-water flow shows a combination of an outward pattern as we move away from the centre of the tube and an inward pattern only at the wall on the negative x-axis. Figure 6.8(D and E) show that the radial velocity profiles of water-only flow is directed inwards as we move away from the centre of the tube. However, moving closer to the wall section at positive values of x-axis, an upward flow begins to develop. The radial velocity profile of the air-water flow shows an inward pattern close to the wall and an upward pattern at the centre of the tube. As can be seen in Figure 6.8(A-D), there is an increase in the magnitude of the radial velocity profiles of the air-water flow in comparison to that of the water flow as we move away from the centre of the tube. This was expected, since radial velocity is found to be directly proportional to the flow rate of fluid at the inlet.

In Figure 6.8(F), the radial velocity profiles of both the water and air-water flow fields indicate an inward flow pattern at the wall and an outward flow pattern at the centre of the tube. At small water flow rates, it was observed that the value of radial velocity for the water-only flow is larger than that of air-water flow at all the x-axis coordinates.

As can be seen in Figure 6.9 (B-F), the radial velocity profiles of both the water and air-water flow fields are found to be directed outwards at all x-axis coordinates. In Figure 6.9 (B and C), the magnitude of the radial velocity profile for the air-water flow is found to be larger than that of the water flow at negative values of x. However, at positive values of x, the magnitude of the radial velocity profile for the air-water flow is smaller than that of the water flow. Figure 6.9 (D-F) shows that the magnitude of the radial velocity profiles for the air-water flow is observed to be greater than that for the water flow as we move away from the centre of the tube.

In Figure 6.10(A-B), the radial velocity profiles of both the water and air-water flows show an inward flow pattern as we move away from the centre of the tube.

The magnitude of radial velocity profiles for the air-water flow is observed to be larger than that of water only flow. For example, Figure 6.10(A) shows that the maximum radial velocity for the air-water is 0.25m/s whereas for the water-only flow, it is 0.23m/s.

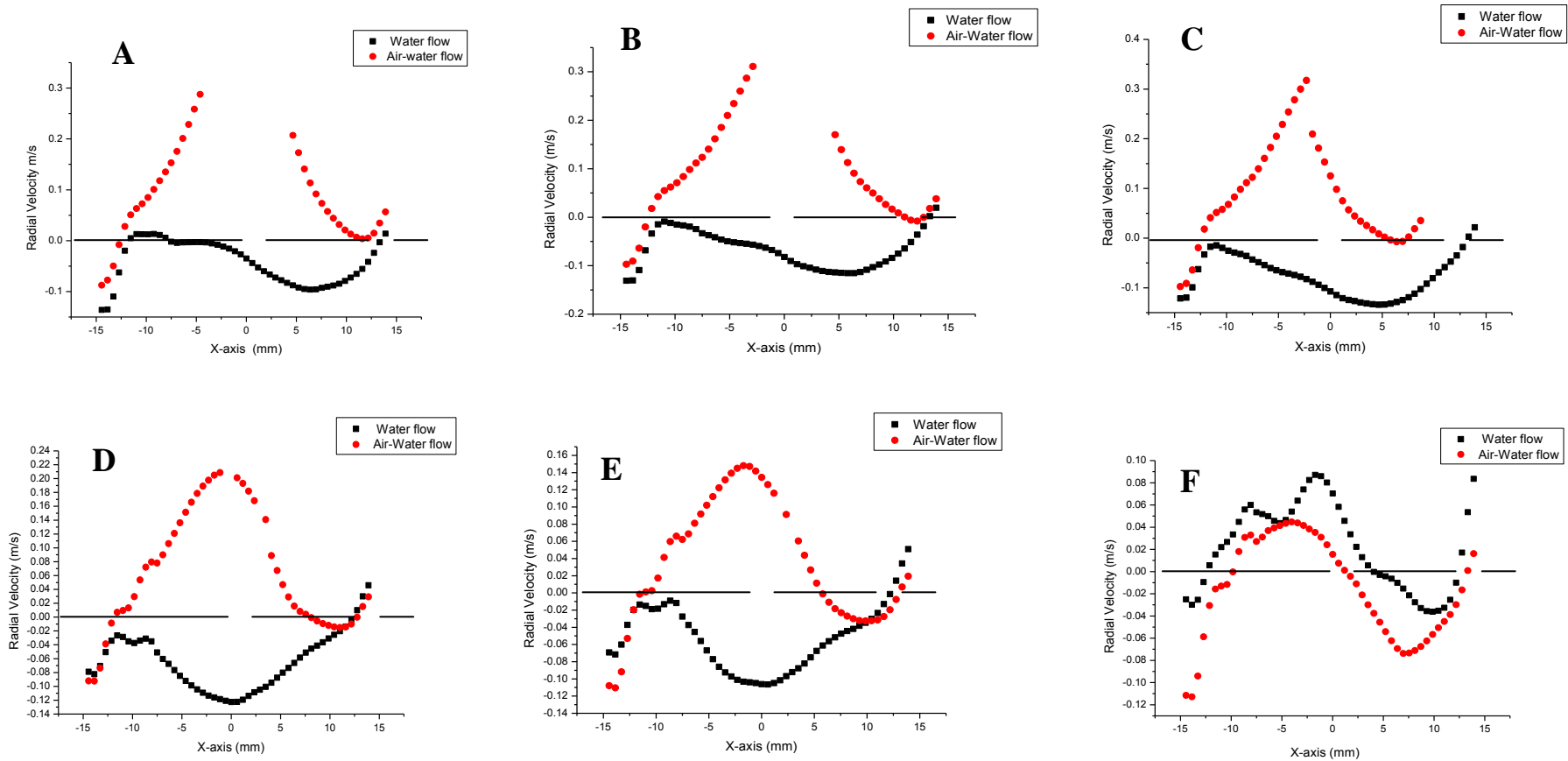


Figure 6.8: Profiles of the Mean Radial Velocity for Water Flow and Air-Water Flow at $Z = -395$ mm Axial Position;
A: 12.3 litre/min (water), 2.7 litre/min (air); **B:** 11.76 litre/min (water), 2.7 litre/min (air); **C:** 11.1 litre/min (water), 2.7 litre/min (air);
D: 9.48 litre/min (water), 2.7 litre/min (air); **E:** 8.88 litre/min (water), 2.7 litre/min (air); **F:** 7.92 litre/min (water), 2.7 litre/min (air)

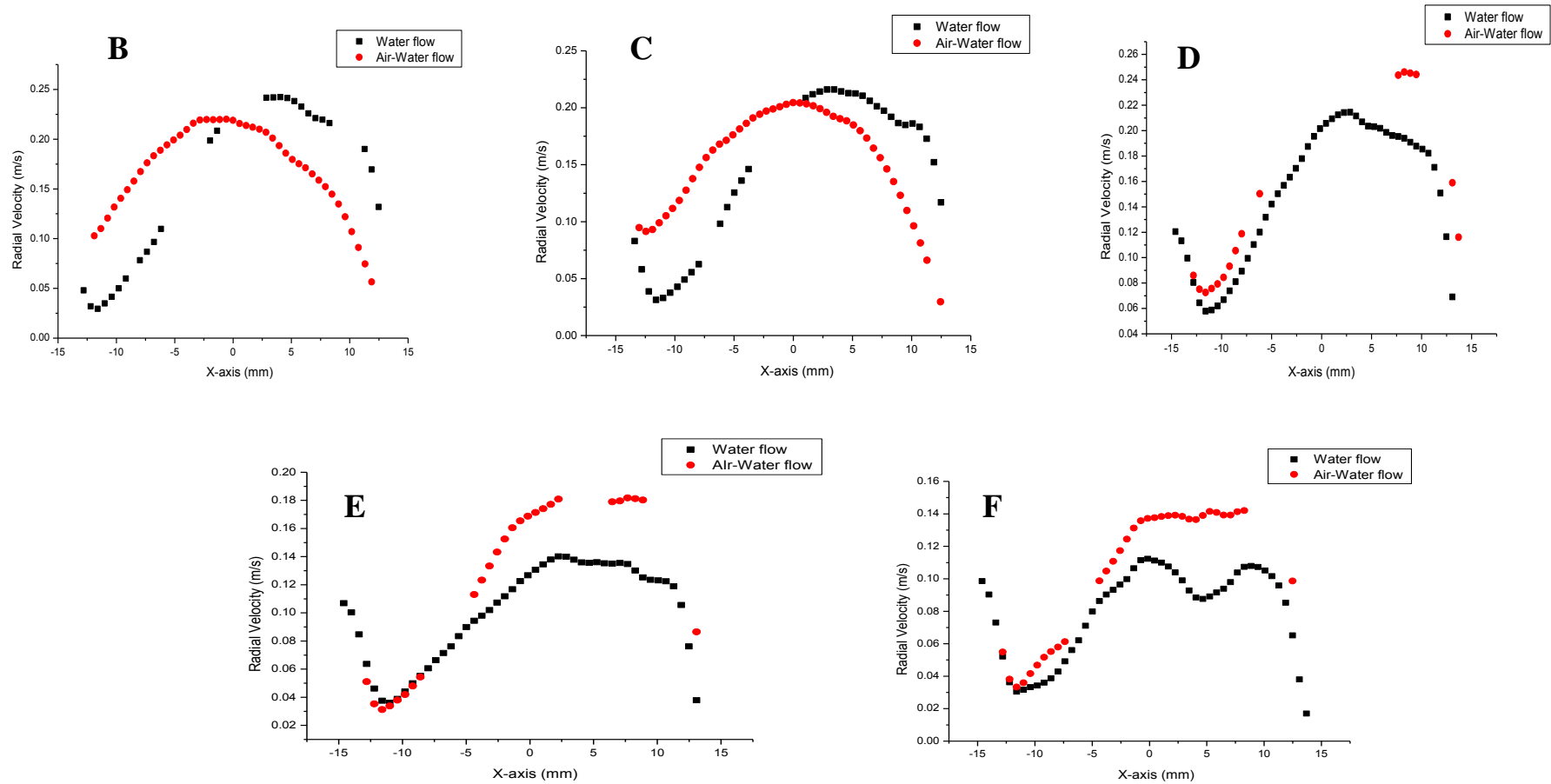


Figure 6.9: Profiles of the Mean Axial Velocity for Water Flow and Air-Water Flow at $Z = -75$ mm Axial Position;

B: 11.76 litre/min (water), 2.7 litre/min (air);

C: 11.1 litre/min (water), 2.7 litre/min (air);

D: 9.48 litre/min (water), 2.7 litre/min (air);

E: 8.88 litre/min (water), 2.7 litre/min (air);

F: 7.92 litre/min (water), 2.7 litre/min (air)

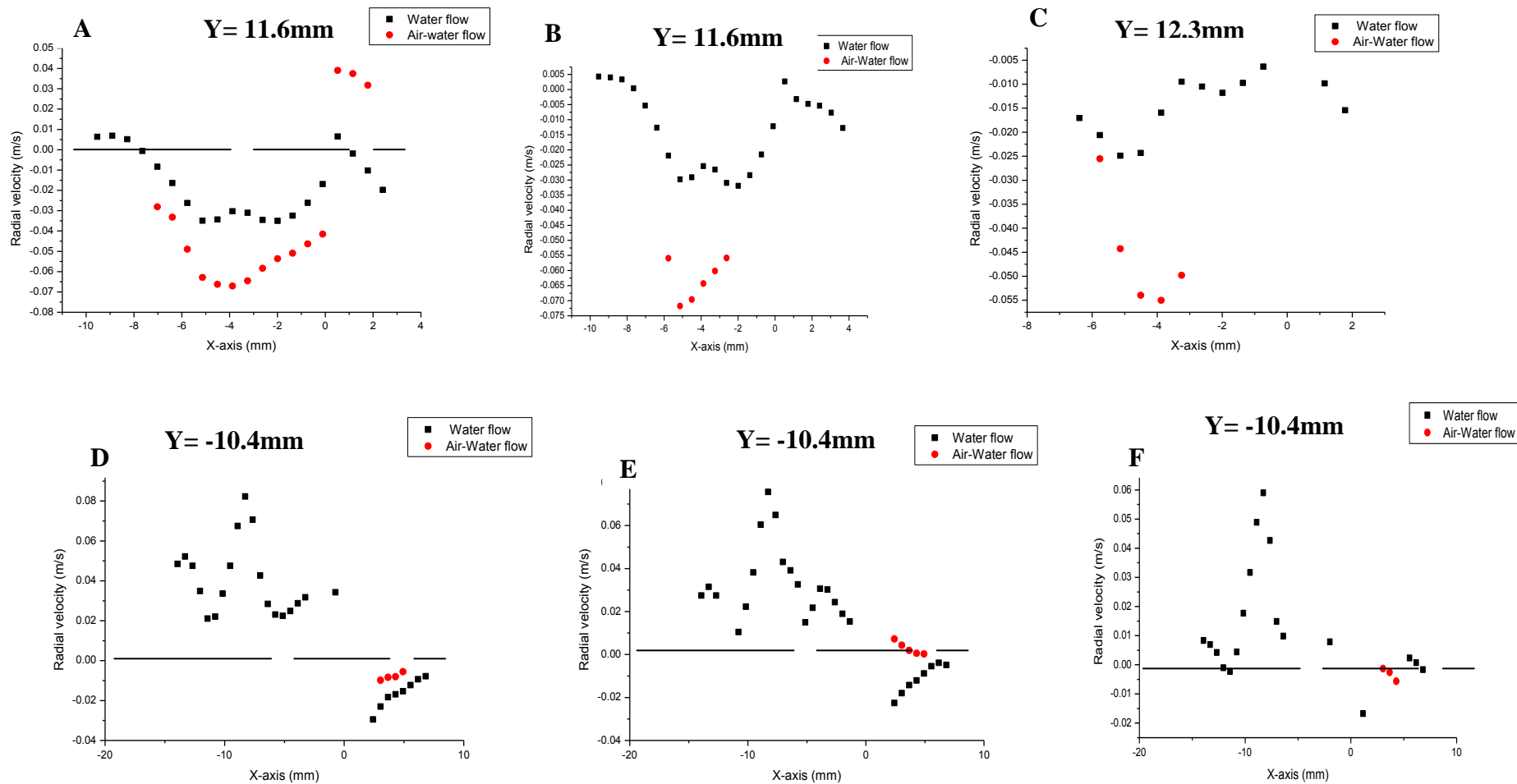


Figure 6.10: Profiles of the Mean Radial Velocity for Water Flow and Air-Water Flow at $Z = 295\text{ mm}$ Axial Position;

A: 12.3 litre/min (water), 2.7 litre/min (air); **B:** 11.76 litre/min (water), 2.7 litre/min (air); **C:** 11.1 litre/min (water), 2.7 litre/min (air);

D: 9.48 litre/min (water), 2.7 litre/min (air); **E:** 8.88 litre/min (water), 2.7 litre/min (air); **F:** 7.92 litre/min (water), 2.7 litre/min (air)

6.2 Effect of Air Volume Fraction on the Velocity Field

In this section, the effect of changes in the volume fraction of air on the velocity profile of the air-water flow in a pipe separator is considered. The volume fraction of the air flow varied between 18% and 25.42%. Comparisons of the effect of the air volume fraction on the velocity field profiles as obtained by the SPIV technique at the three axial positions of $Z = -395$ mm, -75 mm and 295 mm are shown in Figures 6.11-6.13.

Figure 6.11(A-C) shows the effect of air volume fraction on the averaged tangential velocity in the pipe separator. It can be observed that the tangential velocity of the air-water flow at the $Z = -395$ mm and -75 mm axial positions increases as we move away from the centre of the tube, reaching a maximum and then decreasing close to the wall. The tangential velocity profiles presented in Figure 6.11(A-B) show that the magnitude of this parameter increases at any x-axis coordinate as the air volume fraction decreases. This is expected, since tangential velocity is found to increase with water volume fraction. However, there is no significant difference in the tangential velocity flow pattern. As shown in Figure 6.11(C), the maximum tangential velocity of the air-water flow increases with air volume fraction at the inlet.

Figure 6.12(A-C), shows the effect of air volume fractions on the mean axial velocity at the three axial positions. The axial velocity profiles show an upward flow region at the centre of the tube and a downward flow region at the wall. These profiles, however, do have similar shapes. That is, a difference in air volume fraction does not affect the axial velocity flow pattern. Figure 6.12(A) shows that the magnitude of the axial velocity profiles increases with an increase in air volume fractions in the upward flow region. At positive values of the x-axis, axial velocity decreases with increasing air volume fractions. However, at negative values of the x-axis, axial velocity increases with air volume fraction.

Figure 6.12(B) shows that the magnitude of the axial velocity profiles increases with air volume fraction as we move away from the centre of the tube. However, close to the wall at positive x-axis coordinates the magnitude of the axial velocity profiles increases with the volume fraction of air.

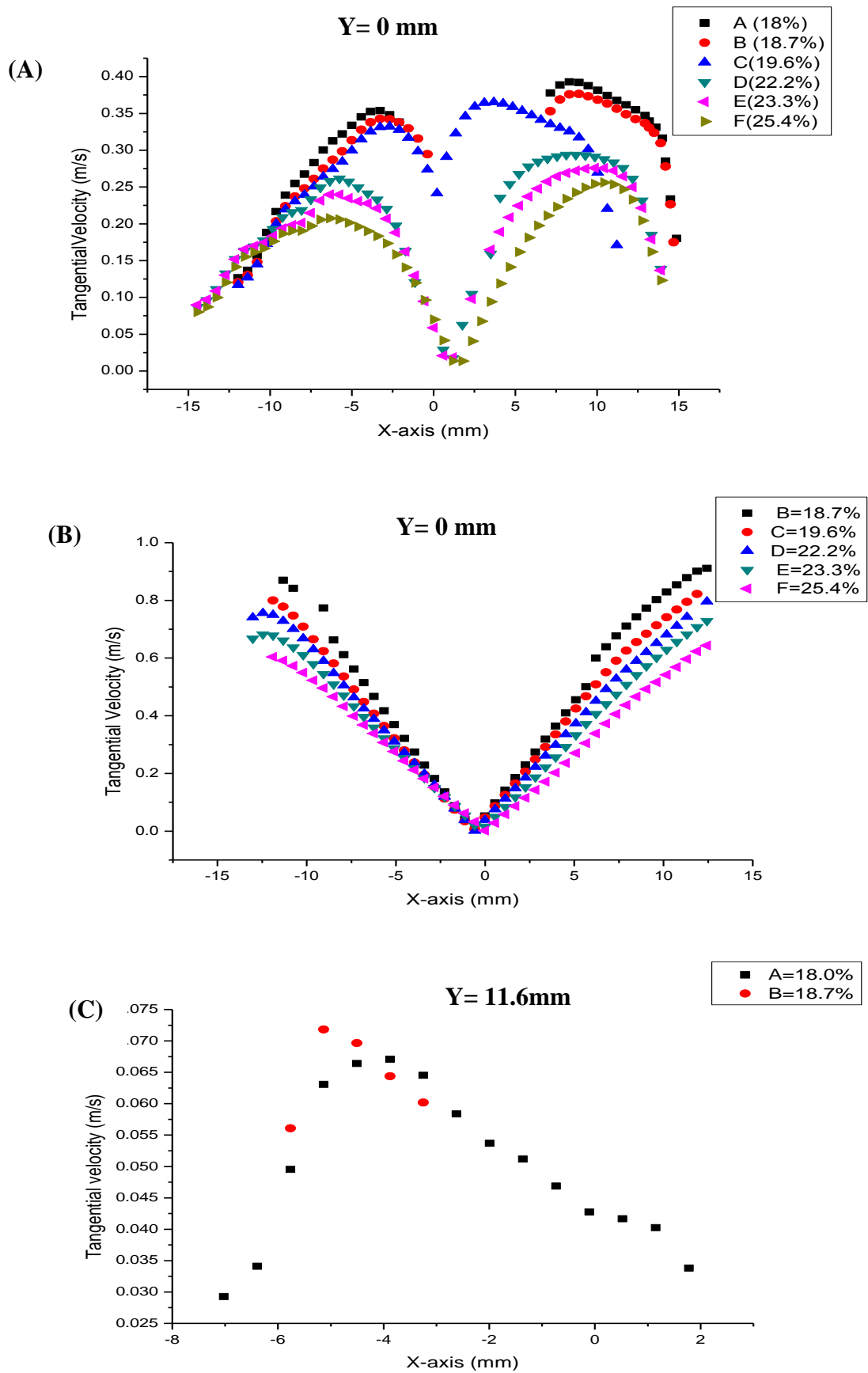


Figure 6.11: Effect of Air Volume Fraction on the Averaged Tangential Velocity of Water-Air Flow at Axial Positions of (A) $Z=-395\text{mm}$ (B) $Z=-75\text{mm}$ (C) $Z=295\text{mm}$.

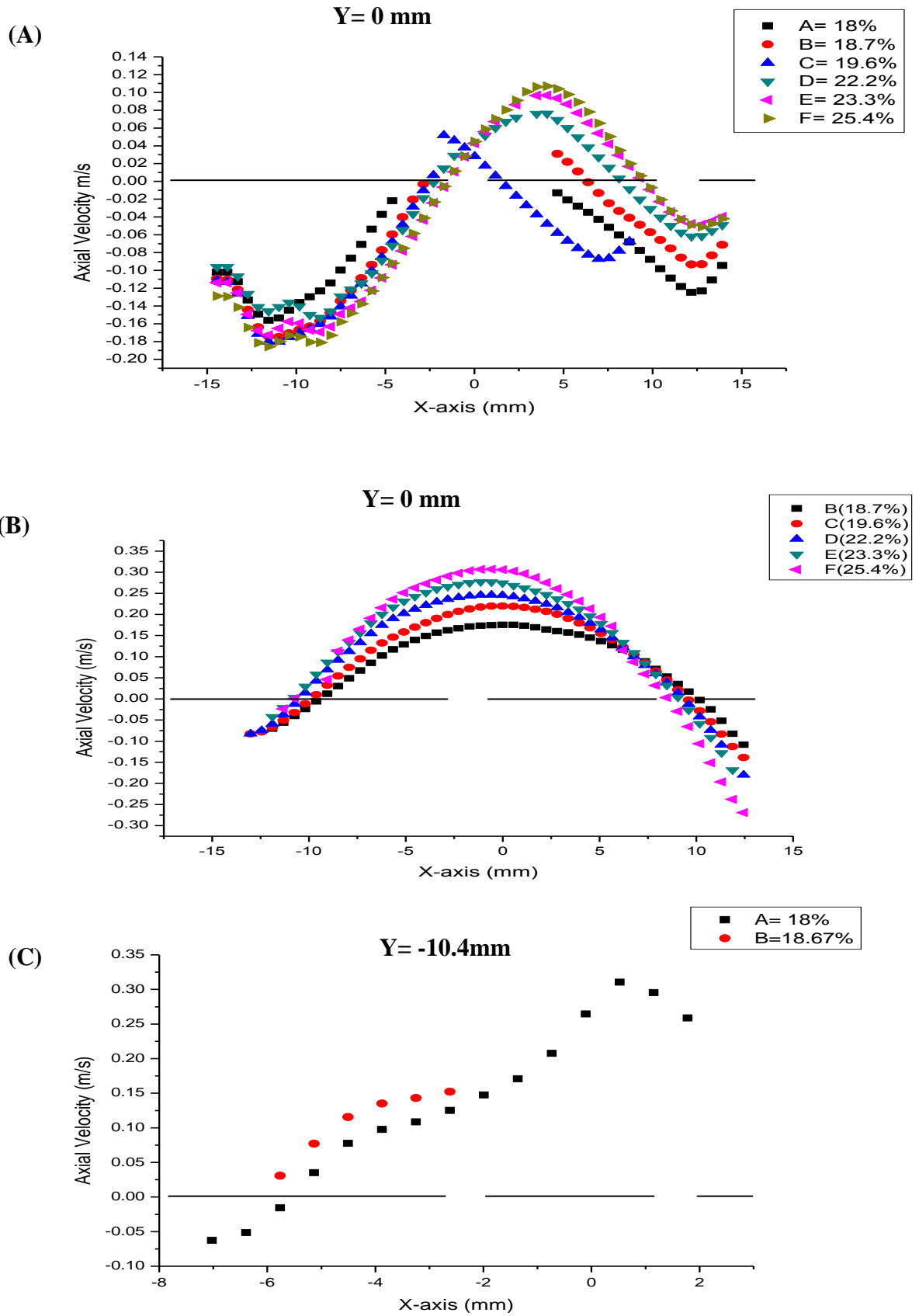


Figure 6.12: Effect of Air Volume Fraction on the Averaged Axial Velocity of Water-Air Flow at Axial Position of (A) $Z=-395$ mm (B) $Z=-75$ mm (C) $Z=295$ mm.

The axial velocity profiles presented in Figure 6.12(C) show that the magnitude of axial velocity increases with air volume fraction at the inlet. Therefore, we can conclude that the axial velocity magnitude is dependent on the flow rate at the inlet of the separator.

Figures 6:13 (A-C) shows the mean radial velocity field plotted as a function of air volume fraction. As shown in Figure 6.13(a), the magnitude of radial velocity decreases with an increase in the air volume fraction at all x-axis coordinates. Figure 6.13(B) shows that the magnitude of radial velocity profiles decreases with increasing air volume fraction at the centre of tube and at positive x-axis coordinates. However, Figure 6.13(C) shows that the magnitude of radial velocity profile first decrease, then-after increase at negative values of the x-axis as air volume fraction increases. The shapes of the radial velocity profiles are observed to be unaffected by different air volume fractions at the inlet. Therefore, we can conclude that, radial profiles are essentially independent of the air volume fraction at the inlet.

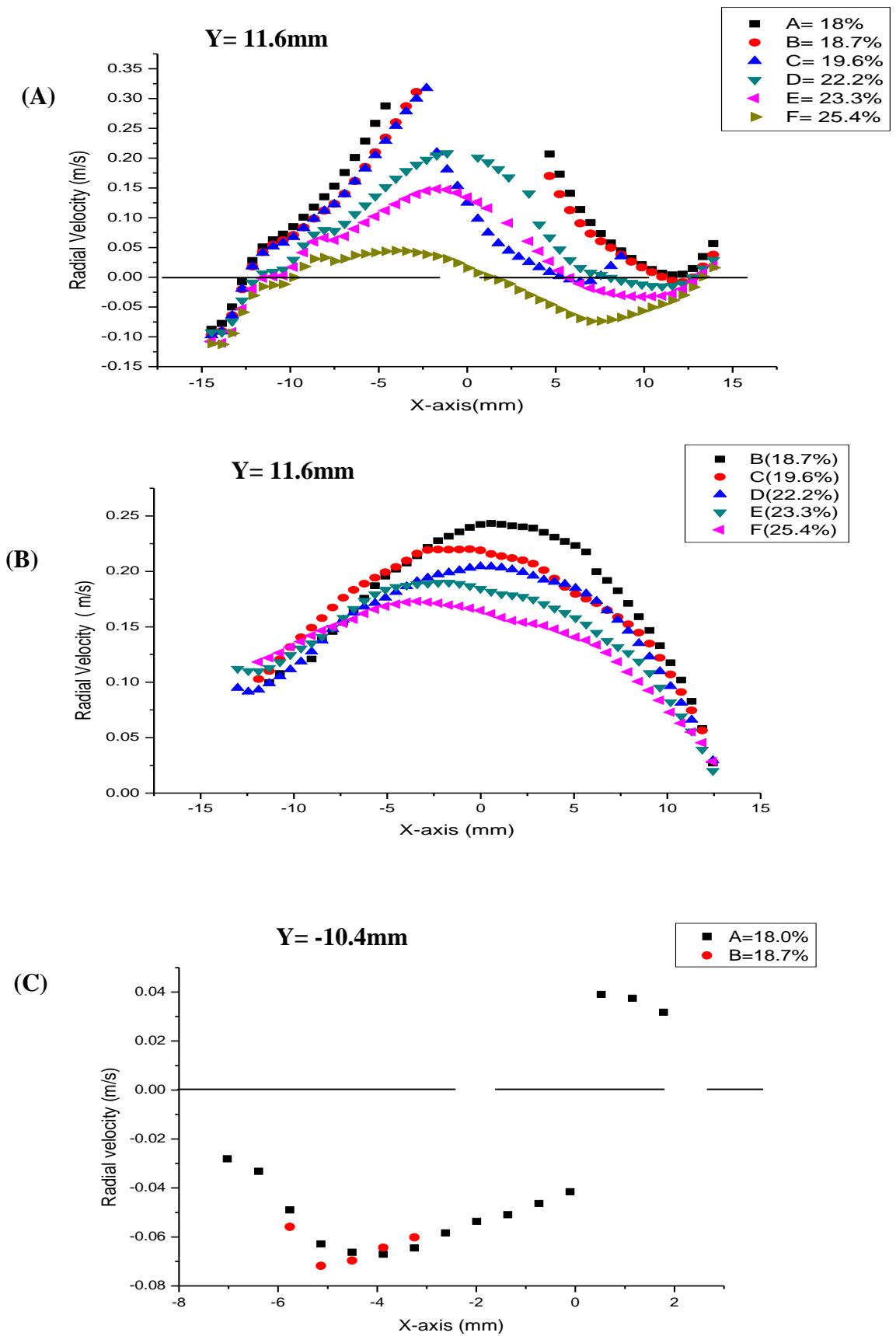


Figure 6.13: Effect of Air Volume Fraction on the Averaged Radial Velocity of Water-Air flow at Axial Positions of (A) $Z=-395$ mm (B) $Z=-75$ mm (C) $Z=295$ mm.

6.3 Comparison of the Numerical Simulation of the Velocity Field with the Experimental Measurements

In this section, comparison are made between the CFD simulation of the air-water flow and the experimental data obtained using the Stereoscopic PIV technique at the three different axial positions of $Z= -395\text{mm}$, 75mm and 295mm . Data for this comparison was collected at the same locations as shown in Figure 5.1 for $Z=-395\text{mm}$ and -75mm and in Figure 6.1 for $Z=295\text{mm}$. The numerical simulation used a Eulerian-Eulerian multiphase flow model for the air-water flow and the Reynolds Stress Model to capture the anisotropic turbulence features within the pipe separator, as described in section 4.4.3.

6.3.1 Tangential Velocity

Figures 6.14-6.16 show the comparison between the mean tangential velocity profiles obtained by SPIV measurements and the CFD simulations at axial position of $Z=-395\text{mm}$, -75mm and 295 axial positions respectively. These comparisons show that the tangential velocity distributions inside the pipe separator are symmetry and increases with distance from the centre of the tube, reaching a peak value and thereafter decreases close to the wall. The tangential velocity profiles indicate that the tangential flow is characterized by a forced- vortex close to the centre and a free vortex-type as we move close to the wall. A general feature of this comparison is that the shapes of the experimental and simulated tangential velocity profiles are similar.

As can be seen in Figure 6.14(A-C), the CFD simulation under-predicted the tangential velocity profiles moving away from the centre of the tube. For example, Figure 6.14(B) shows that the measured tangential velocity was 0.29m/s at $x= -2.5\text{mm}$. However, the CFD prediction at this point is 0.25m/s . Towards the wall; however the computational model over-predicted the tangential velocity profile on comparison with the experimental data. For example, Figure 6.14(C) shows that the predicted tangential velocity is 0.24m/s at $x= -10\text{mm}$. However, the experimental result at $x= -10\text{mm}$ was 0.20m/s .

The predicted tangential velocity profiles in Figure 6.14(D-F) generally display good quantitative agreement with experimental results as we move close to the centre of the tube.

The computed mean tangential velocity profiles agreed to within $\pm 1\%$ for the majority of the measured values at the centre of the tube. However, moving close to the wall, the simulation results are observed to over-predict mean tangential velocity as seen in Figure 6.14(D). In the same manner, Figure 6.14(E-F) show that, close to the wall, the predictions are higher at negative values of the x-axis and lower at positive values.

The tangential velocity profiles presented in Figure 6.14(A-D) show that free vortex region begins at larger values of the x-axis in the simulation results. For example, Figure 6.14(C) shows that the maximum tangential velocity from the experimental data occurs at $x = 2.5$ mm and -3.5 mm. However, from the simulation results it occurs at $x = 7.5$ mm and -5.5 mm. In Figure 6.14(E-F), in the simulation results the free vortex region begins at smaller values of the x-axis. For example, Figure 6.14(F) shows that the maximum tangential velocity from the experimental results result occurs at $x = 10.25$ mm and -6.75 mm, whereas in the simulation it occurs at $x = 7.5$ mm and -4.5 mm.

In Figure 6.15(B-F), the predicted tangential velocity profiles give good qualitative agreement when compared with the experimental measurements at the centre of the tube. The best agreement occurred at the inner core, $x = \pm 5$ mm, where the prediction was within 5% of the experimental profile for the majority of values of the x-axis at the centre of the tube. However, moving closer to the wall, the simulation is observed to under-predict the tangential velocity. For example, Figure 6.15(C) shows that the maximum tangential velocity for the experimental profile is 0.78m/s, but in the simulation it is 0.58m/s. The biggest discrepancy, as shown in Figure 6.15 (F) occurred at $x = 10$ mm, where the computational model under-predicted the tangential velocity by 35%. As can be seen in Figure 6.15 (B-F), the simulated free vortex region begins at the same radius when compared with the experimental data. For example, Figure 6.15(C) shows that the free vortex region in both the simulation and experimental profiles starts at $x = -11.75$ mm.

Figure 6.16 (A-C) shows that the values of the measured and predicted tangential velocity increase as we move away from the centre to the negative values of the x-axis, reaching a maximum value and then gradually decreasing close to the wall. The CFD simulation result is here found to over-predict when compared to the experimental data.

For example, Figure 6.16(C) shows that the maximum tangential velocity for the experimental data is 0.05m/s. However, the simulation result indicates that the maximum tangential velocity is 0.225m/s.

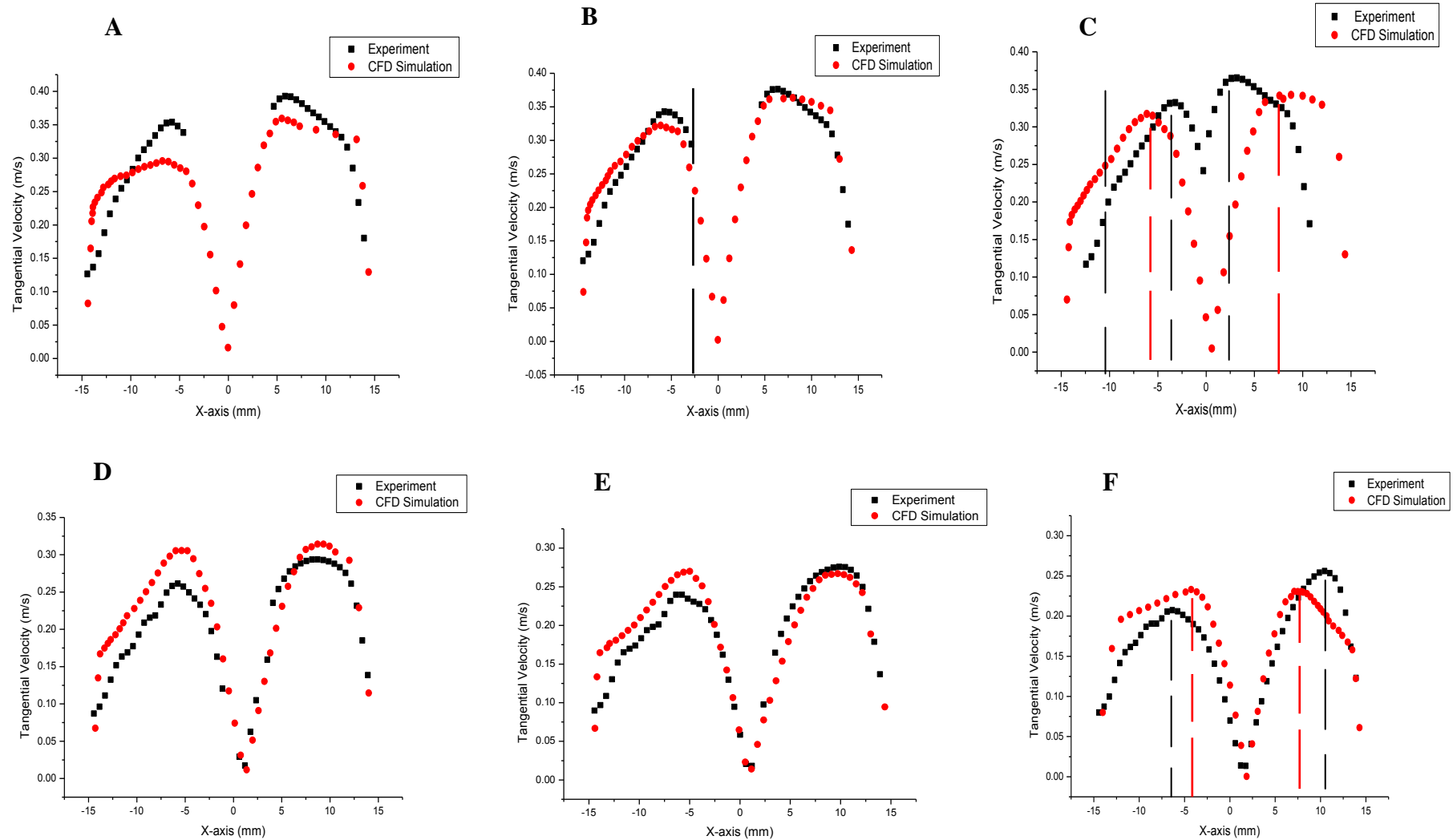


Figure 6.14: Comparison of the CFD Results with Experimental Data for Mean Tangential Velocity of Air-Water Flow at the $Z = -395$ mm Axial Position;
A: 12.3 litre/min (water), 2.7 litre/min (air); **B:** 11.76 litre/min (water), 2.7 litre/min (air); **C:** 11.1 litre/min (water), 2.7 litre/min (air);
D: 9.48 litre/min (water), 2.7 litre/min (air); **E:** 8.88 litre/min (water), 2.7 litre/min (air); **F:** 7.92 litre/min (water), 2.7 litre/min (air)

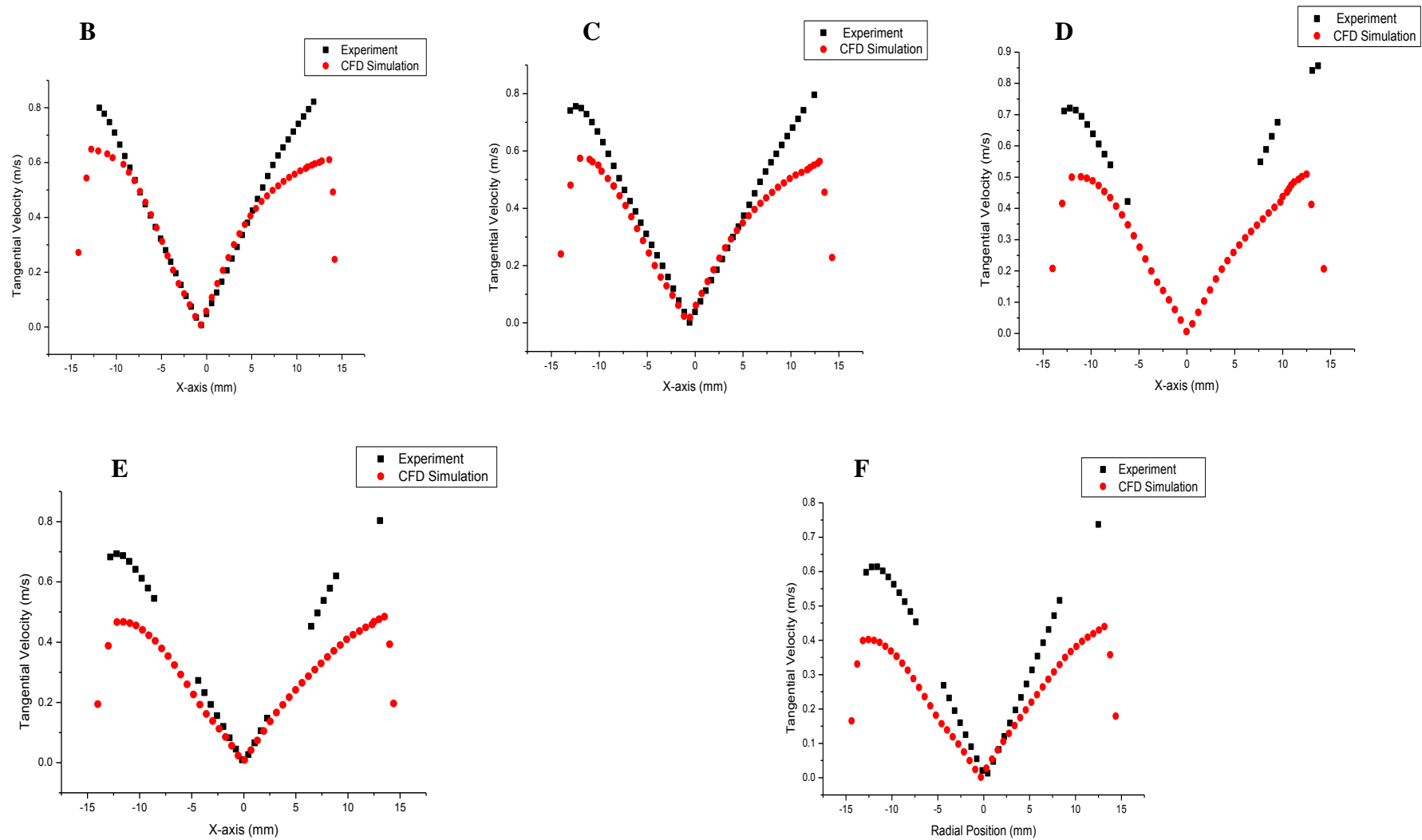


Figure 6.15: Comparison of the CFD Results with Experimental Data for Mean Tangential Velocity of Air-Water Flow at the $Z = -75$ mm Axial Position;
B: 11.76 litre/min (water), 2.7 litre/min (air); **C:** 11.1 litre/min (water), 2.7 litre/min (air); **D:** 9.48 litre/min (water), 2.7 litre/min (air);
E: 8.88 litre/min (water), 2.7 litre/min (air); **F:** 7.92 litre/min (water), 2.7 litre/min (air)

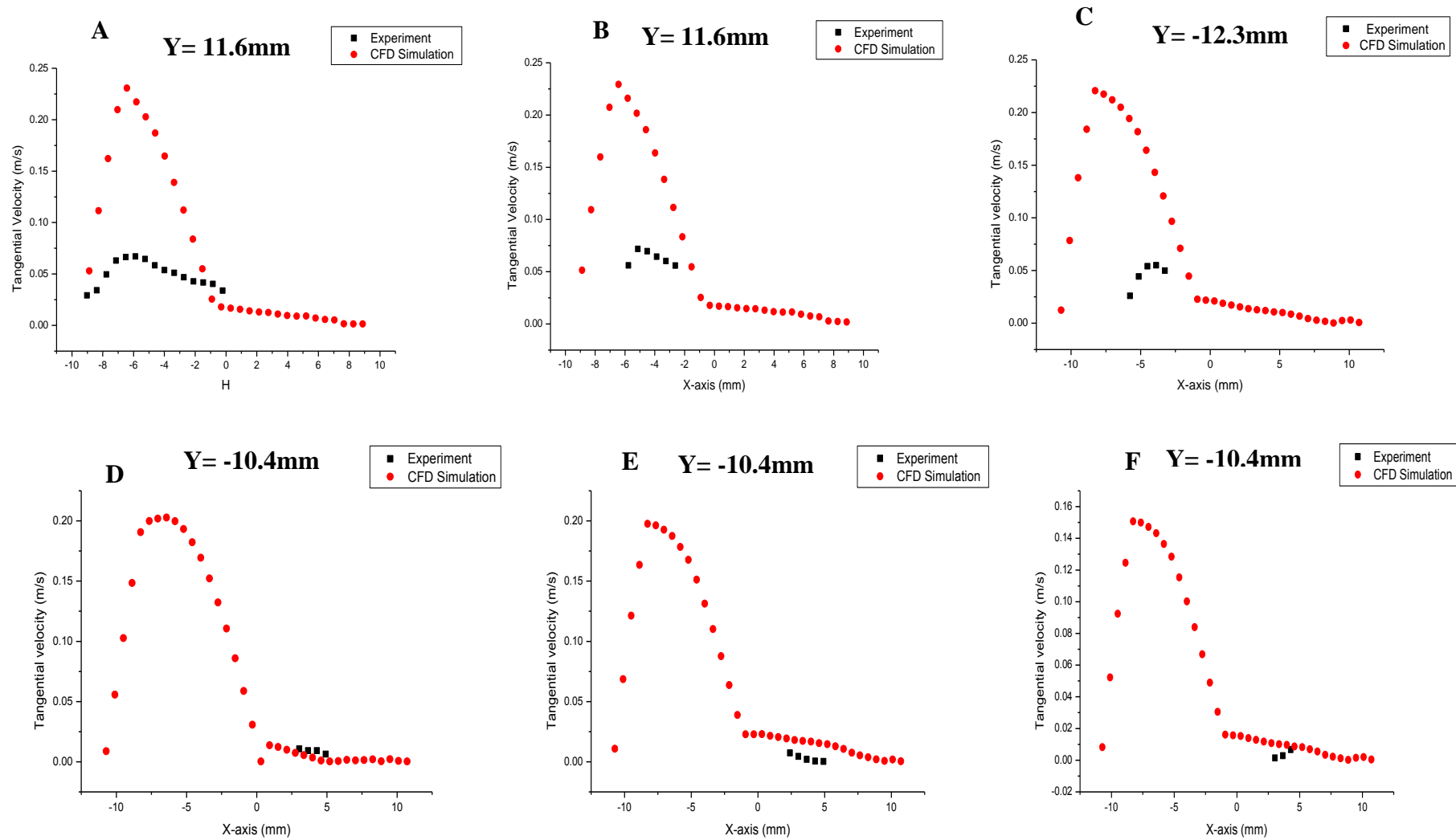


Figure 6.16: Comparison of the CFD Results with Experimental Data for Mean Tangential Velocity of Air-Water Flow at the Z= 295 mm Axial Position;
A: 12.3 litre/min (water), 2.7 litre/min (air); **B:** 11.76 litre/min (water), 2.7 litre/min (air); **C:** 11.1 litre/min (water), 2.7 litre/min (air);
D: 9.48 litre/min (water), 2.7 litre/min (air); **E:** 8.88 litre/min (water), 2.7 litre/min (air); **F:** 7.92 litre/min (water), 2.7 litre/min (air)

6.3.2 Axial Velocity

Figures 6.17-6.19 show the comparison between the mean axial velocity profiles obtained by the CFD simulation and the SPIV measurements. As can be seen in Figure 6.17(A), the measured and experimental axial velocity profiles show a downward flow region at all x-axis coordinates. In the same manner, Figures 6.17(B, C and F) show that the predicted axial velocity profiles are mainly of a downward flow region at all x-axis coordinates. However, the measured axial velocity profiles indicate an upward flow pattern at the centre of the tube and a downward flow pattern at the wall. The predicted and measured axial velocity profiles are shown in Figure 6.17 (D, E), indicating the presence of upward and downward flow regions at the centre of the tube and close to the wall respectively. Therefore, from Figure 6.17 (B, C and F) the computational model fails to predict the upward flow as observed in the measured axial velocity profiles. This disagreement is due to the effect of natural rubber bungs used in experimental measurements to specify the split ratio as a function of mass flow rate passing through each outlet. The flow direction is expected to have changed as the flow reaches the bung at the outlet.

The axial velocity profiles presented in Figure 6.17(A-F) show that the simulation results are generally under-predicted when compared with the experimental data. For example, Figure 6.17(D) shows that the maximum upward axial velocity for the experimental data is 0.08m/s, but in the simulation result it is 0.045m/s. The best correlation between the experimental measurements and the predicted results in Figures 6.17(A-C) was obtained close to the wall region at negative values of the x-axis. Here, agreement was within 5-10%. The same trend is obtained as we move close to the wall at positive values of the x-axis, as shown in Figure 6.17(D-E).

The predicted and measured axial velocity profiles as shown in Figure 6.18 (B-F) indicate the presence of upward and downward flow regions at the centre of the tube and the wall respectively. As can be seen in Figure 6.18 (Band C), the predicted axial velocity profile is found to be greater than the experimental data at the centre of the tube. However, as we move close to the wall, the simulation results are found to under-predict when compared with the experimental data.

The predicted axial velocities agree with the experimental data in Figure 6.18 (D-F) to within approximately $\pm 2\%$ as we move from $x = -5\text{mm}$ to the wall region at negative values of the x -axis. However, moving from $x = -5\text{mm}$ to the wall region at positive values of the x -axis, the simulated profiles are found to under-predict.

In Figure 6.19(A), the measured axial velocity profile is a combination of a downward flow pattern as we move close to the wall at negative values of the x -axis and an upward flow occurring at the centre of the tube. However, the predicted axial velocity profile shows an upward flow pattern at all x -axis coordinates. As can be seen in Figure 6.19 (B, F), the measured and simulated axial velocity profiles indicate an upward flow region at all x -axis coordinates. The computational model over predicts the axial velocity profile when compared with the experimental data. For example, Figure 6.19(B) shows that the experimental result for maximum axial velocity is 0.15m/s , but in the CFD simulation is 0.24m/s .

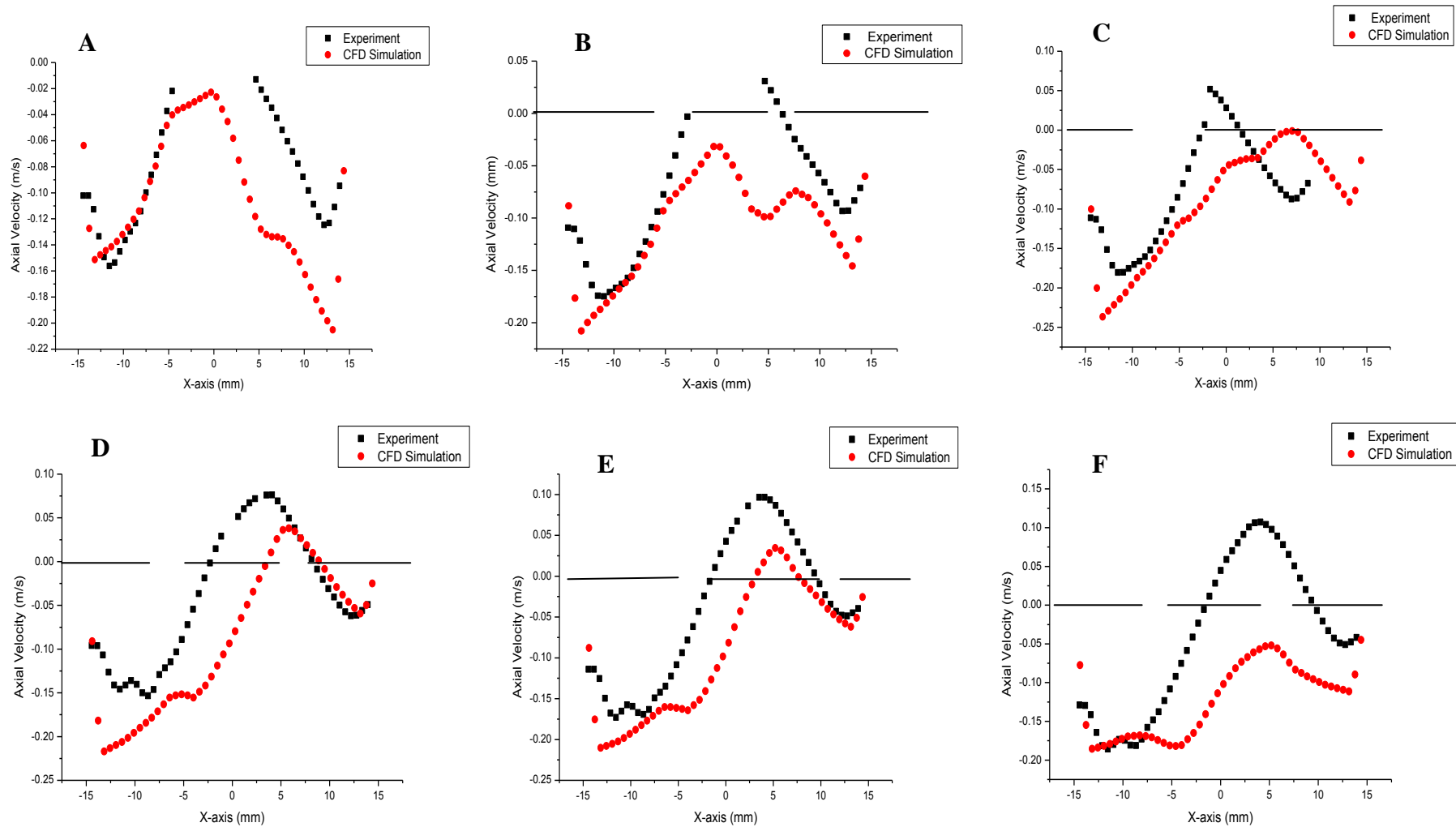


Figure 6.17: Comparison of the CFD Results and Experimental Data for Mean Axial Velocity of Air-Water Flow at the $Z = -395$ mm Axial Position; **A:** 12.3 litre/min (water), 2.7 litre/min (air); **B:** 11.76 litre/min (water), 2.7 litre/min (air); **C:** 11.1 litre/min (water), 2.7 litre/min (air); **D:** 9.48 litre/min (water), 2.7 litre/min (air); **E:** 8.88 litre/min (water), 2.7 litre/min (air); **F:** 7.92 litre/min (water), 2.7 litre/min (air)

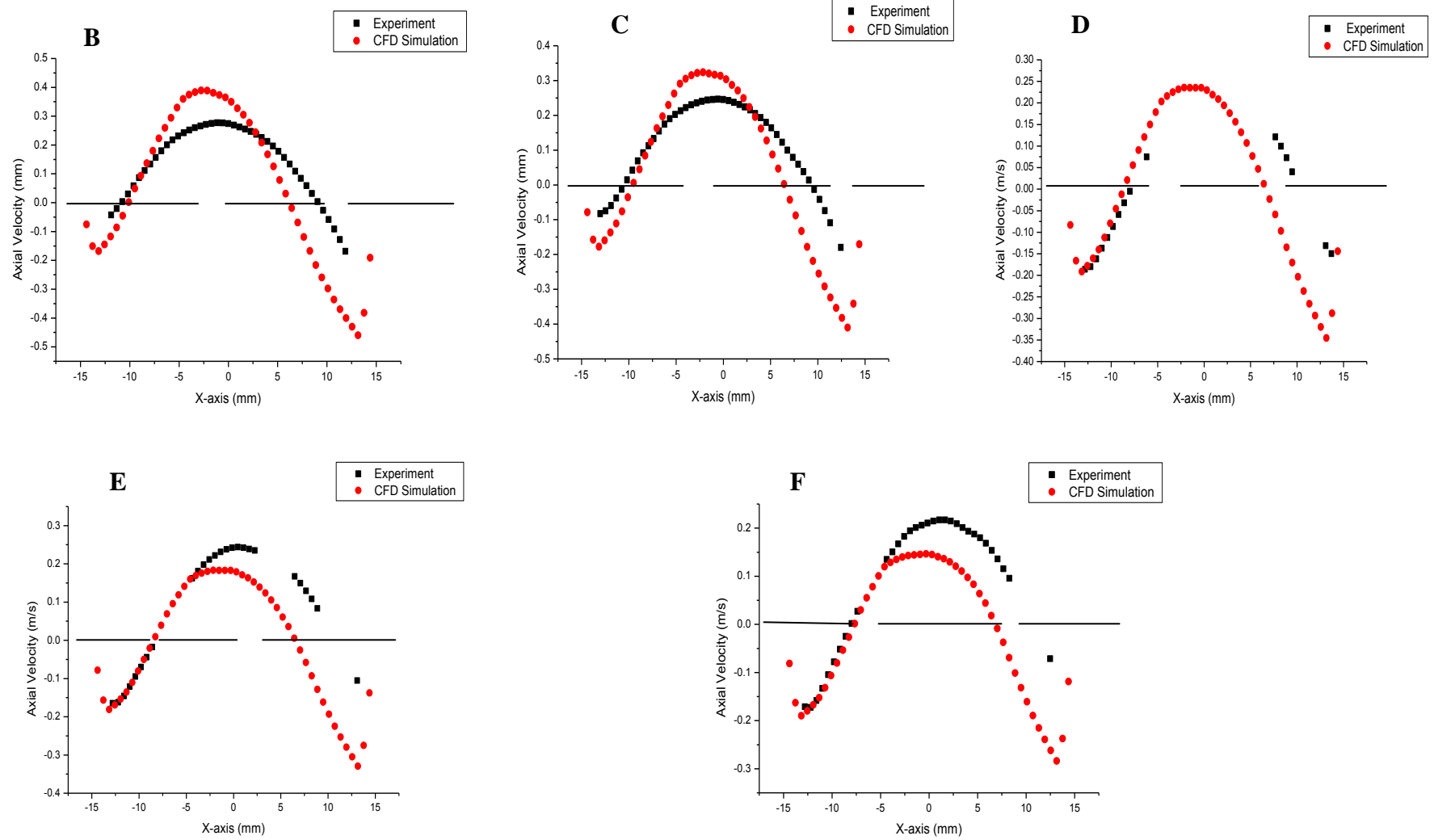


Figure 6.18: Comparison of the CFD Results and Experimental Data for Mean Axial Velocity of Air-Water Flow at the Z= -75 mm Axial Position;
B: 11.76 litre/min (water), 2.7 litre/min (air); **C:** 11.1 Litre/min (water), 2.7 litre/min (air); **D:** 9.48 litre/min (water), 2.7 litre/min (air);
E: 8.88 litre/min (water), 2.7 litre/min (air); **F:** 7.92 litre/min (water), 2.7 litre/min (air)

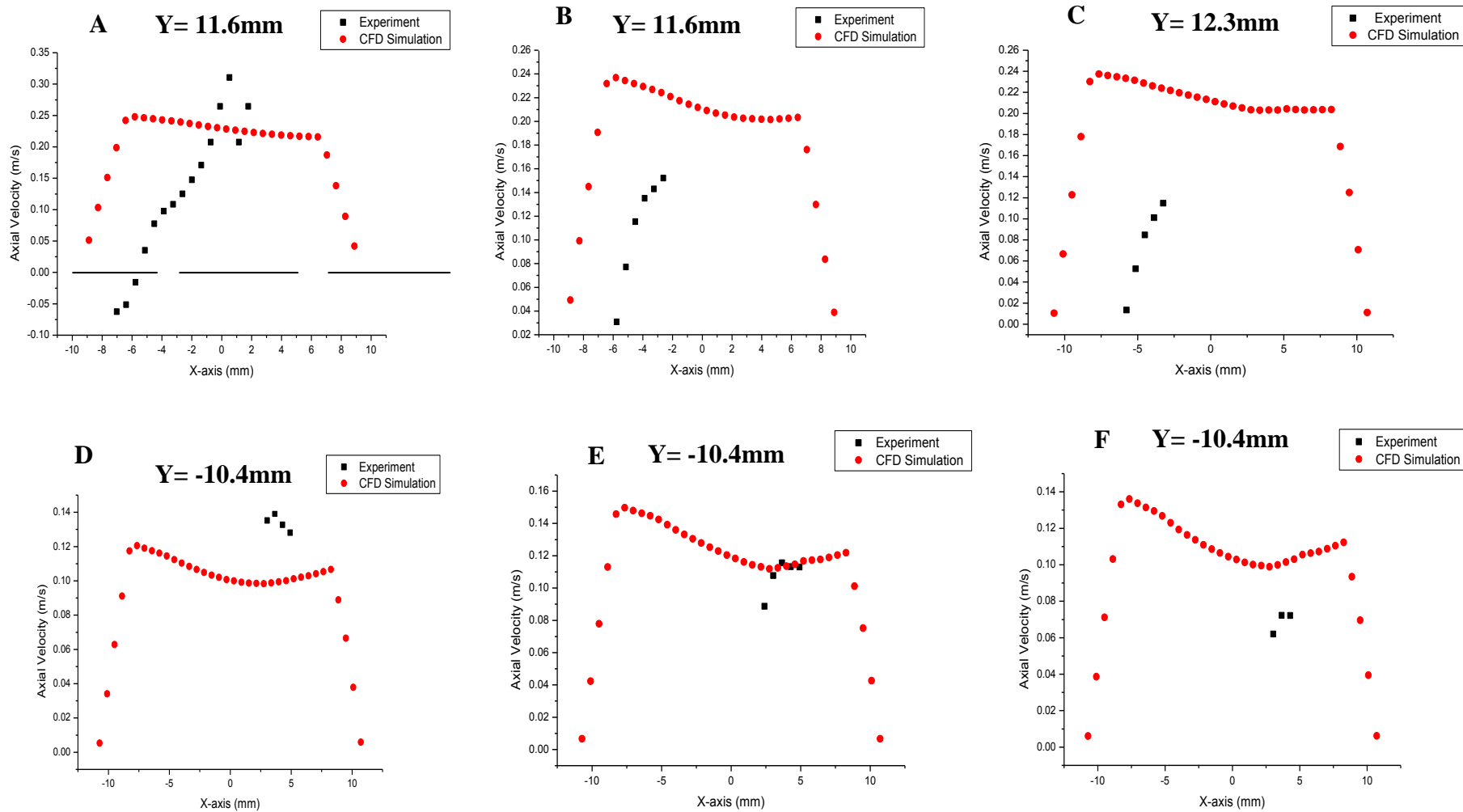


Figure 6.19: Comparison of the CFD Results and Experimental Data for Mean Axial Velocity of Air-Water Flow at the Z= 295 mm Axial Position;
A: 12.3 litre/min (water), 2.7 litre/min (air); **B:** 11.76 litre/min (water), 2.7 litre/min (air); **C:** 11.1 litre/min (water), 2.7 litre/min (air);
D: 9.48 litre/min (water), 2.7 litre/min (air); **E:** 8.88 litre/min (water), 2.7 litre/min (air); **F:** 7.92 litre/min (water), 2.7 litre/min (air)

6.3.3 Radial Velocity

The radial velocity profiles presented in Figures 6.20-6.22 show the comparison between the mean radial velocity distributions at three axial positions as measured experimentally and simulated using CFD. As can be seen in Figure 6.20(A-F), the computational models give qualitative agreement with the experimental measurements except at wall region at negative values of the x-axis where an inward flow pattern is observed. There is disagreement between the experimental and computational results for Figure 6.20 (B-F), and they even contradict each other.

In Figure 6.21 (B-F), the predicted and measured radial velocity profiles show an outward flow pattern at all x-axis coordinates. The results demonstrate that ANSYS FLUENT give a good qualitative agreement with measured data at most x-axis coordinates. As shown in Figure 6.21 (B, C), the experimental and predicted radial velocity profiles show a maximum radial velocity occurring at the centre of the tube. However, in Figure 6.21 (D-F), the maximum radial velocity in the experimental data is found to be off-centre when compared with the simulation results. Figure 6.21(B-C) shows that the computational model over-predicts the radial velocity profiles at the centre of the tube. However, a better correlation between the experimental measurements and predicted results was obtained close to the wall region of the separator. As can be seen in Figure 6.21(D-F), the simulation result is over-predicts at negative values of the x-axis and under-predicts at positive values of the x-axis.

In Figure 6.22 (A), radial velocity is directed inwards at negative values of the x-axis and upwards at positive values. The maximum inward flow is 0.07m/s at $x = -4\text{mm}$ and 0.04m/s at $x = -4.5\text{mm}$. Therefore, we can conclude that there is a fairly good agreement between the experimentally measured radial velocity profiles and those predicted by CFD.

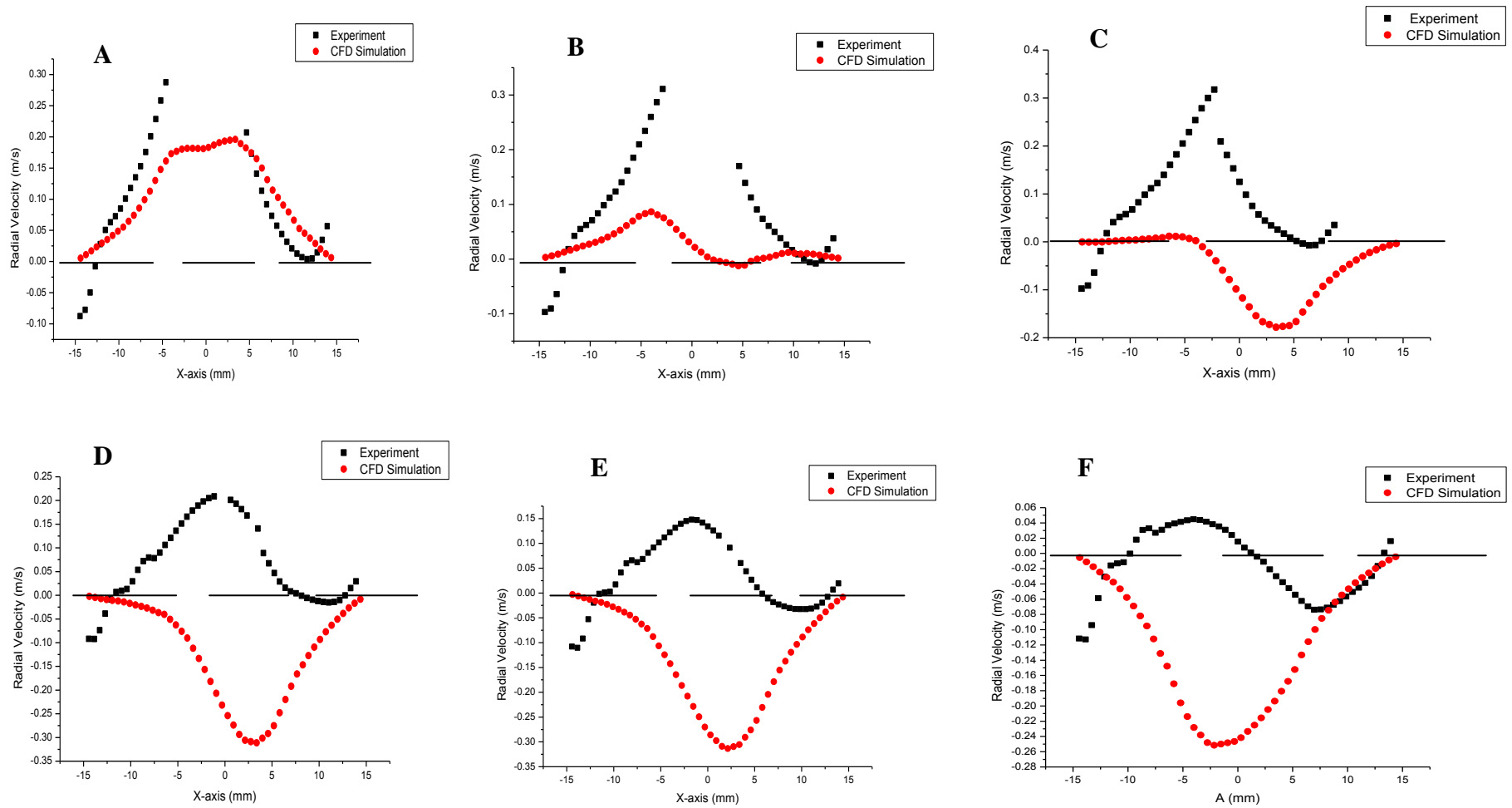


Figure 6.20: Comparison of the CFD Results and Experimental Data for Mean Radial Velocity of Air-Water Flow at the $Z = -395$ mm Axial Position;
A: 12.3 litre/min (water), 2.7 litre/min (air); **B:** 11.76 litre/min (water), 2.7 litre/min (air); **C:** 11.1 litre/min (water), 2.7 litre/min (air);
D: 9.48 litre/min (water), 2.7 litre/min (air); **E:** 8.88 litre/min (water), 2.7 litre/min (air); **F:** 7.92 litre/min (water), 2.7 litre/min (air).

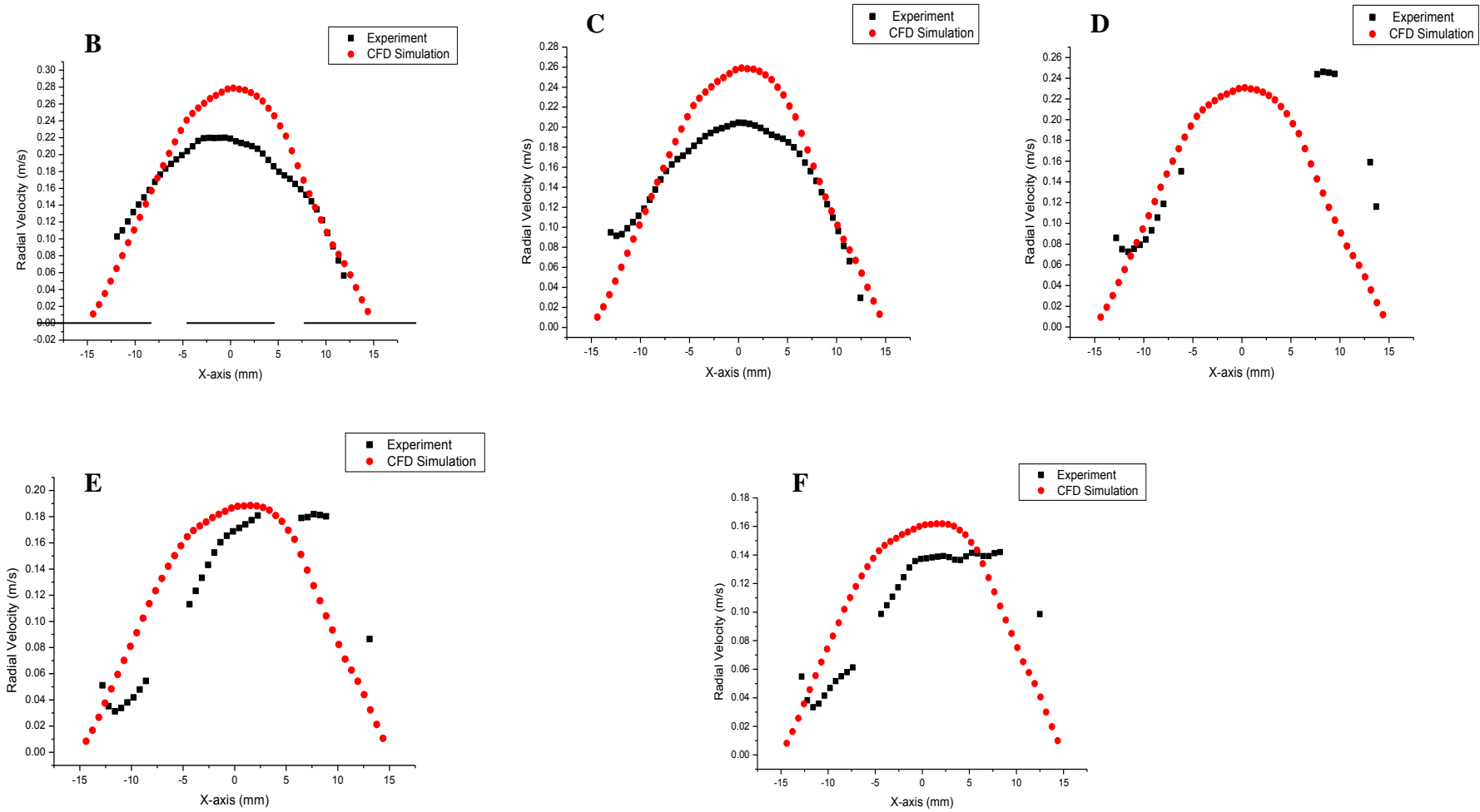


Figure 6 .21: Comparison of the CFD Results and Experimental Data for Mean Radial Velocity of Air-Water Flow at the $Z = -75$ mm Axial Position;
B: 11.76 litre/min (water), 2.7 litre/min (air); **C:** 11.1 Litre/min (water), 2.7 litre/min (air); **D:** 9.48 litre/min (water), 2.7 litre/min (air);
E: 8.88 litre/min (water), 2.7 litre/min (air); **F:** 7.92 litre/min (water), 2.7 litre/min (air)

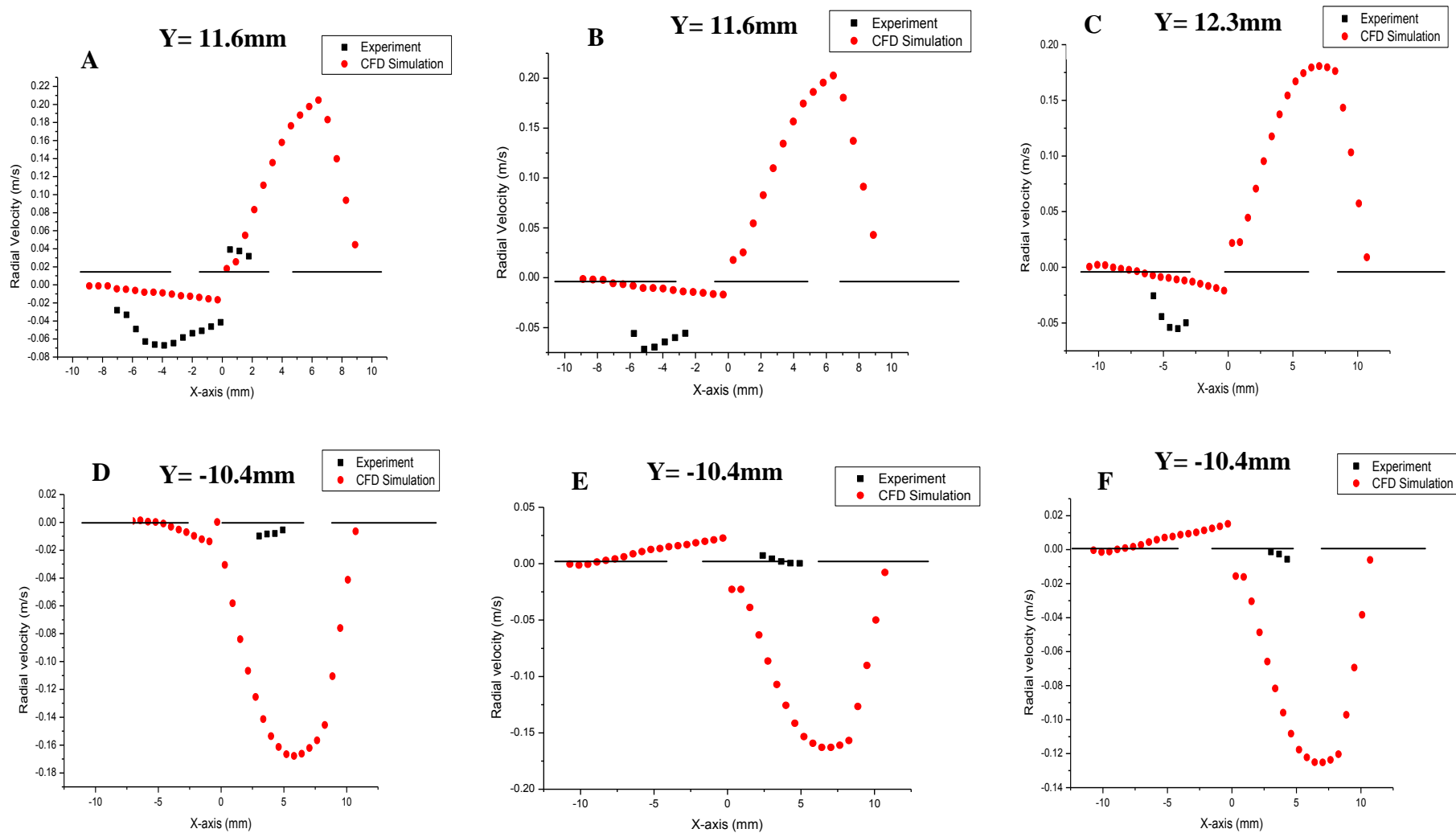


Figure 6.22: Comparison of the CFD Results and Experimental data for Mean Radial Velocity of Air-Water Flow at the $Z=295$ mm Axial Position;
A: 12.3 litre/min (water), 2.7 litre/min (air); **B:** 11.76 litre/min (water), 2.7 litre/min (air); **C:** 11.1 litre/min (water), 2.7 litre/min (air);
D: 9.48 litre/min (water), 2.7 litre/min (air); **E:** 8.88 litre/min (water), 2.7 litre/min (air); **F:** 7.92 litre/min (water), 2.7 litre/min (air).

The velocity profiles presented in section 6.1 to 6.3 show that no meaningful comparison between the CFD simulation and the experimental data at $Z=295\text{mm}$ for air-water flow field could be established due to insufficient experimental data. Therefore, the volume fraction of air distribution in pipe separator was investigated using the CFD simulation.

Figures 6.23-6.25 show the contours of air volume fractions at $Z=-395\text{mm}$, -75mm and 295mm from the CFD simulations of the air-water mixture. Since the main objective of the operation of a pipe separator is the separation of multiphase flows, contour plots of the volume fraction provide a better insight into the phase distribution within the separator. The results indicated the presence of air core at the centre of the cross section while the outer part is occupied by water. As can be seen in Figure 6.25, the magnitude of the air void fraction distribution increases with an increase in the volume fraction of air from 18% to 25%. This confirmed why fewer SPIV data were collected at $Z=295\text{mm}$ as volume fraction of air increases from 18% to 25%.

Figure 6.26 show the contour plot of air volume fractions for air volume fraction of 0.4 at the inlet. It can be observed that scale of separation increases with the volume fraction of air at the inlet. This can be attributed to an increase in air volume fraction at the inlet that led to an increase in the amount of air flow accumulated at the centre of the tube.

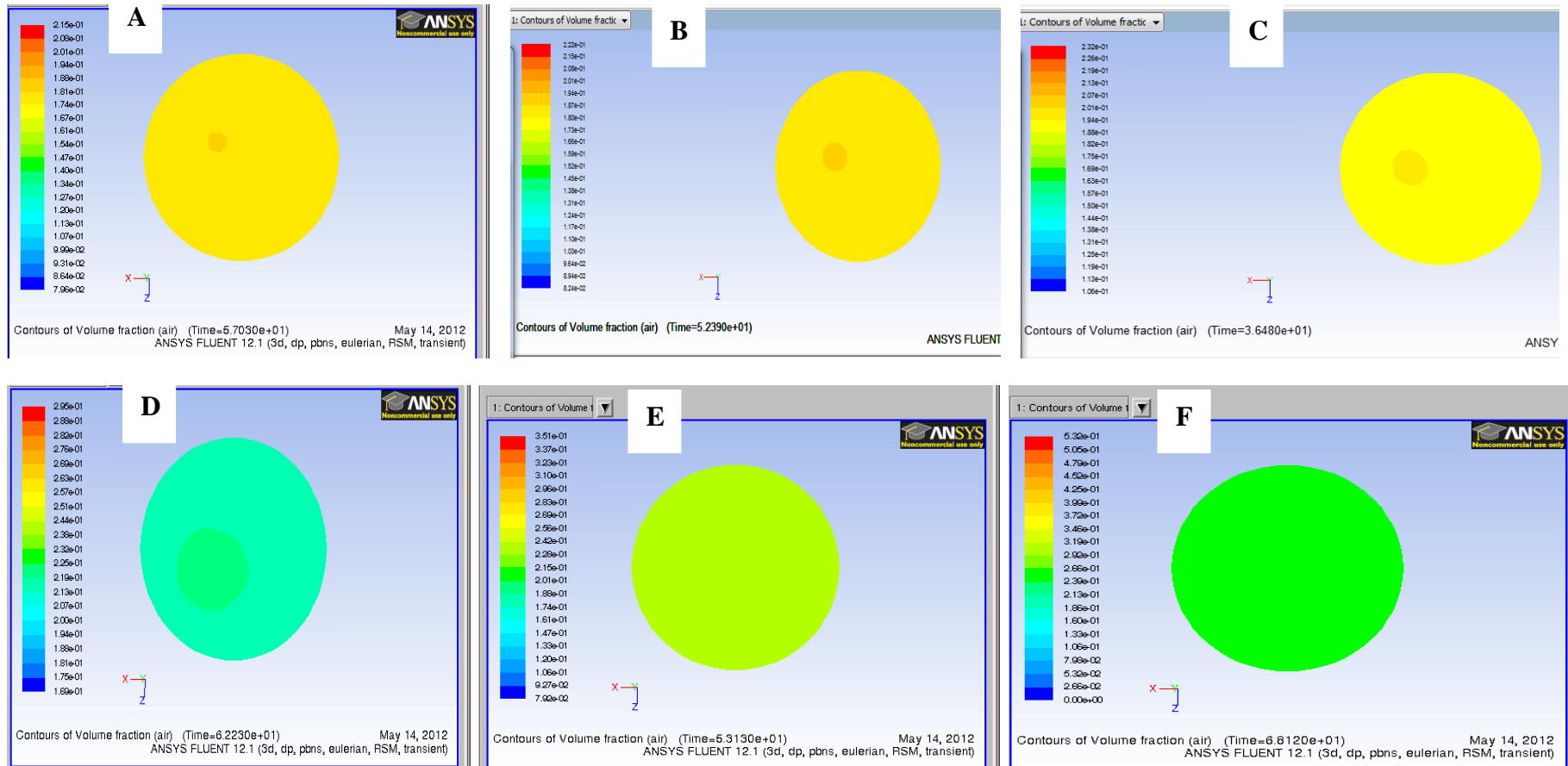


Figure 6.23: Contours of the Air Volume Fraction at the Z = -395 mm Axial Position

A: 12.3 litre/min (water), 2.7 litre/min (air); **B:** 11.76 litre/min (water), 2.7 litre/min (air); **C:** 11.1 litre/min (water), 2.7 litre/min (air);
D: 9.48 litre/min (water), 2.7 litre/min (air); **E:** 8.88 litre/min (water), 2.7 litre/min (air); **F:** 7.92 litre/min (water), 2.7 litre/min (air)

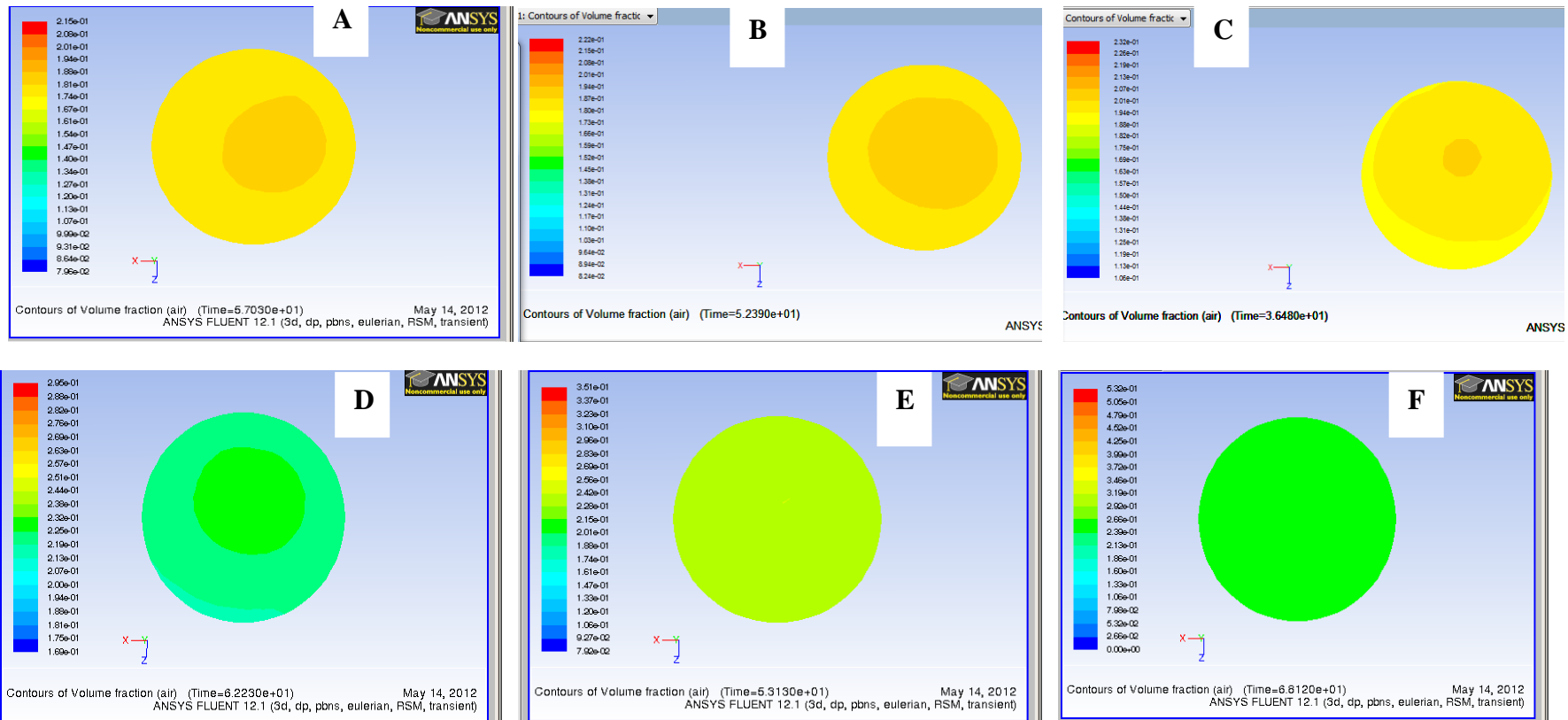


Figure 6.24: Contours of the Air Volume Fraction at the Z = -75 mm Axial Position

A: 12.3 litre/min (water), 2.7 litre/min (air); B: 11.76 litre/min (water), 2.7 litre/min (air); C: 11.1 litre/min (water), 2.7 litre/min (air);
D: 9.48 litre/min (water), 2.7 litre/min (air); E: 8.88 litre/min (water), 2.7 litre/min (air); F: 7.92 litre/min (water), 2.7 litre/min (air)

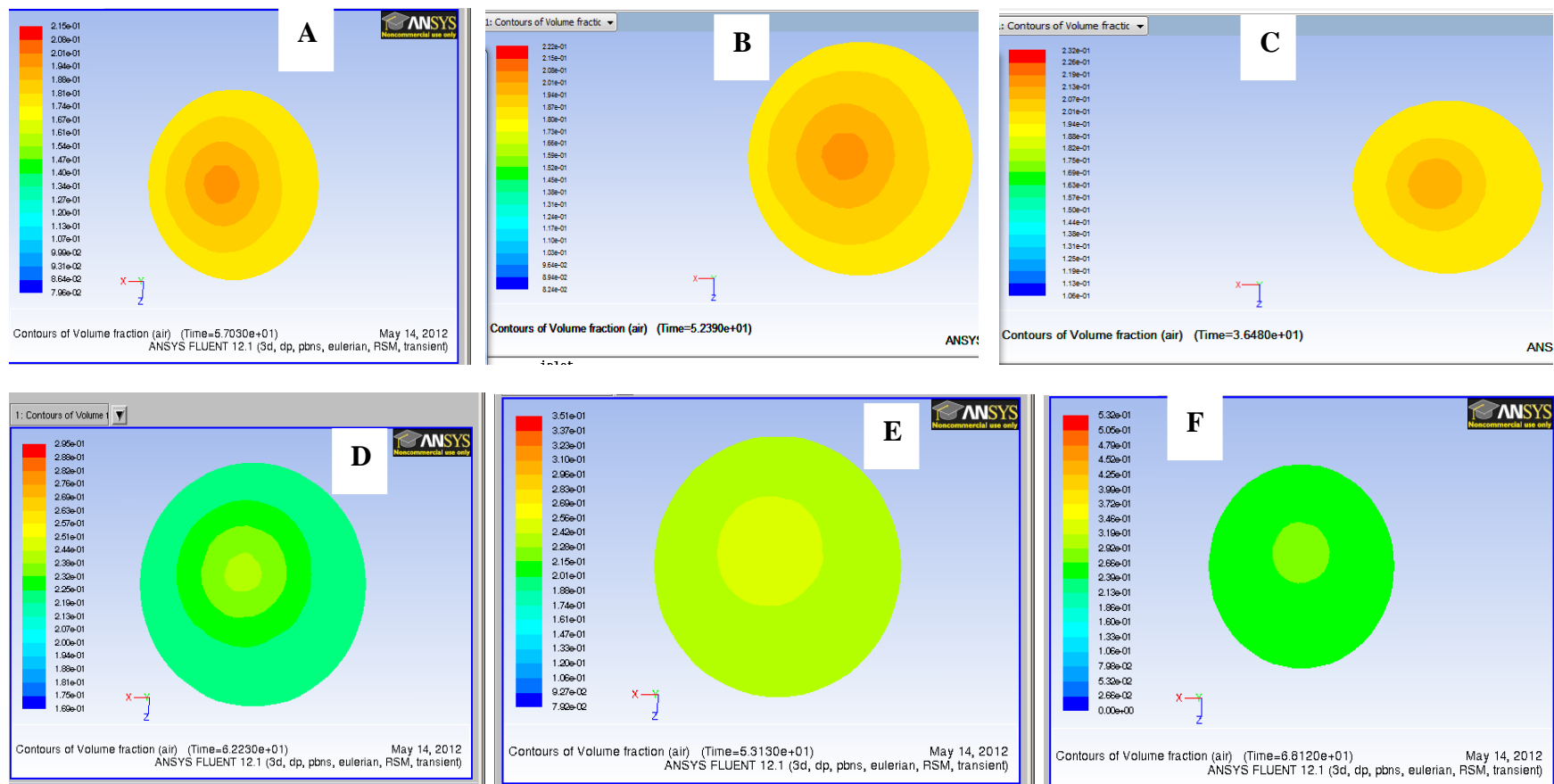
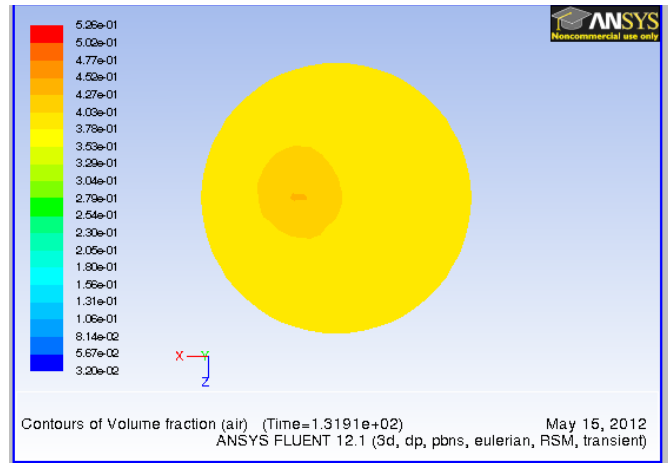


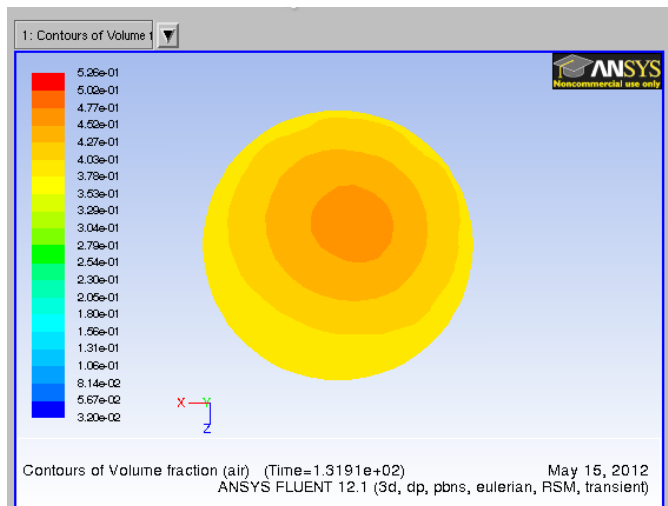
Figure 6.25: Contours of the Air Volume Fraction at the Z= 295 mm Axial Position

A: 12.3 litre/min (water), 2.7 litre/min (air); **B:** 11.76 litre/min (water), 2.7 litre/min (air); **C:** 11.1 litre/min (water), 2.7 litre/min (air);
D: 9.48 litre/min (water), 2.7 litre/min (air); **E:** 8.88 litre/min (water), 2.7 litre/min (air); **F:** 7.92 litre/min (water), 2.7 litre/min (air)

(A)



(B)



(C)

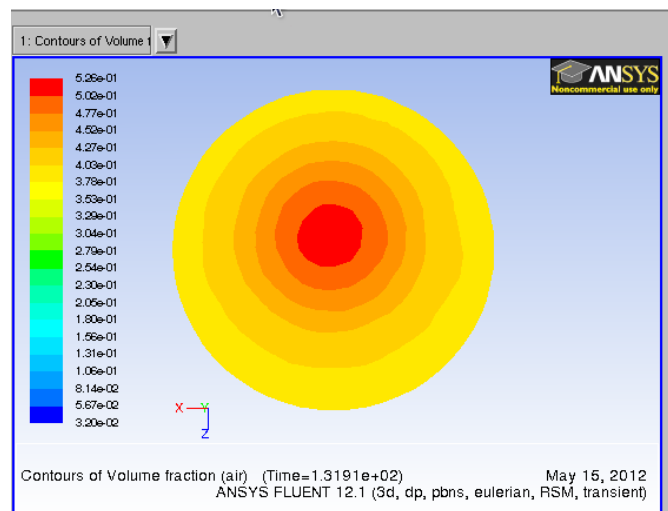


Figure 6.26: Contours of the Air Volume Fraction at the Axial Position of:

(A) $Z = -395 \text{ mm}$ (B) $Z = -75 \text{ mm}$ (C) $Z = 295 \text{ mm}$

6.4: Verification of the Computation Results with Experimental Data

The comparisons between the predicted results and experimental data (Sections 5.2 and 6. 3) showed that:

- (1) The shape of the tangential velocity profiles appeared to be properly modelled at all axial positions, but the predicted tangential velocity magnitudes were either over-predicted or under-predicted. At $Z= -395\text{mm}$, the magnitude of the tangential velocity profile is found to be over-predicted close to the wall and under-predicted at the centre of the tube (Figure 6.14). However, it is under-predicted at most of the x-axis coordinates (Figure 6.15).
- (2) The general shape of the axial velocity profiles was predicted correctly at $Z= -75\text{mm}$, but the magnitudes of the predicted axial velocity were consistently computed close to the wall especially for small flow rates (Figure 6.18). At the centre of the tube, the CFD results were found to be over-predicted at high flow rates and under-predicted as flow rate decreases (Figures 6.18). However there is disagreement in the qualitative analysis at $Z= -395\text{mm}$. The computational models failed to predict the upward flow pattern at the centre of the tube. ANSYS FLUENT under-predict the magnitude of the axial velocity at most of all x-axis coordinates.
- (3) The flow pattern of the radial velocity was correctly predicted at $Z= -75\text{mm}$ with the computed radial velocity magnitudes over-predicted at the centre of the tube, but the radial velocity magnitude was observed to be reducing with a decrease in the inlet flow rates. As we move close to the wall, the magnitude of the radial velocity was observed to be under-predicted at high flow rate, but over-predicted at small flow rates (Figure 6.21). At $Z= -395\text{mm}$, the qualitative analysis showed that the predicted and measured results were not the same (Figure 6.20).

The observations above (1-3) were all independent of velocity profiles at $Z= 295\text{mm}$.

- (4) The measured and predicted results show retardation of the velocity near the walls and this satisfy no slip boundary conditions at the wall of the pipe separator.

- (5) The CFD results confirmed the presence of air core at the centre of the cross section and the magnitude of this air void fraction increases with an increase in the air volume fraction at the inlet (Figure 6.25 and 6.26). This confirmed the reason why fewer SPIV data are recorded at $Z= 295\text{mm}$.

We can then conclude that RSM in conjunction with Eulerian-Eulerian approach are good option for the numerical simulation of air-water flow in a pipe separator. This is true as the computational models were able to capture the basic patterns of flow in a pipe separator.

The computational models have produced some very encouraging results for both single and multiphase flow in pipe separator, giving both qualitative and quantitative agreement. However, there were discrepancies and inaccuracies between the CFD and measured results. It is then important to identify limitations of this verification exercise and the antecedent consequences.

- (1) Turbulent flows are significantly affected by the presence of walls and all turbulence models are found to be more valid for flows in regions far from walls. The standard wall function is ineffective when near-wall flows are subjected to strong body force, severe pressure gradients associated with boundary layer separation, and regions of high curvature. In pipe separators, swirling flows provide the highest curvature and this means that the wall function is less reliable (Versteeg and Malalasekera, 2007).

It may be better to investigate swirl flows in pipe separator with an enhanced near-wall modelling approach combined with adequate mesh resolution in the near-wall region. The enhanced wall approach would be able to resolve the laminar sub-layer, typically $Y^+=1$, if the near-wall mesh is sufficiently fine. However, resolving a highly swirling flow with small mesh resolution using the RSM model is found to require more computational resources in term of cost and time (Versteeg and Malalasekera, 2007; Kader, 1981). Enhanced wall treatment combined with adequate mesh resolution in the near-wall region is expected to capture the severe pressure gradients at the centre of the cross section leading to boundary layer separation close to the wall and the high 3D

flow structure in the near-wall region of the separator. Since the pipe separator we are considering is 30mm wide, flows through it will be strongly affected by the influence of the wall. Here, solution variables have large gradients, and the momentum and other scalar transports occur most vigorously. In addition, the mean flow and turbulence in the pipe separator are subjected to severe pressure gradients and changes rapidly; enhanced wall treatment is expected to correctly account for this effect of pressure gradients at the centre and secondary eddies close to the wall.

- (2) Although the Eulerian model can usually provide more accurate results than the mixture model, the complexity of the former can sometimes make it less computationally stable. This may be due to the fact that the Eulerian model solves a larger number of equations than the mixture model (Cokljat et al., 2003). There is no single multiphase model that is appropriate for solving all multiple flow regimes as observed within the pipe separator. The accuracy of results will not be as good as those for flows that involve just one flow regime, since the model chosen will only be valid for part of the flow under investigation. However, it is not possible to split the flow domain within the pipe separator into zones where different models apply. In addition, an inter-phase drag function suitable for the wide distribution of dispersed phases observed in the pipe separator is not yet well understood. For instance, bubble or droplet in the dispersed phase interacts only with the primary phase, neglecting the interactions between bubbles/droplets. Such interaction causes coalescence and breakage that are proved to generate a considerable influence on the separation efficiency in the pipe separator (Utikar et al., 2010). The default Schiller and Neumann model used for the inter-phase air-water drag function may not be sufficient to account for the exchanges of momentum between the phases (Schiller and Naumann, 1935). ANSYS FLUENT recommended the symmetric model for flows such as in pipe flow, where the secondary (dispersed) phase in one region of the domain becomes the primary (continuous) phase in another. However, numerical solution with symmetric model is found to be prone to numerical instability.

(3) Dispersed systems are always more viscous than the pure continuous phase and the more dispersed particles present, the greater the viscosity of the multiphase flow. When particles or bubbles are included in the fluid stream they disrupt the streamlines as they force liquid to flow around them. This increases the amount of energy needed to achieve a given velocity gradient and increases the viscosity. Therefore, the effects of particles or bubbles on a flowing liquid are the basis of the increased viscosity of dispersed systems. The Einstein equation (Coupland, 2004) describes the magnitude of the effect of dispersed phase on the continuous phase and is given by:

$$\eta = \eta_o (1 + 2.5\phi) \quad \text{-----} \quad (6.1)$$

Where η is the viscosity of the dispersion, η_o is the viscosity of the continuous phase and ϕ is the volume fraction of the dispersed phase. For example, at volume fraction of 18% the viscosity of the dispersion is calculated to be 0.00145kg/ms. The CFD simulation used the viscosity of water flow (0.001003kg/ms) instead of the dispersed system (Say 0.00145kg/ms at volume fraction of 18 %). For multiphase flow, Einstein equation shows that an increase in viscosity leads to smaller velocity gradient with one layer of fluid flowing relative to another. Therefore, the predicted velocity profiles are exceptional high due to small viscosity of water flow by a factor of about 0.45.

(4) Despite great care taken in SPIV measurements, the systematic error is observed to be greater than random error. Detailed information on uncertainty calculation is given in Appendix A. The systematic uncertainty of the SPIV measurement is calculated to be 0.11m/s and observed to be higher than the random uncertainties. This is majorly responsible for the variation in the computed velocity magnitudes when compares with measured profile.

(5) Effect of the natural rubber bungs used in the experimental set-up to specify the split ratio as a function of mass flow rate passing through each outlet was ignored in the CFD computation. The CFD simulation is based on the assumption that the length of the outlet is sufficiently long enough to ensure fully developed flow as the outlet boundary condition. However, at high flow rate reverse flow is strongly believed to have occurred as a result of flow

changing direction on approaching the bung at the outlet. This effect can be better avoided if the length of the outlet increases up to about 40 diameters of the pipe separator diameter (Tu et al., 2008; Nikuradse, 1933). Another option is to use pressure outlet boundary type, but this boundary type will require static pressure estimate at each of the outlet which are not presently known.

- (6) Although a combination of RSM and Eulerian model shows better performance, it is computationally intensive and subject to numerical instability. In this study, SPIV technique was used for simultaneous velocity measurements at three different axial positions and quantitatively compared with CFD calculations. The operation of the SPIV technique as discussed in chapter three was such that multiple (200 images per camera) images of the pipe separator were captured by the high speed camera of the SPIV system at regular time intervals continuously to constitute one data set. These images obtained over a period of 4 minutes were then ensemble-averaged by the image processing software of the SPIV system to derive the velocity graphs presented in chapters 5 and 6. On the other hand, it was too computationally demanding to carry out a 4 minutes transient simulation via the RSM methodology to obtain similar ensemble-averaged results numerically. As such, the difference in the timescale is a major factor for the poor quantitative agreement between the CFD results and the experimental data.

CHAPTER SEVEN

SEPARATION EFFICIENCY OF A PIPE SEPARATOR

In this chapter, the separation efficiency of the pipe separator is discussed, along with a comparison of the experimental data for separation efficiency and the CFD predictions.

7.1 Experimentally Determined Separation Efficiency

The primary objective of the pipe separator is to obtain a high purity of water through the water-rich outlet. Therefore, the efficiency of the separation of oil, water and air was investigated. The percentage of clean water by volume at the water-rich outlet is plotted as a function of:

- (i) the water volume fraction at the inlet;
- (ii) the oil volume fraction at the inlet; and
- (iii) the Split ratio, which is the ratio of liquid flow rate passing through the water rich outlet to the total liquid (water and oil) flow rate at the inlet.

The percentage clean water at the water-rich outlet is defined as the ratio of the volumetric flow rate of water to the total liquid volumetric flow rate at the water-rich outlet. Figure 7.1 compares the percentage of water at the water-rich outlet as a function of water volume fraction at 2.7 litres/min of air flow, 1.08 litres/min of oil flow and the range of water flow is between 6 to 11 litre/min. Here, the percentage of clean water at the water-rich outlet increases as the water volume fraction increases.

Figure 7.2 shows a plot of the percentage of clean water at the water-rich outlet as a function of oil volume fraction at 2.7 litres/min of air flow, 8.5 litres/min of water flow and the range of oil flow is 0.15 to 3.3 litre/min. It can be observed that as oil volume fraction increases at the inlet section of the cyclone, the percentage of clean water at the water rich outlet decreases. From this plot, a volume fraction of less than or equal to 5% will give a good water purity at the water-rich outlet. A similar observation was made by Vasquez (2001), in which an estimated oil volume fraction of less than 10% was suggested as appropriate in order to ensure high separation efficiency.

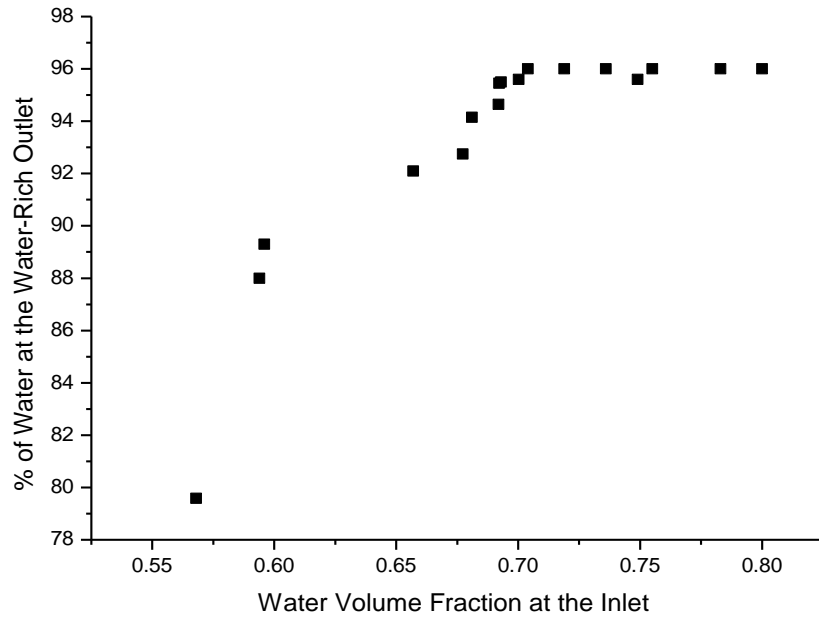


Figure 7.1: Percentage of Water at the Water-Rich Outlet against Water Volume Fraction

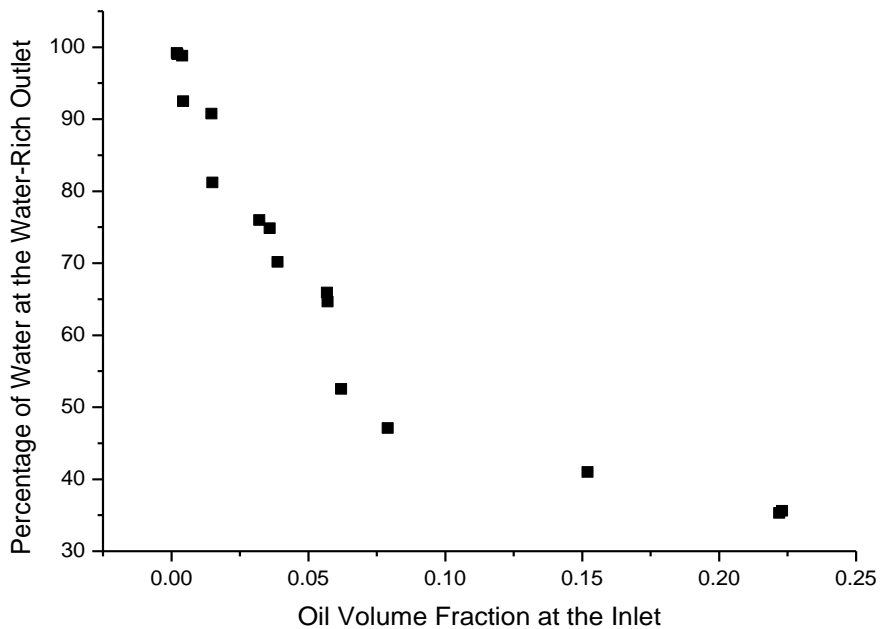


Figure 7.2: Percentage of Water at the Water-Rich Outlet against Oil Volume Fraction

Figure 7.3 shows a plot of the percentage of clean water at the water-rich outlet against the split ratio at 2.7 litres/min of air, 9.84 litres/min of water and 0.5 litres/min of oil flows. The examination of this Figure reveals that an increase in the percentage of clean water at the water rich outlet is associated with a decrease in the split ratio. This means that increasing the split ratio beyond 55% leads to more of the dispersed oil droplets leaving with the water through the water-rich outlet.

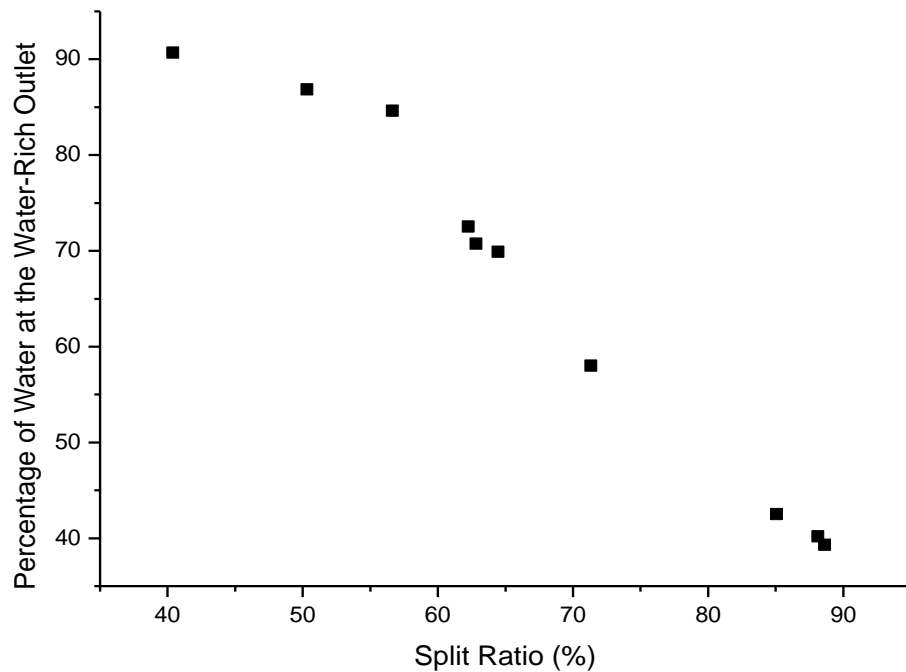


Figure 7.3: Plot of % Water Cut at the Water Outlet against Split Ratio

7.2 Comparison between Measured and Predicted Separation Efficiency

Figure 7.4 shows the comparison between the measured and predicted separation efficiency in term of the percentage of clean water passing through the water-rich outlet. The results show that the percentage of clean water at the water-rich outlet is observed to be over-predicted when compared with the experimental data. However, the capability of the pipe separator to produce clean water through the water-rich outlet is clearly indicated. As shown in Figure 7.5, the measured and CFD profiles indicates that the percentage of water reduces with an increase in oil volume fraction at the inlet.

However, there exist a large differences between the measured and CFD results. This deviation is strongly believed to be as a result of inherent drawbacks associated with Eulerian-Eulerian approach used for air-water simulation before tracking the oil droplets. For instance, bubble or droplet in the dispersed phase interacts only with the primary phase, neglecting the interactions between bubbles/droplets. This interaction causes coalescence and breakage that are proved to generate a considerable influence on the separation efficiency in the pipe separator (Utikar et al., 2010).

The CFD models over-predicted the % of water at the water-rich outlet when compared with measured data by 2% - 9 % for the water-volume fraction and 8% - 95 % for the oil-volume fraction.

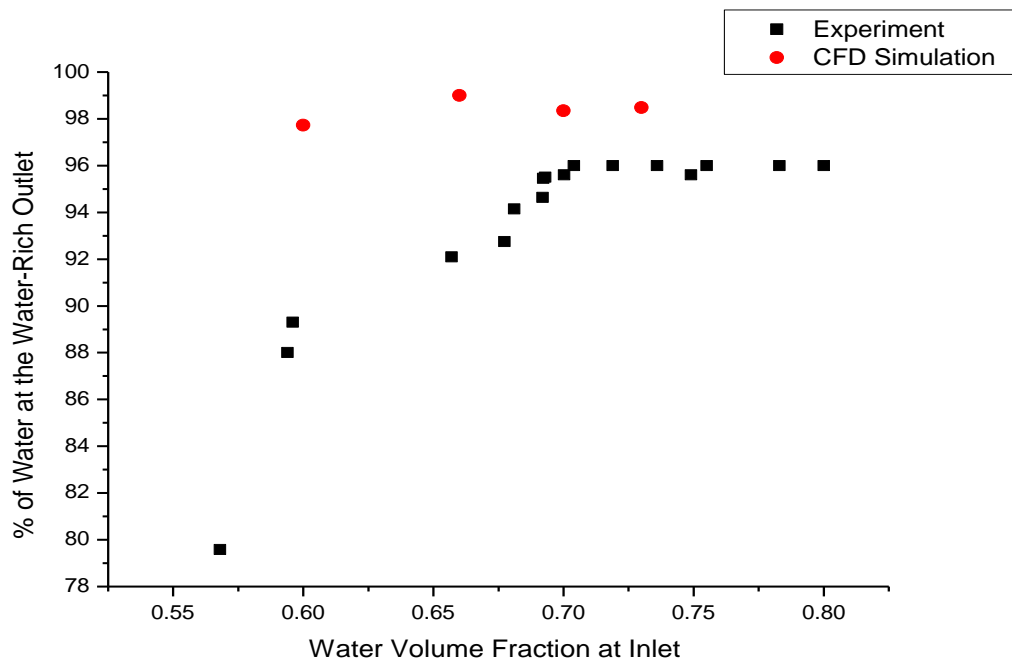


Figure 7.4: Comparison of the Percentage of Water at the Water Rich Outlet against Water Volume Fraction at the Inlet as Measured Experimentally and CFD Prediction

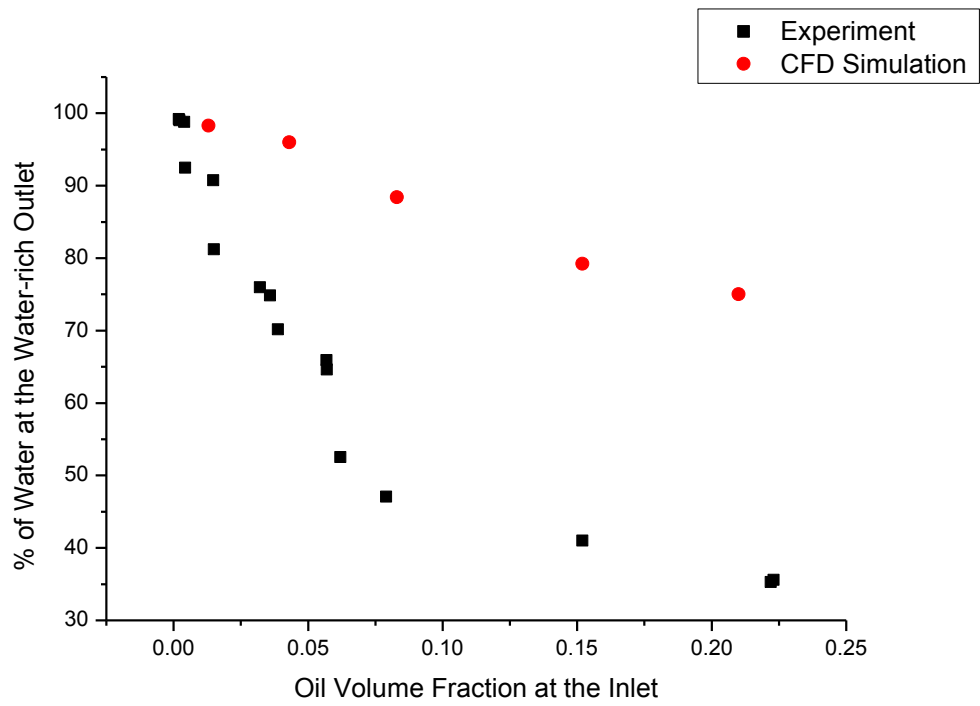


Figure 7.5: Comparison of the Percentage of Water at the Water Rich Outlet against Oil Volume Fraction at the Inlet as Measured Experimentally and CFD Prediction

CHAPTER EIGHT

CONCLUSIONS AND RECOMMENDATIONS

The stereoscopic PIV technique and a CFD commercial package, ANSYS FLUENT, have been used to investigate the hydrodynamic behaviour of single and multiphase flows within a pipe separator. The separation efficiency of the air-water-oil flow was determined as a function of the clean water stream coming through the water rich outlet of the pipe separator.

8.1 CONCLUSIONS

A laboratory scaled-down prototype of a three phase pipe separator was built to investigate the hydrodynamic behaviour of the multiphase flow and separation efficiency.

The stereoscopic PIV measurements were taken to investigate the single phase, water flow fields at three different axial positions within the pipe separator. Tangential velocity measurements for the single phase flow showed that a forced vortex occurs at the centre of the tube, with a free vortex near the wall region. The location of zero tangential velocity was observed to be off the axis of the pipe separator. The shape of the tangential velocity profile was found to be independent of axial positions within the pipe separator.

The tangential velocity profiles indicate that the magnitude of the mean tangential velocity decreases as we move away from the inlet section towards the outlets. Therefore, it can be concluded that most of the fluid separation occurs immediately at the inlet region where the inlet section joins the vertical axis of the cyclone. The surface area occupied by the forced vortex decreases moving away from the inlet section, while that of the free vortex increases as we move away from $Z=-395\text{mm}$.

The axial velocity measurements had shown a downward flow near the wall of the pipe separator and an upward flow near the centre of the tube. There is no general pattern for the radial velocity within the pipe separator. At the inlet section, the radial velocity was found to be directed outward. However, away from the inlet region, a pattern of both outwards and inwards flows was observed.

A comparison of the experimental and computational results showed that good qualitative agreement was obtained at most axial positions, but the magnitude of the velocity profiles was not predicted correctly. The tangential velocity profiles predicted by the CFD simulation are similar to those of the experimental data. Far away from the inlet region, the CFD model was found to predict different axial and radial velocity profiles at the centre of the tube.

The numerical CFD simulation using ANSYS FLUENT can predict the flow pattern quantitatively correctly and can provide an alternative method for studying fluid dynamics inside pipe separators and improve performance parameters.

Air-water velocity measurements were taken for six different water flow rates and a constant air flow rate. The effect of air flow on the air-water velocity fields was established by comparing the air-water and water-only flows. The flow visualization studies showed that the free vortex region of the tangential velocity profile begins at different values of radius for the air-water flow. This is an indication that addition of air flow leads the core of the tangential velocity distribution within the pipe separator to be transient. The velocity measurements for the liquid phase in the air-water flow indicate that the flow pattern does not change when compared to water-only flow fields. However, the magnitude of the air-water velocity fields is observed to be higher than that of the water-only flow. This was expected, since the magnitude of the velocity field is directly proportional to the flow rate of the fluid.

The CFD simulation of air-water flow at most axial positions shows the same flow pattern as in the measured profiles, but the magnitude of the velocity profile is not correctly predicted. Therefore, it can be concluded that the combination of the Reynolds stress model and the Eulerian model of ANSYS FLUENT can adequately predict the anisotropic turbulence features of swirling flow within the pipe separator. The CFD contour plot of air volume fractions showed that the size of the air core at the centre of the cross section increased with the air volume fraction.

The possibility of the pipe separator producing clean water at the water-rich outlet has been demonstrated experimentally and numerically. It was observed that a clean water stream at the water-rich outlet of the pipe separator is achievable at high water volume

fractions and low oil content. Therefore, this pipe separator is capable of functioning as a free water knock-out device.

8.2 RECOMMENDATIONS

This section considers possible further work which would improve the general understanding of the hydrodynamic behaviour of the multiphase flow in a pipe separator.

1. There is a need for improvements to the current experimental facility so as to provide pressure data at the inlet and outlets of the separator.
2. Since there is slip velocity when phases move at different velocities and the flow treated as non-homogeneous multiphase flow, there is a need to measure the void fraction of air. This is based on the assumption that void fraction cannot be equated to volume fraction whenever the flow is considered as a non-homogeneous multiphase flow.
3. Control valves should be used to choke and control the flow passing through the outlets. Also, this would prevent air flow being drawn through any of the outlets.
4. There are a number of limitations to FLUENT simulation when using the outflow boundaries condition. Implementation of pressure outlet conditions is expected to prevent the possibility of backflow and air flow being drawn from the atmosphere through the outlet.
5. The enhanced wall treatment should be used for wall function approximation. This will help in predicting correctly the strong body forces and multiphase flow passing through pipe separators of small diameter.
6. The implementation of a structured mesh is expected to greatly reduce the problems of grid skew.

APPENDIX A

Uncertainty Analysis for Stereoscopic PIV Measurements

Uncertainty introduced in the vector field computation is mainly related, firstly, to the accuracy of the detection of particle shift (ds) by the cross-correlation procedure. Secondly, the geometric error is related to the stereoscopic configuration of the optical system used to record the images (Lawson and Wu, 1997). Generally, the reconstruction uncertainty associated with the processing software (INSIGHT 3G from TSI Inc.) is 0.1 pixel for each of the average particle shift in the image plane. With a camera resolution of $8.14 \mu\text{m}/\text{pixel}$, the uncertainty is considered the same for all directions of the coordinates in the image planes.

$$e_{ds} = \delta^r(\Delta X_1) = \delta^r(\Delta Y_1) = \delta^r(\Delta X_2) = \delta^r(\Delta Y_2) = 0.1 \text{ pixel} = 0.814 \mu\text{m} \quad (\text{A.1})$$

The camera's optical axes are rotated by an angle α with respect to the z axes. From the experimental set up in chapter three:

$$\alpha = 45^\circ \quad (\text{A.2})$$

The object distance is 30mm and the image distance is 200mm. Magnification is assumed to be the same for both cameras due to the symmetry of the system. Therefore, camera magnification can be assumed to be uniform in the object plane because of the Scheimpflug mounts that have been applied. Magnification, M is then equal to 0.15

The uncertainty model proposed by Lawson and Wu (1997) defines geometric error in the object plane coordinates as a function of the uncertainty in the image plane:

$$\delta^r(\Delta x) = \delta^r(\Delta y) = \delta^r(\Delta z) = \frac{1}{M} e_{ds} = 5.43 \mu\text{m} \quad (\text{A.3})$$

For a laser pulse separation of $dt = 50 \mu\text{s}$, the three dimensional velocity vector is characterized by the following uncertainty in each of its components:

$$e_v = \frac{\delta^r(\Delta x)}{dt} = 0.11 \text{ m/s} \quad (\text{A.4})$$

Standard deviation is associated with the uncertainty in each individual measurement X_i . However, we need to calculate the uncertainty in the best estimate of X , represented as the standard deviation of the mean (σ_m). The accuracy of the measurements can be computed from the root mean square fluctuation (Hassan *et al.*, 1998; Raffel *et al.*, 1998):

$$\sigma = \sqrt{\frac{1}{N} \sum_{i=1}^N (X_i - \bar{X})^2} \quad (\text{A.5})$$

Where

σ is the standard deviation of the X_i and N is the number of valid measurements, X_i

$$\bar{X} = \frac{1}{N} \sum_{i=1}^N X_i \quad (\text{A.6})$$

The standard deviation of the mean (σ_m) is given by:

$$\sigma_m = \frac{\sigma}{\sqrt{N}} \quad (\text{A.7})$$

Therefore, the true measured value of X_i is given by (JCGM, 2009, Taylor, 1982);

$$X = \frac{\sigma}{\sqrt{N}} \quad (\text{A.8})$$

Assuming that the data are normally distributed, the upper and lower confidence limits are calculated as

$$\bar{X} \pm \sigma_m \cdot 1.96$$

Where σ_m equal to the standard error for the sample mean and 1.96 is the 0.975 quantile of the normal distribution.

Table A: 1 Uncertainty Analysis for Water Flow Measurements

Component	Standard deviation (m/s)	Mean (m/s)	Standard deviation of the mean (m/s)	Number of samples
Axial velocity	0.282	-0.0586	0.00524	2891
Radial velocity	0.573	0.115	0.0107	2891
Tangential velocity	0.48	0.127	0.0089	2891

The margin of uncertainty for the water flow measurements at $Z = -75\text{mm}$ is as follows:

Axial velocity, (m/s)	-0.0586 ± 0.0123
Radial velocity, (m/s)	0.115 ± 0.021
Tangential velocity, (m/s)	0.127 ± 0.0174

		At $x = 0.2\text{mm}$	At $x = 12.5\text{ mm}$
Axial Velocity	EXP	0.1873	-0.375
	CFD	0.275	-0.1623
	%	33.5	131

		At $x = 2\text{mm}$	At $x = 12.5\text{ mm}$
Radial Velocity	EXP	0.231	0.1
	CFD	0.225	0.045
	%	2.6	55

		At $x = -11\text{mm}$	At $x = 11.5\text{ mm}$
Tangential Velocity	EXP	0.53	0.60
	CFD	0.5	0.48
	%	6	20

Table A: 2 Uncertainty Analysis for Air-Water Flow Measurements

The random uncertainty for the air-water velocity distribution is as follow:

Component	Standard deviation (m/s)	Mean (m/s)	Standard deviation of the mean (m/s)	Number of samples
Axial velocity	0.221	-0.063	0.0041	2886
Radial velocity	0.407	0.09	0.00758	2886
Tangential Velocity	0.336	0.135	0.0062	2886

Table A.2: Statistical Parameters for Normalized Air-Water Flow Velocity Probability Distributions.

The margin of uncertainty for the air-water flow measurements at Z= -75mm is as follows:

Axial velocity, (m/s)	-0.063 ± 0.008
Radial velocity, (m/s)	0.09 ± 0.015
Tangential velocity, (m/s)	0.135 ± 0.012

		At x = 0 mm	At x = 10 mm
Axial Velocity	EXP	0.31	-0.375
	CFD	0.258	-0.18
	%	20.2	108
		At x = -10mm	At x = 7.5 mm
Radial Velocity	EXP	0.06	0.06
	CFD	0.05	0.075
	%	17	25

		At $x = -10\text{mm}$	At $x = 12.5 \text{ mm}$
Tangential Velocity	EXP	0.688	0.708
	CFD	0.62	0.60
	%	9.88	15.25

Uncertainty Analysis for Air-Water-Oil Flow

Percentage of Water at the Water Rich Outlet against Water Volume Fraction at the Inlet

		At $x = 0.6$	At $x = 0.74$
	EXP	90	95
% of Water at the Water rich outlet	CFD	98	97
	%	8.89	2.1

Percentage of Water at the Water Rich Outlet against Oil Volume Fraction at the Inlet

		At $x = 0.1$	At $x = 0.15$
	EXP	91	40
% of Water at the Water rich outlet	CFD	98	78
	%	7.7	95

APPENDIX B

GRID INDEPENDENCE STUDIES

Grid independence tests have been performed to investigate the dependence of the simulation results on grid resolution with three different mesh interval sizes. All simulation parameters except for the grid size were kept constant throughout the study. The study was performed with different mesh interval sizes relative to overall dimension of the geometry (0.05, 0.04, and 0.03) and then increased cell nodes around the inlet section (for a grid size of 0.03) until a grid independent solution was achieved.

The process of finding a grid independent solution can be complex, especially when three-dimensional grids are considered, as the grid properties in each dimension are often interrelated with regard to the flow field variables. By using these grids, the tangential, axial and radial velocity profiles at $Z=-0.05\text{mm}$ were used to check the sensitivity of the grid. It can be observed that there is a variation in the velocity profiles as the mesh interval size decreases from 0.05 to 0.03. In addition, upon grid refinement, more flow structures are captured. Since flow solutions are sensitive to the number of grid points, the simulation results of D and E do not change significantly despite the increase in cell counts. Therefore, a mesh with a cell count of 225,000 was used for all numerical simulation in this work.

	Mesh size	Cell count
A	0.05	60,000
B	0.04	100,000
C	0.03	185,000
D	0.03 +Refinement	225,000
E	0.03+Refinement	275,000

Table B: 1 Details of Grids used in Mesh independence Studies

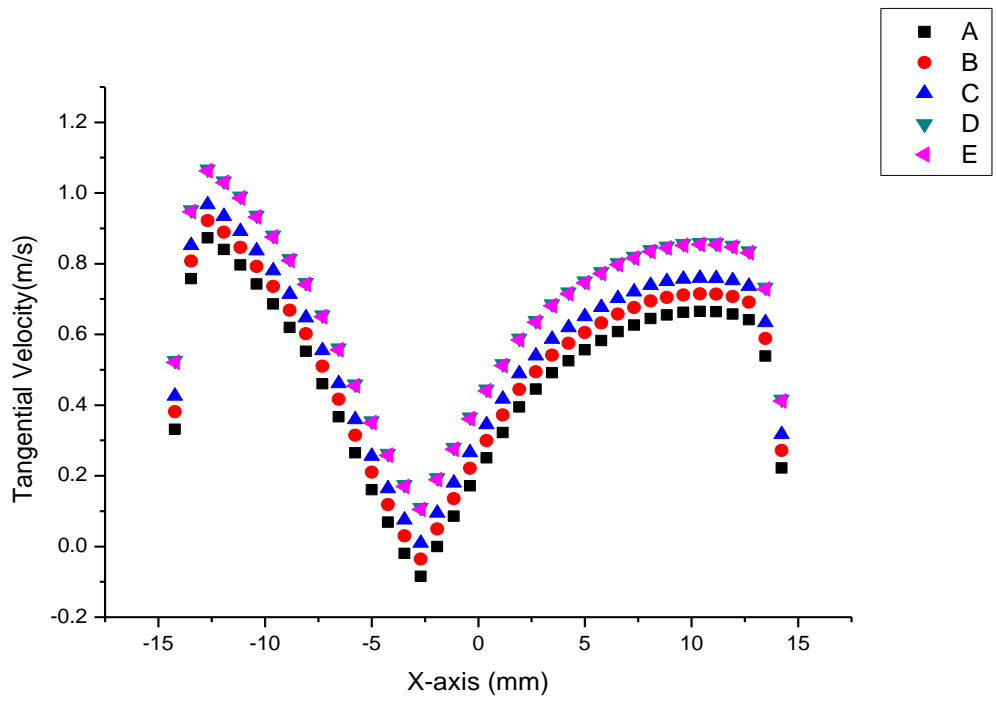


Figure B: 1 Tangential Velocity Profiles for Different Grids

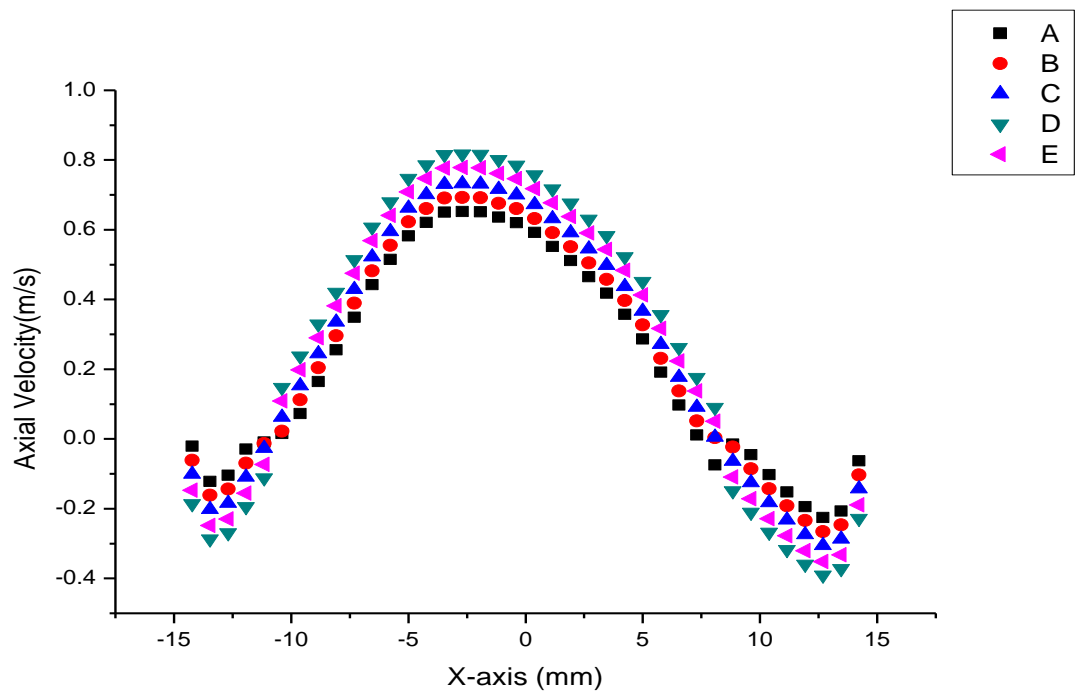


Figure B: 2 Axial Velocity Profiles for Different Grids

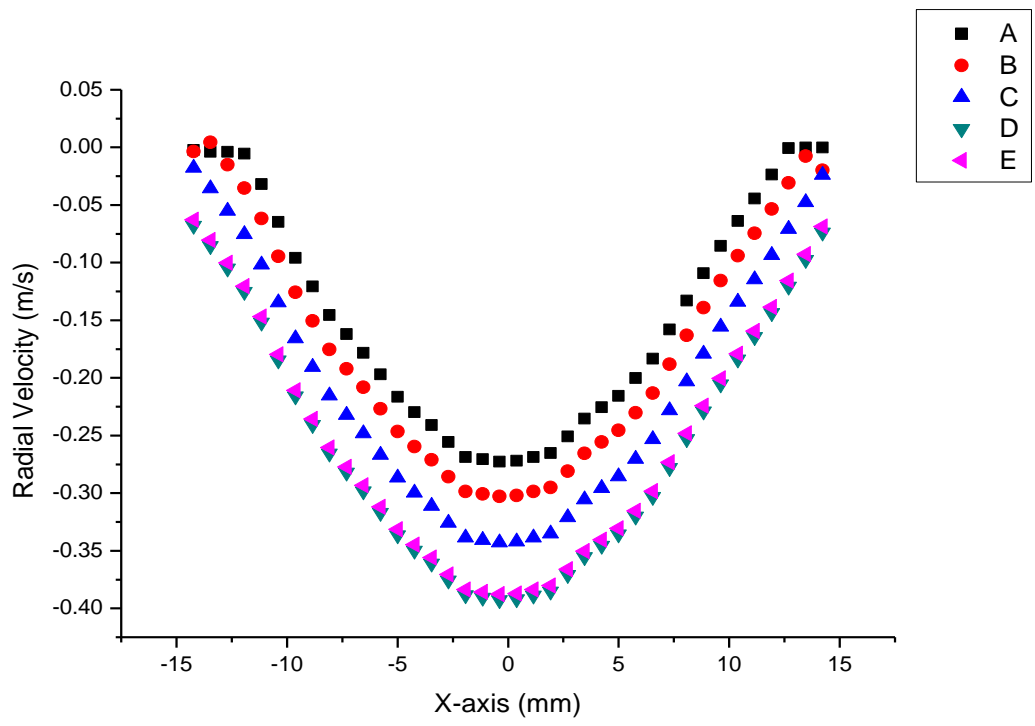


Figure B: 3 Radial Velocity Profiles for Different Grids

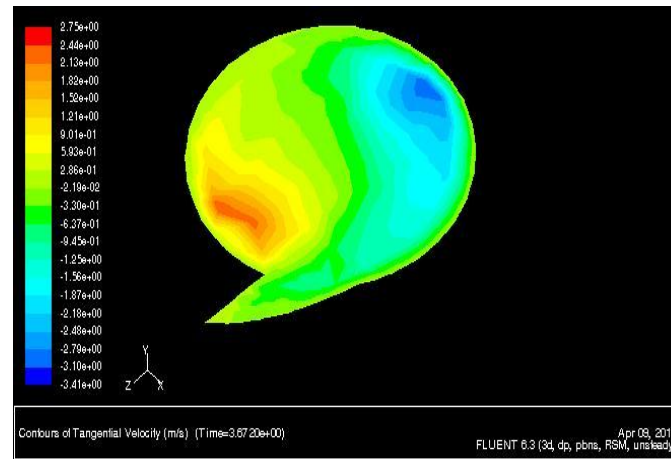
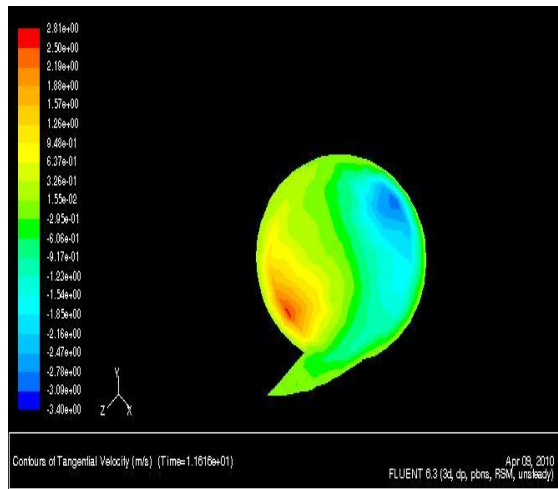
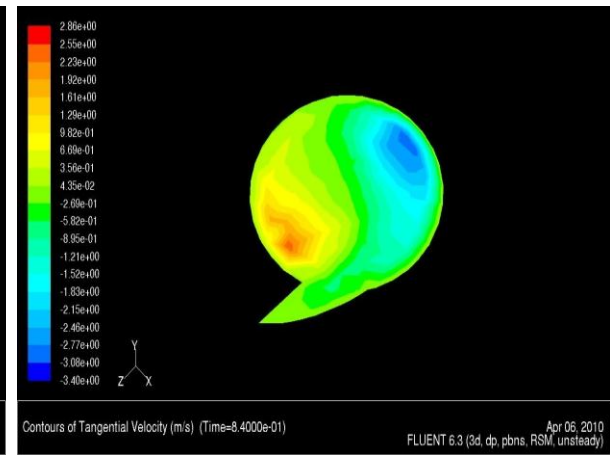
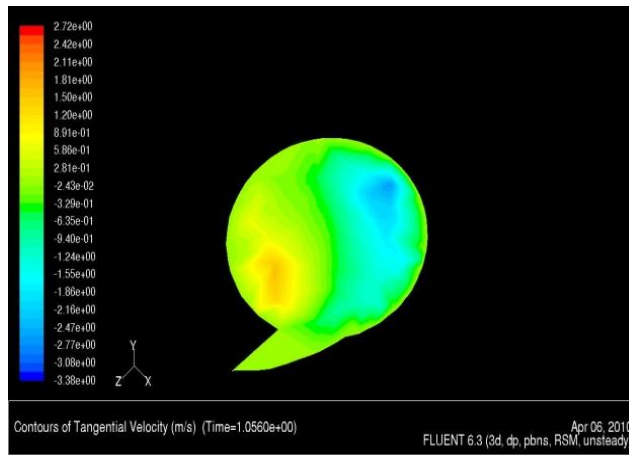
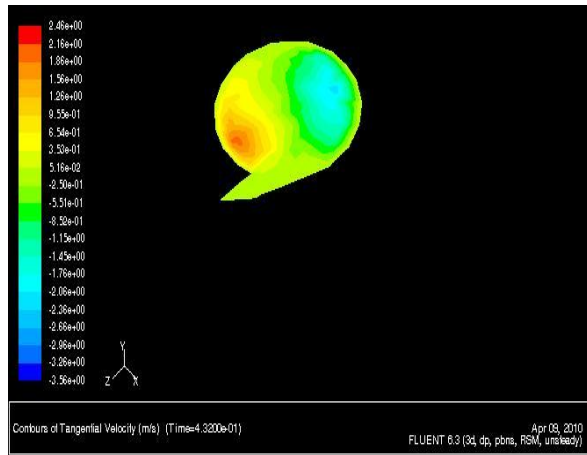


Figure B: 4 Contour of Tangential Velocity at Axial Position of $Z = -0.05\text{mm}$

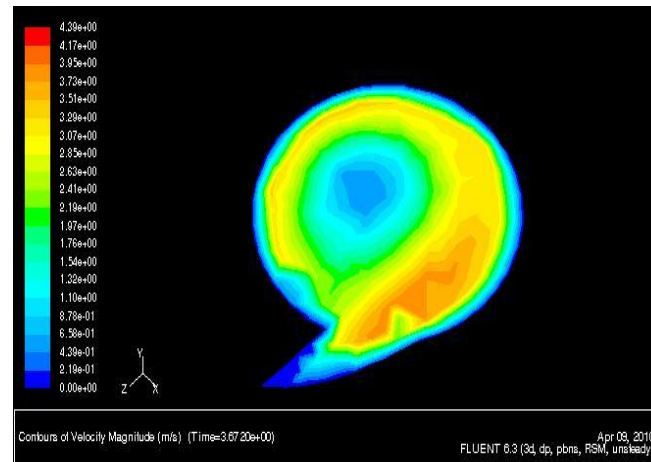
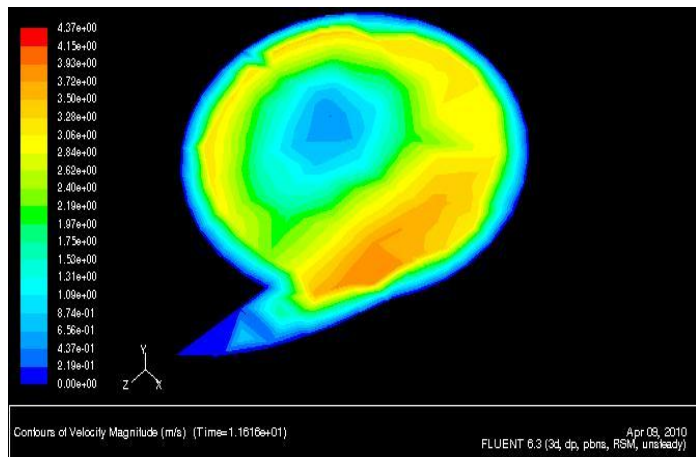
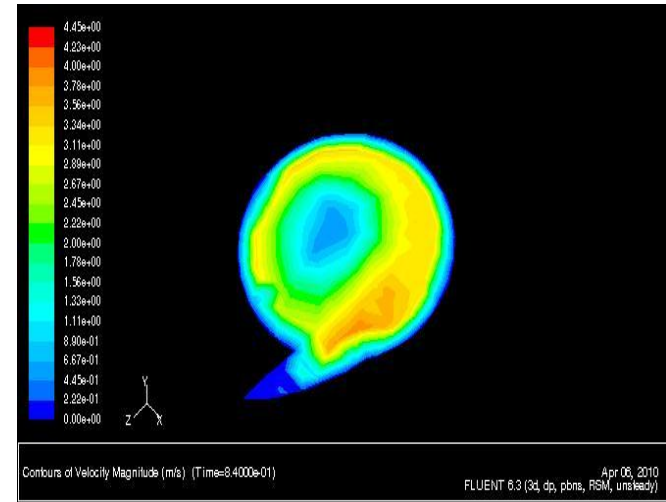
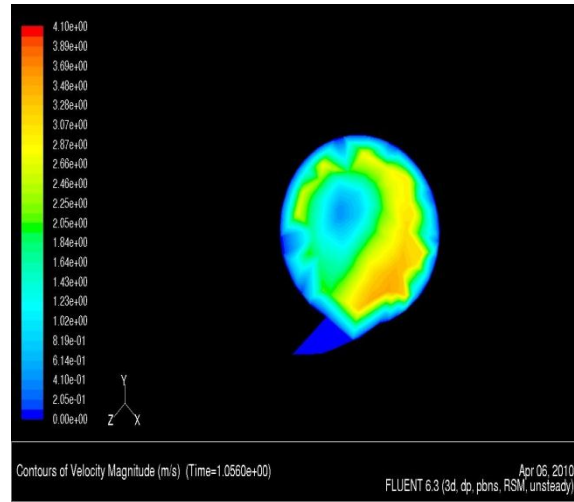
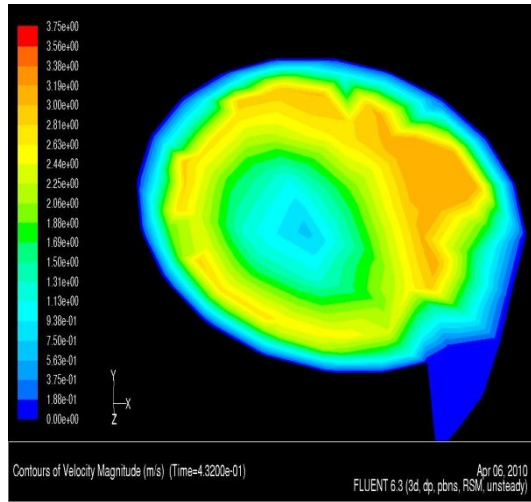


Figure B: 5 Contour of Tangential Velocity at Axial Position of $Z = -0.05\text{mm}$

APPENDIX C

CALCULATION OF PRESSURE DROP IN A PIPE SEPARATOR

The total pressure drop over a cyclone consists of losses at the inlet, outlet and within the cyclone body. Pressure drops are caused by the energy dissipation by the viscous stress of the turbulent rotational flow, contraction of the fluid flow, expansion and fluid friction on the cyclone wall surface. The rotation of the fluid flow establishes a pressure field in a cyclone. The pressure decreases with the reduction of the rotational radius because of the increasing tangential velocity. In the radial direction, there is a significant pressure drop caused by the change of the tangential velocity, since the increase of the tangential velocity causes a large radial acceleration (Chuah et al., 2003). This pressure change in the radial direction can be expressed by the following equation:

$$\frac{dP}{dr} = \rho * \frac{V_t^2}{r} \quad (D.1)$$

Where:

dP = change of the pressure

V_t = tangential velocity (0.6m/s)

dr = change of the rotation radius

r = rotational radius (0.015m)

ρ = air density

From pressure field numerical calculation for single phase flow, the ΔP is then calculated to be 29.9 Pa. This pressure drop is considered very small when compare with the atmospheric pressure boundary condition set at the inlet.

REFERENCES

- Adrian, R. J. (1991) 'Particle-imaging techniques for experimental fluid mechanics', *Annual Review of Fluid Mechanics*, 23, pp. 261-304.
- Adrian, R. J. (2004) 'Twenty years of particle image velocimetry', *12th International Symposium on Applications of Laser Techniques to Fluid Mechanics, Lisbon, July 12-15, 2004*
- Adrian, R. J. and Westerweel, J. (2011) '*Particle Image Velocimetry*'. London: Cambridge University Press.
- Algifri, A. H., Bhardwaj, R. K. and Rao, Y. V. N. (1988) 'Turbulence Measurements in Decaying Swirl Flow in a Pipe', *Appl. Sci. Res.*, 45, (233-250).
- Almgren, A.S.; Bell, J.B.; Rendleman, C.A.; Zingale, M. (2006). 'Low Mach Number Modelling of Type Ia Supernovae. I. Hydrodynamics'. *Astrophysical Journal* 637 (2): 922–936.
- Ashrul Ishak M.S and Jaafar, M.N. (2004) '*The Effect of Swirl Number on Discharged Coefficient for various Orifice Sizes in a Burner System*' *Jurnal Mekanikal* Jun 2004, Bil. 17, 99 – 108
- Anderson, J. D. (2007) '*Fundamentals of Aerodynamics*', 4th ed. McGraw-Hill. ISBN 0-07-125408-0.
- Arnold, K and Stewart, M. (1999) 'Surface Production Operation: Design of Oil-Handling Systems and Facilities' 2nd ed. Woburn, MA: Butterworth-Heinemann, 1999, Vol. 1.
- Bai, Z. S., Wang, H. I. and Tu, S. T. (2009) 'Experimental study of flow patterns in deoiling hydrocyclone', *Minerals Engineering*, 22, (4), pp. 319-323.

Barnea, D. (1987) 'A unified model for predicting flow-pattern transitions for the whole range of pipe inclinations', *International Journal of Multiphase Flow*, 13, (1), pp. 1-12.

Barnea, D. and Taitel, Y. (1994) 'Structural stability of stratified flow-the two-fluid model approach', *Chemical Engineering Science*, 49, (22), pp. 3757-3764.

Baxter, L. L. and Smith, P. J. (1993) 'Turbulent Dispersion of Particles: The STP Model', *Energy & Fuels*, 7, pp. 852 -859.

Beer, J.M. and Chigier, N.A. (1972), '*Combustion Aerodynamics*', Applied Science Publishers Ltd.

Bellani, G. (2011) '*Experimental Studies of Complex flow through Image-based Techniques*'. Royal Institute of Technology KTH, Stockholm, Sweden .

Benim, A.C, Gul,F. and Pasqualotto,E (2007) 'Numerical investigation into the role of inlet swirl velocity profile on the decay of swirl in pipe flow', Proceeding of the 5th IASME/WSEAS Intl Conf Fluid Mechanics and Aerodynamics, Athens, Greece , Aug 2007, pp 238-243.

Bergström, J. and Vomhoff, H. (2007) 'Experimental hydrocyclone flow field studies', *Separation and Purification Technology*, 53, (1), pp. 8-20.

Boysan, F., Ewan, B. C. R., Swithenbank, J. and Ayers, W. H. (1983) ' Experimental and Theoretical Studies of Cyclone Separator Aerodynamics' *Institution of Chemical Engineers Symposium Series*. Birmingham, West Midl, England.

Bradley, D. and Pulling, D. J. (1994) 'Flow patterns in the hydrocyclone and their interpretation in terms of performance', *Transactions of the Institution of Chemical Engineers*, (37), pp. 34-45.

Brennan, M. S., Narasimha, M. and Holtham, P. N. (2007) 'Multiphase modelling of hydrocyclones - prediction of cut-size', *Minerals Engineering*, 20, (4), pp. 395-406.

- Bröder, D. and Sommerfeld, M. (2002) 'Experimental studies of bubble interaction and coalescence in a turbulent flow by an imaging PIV/PTV system', *Exp. Fluids* 33, pp. 826 -837.
- Chang, F. and Dhir, V. K. (1994) 'Turbulent flow field in tangentially injected swirl flows in tubes', *International Journal of Heat and Fluid Flow*, 15, (5), pp. 346-356.
- Chen, J., Haynes, B.S and Fletcher, D.F (1999), 'A numerical and experimental study of tangentially injected swirling pipe flows, 2nd Intl Conf CFD in the Minerals and Process Industries, CSIRO, Melbourne, Dec 1999, pp 485-490
- Chen, M., Mees, P. A. and Kresta, S. M. (1999) *Proceedings of the 3rd ASME/JSME Joint Fluids Conference, San Francisco, California, USA,*
- Chine, B. and Concha, F. (2000) 'Flow patterns in conical and cylindrical hydrocyclones', *Chemical Engineering Journal*, 80, (1-3), pp. 267-273.
- Choudhury, D. (1993) 'Introduction to the Renormalization Group Method and Turbulence Modeling', Fluent Inc. Technical Memorandum, TM.107.
- Chuah, T.G, Gimbin, J., Choong, T.S.Y and Fakhrul-razi, A. (2003) 'Numerical Prediction of Cyclone Pressure Drop' *Journal of Chemical Engineering and Environments*, Vol. 2, No. 2 pp. 67-71.
- Claypole, T.C. and Syred, N. (1981) 'The Effect of Swirl Burner Aerodynamic on NOx Formation', *18th Symposium on Combustion*. The Combustion Institute.
- Coker, A. K. (1993) 'Computer Program Enhances Guidelines for Gas-Liquid Separation Designs', *Oil & Gas Journal*.
- Cokljat, D., Slack, M., Vasquez, S. A., Bakker, A. and Montante, G. (2006) 'Reynolds-stress model for Eulerian multiphase', *Progress in Computational Fluid Dynamics*, 6, (1-3), pp. 168-178.

Cole-Parmer (2010) 'Technical Resource, Cole-Parmer Instrument Co. Ltd', London, UK.

Concha, F. (2007) 'Flow Pattern in Hydrocyclones', *Kona-Powder and Particle*, 25, pp. 97-132.

Cortes, C., Gil, A. (2007) Modelling the particle flow inside cyclone separators. *Progress in energy and combustion Science* (33).

Coulson, J.M; Harker, J.H; Backhurst, J.R; Richardson, J.R (2002) 'Chemical engineering. Vol. 2, Particle technology and separation processes' 5th ed. Oxford: Butterworth-Heinemann

Coupland, J. (2004) 'Food Chemistry Course Materials, (FDSC 400)', website for fall 2004 https://www.courses.psu.edu/fd_sc/fd_sc400_jnc3/dispersion/3Dispersed%20systems.pdf

Crowe, C.S., M; Tsuji, Y (ed.) (1998) '*Multiphase flows with droplets and particles*' London CRC Press.

Cullivan, J. C., Williams, R. A. and Cross, C. R. (2003a) 'New insights into hydrocyclone operation', *Particulate Science and Technology*, 21, (1), pp. 83-103.

Cullivan, J. C., Williams, R. A. and Cross, C. R. (2003b) 'Understanding the hydrocyclone separator through computational fluid dynamics', *Chemical Engineering Research and Design*, 81, (4), pp. 455-466.

Cullivan, J. C., Williams, R. A., Dyakowski, T. and Cross, C. R. (2004) 'New understanding of a hydrocyclone flow field and separation mechanism from computational fluid dynamics', *Minerals Engineering*, 17, (5), pp. 651-660.

Dabir, B. and Petty, C. A. (1984) 'Laser Doppler anemometry measurements of tangential and axial velocities in a hydrocyclone operating without an air core', 2nd International Conference on Hydrocyclones, Bath, England, Sept. 19-21, 1984.

Dai, G. Q., Li, J. M. and Chen, W. R. (1999) 'Numerical prediction of the liquid flow within a hydrocyclone', *Chemical Engineering Journal*, 74, (3), pp. 217-223.

Davidson, M. R. (1988) 'Numerical calculations of flow in a hydrocyclone operating without an air core', *Applied Mathematical Modelling*, 12, (2), pp. 119-128.

Davidson, M. R. (1995) 'An adaptive method of predicting the air core diameter for numerical models of hydrocyclone flow', *International Journal of Mineral Processing*, 43, (3-4), pp. 167-177.

De Souza, F. J. and Neto, A. S. (2002) 'Large eddy simulations of a hydrocyclone' Proceedings of FEDSM 2002, *American Society of Mechanical Engineers, Fluids Engineering Division (Publication) FED*. Montreal, Que.,

Delgadillo, J. A. and Rajamani, R. K. (2007) 'Exploration of hydrocyclone designs using computational fluid dynamics', *International Journal of Mineral Processing*, 84, (1-4), pp. 252-261.

Delgadillo, J. A. and Rajamani, R. K. (2009) 'Computational fluid dynamics prediction of the air-core in hydrocyclones', *International Journal of Computational Fluid Dynamics*, 23, (2), pp. 189-197.

Devulapalli, B. and Rajamani, R. K. (1996) 'A Comprehensive CFD Model for Particle Size Classification in Industrial Hydrocyclones', *Hydrocyclones '96*. pp. pp. 83-104.

Dinesh Suresh, P., Kumar, V., Sripriya, R., Chakraborty, S. and Meikap, B. C. (2010) 'Performance characteristics of pilot plant dense media hydrocyclone for beneficiation of coal and 3-D CFD simulation', *Chemical Engineering Science*, 65, (16), pp. 4661-4671.

Dlamini, M. F., Powell, M. S. and Meyer, C. J. (2005) 'A CFD simulation of a single phase hydrocyclone flow field', *Journal of The South African Institute of Mining and Metallurgy*, 105, (10), pp. 711-717.

- Dueck, J., Schneider, M. and Neeße, T. (2003) 'Numerical calculation of the umbrella and rope discharge of a hydrocyclone', *Numerische berechnung von schirm- und strangaustrag eines hydrozyklons*, 44, (8), pp. 12-21.
- Dyakowski, T. and Williams, R. A. (1993) 'Modelling turbulent flow within a small-diameter hydrocyclone', *Chemical Engineering Science*, 48, (6), pp. 1143-1152.
- Erdal, F. M. (2001) ‘*Local Measurements and Computational Fluid Dynamic Simulations in a Gas–Liquid Cylindrical Cyclone Separator*,’ Ph.D. dissertation, The University of Tulsa.
- Fan, L.S and Zhu, C (1998) ‘Principle of Gas-Solid Flows’ Cambridge University Press
- Ferziger, J. H. and Peric, M. (2002) *Computational methods for fluid dynamics*. 3rd, ed Berlin, London: Springer.
- Fisher, M. J. and Flack, R. D. (2002) 'Velocity distributions in a hydrocyclone separator', *Experiments in Fluids*, 32, (3), pp. 302-312.
- Garcia, J. C., Sierra, F. Z., Kubiak, J. and Juárez, D. (2003) 'Separating Three Phase Cyclones from the Rest', *Fluent News*.
- Gatski, T. B., Hussaini, M. Y. and Lumley, J. L. (1996) *Simulation and modeling of turbulent flows*. New York: Oxford University Press.
- Green, R. and McAlister, K. W. (2004) *Systematic Errors in Stereo PIV When Imaging through a Glass Window*. Ames Research Centre, Moffett Field, California 94035-1000:
- Gui, L. and Merzkirch, W. (1996) 'Phase separation of PIV measurements in two-phase flow by applying a digital mask technique ', *ERCOFTAC Bull.*, 30, pp. 45-48.
- Halter, E.J (1966), “Separation Handbook” 1st ed. Burgess Manning Company
- Hargreaves, J. H. and Silvesters, R. S. (1990) 'Computational fluid dynamics applied to the analysis of deoiling hydrocyclone performance.', *Trans. Inst. Chem. Eng*, 68, pp.

365–383.

Hassan, Y. A. (2002) 'Multiphase Bubbly Flow Visualization Using Particle Image Velocimetry', *Annual New York Academy of Sciences.*, 972.

Hassan, Y. A., Schmidl, W. and Ortiz-Villafuerte, J. (1998) 'Investigation of three-dimensional two-phase flow structure in a bubbly pipe flow', *Measurement Science and Technology*, 9, (3), pp. 309-326.

Hassan, Y. A., Schmidl, W.D and Ortiz- Villafuerte, J. (1999) 'Three Dimensional Bubbly Flow Measurement Using PIV', *Journal of Visualization*, 1, (3), pp. 291 - 301.

Harasek, M., Horvath, A., Jordan, C. (2004) '*Investigation of dependence of gas flow on the geometry of cyclonic separators by CFD simulation*'. Paper presented at the CHISA 2004 - 16th International Congress of Chemical and Process Engineering.

He, P., Salcudean, M. and Gartshore, I. S. (1999) 'A numerical simulation of hydrocyclones', *Chemical Engineering Research & Design*, 77, (A5), pp. 429-441.

Hewitt, G. F. and Vassilicos, J. C. (2005) '*Prediction of turbulent flows*'. Cambridge: Cambridge University Press.

Hinze, J. (ed.) (1975) '*Turbulence*'. New York: McGraw-Hill Publishing Co.

Hirt, C. W. and Nichols, B. D. (1981) 'Volume of fluid (VOF) method for the dynamics of free boundaries', *Journal of Computational Physics*, 39, (1), pp. 201-225.

Hreiz, R., Gentric, C. and Midoux, N. (2011) 'Numerical investigation of swirling flow in cylindrical cyclones', *Chemical Engineering Research and Design*, 89, (12), pp. 2521-2539.

Hsieh, K. T. (1988) '*A Phenomenological model of the hydrocyclone*'. PhD Thesis. University of Utah, USA.

Hsieh, K. T. and Rajamani, R. K. (1991) 'Mathematical model of the hydrocyclone based on the physics of the fluid flow', *AIChE .J.*, 37, pp. 735-746.

Huang, H., Dabiri, D. and Gharib, M. (1997) 'On errors of digital particle image velocimetry', *Measurement Science and Technology*, 8, (12), pp. 1427-1440.

Huang, S. (2005) 'Numerical simulation of oil-water hydrocyclone using reynolds-stress model for Eulerian multiphase flows', *Canadian Journal of Chemical Engineering*, 83, (5), pp. 829-834.

Ito, S., Ogawa, K. and Kuroda, C. (1979) 'Decay Process of Swirling Flow in a Circular Pipe', *International Chemical Engineering*, 19, (4), pp. 600-611.

Jarrin, N. (2008) '*Synthetic inflow Boundary conditions for Numerical Simulation of Turbulence*'. Thesis. University of Manchester, UK.

JCGM (2009), 'Evaluation of measurement data — An introduction to the “Guide to the expression of uncertainty in measurement” and related documents, JCGM, 104:2009

Kader, B. (1981) 'Temperature and Concentration Profiles in Fully Turbulent Boundary Layers.', *Int. J. Heat Mass Transfer*, 24, (9), pp. 1541-1544.

Keane, R. D. and Adrian, R. J. (1992) 'Theory of cross-correlation analysis of PIV images', *Applied Scientific Research*, 49, (3), pp. 191-215.

Kelsall, D. F. (1952) 'A study of the motion of solid particles in a hydraulic cyclone', *Trans. Inst. Chem. Eng.*, 30, pp. 87- 108.

Kim, S. E. and Choudhury, D. (1995) 'A Near-Wall Treatment Using Wall Functions Sensitized to Pressure Gradient. ', *IASME FED Separated and Complex Flows*, ASME, 217.

Kitoh, O. (1991) 'Experimental Study of Turbulent Swirling Flow in a Straight Pipe', *J. Fluid Mech.*, 225, pp. 445-479.

Kompenhans, J., Kähler, C., Rodi, W. and Fueyo, N. (2002) 'Particle image velocimetry -An advanced experimental tool for the investigation of turbulent flow fields', in *Engineering Turbulence Modelling and Experiments*, 5, Oxford: Elsevier Science Ltd, pp. 79-94.

Kurokawa, J. (1995) 'Gas-Liquid Flow Characteristics and Gas-Separation Efficiency in a Cyclone Separator', *American Society of Mechanical Engineers, Fluid Engineering Division Summer Meeting*, 225, pp. 51-57.

Lauder, B. E. and Spalding, D. B. (1974) 'The numerical computation of turbulent flows', *Computer Methods in Applied Mechanics and Engineering*, 3, (2), pp. 269-289.

Lawson, N. J. and Wu, J. (1997) 'Three-dimensional particle image velocimetry: Experimental error analysis of a digital angular stereoscopic system', *Measurement Science and Technology*, 8, (12), pp. 1455-1464.

Leeuwner, M. J. and Eksteen, J. J. (2008) 'Computational fluid dynamic modelling of two phase flow in a hydrocyclone', *Journal of The South African Institute of Mining and Metallurgy*, 108, (4), pp. 231-236.

Lim, E.W, Chen, Y-Ren, Wang, C.H and Wu, R.M, W. (2010); 'Experimental and Computational Studies of Multiphase Hydrodynamics in a Hydrocyclone Separator System' *Chemical Engineering Science*, 65, pp. 6415-6424.

Lindken, R., Gui, L. and Merzkirch, W. (1999) 'Velocity measurements in multiphase flow by means of particle image velocimetry', *Chemical Engineering and Technology*, 22, (3), pp. 202-206.

Liu, H. S., Ai, Z. J., He, H. Q. and Xiao, L. (2006a) 'Numerical simulation of the inner flow field in the single-cone hydrocyclone for oil-water separation', *Xi'an Shiyou Daxue Xuebao (Ziran Kexue Ban)/Journal of Xi'an Shiyou University, Natural Sciences Edition*, 21, (6), pp. 83-86.

Liu, X., Tan, R., Liu, Y. and Zhao, L. (2006b) 'Numerical simulation on flowing distribution characteristics of separated medium inside the Hydrocyclone', *Shiyou Xuebao/Acta Petrolei Sinica*, 27, (2), pp. 129-132-136.

Liu, Z., Jiao, J., Zheng, Y., Zhang, Q. and Jia, L. (2006c) 'Investigation of turbulence characteristics in a gas cyclone by stereoscopic PIV', *AIChE Journal*, 52, (12), pp. 4150-4160.

Malhotra, A., Branion, R. M. R. and Hauptman, E. G. (1994) 'Modelling the flow in a hydrocyclone', *The Canadian Journal of Chemical Engineering*, (72), pp. 953-960.

Mantilla, I., Shirazi, S. A. and Shoham, O. (1999) 'Flow Field Prediction and Bubble Trajectory Model in Gas-Liquid Cylindrical Cyclone (GLCC) Separators' Proceedings of the ASME Energy Resources Technology Conference and Exhibition. Houston, Texas:

McQuillen, J.B, Vernon, R, Dukler, A.E (1981) 'Two Phase Flow Regimes in Reduced Gravity', NASA Lewis Research Centre Motion Picture Directory 1704.

Melling, A. (1997) 'Tracer particles and seeding for particle image velocimetry', *Measurement Science and Technology*, 8, (12), pp. 1406-1416.

Meyer, M. and Bohnet, M. (2002) 'Einfluss von Tropfengrößenverteilung und Konzentration der dispersen Phase auf die Flüssig/Flüssig-Trennung im Hydrozyklon, ' *Chemie-Ingenieur-Technik*, 74, (1-2), pp. 95-100.

Millington, B. C. and Thew, M. T. (1987) 'Preliminary Investigations on a Cyclone for Steam-Water Cyclone Separators' *Proceeding of the 3rd International Conference on Multiphase Flow*. The Hague, Netherlands, pp. 115-125.

Monredon, T. C., Hsieh, K. T. and Rajamani, R. K. (1992) 'Fluid flow model of the hydrocyclone: an investigation of device dimensions', *International Journal of Mineral Processing*, 35, (1-2), pp. 65-83.

Motta, B. R., Erdal, F. M., Shirazi, S. A., Shoham, O. and Rhyne, L. D. (1997) 'Local Velocity Measurements and Computational Fluid Dynamics (CFD) Simulations of Swirling Flow in a Cylindrical Cyclone Separator' *American Society of Mechanical Engineers, Fluids Engineering Division (Publication)* Vancouver, Canada.

Mousavian, S. M. and Najafi, A. F. (2008a) 'Influence of geometry on separation efficiency in a hydrocyclone', *Archive of Applied Mechanics*, 79(11) pp.1033-1050.

Mousavian, S. M. and Najafi, A. F. (2008b) 'Numerical simulations of gas-liquid-solid flows in a hydrocyclone separator', *Archive of Applied Mechanics*, 79(5) pp.395-409.

Nafaji, A.F, Mousavian, S.M and Amini, K. (2011) 'Numerical investigations on swirl intensity decay rate for turbulent swirling flow in a fixed pipe' *International Journal of Mechanical Sciences* (53)801–811

Narasimha, M., Brennan, M. and Holtham, P. N. (2006) 'Large eddy simulation of hydrocyclone-prediction of air-core diameter and shape', *International Journal of Mineral Processing*, 80, (1), pp. 1-14.

Nikuradse, J. (1933) 'Laws of flow in rough pipes', VDI Forschungsheft **361**. In translation, NACA TM 1292, 1950.

Nissan, A. H. and Bressan, V. P. (1961) 'Swirling Flow in Cylinders,' *AIChE. J.*, 7, pp. 543-547.

Patterson, P. A. and Munz, R. J.(1989) 'Cyclone Collection Efficiencies at very High Temperatures', *The Canadian Journal of Chemical Engineering*, Vol. 67, pp. 321-328.

Peng, W., Hoffmann, A. C., Boot, P. J. A. J., Udding, A., Dries, H. W. A., Ekker, A. and Kater, J. (2002) 'Flow pattern in reverse-flow centrifugal separators', *Powder Technology*, 127, (3), pp. 212-222.

Peng, W., Hoffmann, A. C., Dries, H., Regelink, M. and Foo, K. K. (2007) 'Reverse-flow centrifugal separators in parallel: Performance and flow pattern', *AIChE Journal*,

53, (3), pp. 589-597.

Pericleous, K. A. (1987) 'Mathematical simulation of hydrocyclones', *Applied Mathematical Modelling*, 11, (4), pp. 242-255.

Pericleous, K. A. and Rhodes, N. (1986) 'The hydrocyclone classifier - A numerical approach', *International Journal of Mineral Processing*, 17, (1-2), pp. 23-43.

Perry's Chemical Engineers' Handbook, 6th Edition, McGraw-Hill, New York, 1984, Chap. 18, pp.48-56.

Pope, S. B. (2000) '*Turbulent flows*'. Cambridge ; New York: Cambridge University Press.

Prasad, A. K. (2000a) 'Particle Image Velocimetry', *current Science*, 79, (1), pp. 51-60.

Prasad, A. K. (2000b) 'Stereoscopic Particle Image Velocimetry', *Experiments in Fluids*, 29, pp. 103-116.

Prasad, A. K. (2000c) 'Stereoscopic particle image velocimetry', *Experiments in Fluids*, 29, (2), pp. 103-116.

Prasad, A. K. and Jensen, K. (1995) 'Scheimpflug Stereocamera for Particle Image Velocimetry in Liquid Flows.', *Applied Optics*, 34, (30), pp. 7092 - 7099.

Raffel, M., Willert, C. and Kompenhans, J. (1998) *Particle Image Velocimetry: A Practical Approach*. London: Springer.

Rajamani, R. K. and Devulapalli, B. (1995) 'Hydrodynamic Modeling of Swirling Flow and Particle Classification in Large-Scale Hydrocyclones', *KONA Powder and Particle* 12, pp. 95-104.

Reyes-Gutiérrez, M. A., Rojas-Solórzano, L. R., Colmenares, J., Marín-Moreno, J. C. and Meléndez-Ramírez, A. J. (2006) 'Eulerian-Eulerian modeling of disperse two-phase

flow in a gas-liquid cylindrical cyclone', *Journal of Fluids Engineering, Transactions of the ASME*, 125, pp. 832-838.

Richardson, L. F. (1922) '*Weather Prediction by Numerical Process*'. Cambridge University Press.

Sayda, A.F and Taylor, J.H (2007) 'Modeling and Control of Three-Phase Gravity Separators in Oil Production Facilities' American Control Conference, July 2007, pp.4847-4853

Schiller, L. and Naumann, Z. (1935) 'Z. Ver. Deutsch. Ing', 77, pp. 318.

Schmitt, F. G. (2007) 'About Boussinesq's turbulent viscosity hypothesis: historical remarks and a direct evaluation of its validity', *Comptes Rendus - Mecanique*, 335, (9-10), pp. 617-627.

Schweitzer, P.A (1997) '*Handbook of Separation Techniques for Chemical Engineers*' Mc- Graw Hill Company, Inc.

Siangsananun, V., Guigui, C., Morchain, J., Marteil, P., Levecq, C., Puprasert, C. and Hébrard, G. (2011) 'Velocity measurement in the hydrocyclone by oil droplet, doppler ultrasound velocimetry, and CFD modelling', *Canadian Journal of Chemical Engineering*, 89, (4), pp. 725-733.

Sierra, F. Z., Juarez, D., Garcia, J. C., Kubiak, J. and Nicolas, R. (2003) 'A computational analysis of multiphase flow cyclonic separator for clean combustion in power plants', *Proceedings of the 2003 International Joint Power Generation Conference*. Atlanta, GA, pp. 701-708.

Slack, M., Cokljat, D. and Vasquez, S. A. (2003) 'Reynolds-Stress Model for Eulerian Multiphase,' *Proc 4th Int. Symp on Turbulence Heat and Mass Transfer*. Begell House Inc, pp. 1047-1054.

Slack, M. D. (1997) '*Separation of particles from liquids by the solid core cyclone*' Thesis. Newcastle University, UK.

Slack, M. D., Del Porte, S. and Engelman, M. S. (2004) 'Designing automated computational fluid dynamics modelling tools for hydrocyclone design', *Minerals Engineering*, 17, (5), pp. 705-711.

Slack, M. D., Prasad, R. O., Bakker, A. and Boysan, F. (2000) 'Advances in cyclone modelling using unstructured grids', *Chemical Engineering Research and Design*, 78, (8), pp. 1098-1104.

Slack, M. D. and Wraith, A. E. (1997) 'Modelling the velocity distribution in a hydrocyclone', *4th International Colloquium on Process Simulation*, 11–13 June, Espoo Finland, pp. 65–83.

Small, D. M. and Thew, M. T. (1995) 'The Influence of Swirl and Turbulent Anisotropy on CFD Modelling for Hydrocyclones'.

Solero, G. and Coghe, A. (2002) 'Experimental fluid dynamic characterization of a cyclone chamber', *Experimental Thermal and Fluid Science*, 27, (1), pp. 87-96.

Soloff, S. M. A., R J and Liu,Z-C (1997) 'Distortion compensation for generalized stereoscopic particle image velocimetry', *Meas. Sci. Technol.* , 8 pp. 1441–1454.

Stanislas, M. a. M., J C (1997) 'Practical aspects of image recording in particle image velocimetry', *Meas. Sci. Technol.*, 8, pp. 1417–1426.

Suasnabar, D. (2000) '*Dense Medium Cyclone Performance, Enhancements via Computational modeling of the physical process*'. Thesis. University of New South Wales.

Syamlal, M., Rogers, W. and J., O. B. T. (1993) '*MFIx Documentation: Volume 1, Theory Guide*' National Technical Information Service, Springfield, VA, .DOE/METC-9411004, NTIS/DE9400087.

Taylor, J. R. (ed.) (1982) '*An Introduction to Error Analysis*'. California.: University Science Books, Mill Valley

Tennekes, H. and Lumley, J. L. (1972) '*A first course in turbulence*'. Cambridge, Mass.,: MIT Press.

Theodore, L. (1971) '*Transport phenomena for engineers*' Scranton,,: International Textbook Co.

TSI Inc. (2006) *Model 640050 Stereoscopic PIV Camera System*.

Tu, J., Yeoh, G.H, and Liu, C. (2008) 'Computational Fluid Dynamics: A Practical Approach' First edition, Elsevier Inc. Oxford UK.

Utikar, R., Darmawan, H., Tade, M., Li, Q., Evans, G., Glenny, M. and Pareek, V. (eds.) (2010) '*Hydrodynamic Simulation of Cyclone Separators*' Computational Fluid Dynamics, Book edited by: Hyoung Woo OH, ISBN 978-953-7619-59-6, www.intechopen.com

Van Dyke, M. (1982) '*An Album of Fluid Motion*'. The Parabolic Press, Stanford, California, USA.

Vazquez, C. O. (2001) '*Multiphase flow separation in Liquid-Liquid cylindrical cyclone and Gas-Liquid -Liquid cylindrical cyclone compact separators*' Thesis. The University of Tulsa.

Versteeg, H. K. and Malalalsekera, W. (2007) '*An introduction to computational fluid dynamics : the finite volume method*' Harlow Prentice Hall, 2007.

Veil, J.A., M.G. Puder, D. Elcock, and Redweik, R.J (2004) 'A White Paper Describing Produced Water from Production of Crude Oil, Natural Gas, and Coal Bed Methane', prepared by Argonne National Laboratory for the U.S. Department of Energy, National Energy Technology Laboratory.

Wang, S., Fang, M., Luo, Z., Li, X., Ni, M., Chen K.(1999) 'Instantaneous separation model of a square cyclone', *Powder Technology* (102), 65-70.

Wang, B. and Yu, A. B. (2008) 'Numerical study of the gas-liquid-solid flow in hydrocyclones with different configuration of vortex finder', *Chemical Engineering Journal*, 135, (1-2), pp. 33-42.

Westerweel, J. (1997) 'Fundamentals of digital particle image velocimetry', *Measurement Science and Technology*, 8, (12), pp. 1379-1392.

Wilcox, D. C. (1993) '*Turbulence modeling for CFD*'. La Canada, DCW Industries Inc.

Willert, C. (1997) 'Stereoscopic digital particle image velocimetry for application in wind tunnel flows', *Meas. Sci. Technol.* , 8, pp. 1465–1479.

Xiang, R. B., Lee, K.W. (2005) 'Numerical study of flow field in cyclones of different height'. *Chem. Eng. Sci.*, 44, 877-883.

Yakhot, V. and Orszag, S. A. (1986) 'Renormalization Group Analysis of Turbulence: I. Basic Theory', *Journal of Scientific Computing*, 1, (1), pp. 1-51.

Yakhot, V., Orszag, S. A., Thangam, S., Gatski, T. B. and Speziale, C. G. (1992) 'Development of turbulence models for shear flows by a double expansion technique', *Physics of Fluids A*, 4, (7), pp. 1510-1520.

Zhao, H. Q., Li, Z. L. and Sun, H. Y. (2007) 'Numerical simulation of flow field in downhole hydrocyclone oil-gas separator', *Zhongguo Shiyou Daxue Xuebao (Ziran Kexue Ban)/Journal of China University of Petroleum (Edition of Natural Science)*, 31, (4).

Zhao, B., Su, Y., Zhang, J. (2006). 'Simulation of gas flow pattern and separation efficiency in cyclone with conventional single and spiral double inlet configuration' *Chemical Engineering research and Design*, A12 (84), 1158-1165.

